DTU Library

Characterization of atmospheric turbulence using nacelle-lidar measurements and applications

Fu, Wei

Link to article, DOI:
[10.11581/DTU.00000273](10.11581/DTU.00000273)

Publication date:
2023

Document Version
Publisher's PDF, also known as Version of record

Link back to DTU Orbit

Citation (APA):
Fu, W. (2023). *Characterization of atmospheric turbulence using nacelle-lidar measurements and applications*. Technical University of Denmark. https://doi.org/10.11581/DTU.00000273

Characterization of atmospheric turbulence using nacelle-lidar measurements and applications

Wei Fu
PhD Thesis

Preface

This Doctor of Philosophy (PhD) thesis was prepared at the Department of Wind and Energy Systems at the Technical University of Denmark (DTU) and external stays at the Renewable Energy Systems and at the Flensburg University of Applied Science to fulfill the requirements for acquiring a PhD degree. The presented work was done between April 2020 and April 2023, and was supervised by Alfredo Peña, with co-supervision from Jakob Mann and David Schlipf. The research conducted in this PhD thesis was supported by the project LIKE (Lidar Knowledge Europe) H2020-MSCA-ITN-2019 with Grant number 858358 funded by the European Union.

The thesis contains Part I (synopsis) and Part II (scientific manuscripts). Part I gives an overview of the PhD project and defines the research objectives, hypotheses, and research questions, followed by the summary of methods, the description of analyzed measurements, and the summary of the main findings. Part I finishes with an overall conclusion, possible industrial applications, and an outlook for future research. Part II contains five scientific manuscripts and a list summarizing conference and workshop contributions.

Wei Fu
Risø, April 2023

Abstract

Atmospheric turbulence, i.e., the random fluctuations of the wind, impacts both the power output and the structural load of wind turbines. Understanding and characterizing atmospheric turbulence are essential for the assessment of site conditions, to effectively use wind energy, and to evaluate the structural integrity of wind turbine components. Traditionally, anemometers mounted on meteorological masts are used to measure turbulence. However, with the increasing size of modern wind turbines, installing and operating meteorological masts that reach 200 m above the ground are very expensive and infeasible, especially offshore. In those cases, lidar is a cost-effective alternative to mast-mounted anemometers. Particularly, nacelle-based lidars have the advantage that they yaw with the wind turbine and track the inflow. Therefore, they have the potential to better characterize the flow that actually interacts with the turbine than in-situ anemometers on masts.

This thesis presents research on characterizing atmospheric turbulence using measurements from nacelle lidars and applications for wind turbine control and wake studies. The thesis objectives are (1) to investigate the methodologies to characterize atmospheric turbulence from nacelle-lidar measurements, (2) to study the impact of nacelle lidar scanning strategies on characterizing atmospheric turbulence, and (3) to make the best use of a single-beam lidar for wind turbine control and wake studies. Virtual and field measurements of nacelle lidars and aero-elastic wind turbine simulations are used to achieve these objectives.

The study in this thesis demonstrates that different nacelle lidars are able to measure the along-wind variance as well as a sonic anemometer, if the Doppler spectra of the radial velocities are used to account for the probe volume averaging effect. Nacelle lidars with more than six beams and two different beam opening angles are able to accurately estimate the Reynolds stress tensor following a least-square procedure. The best estimations of the six Reynolds stresses are found by a six-beam lidar measuring at a close focus distance with a large opening angle. These findings help lidar users to obtain accurate and detailed turbulence characteristics, which benefit wind turbine power performance assessments and optimizations, load validations and wind turbine design, and wind resource assessments in met-ocean applications.

Furthermore, the study shows that a single-beam lidar mounted in the wind turbine spinner achieves much more control benefits compared to the same lidar based on the nacelle. Being lower in cost and more flexible, the single-beam lidar in the spinner performs similarly to a four-beam nacelle lidar for feedforward pitch control. In addition, by using measurements from an inland wind farm, the study shows that the wake-induced power deficit of the downstream wind turbine decreases with increasing turbulence intensity, which is measured by a single-beam nacelle lidar on the upstream wind turbine. These findings demonstrate the potential of using a single-beam lidar for wind turbine control and wake studies.

Acknowledgements

Contents

Part I

Synopsis

1 | **Introduction**

1.1 Motivation

Climate change and the global energy crisis are promoting independence from fossil fuels and accelerating the renewable energy transition, in which wind along solar energy are seen as important pillars for a sustainable future. Wind energy has been growing exponentially in the past decades. Now wind power helps the world reduce carbon dioxide emissions by over 1.2 billion tonnes a year (Global Wind Energy Council, 2022) and meets 17% of Europe's electricity demand annually (WindEurope, 2023). Wind power is not only a cost-effective resource for electricity in our daily lives but is also used for water pumping, oil and gas platforms powering, and hydrogen production.

To effectively harvest wind power, it is essential to measure and understand the flow upcoming to the rotor plane. Atmospheric turbulence, i.e., the random fluctuation of the wind, impacts both the power output (Gottschall et al., 2008; Wagner et al., 2015) and the structural loads (Conti et al., 2021; Conti et al., 2020; Dimitrov et al., 2019; Sathe, Mann, et al., 2013) of wind turbines. Thus, accurate turbulence characteristics can potentially optimize wind turbines' energy yields and extend their lifetime. Atmospheric turbulence characteristics are also useful for studying wind profiles (Peña, 2009; Wyngaard, 2010) and test flow models (Mann, 1994) in the atmospheric boundary layer. In addition, aviation engineering (Wang et al., 2022) and bridge engineering (Cheynet et al., 2016) benefit from turbulence measurements for safety considerations.

Turbulence typically has a length scale from ten to a few hundred meters and a time scale from one to ten minutes (see Fig. 1.1). Under the assumption of statistical stationarity, turbulence can be characterized by the Reynolds stress tensor, which contains the second-order statistics (variances and covariances) of the three-dimensional wind components. The traditional way to measure turbulence is using in-situ anemometers, such as cup and sonic anemometers, installed on the upwind meteorological masts (met-masts) (International Electrotechnical Commission, 2019). However, with the increasing size of modern wind turbines (Vestas, 2022), installing and operating a met-mast at heights over 200 m are very expensive and infeasible, especially offshore, since large foundations are needed to support the masts. The masts are also vulnerable to high winds and they cannot be easily moved from one place to another. Thus, it becomes quite challenging to collect measurements at different locations or at heights that extend to the top of a very large rotor.

Coherent Doppler lidar (hereafter lidar, which stands for light detection and ranging) is a type of remote-sensing device that measures wind velocity by emitting a coherent light beam and detecting the laser signals backscattered from natural aerosols in the atmosphere. Com-

2
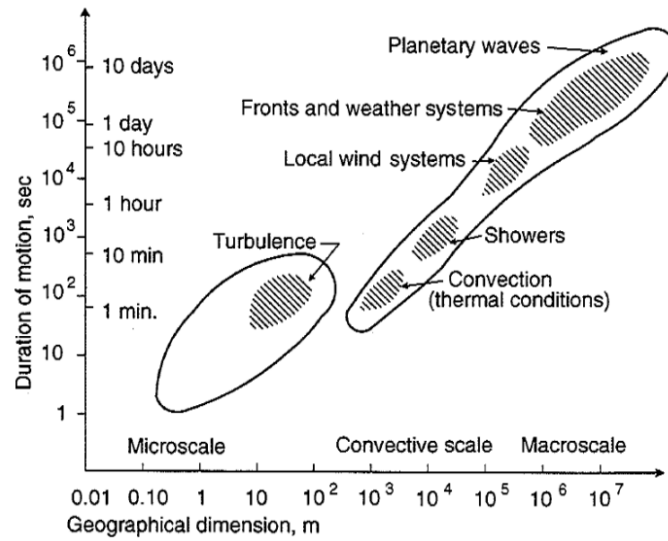
Figure 1.1: Overview of the fluctuations' length scales and durations in the atmosphere, adopted from Berg et al., 2022.

pared to met masts, lidars are able to scan the atmospheric flow with high spatial resolution. Lidars are also compact, portable, and safe in high winds. Nowadays, the use of nacelle-mounted lidar systems becomes one of the key technologies for various applications. An advantage of the forward-looking nacelle lidars is that they yaw with the wind turbine and track the inflow. Therefore, they have the potential to better characterize the flow that actually interacts with the wind turbine. In addition, nacelle lidars can provide a preview of the approaching wind, which is useful for wind turbine control to react to the disturbance before the aerodynamic impacts on the turbine structures occur.

1.2   Background

Nacelle lidars in different types and configurations have proven to be precise for measuring wind speeds and wind profiles (Bossanyi et al., 2012; Mikkelsen et al., 2013) for improving wind turbine power performance assessment (Borraccino et al., 2017; Wagner et al., 2014), supporting wind turbine control (Harris et al., 2007; Held et al., 2019; Schlipf, 2016; Simley, 2015), and reducing the uncertainty of load validations (Dimitrov et al., 2019; Dimitrov et al., 2016). Using nacelle lidars to estimate second-order statistics has not yet been widely accepted.

A common practice to estimate the second-order statistics using lidars could be by taking the variance of the mean wind velocity reconstructed from the lidar measurements. However, two effects can contribute to the systematic error of the estimations. First, the probe volume inherent to a lidar system is generally larger compared to sonic anemometers. Consequently, lidar measurements are the weighted average of wind velocities sampled along the laser beam. The probe volume acts like a 'low-pass filter' such that the high-frequency velocity variations cannot be detected. Therefore, the second-order statistics computed from lidar radial velocities are attenuated compared to those from cup or sonic anemometers. Those estimates are

called the 'filtered' variances. Second, one lidar beam only measures the wind velocity along its radial axis, which is usually not along any wind components. Thus, the radial velocity variance can be 'contaminated' by the correlations of different wind vector components (Kelberlau et al., 2020; Sathe & Mann, 2013) and consequently be higher or lower than the along-wind variance depending on the beam orientations. When combining radial measurements in different directions to estimate turbulence, 'correct' values can be obtained for the 'wrong' reason.

Two types of nacelle lidars are extensively used in wind energy applications, namely the continuous-wave (CW) and pulsed lidar systems. As implied in their names, the two systems mainly differ in their emission waveform, which is closely related to their probe volume and scanning patterns. CW lidars operate by focusing a continuously transmitting laser beam at a particular range. They scan at one point at a time at a high sampling rate. The probe volume associated with the focal depths increases quadratically with the measurement range (Sjöholm et al., 2009; Sonnenschein et al., 1971). Thus, the CW lidars usually measure wind speed accurately within a range of approximately $10 - 200$ m (Sathe, Banta, et al., 2015). Pulsed lidars emit short laser pulses in bursts in the atmosphere. The backscattered signals from several given distances can be detected, which are informed by the time delays between the pulse start and measurement time (Peña et al., 2015). Thus, pulsed lidars are capable of measuring at multiple distances all at once, but they require longer sampling time than the CW lidars. The probe volume of the pulsed lidars remains constant regardless of the measurement ranges. They can measure the wind from $40 - 50$ m up to a few kilometers.

Some recent studies put substantial efforts toward overcoming the barriers of using nacelle lidars to measure second-order statistics. Mann et al., 2010 demonstrated a method to circumvent the probe volume averaging effect for a conically scanning CW lidar. The method is based on the assumption that the lidar Doppler spectrum is equal to the probability density function of the radial velocities in the probe volume. This method was tested experimentally by Branlard et al., 2013, which accounts for the probe volume averaging effect and provides estimates of the 'unfiltered' variances. Using the Doppler spectra of a conically scanning CW lidar, Peña et al., 2017 showed that the lidar-estimated 'unfiltered' along-wind variance had a bias of just 2% compared to that from a cup anemometer installed on a nearby met mast. However, the authors found that other lidar-estimated Reynolds stresses do not agree with those from a mast-based sonic anemometer partly due to the lidar scanning configuration.

To estimate all Reynolds stresses using lidars, Sathe, Mann, et al., 2015 proposed a six-beam method for a ground-based lidar based on the study of Eberhard et al., 1989. The method needs radial measurements at five equally spaced azimuth angles over the lidar scanning cone and measurements from a vertical beam in the center of the cone. The beam orientations were optimized using an objective function that minimizes the total random errors of Reynolds stress estimations. Moreover, Peña et al., 2019 showed that the nacelle-based SpinnerLidar, i.e., a research Doppler wind lidar that scans the wind turbine inflow in very high spatial and temporal resolutions, is able to estimate all Reynolds stresses accurately following a least-square procedure.

The lidar scanning strategy influences not only turbulence estimations but also the wind preview quality for wind turbine control (Schlipf, Haizmann, et al., 2015). The wind preview can be evaluated by the coherence between the true rotor-effective wind speed (REWS) and the lidar-estimated one (Schlipf et al., 2013). The true REWS can be calculated from turbine measurements using the torque-balance method (Held et al., 2019) or defined as the spatially

averaged longitudinal wind component over the rotor-span area in aero-elastic simulations (Schlipf, 2016).

This thesis aims at exploiting the ability of forward-looking nacelle lidars for characterizing atmospheric turbulence. The thesis also shows the application of a single-beam forward-looking lidar for wind turbine control and wake studies. The findings from the thesis can ultimately help optimize wind turbines' energy capture and mitigate the loads on turbine structures.

2 | Objectives, hypotheses and research questions

The three main objectives of this thesis are described in this chapter. Short introductions for each scientific paper produced in the project are given at the end of this chapter.

2.1 Objectives

The first objective is *to investigate methodologies to characterize atmospheric turbulence from nacelle-lidar measurements.* As introduced in Section 1.2, previous studies showed the potential of nacelle lidars for measuring atmospheric turbulence. There is not yet a procedure that one can routinely follow to estimate the second-order statistics from nacelle-lidar measurements. A robust algorithm is needed to reconstruct the Reynolds stress tensor from lidar measurements, especially the along-wind variance, which is the key parameter for wind energy applications. Therefore, **Paper I-III** (Appendix A.1, A.2 and A.3) apply a least-square procedure to estimate Reynolds stresses from different nacelle lidars. The three papers aim to answer

- Can nacelle lidars provide the Reynolds stress tensor as accurately as a sonic anemometer at the turbine's hub height? If yes, how?

- How to accurately estimate the along-wind variance using nacelle lidars?

To achieve the *Objective 1*, a hypothesis is formulated:

> Hypothesis I:
> Nacelle lidars can be as accurate as a sonic anemometer to estimate the Reynolds stress tensor.

The second objective is *to study the impact of nacelle lidar scanning strategies on characterizing atmospheric turbulence.* Although the Reynolds stress tensor can be estimated using lidars relying on complex scanning patterns, e.g., the SpinnerLidar, they are too expensive to be widely used for turbulence characterization. Following **Paper I**, which shows the benefit of using multiple-beam lidar for turbulence estimation, **Paper II** and **Paper III** study comprehensively the dependence of Reynolds stress estimations on the main features of the lidar scanning strategy. The two papers aim to answer

- How does the lidar scanning pattern impact the turbulence estimations?

- What is the best way to scan the wind turbine's inflow for turbulence characterization?

To achieve the *Objective 2*, a hypothesis is formulated:

> Hypothesis II:
> A six-beam nacelle lidar measuring at a close distance with a large opening angle is the best way to scan the inflow for turbulence characterization.

The third objective is *to make the best use of a single-beam lidar for wind turbine control and wake studies*. A single-beam nacelle lidar is flexible and low in cost. If the along-wind characteristics are the features of interest, the nacelle lidar should measure ideally in parallel to the mean wind direction at the turbine's hub height. For feedforward pitch control that uses REWS, however, measurements along a single beam cannot well represent the flow interacting with the rotor. Therefore, **Paper IV** (Appendix A.4) and **Paper V** (Appendix A.5) focus on two different applications of a single-beam lidar and aim to answer

- How to best use a single-beam lidar for wind turbine feedforward control?

- Can we use a single-beam nacelle lidar to study the impact of the ambient turbulence intensity on the wake losses?

- Can we estimate the turbulence length scale from measurements of a single-beam lidar?

To achieve the *Objective 3*, two hypotheses are formulated:

> Hypothesis III:
> A single-beam spinner-based lidar can be as useful as a four-beam nacelle lidar for wind turbine control.

> Hypothesis IV:
> The wake-induced power deficit decreases with the increasing ambient turbulence intensity measured by a single-beam nacelle lidar.

2.2 Outline of the thesis

This thesis consists of two parts: the synopsis and the appendix. This chapter introduces the scope of the thesis. Chapter 3 provides the scientific background and Chapter 4 describes the analyzed measurements. Chapter 5 summarizes the essence of the research findings. The main research topics in the project are illustrated in Fig. 2.1, which spans from the estimation of Reynolds stresses using different nacelle lidars to the application of a single-beam lidar. Chapter 6 concludes the thesis and gives the outlook.

The appendix collects the conference and journal papers produced in this project. The attached papers are introduced below:

- **Paper I:** *Fu, W., Peña, A., and Mann, J.: Turbulence statistics from three different nacelle lidars, Wind Energy Science, 7, 831–848. (Fu, Peña, et al., 2022)*

  Through both numerical simulations and measurements, this study investigates the benefit of using multiple-beam nacelle lidars for measuring atmospheric turbulence. For the first time, Reynolds stress estimations of the multiple-beam SpinnerLidar are compared with those from two commercial nacelle lidars, which have two and four beams, respectively. Doppler spectra of the SpinnerLidar measurements are processed to account for the probe volume effect and to reduce the systematic error of turbulence estimations.
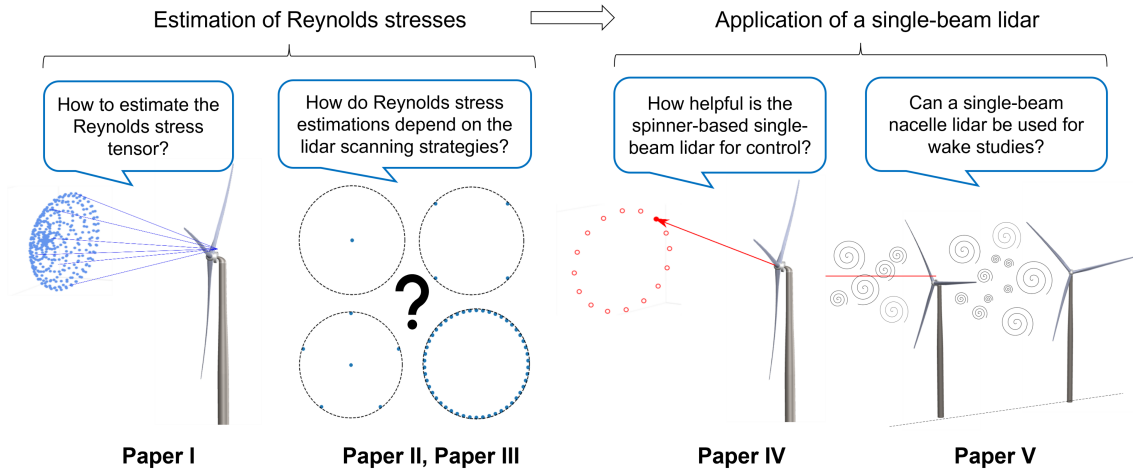
Figure 2.1: Main research topics in the project.

Then, a least-square procedure is used to compute the Reynolds stresses from three li-dars. We found that all three lidars can estimate well the along-wind variance. In addition, the SpinnerLidar is able to accurately measure all components in the Reynolds stress tensor.

- **Paper II:** *Fu, W., Sebastiani, A., Peña, A., and Mann, J.: Influence of nacelle-lidar scanning patterns on inflow turbulence characterization, Journal of Physics: Conference Series, 2265, 022 016. (Fu, Sebastiani, et al., 2022b)*

This study investigates the influence of nacelle-lidar scanning strategies on Reynolds stress estimations. Nacelle lidars with different numbers of beams, opening angles, and focus distances are simulated. The lidar probe volume is neglected. The Reynolds stresses are computed using the same least-square procedure as in **Paper I** and compared with those from a virtual sonic anemometer. Results show that a nacelle lidar with at least six beams and two different opening angles is needed to reconstruct all Reynolds stresses. Increasing the number of measurement points in the same beam directions has only a marginal effect on the estimations. Enlarging the beam opening angle improves the estimations on the transverse Reynolds stress components, whereas increasing the focus distance has the opposite effect.

- **Paper III:** *Fu, W., Sebastiani, A., Peña, A., and Mann, J.: Dependence of turbulence estimations on nacelle-lidar scanning strategies, Wind Energ. Sci. Discuss. (Fu, Sebastiani, et al., 2022a)*

Building upon **Paper II**, this work includes field measurements to comprehensively study the dependency of Reynolds stress estimations on the nacelle lidar scanning strategies. Apart from the number of measurement points, the opening angle, and the focus distance, this work also considers the probe volume of CW and pulsed lidars. Field measurements from the multiple-beam SpinnerLidar in **Paper I** are reused, and radial velocities at certain beam directions are carefully selected to mimic different scanning patterns

considered in the simulations. Results from field measurements validated our findings from the simulations. The best estimations of the six Reynolds stresses are provided by a 6-beam lidar measuring at a close distance with a large opening angle. In addition, the along-wind variance can be estimated well from all considered lidars.

- **Paper IV:** *Fu, W., Guo, F., Schlipf, D., and Peña, A.: Feedforward control for a 15-MW wind turbine using a spinner-mounted single-beam lidar.*

  This work demonstrates the usefulness of a single-beam lidar mounted in the spinner for feedforward pitch control compared to the same lidar on the nacelle. The single-beam lidar mounted in the spinner can rotate with the rotor and scan in a conical pattern in the wind turbine above-rated operations. Also, the spinner-based set-up avoids the blockage of lidar signals by the running blades. In this paper, we optimize the opening angle and focus distance of the spinner-based single-beam lidar for the best coherence between the lidar-estimated REWS and the true one. Then, the control benefits using the optimized lidar configurations are evaluated using time-domain simulations performed in OpenFAST. Results show that a single-beam lidar in the spinner brings much more control benefits than the one based on the nacelle, and the benefits are on the same level as a four-beam CW nacelle lidar for feedforward control.

- **Paper V:** *Fu, W., Peña, A., Mann, J., and Young, T.: Impact of the lidar-measured ambient flow turbulence intensity on the wake losses.*

  This work demonstrates the potential of using a single-beam nacelle lidar for wake studies. Using measurements of an inland wind farm, the power outputs of a pair of wind turbines are analyzed in different ambient turbulence intensity groups, which are measured by a single-beam nacelle lidar on the upstream wind turbine. We found a clear trend that the power deficit decreases with the increasing ambient turbulence intensity, which indicates that the wake recovers faster when the ambient flow is more turbulent. Moreover, we attempt to estimate the turbulence length scale and dissipation rate using the radial velocity spectra of the single-beam lidar. This part of the work is still in progress.

3 | Methods

This chapter introduces the methods used in this thesis to simulate turbulence fields and nacelle lidar measurements, including the turbulence spectral model (Section 3.1), the nacelle lidar model (Section 3.2), and the rotor-effective wind speed (Section 3.3). This chapter also provides methods to estimate lidar radial statistics (Section 3.4), mean wind speeds (Section 3.5), and Reynolds stresses (Section 3.6) from nacelle lidar measurements.

3.1 Turbulence spectral model

Turbulence background

Under Taylor's frozen hypothesis, the turbulent wind field can be described by a vector field $\boldsymbol{u}(\boldsymbol{x}) = (u, v, w) = (u_1, u_2, u_3)$, and $\boldsymbol{u}(\boldsymbol{x}, t) = \boldsymbol{u}(\boldsymbol{x} - Ut, 0)$, where $\boldsymbol{x} = (x, y, z)$ is the position vector described in a right-handed coordinate system, t represents the time, u, v, w are the horizontal along-wind component, the horizontal lateral component and the vertical component, respectively. U is the mean wind velocity along the x-direction. Assuming that the turbulent wind field $\boldsymbol{u}(\boldsymbol{x})$ is incompressible, statistically stationary and homogeneous, $\boldsymbol{u}(\boldsymbol{x})$ can be decomposed into the mean value $\langle \boldsymbol{u}(\boldsymbol{x}) \rangle = (U, 0, 0)$ and the fluctuating part $\boldsymbol{u}'(\boldsymbol{x}) = (u', v', w')$, where $\langle \, \rangle$ denotes the ensemble averaging. Thus, the auto- or cross-covariance of the velocity components is

$$R_{ij}(\boldsymbol{r}) \equiv \langle u_i'(\boldsymbol{x}) u_j'(\boldsymbol{x} + \boldsymbol{r}) \rangle, \tag{3.1}$$

where $\boldsymbol{r}$ is the separation vector and $i, j = 1, 2, 3$. Denoting the wave number vector $\boldsymbol{k} = (k_1, k_2, k_3)$ in the (x, y, z) directions, the spectral velocity tensor $\Phi_{ij}(\boldsymbol{k})$, which is the Fourier transform of the covariance tensor, describes the turbulence spectral properties of the three-dimensional homogeneous wind field (Kristensen et al., 1989):

$$\Phi_{ij}(\boldsymbol{k}) = \frac{1}{(2\pi)^3} \int R_{ij}(\boldsymbol{r}) \exp(-i\boldsymbol{k} \cdot \boldsymbol{x}) \mathrm{d}\boldsymbol{x}. \tag{3.2}$$

The one-point spectra of velocity fluctuations are calculated by

$$F_{ij}(k_1) = \iint \Phi_{ij}(\boldsymbol{k}) \mathrm{d}k_2 \mathrm{d}k_3. \tag{3.3}$$

The variances of the velocity components are the integral of the auto-spectra

$$\sigma_{u,v,w}^2 = \int_{-\infty}^{\infty} F_{u,v,w}(k_1) \mathrm{d}k_1. \tag{3.4}$$

The single-point turbulence statistics can be obtained when the separation vector $\boldsymbol{r} = 0$. The variances and covariances of the three velocity components form the Reynolds stress tensor

$$\boldsymbol{R} \equiv \boldsymbol{R}(0) = \begin{bmatrix} \sigma_u^2 & \langle u'v' \rangle & \langle u'w' \rangle \\ \langle v'u' \rangle & \sigma_v^2 & \langle v'w' \rangle \\ \langle w'u' \rangle & \langle w'v' \rangle & \sigma_w^2 \end{bmatrix}. \tag{3.5}$$

Mann turbulence model

Modelling of the turbulence spectra is essential for lidar simulations and aero-elastic simulations. In this thesis, the spectral velocity tensor $\Phi_{ij}(\boldsymbol{k})$ is assumed to be described by the Mann turbulence model (Mann, 1994) among others (Kaimal et al., 1972; Veers, 1988), because the characteristic of the model permits the modeling of three-dimensional spectra and coherence in the atmospheric surface layer, which is important for estimating turbulence statistics by combining lidar measurements in different beam directions. Besides the wave number $\boldsymbol{k}$, the Mann model contains three adjustable parameters:

- $\alpha\varepsilon^{2/3}$ [m$^{4/3}$s^{-2}]: a product of the spectral Kolmogorov constant α and the dissipation rate of turbulence energy ε to its two thirds power. This parameter acts as a proportional factor to the turbulence intensity;

- L [m]: a length scale describing the size of the most energetic eddies;

- Γ [-]: a parameter describing the anisotropy of the turbulence. The smaller the Γ, the more isotropic the turbulence. When $\Gamma = 0$, $\sigma_u = \sigma_v = \sigma_w$. Otherwise, $\sigma_u > \sigma_v > \sigma_w$.

Temporal evolution of turbulence

The structure of turbulence evolves when it approaches the rotor plane from the lidar measurement plane. The evolution affects the longitudinal coherence from upstream to the rotor plane and thus is a factor of interest for control applications (Laks et al., 2013; Schlipf et al., 2011; Simley et al., 2012).

It is assumed that the turbulent wind fields travel with the mean wind speed U, and the turbulence eddies in the wind fields decay exponentially with time Δt. Then, the space-time turbulence spectral tensor Θ_{ij} is (Guo, Mann, et al., 2022)

$$\Theta_{ij}(\boldsymbol{k}, \Delta t) = \exp\left(\frac{-\Delta t}{\tau_e(\boldsymbol{k})}\right) \Phi_{ij}(\boldsymbol{k}), \tag{3.6}$$

where τ_e is a parameter for wind evolution describing the lifetime of small eddies

$$\tau_e(\boldsymbol{k}) = \gamma \left[a(|\boldsymbol{k}|L)^{-1} \left((|\boldsymbol{k}|L)^{10} + 1 \right)^{-\frac{2}{15}} \right]. \tag{3.7}$$

Here, γ is a constant representing the strength of turbulence evolution, which depends on the turbulence condition. The more unstable the atmosphere, the higher the γ (Guo, Mann, et al., 2022).

The one-dimensional cross-spectra of velocity fluctuations with separations of $\Delta x = U\Delta t$,

Δy and Δz considering wind evolution is

$$F_{ij}(k_1, \Delta t, \Delta y, \Delta z) = \iint \Theta_{ij}(\boldsymbol{k}, \Delta t)\exp(\mathrm{i}(k_2\Delta y + k_3\Delta z))\mathrm{d}k_2\mathrm{d}k_3. \tag{3.8}$$

The magnitude of squared coherence is

$$\mathrm{coh}_{ij}^2(k_1, \Delta t, \Delta y, \Delta z) = \frac{|F_{ij}(k_1, \Delta t, \Delta y, \Delta z)|^2}{F_{ii}(k_1, \Delta t = 0)F_{jj}(k_1, \Delta t = 0)}, \tag{3.9}$$

where $F_{ii}(k_1, \Delta t = 0)$ can be calculated using Eq. (3.3). Equations (3.8) and (3.9) are used to study the wind preview quality, i.e., REWS coherence estimated by the lidars.

3.2 Modelling of nacelle lidar system

Definition of lidar coordinate system and beam angles

In the simulations, the nacelle-lidar coordinate system is assumed to coincide with the turbine coordinate system, as shown in Fig. 3.1. The unit vector $\boldsymbol{n}$ describing the beam orientation is expressed as (Peña et al., 2017)

$$\boldsymbol{n}(\phi, \theta) = (-\cos\phi, \cos\theta\sin\phi, \sin\theta\sin\phi), \tag{3.10}$$

where ϕ is the *half-cone opening angle* (also called the *angle to center line*), i.e., the angle between the beam and the negative x-axis since the lidar measures upwind, and θ is the *angle around center line*, i.e., the angle between the y-axis and $\boldsymbol{n}$ projected onto the y-z plane.

Some tools such as the OpenFAST embedded lidar simulator (Guo, Schlipf, et al., 2022) require the *azimuth angle* α (also called *horizontal opening angle*) and the *elevation angle* β as inputs to describe the beam unit vector:

$$\boldsymbol{n}(\alpha, \beta) = (-\cos\alpha\cos\beta, \sin\alpha\cos\beta, \sin\beta). \tag{3.11}$$

In addition, some lidar manufacturers use the *vertical opening angle* ζ, which is the angle from the center line to $\boldsymbol{n}$ projected on the x-z plane. The five commonly used beam angles are illustrated in Fig. 3.1. Denoting the coordinates of a lidar scanning location as (x_1, y_1, z_1) in the nacelle-lidar coordinate system, the definitions of the five angles are

$$\tan(\phi) = \frac{\sqrt{y_1^2 + z_1^2}}{x_1}, \tag{3.12}$$

$$\tan(\theta) = \frac{z_1}{y_1}, \tag{3.13}$$

$$\tan(\alpha) = \frac{y_1}{x_1}, \tag{3.14}$$

$$\tan(\beta) = \frac{z_1}{\sqrt{x_1^2 + y_1^2}}, \tag{3.15}$$

$$\tan(\zeta) = \frac{z_1}{x_1}, \tag{3.16}$$

which are useful to calculate any angle of interest from the others. We mostly use Eq. (3.11) to define beam orientations (Fig. 3.1(a)).
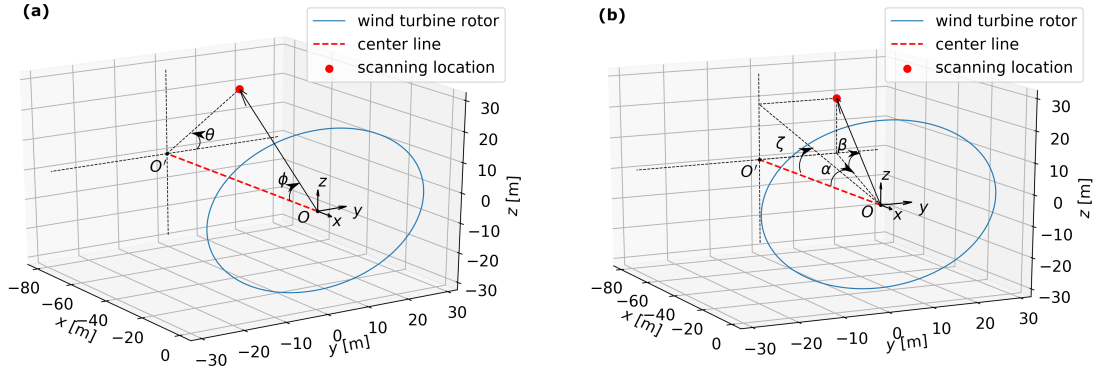
Figure 3.1: Sketch of the nacelle-lidar coordinate system and the lidar angles. ϕ is the half-cone opening angle (also called angle to center line), ζ is the vertical opening angle, α is the azimuth angle (also called horizontal opening angle), and β is the elevation angle.

Lidar measurements and the probe volume

Assuming that the yaw misalignment of the wind turbine is zero, the probe volume of a nacelle lidar is negligible, and u, v, w are homogeneous over the lidar scanning area, the radial velocity is the sum of the projection of the three wind components on the beam direction

$$v_{\mathrm{r}}(\phi, \theta) = -u \cos \phi + v \cos \theta \sin \phi + w \sin \theta \sin \phi. \tag{3.17}$$

The radial variance can be derived by taking the second-order moment of Eq. (3.17) (Eberhard et al., 1989)

$$\begin{aligned} \sigma_{v_{\mathrm{r}},\mathrm{unf}}^2(\phi, \theta) = {} & \sigma_u^2 \cos^2 \phi + \sigma_v^2 \cos^2 \theta \sin^2 \phi + \sigma_w^2 \sin^2 \theta \sin^2 \phi - 2\langle u'v' \rangle \cos \phi \cos \theta \sin \phi \\ & - 2\langle u'w' \rangle \cos \phi \sin \theta \sin \phi + 2\langle v'w' \rangle \sin^2 \phi \cos \theta \sin \theta, \end{aligned}$$

where the subscript 'unf' denotes the 'unfiltered variance' that is not affected by the probe volume averaging effect.

Considering the lidar probe volume, and assuming the radial velocity v_{r} is calculated from the Doppler spectrum by the centroid method or as the center of gravity, v_{r} can be written as (Mann et al., 2010)

$$v_{\mathrm{r}}(\phi, \theta, f_d) = \int_{-\infty}^{\infty} \varphi(s) \boldsymbol{n}(\phi, \theta) \cdot \boldsymbol{u}[\boldsymbol{n}(\phi, \theta)(f_d + s)] \mathrm{d}s, \tag{3.18}$$

where f_d is the beam focus distance, $\varphi(s)$ is the lidar weighting function approximating the shape of the probe volume and s is the distance along the beam from the focus point. In addition to the centroid method, the radial velocity can also be determined by the median and the maximum methods from the Doppler spectrum, which is explained in Section 3.4.

The weighting function of a CW lidar is approximated by a Lorentzian function (Sonnenschein et al., 1971):

$$\varphi(s) = \frac{1}{\pi} \frac{z_{\mathrm{R}}}{z_{\mathrm{R}}^2 + s^2}, \tag{3.19}$$

where the Rayleigh length z_{R} is determined by the focus distance, the laser wavelength λ (typically 1.565 μm), and the transmitted beam radius at the optical lens exit r_{b}

$$z_{\mathrm{R}} = \frac{\lambda f_d^2}{\pi r_{\mathrm{b}}^2}. \tag{3.20}$$

Therefore, the Full Width at Half Maximum (FWHM) of a Lorentzian function is $2z_{\mathrm{R}}$.

For pulsed lidar systems, the weighting function is approximated by a Gaussian shape, which can be expressed as (Schlipf, 2016)

$$\varphi(s) = \frac{1}{\sigma_{\mathrm{L}}\sqrt{2\pi}}\exp(-\frac{s^2}{2\sigma_{\mathrm{L}}^2}) \quad \text{with } \sigma_L = \frac{\Delta l}{2\sqrt{2\ln 2}}, \tag{3.21}$$

or as (Meyer Forsting et al., 2017; Simley, 2015)

$$\varphi(s) = \frac{1}{2\Delta p}\left\{\mathrm{Erf}\left[\frac{s+\Delta p/2}{r_p}\right] - \mathrm{Erf}\left[\frac{s-\Delta p/2}{r_p}\right]\right\}$$
$$\text{with the error function } \mathrm{Erf}(x) = \frac{2}{\sqrt{\pi}}\int_0^x \exp(-t^2)\mathrm{d}t \quad \text{and} \quad r_p = \frac{\Delta l}{2\sqrt{\ln(2)}}, \tag{3.22}$$

where Δp is the range-gate length and Δl is the FWHM of the Gaussian function.

It can be seen from Eqs. (3.19), (3.22), and (3.21) that the probe volume of the CW systems increases with the square of the focus distance, while the probe volume of the pulsed systems does not depend on the measurement range. As shown in Fig. 3.2, the CW probe volume can be smaller than the pulsed one when the lidar measures at a close distance. Assuming $\lambda = 1.565\ \mu$m, $r_{\mathrm{b}} = 28$ mm and $W_L = 30$ m, the two types of lidar have similar probe volume size at a measurement range of 155 m.
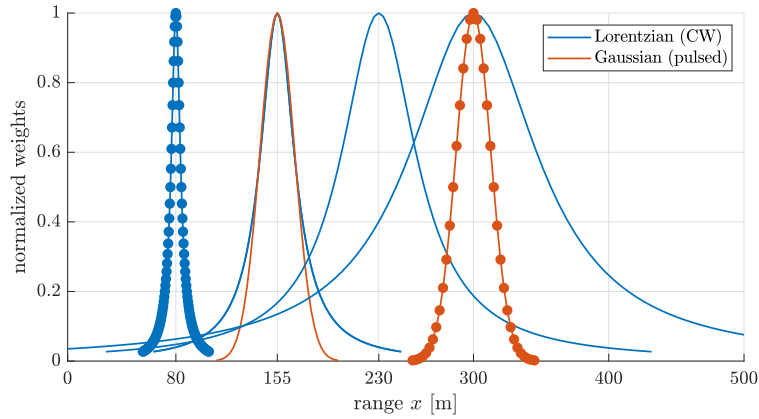
Figure 3.2: Comparison of the weighting functions of the CW measuring at $80,\ 155,\ 230,\ 300$ m and the pulsed lidar systems measuring at $155,\ 300$ m. The markers indicate the discretization of the theoretical weighting functions. The weights are normalized by the peak values. Source: **Paper IV**.

Doppler spectra of radial velocities

The Doppler spectra of radial velocities describe the distribution of wind velocities sampled along the beams within the lidar probe volume, from which the radial velocity is estimated. Assuming frozen turbulence, the wind field $\boldsymbol{u}(\boldsymbol{x})$ is moving with the mean wind $\boldsymbol{U}$. The Doppler spectrum can be obtained from the simulated wind fields as (Held et al., 2018)

$$S(v_{\mathrm{r}}, t) = \int_{-M}^{M} \varphi(s)\delta(v_{\mathrm{r}} - \boldsymbol{u}(\boldsymbol{n}s - \boldsymbol{U}t) \cdot \boldsymbol{n})\mathrm{d}s, \tag{3.23}$$

where v_{r} is the radial velocity, δ is the Dirac delta function, and M is the distance along the beam that used to truncate the integral in order to simulate the Doppler spectrum using virtual turbulence fields in finite lengths. The amount of truncation and discretization of the Doppler spectrum needs to be balanced between the realistic probe volume and the computational cost.

Radial velocity spectra

A radial velocity spectrum represent the lidar measurements in the wave-number domain. The theoretical radial velocity spectrum is expressed as (Mann et al., 2009)

$$F_{v_{\mathrm{r}}}(k_1) = n_i n_j \iint |\hat{\varphi}(\boldsymbol{k} \cdot \boldsymbol{n})|^2 \, \Phi_{ij}(\boldsymbol{k})\mathrm{d}k_2\mathrm{d}k_3, \tag{3.24}$$

where $\hat{\varphi}$ is the Fourier transform of the lidar weighting function $\varphi(s)$. For CW lidar systems, the Fourier transform of Eq. (3.19) is approximated by

$$\hat{\varphi}(\boldsymbol{k} \cdot \boldsymbol{n}) = \exp\left(-|\boldsymbol{k} \cdot \boldsymbol{n}|z_{\mathrm{R}}\right), \tag{3.25}$$

and for pulsed lidar systems, the Fourier transform of Eq. (3.21) can be expressed as (Schlipf, 2016)

$$\hat{\varphi}(\boldsymbol{k} \cdot \boldsymbol{n}) = \exp\left(-|\boldsymbol{k} \cdot \boldsymbol{n}|^2 \frac{\sigma_L^2}{2}\right), \tag{3.26}$$

Then, the theoretical radial velocity variance considering probe volume can be calculated from the integral of Eq. (3.24)

$$\sigma_{v_{\mathrm{r}},\mathrm{f}}^2 = \int_{-\infty}^{\infty} F_{v_{\mathrm{r}}}(k_1)\mathrm{d}k_1, \tag{3.27}$$

where the subscript 'f' denotes the 'filtered' radial velocity variance.

3.3   Modelling of rotor-effective wind speed

If the turbine yaw misalignment is negligible, REWS sensed by the wind turbine rotor can be calculated as the spatial average of the along-wind velocities across the rotor disk area (Schlipf, 2016):

$$u_{\mathrm{RR}}(x) = \frac{1}{\pi R^2} \iint_{\mathrm{rotor}} u(\boldsymbol{x})\mathrm{d}y\mathrm{d}z, \tag{3.28}$$

$$= \int u(\boldsymbol{k})e^{\mathrm{i}k_1 x_1} \frac{2J_1(\kappa R)}{\kappa R}\mathrm{d}\boldsymbol{k}, \tag{3.29}$$

where R is the rotor radius, $\kappa = \sqrt{k_2^2 + k_2^3}$, J_1 is the Bessel function of the first kind, and the yaw misalignment is neglected. The auto-spectrum of u_{RR} is (Held et al., 2019)

$$S_{\text{RR}}(k_1) = \iint_{-\infty}^{\infty} \Phi_{11}(\boldsymbol{k}) \frac{4J_1^2(\kappa R)}{\kappa^2 R^2} \mathrm{d}k_2 \mathrm{d}k_3. \tag{3.30}$$

Assuming the v and w components are zero, the REWS from lidar measurements can be computed as the mean of the along-wind velocities retrieved from the lidar measurements:

$$u_{\text{LL}}(t) = \frac{1}{N_b} \sum_{i=1}^{N_{\text{b}}} \frac{v_{\text{r},i}(t)}{n_{i1}}, \tag{3.31}$$

where N_b is the number of measurements in a full scan and n_{i1} stands for the first element in the beam's unit vector of the ith measurement. The auto-spectrum of the lidar-estimated REWS is (Guo, Mann, et al., 2022)

$$S_{\text{LL}}(k_1) = \sum_{i,j=1}^{N_{\text{b}}} \sum_{l,m=1}^{3} \frac{1}{N_b^2 n_{i1} n_{j1}} \int n_{il} n_{jm} \Phi_{lm} \exp(\mathrm{i}\boldsymbol{k}\cdot(\boldsymbol{x}_i - \boldsymbol{x}_j)) \hat{\varphi}(\boldsymbol{k}\cdot\boldsymbol{n}_i) \hat{\varphi}(\boldsymbol{k}\cdot\boldsymbol{n}_j) \mathrm{d}k_2 \mathrm{d}k_3, \tag{3.32}$$

where $\boldsymbol{x}_i$ is the position vector of the ith measurement and n_{il} is the lth element in the unit vector $\boldsymbol{n}$ of the ith measurement.

The quality of the wind preview signal provided by the nacelle lidar is evaluated by its coherence to the true REWS. The cross-spectrum of u_{RR} and u_{LL} considers the turbulence evolution from the lidar measurement plane to the rotor plane

$$S_{\text{RL}}(k_1) = \sum_{i=1}^{N_{\text{b}}} \sum_{l=1}^{3} \frac{1}{N_b n_{i1}} \int n_{il} \Theta_{l1}(\boldsymbol{k}, \Delta t_i) \hat{\varphi}(\boldsymbol{k} \cdot \boldsymbol{n}_i) \exp(\mathrm{i}(k_2 x_{i2} + k_3 x_{i3})) \frac{2J_1(\kappa R)}{\kappa R} \mathrm{d}k_2 \mathrm{d}k_3, \tag{3.33}$$

with Δt_i denoting the elapsed time for turbulence propagating from the lidar plane to the rotor plane, i.e., $\Delta t_i = |\Delta x_i|/U$, where Δx_i is the longitudinal separation of the two planes. Thus, the magnitude squared coherence γ_{RL}^2 of the lidar-rotor REWS is expressed as (Held et al., 2019; Schlipf, 2016; Simley et al., 2018)

$$\gamma_{\text{RL}}^2(k_1) = \frac{|S_{\text{RL}}(k_1)|^2}{S_{\text{RR}}(k_1) S_{\text{LL}}(k_1)}, \tag{3.34}$$

which has values between 1 and 0.

Due to wind evolution and the lidar working principle, the lidar-estimated REWS is not perfectly correlated with the true one. A low-pass filter is applied to the lidar-estimated REWS to remove uncorrelated signals in order to avoid unnecessary and harmful pitch actuations. The cutoff frequency of the low-pass filter is selected at which the theoretical REWS transfer function drops at -3 dB (Schlipf, 2016). The REWS transfer function is given as

$$G_{\text{RL}} = \frac{|S_{\text{RL}}(f)|}{S_{\text{LL}}(f)}. \tag{3.35}$$

3.4   Estimation of lidar radial statistics

Estimation of radial velocity

Three state-of-art methods can be used to determine the dominant frequency in a Doppler spectrum of CW lidars, which affects the estimation of the 'filtered' second-order statistics from lidar measurements (Held et al., 2018):

- The centroid method computes the dominant frequency $f_{D,cen}$ from the Doppler spectrum $p(f)$ as

$$f_{D,cen} = \frac{\int f p(f) \mathrm{d} f}{\int p(f) \mathrm{d} f}. \tag{3.36}$$

- The median method uses the Doppler spectrum as a probability distribution and estimates the dominant frequency that corresponds to the median value.

- The maximum method reports the dominant frequency at where the maximum peak of the Doppler spectrum occurs.

Then, the radial velocity is calculated from the dominant frequency as

$$v_r = \frac{\lambda}{2} f_D. \tag{3.37}$$

Figure 3.3 shows a simulated Doppler spectrum using a turbulence box. The estimated radial velocities using different methods are marked in vertical lines.
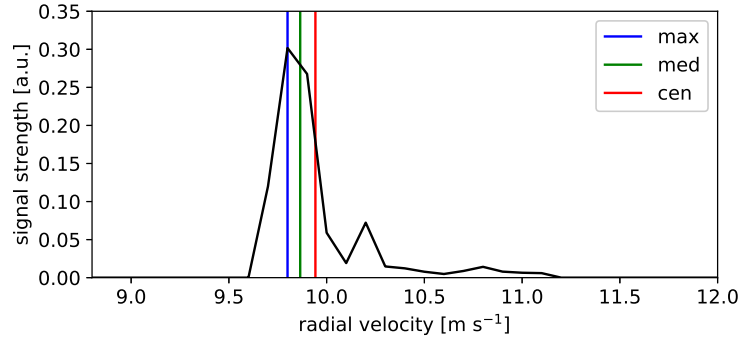
Figure 3.3: A simulated Doppler spectrum and the radial velocity estimates using the maximum (max), the median (med) and the centroid (cen) methods. Source: **Paper I**.

Filtered and unfiltered radial velocity variances

Due to the probe volume averaging effect, some high-frequency variations of the wind cannot be detected. The variances computed from the radial velocity time series (estimated using centroid, maximum, or median methods) are attenuated and called the 'filtered' variances.

If the Doppler spectra of radial velocities are accessible, the ensemble-averaged Doppler spectrum can be used to circumvent the probe volume filtering effect (Mann et al., 2010). Since

nacelle lidars usually measure with a relatively small half-cone opening angle, it can be assumed that the velocity gradient inside the probe volume of a lidar beam is negligible. Supposing that all velocity variations in the probe volume are due to turbulence, the ensemble-averaged Doppler spectrum $p(v_r)$ can be seen as a probability density function of the radial velocity, and the radial variance is estimated as the second central statistical moment

$$\sigma_{v_r,\text{unf}}^2 = \int_{-\infty}^{\infty} (v_r - \mu_{v_r})^2 p(v_r) \mathrm{d}v_r, \tag{3.38}$$

where μ_{v_r} represents the mean radial velocity of the ensemble-averaged Doppler spectrum

$$\mu_{v_r} = \int_{-\infty}^{\infty} v_r p(v_r) \mathrm{d}v_r. \tag{3.39}$$

3.5 Estimation of mean wind speeds

The mean wind speed in the along-wind direction is in the definition of the *turbulence intensity*,

$$\text{TI} = \frac{\sigma_u}{U}, \tag{3.40}$$

which is widely used in wind energy for power performance and loads assessment. The thesis uses two approaches to estimate the mean wind vector from different nacelle lidars.

Least-square procedure to estimate the 3D wind vector

Assuming homogeneity over the lidar scanning area, the mean wind vector $\boldsymbol{U} = \langle \boldsymbol{u}(\boldsymbol{x}) \rangle = (U, V, W)$, the radial velocities and the corresponding beam unit vectors $\boldsymbol{n}$ are fitted to the least-square formulation (Peña et al., 2019)

$$\Delta^2 = \int (\boldsymbol{n} \cdot \boldsymbol{U} - v_r)^2 \mathrm{d}\mu, \tag{3.41}$$

where $\int \mathrm{d}\mu$ represents the area-weighted average of the beam measurements. For nacelle lidars which have a limited number of measurement points, it is the sum of all pairs of radial velocities and the corresponding unit vectors. The mean wind vector is estimated by minimizing the squared difference on the right side of Eq. (3.41)

$$\frac{\partial \Delta^2}{\partial U_i} = 0 \Rightarrow 2 \int (\boldsymbol{n} \cdot \boldsymbol{U} - v_r) n_i \mathrm{d}\mu = 0, \quad \text{for} \quad i = 1, 2, 3. \tag{3.42}$$

Therefore, the mean wind vector can be calculated from

$$\begin{bmatrix} \sum n_1^2 & \sum n_1 n_2 & \sum n_1 n_3 \\ \sum n_1 n_2 & \sum n_2^2 & \sum n_2 n_3 \\ \sum n_1 n_3 & \sum n_2 n_3 & \sum n_3^2 \end{bmatrix} \begin{bmatrix} U \\ V \\ W \end{bmatrix} = \begin{bmatrix} \sum n_1 v_r \\ \sum n_2 v_r \\ \sum n_3 v_r \end{bmatrix}. \tag{3.43}$$

The procedure requires at least three radial velocities measured in different beam directions to solve the three unknowns in the mean wind vector.

Reconstruction of the 2D wind vector

If the vertical wind component is negligible, i.e., $w = 0$, following Eq. (3.17), the radial velocities can be written as

$$v_\text{r}(\phi, \theta) = -u \cos \phi + v \cos \theta \sin \phi. \tag{3.44}$$

Using radial velocities measured in two horizontal directions, the velocity components (u, v) can be computed as

$$u = -\frac{v_\text{r,left} + v_\text{r,right}}{2 \cos \phi},$$
$$v = \frac{v_\text{r,right} - v_\text{r,left}}{2 \sin \phi}. \tag{3.45}$$

Then, the mean wind velocities (U, V) can be computed as the average of the reconstructed (u, v).

The approach requires only two beams at the same height, which can be used to reconstruct the mean wind vector from 2-beam lidars. It's also a very useful method to derive wind profiles from nacelle lidars that have at least two beams at different heights, e.g., 4-beam lidars, circular scanning lidars, the SpinnerLidar, etc.

Induction correction

If the lidar measurement plane is very close to the rotor, they might be measuring within the induction zone, where the wind slows down from the free-stream velocity while approaching the rotor. The undisturbed free-stream velocity U_∞ can be calculated using the method in Simley et al., 2016

$$\frac{U}{U_\infty} = 1 - a \left(1 + \frac{2x}{D} \left(1 + \left(\frac{2x}{D} \right)^2 \right)^{-\frac{1}{2}} \right), \tag{3.46}$$

where x is the distance between the lidar measurement plane and the rotor plane, and a is the induction factor. According to the axial momentum theory, the induction factor is influenced by the turbine's thrust coefficient C_t and thus can be estimated from $C_t = 4a(1 - a)$.

In **Paper I**, the along-wind velocities from the nacelle lidars are induction-corrected and compared with the one derived from a sonic anemometer at the turbine's hub height on the met-mast.

3.6 Estimation of Reynolds stresses

The components in the Reynolds stress tensor are important for different studies. For load validation (Conti et al., 2021; Conti et al., 2020) and wind turbine design (International Electrotechnical Commission, 2019), the most frequently used component is the along-wind variance, whose square root is in the definition of the turbulence intensity. For load simulations, other Reynolds stresses besides the along-wind variance are also needed to determine the parameters in three-dimensional turbulence models (Mann, 1998). To study the vertical wind

profiles, two covariances form the momentum fluxes and are used to calculate the friction velocity (Peña et al., 2016; Wyngaard, 2010). The turbulence kinetic energy is useful to study the structure of turbine wakes, which is half the sum of the three velocity variances (Kumer et al., 2016).

Assuming homogeneity over the lidar scanning area, the Reynolds stress tensor $\boldsymbol{R}$ can be estimated using the least-square procedure (Peña et al., 2019), which fits $\boldsymbol{R}$, the radial velocity variances $\sigma_{v_{\mathrm{r}}}^2$ and the unit vectors of the beams $\boldsymbol{n}$ to the formulation

$$\Delta^2 = \int (\boldsymbol{n} \cdot \boldsymbol{R}\boldsymbol{n} - \sigma_{v_{\mathrm{r}}}^2)^2 \mathrm{d}\mu. \tag{3.47}$$

The Reynolds stresses are estimated by minimizing the squared difference on the right side of Eq. (3.47)

$$\frac{\partial \Delta^2}{\partial R_{ij}} = 0 \Rightarrow 2 \int (\boldsymbol{n} \cdot \boldsymbol{R}\boldsymbol{n} - \sigma_{v_{\mathrm{r}}}^2) n_i n_j \mathrm{d}\mu = 0, \quad \text{for} \quad i, j = 1, 2, 3. \tag{3.48}$$

Therefore, the Reynolds stresses can be calculated from (the full solution can be found in **Paper III**)

$$\begin{bmatrix} \sum n_1^4 & \sum n_1^2 n_2^2 & \sum n_1^2 n_3^2 & \sum 2n_1^3 n_2 & \sum 2n_1^3 n_3 & \sum 2n_1^2 n_2 n_3 \\ \dots & \sum n_2^4 & \dots & \dots & \dots & \dots \\ \dots & \dots & \sum n_3^4 & \dots & \dots & \dots \\ \dots & \dots & \dots & \sum 2n_1^2 n_2^2 & \dots & \dots \\ \dots & \dots & \dots & \dots & \sum 2n_1^2 n_3^2 & \dots \\ \dots & \dots & \dots & \dots & \dots & \sum 2n_2^2 n_3^2 \end{bmatrix} \begin{bmatrix} R_{uu} \\ R_{vv} \\ R_{ww} \\ R_{uv} \\ R_{uw} \\ R_{vw} \end{bmatrix} = \begin{bmatrix} \sum n_1^2 \sigma_{v_{\mathrm{r}}}^2 \\ \sum n_2^2 \sigma_{v_{\mathrm{r}}}^2 \\ \sum n_3^2 \sigma_{v_{\mathrm{r}}}^2 \\ \sum n_1 n_2 \sigma_{v_{\mathrm{r}}}^2 \\ \sum n_1 n_3 \sigma_{v_{\mathrm{r}}}^2 \\ \sum n_2 n_3 \sigma_{v_{\mathrm{r}}}^2 \end{bmatrix}, \tag{3.49}$$

where R_{uu}, R_{vv}, R_{ww} denote $\sigma_u^2, \sigma_v^2, \sigma_w^2$ and R_{uv}, R_{uw}, R_{vw} denote $\langle u'v' \rangle, \langle u'w' \rangle, \langle v'w' \rangle$, respectively. The six Reynolds stresses can be solved from Eq. (3.49) only if both of the following requirements are fulfilled:

- the nacelle lidar has at least six beams (i.e., measures in six different directions),

- the nacelle lidar has at least two different half-cone opening angles.

If the nacelle lidar has fewer than six beams or the half-cone opening angles of all beams are identical, some of the six equations in Eq. (3.49) are linearly dependent and the large matrix on the left side of Eq. (3.49) is degenerate. Consequently, not all Reynolds stresses can be solved. Nevertheless, for wind energy load characterization and power performance assessment, the along-wind variance σ_u^2 is the key turbulence parameter. Focusing the estimation on σ_u^2, one can assume relations between the Reynolds stresses to reduce the number of unknowns in Eq. (3.49). The six equations can be simplified into one equation. We apply three different assumptions:

1. *'LSP-σ_u^2'* assumption: assuming $\sigma_u^2 > 0$ and all other Reynolds stresses in Eq. (3.49) are zero.

2. *'LSP-isotropy'* assumption: assuming turbulence is isotropic, i.e., $\sigma_u^2 = \sigma_v^2 = \sigma_w^2$ and $\langle u'v' \rangle = \langle u'w' \rangle = \langle v'w' \rangle = 0$.

3. *'LSP-IEC'* assumption: assuming the relations between the standard deviation of three velocity components as what recommend in the IEC standard (International Electrotechnical Commission, 2019), i.e., $\sigma_v = 0.7\sigma_u$, $\sigma_w = 0.5\sigma_u$ and $\langle u'v' \rangle = \langle u'w' \rangle = \langle v'w' \rangle = 0$.

3.7 Blade interference

Measurements from forward-looking nacelle lidars are often intercepted by the passing blades, which reduces the lidar data availability. Usually, the measurements in the lower part of the scanning pattern are more easily affected than those in the central or upper parts (Borraccino et al., 2017). For CW lidars, the blade return signals introduce additional backscattering signals in the lidar Doppler spectrum, which are not easily differentiated from the wind signals. In **Paper I** and **Paper III**, the blade signals are filtered out by simulating the blade-returned radial velocity (Angelou et al., 2022; Angelou et al., 2015):

$$v_{\mathrm{r}} = |\Omega S_y h_{\mathrm{L}}|, \tag{3.50}$$

where Ω is the rotational speed, S_y is the lateral component of the beams' unit vector, and h_{L} is the vertical displacement from the turbine rotation axis to the nacelle-lidar scan head. Then, the radial velocities are discriminated when their values are very close to the simulated blade-returned radial velocities.

4 | Sites and measurements

Two datasets collected at the DTU Risø test site in Denmark and in an anonymous wind farm have played key roles in verifying the research hypothesis and achieving the main objectives of this thesis. Two datasets both contain concurrent inflow measurements from CW nacelle lidars and the SCADA of the research wind turbines. The dataset from Risø test site also has measurements of mast-mounted anemometers. Information about the sites and measurements is given in this chapter.

4.1 DTU Risø test site

Paper I-III use measurements collected at the test site located at DTU Risø campus in Roskilde, Denmark, next to the Roskilde fjord. There are four wind turbines in the test site, which are marked in circles in Fig. 4.1(a). The reference wind turbine is a Vestas V52 wind turbine standing at the northernmost position. Around the reference wind turbine, the terrain is almost flat covered by low vegetation and thus can be assumed to be horizontally homogeneous. The V52 turbine has a rotor diameter of 52 m, a hub height of 44 m, and a rated power of 850 kW. The supervisory control and data acquisition data (SCADA) of the V52 wind turbine are available. A V52 meteorological mast is marked in a red square located at a distance of 120 m at the northwest of the V52 turbine.
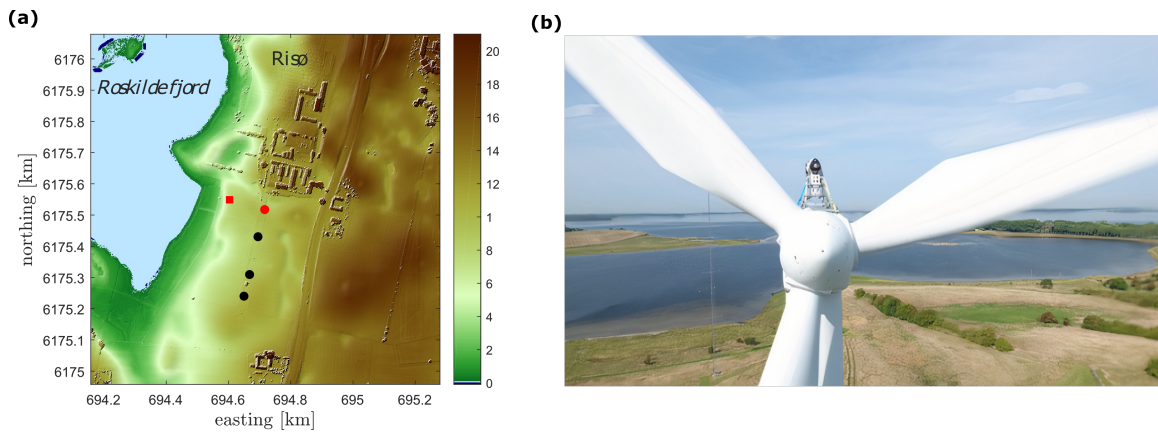

Figure 4.1: (a) A digital surface elevation model of the Risø test site in Roskilde, Denmark. The height above the sea level in meters is indicated in the color bar. (b) A SpinnerLidar (top), a WindVision (middle), and a WindEye (bottom) sat on top of each other on the V52 nacelle at the Risø test site. Source: **Paper I**.

During September 2020 and June 2021, the SpinnerLidar, the WindVision, and the WindEye were measuring the inflow on the nacelle of the V52 wind turbine, as shown in Fig. 4.1(b). The SpinnerLidar (Peña et al., 2019) is a research CW lidar, which scans the inflow in a rosette-curve pattern at 400 different locations per full scan. The beam half-cone opening angle varies between $0-30°$. The WindVision (W4) and WindEye (W2) are commercial CW lidars produced by Windar Photonics A/S (Windar Photonics, 2020), which report four and two radial velocities, respectively, in a full scan per second. The experiment set-up of the three lidars is shown in Fig. 4.2.

The SpinnerLidar dataset contains the raw Doppler spectra of radial velocities and system-reported radial velocities, measurement index, quality of the estimates, spectrum total power, beam unit vectors, focus distance and lidar positions. The W4 and W2 datasets have system-reported radial velocities.
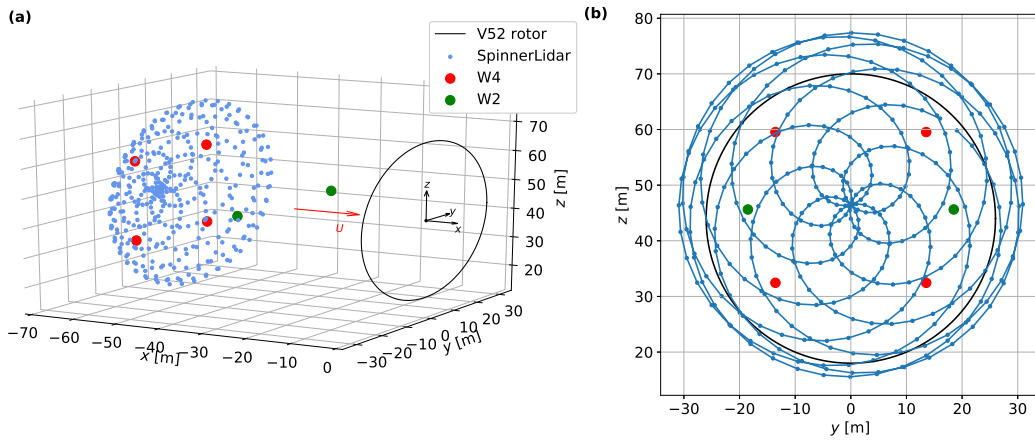
Figure 4.2: (a) A 3D and (b) a 2D upwind view of the theoretical scanning patterns of the SpinnerLidar, the WindVision (W4), and the WindEye (W2). Source: **Paper I**.

The V52 mast (Fig. 4.3) is equipped with sonic anemometers and cup anemometers at different heights above the ground. The wind direction is measured by a wind vane at 41 m (Peña et al., 2019). The precipitation is measured by an opto sensor at 2 m. To evaluate the turbulence estimations from nacelle lidars, statistics from the cup and sonic anemometers at 44 m (equivalent to turbine's hub height) are used as references.

4.2 Wind farm measurements

Paper V uses wind turbine and nacelle lidar measurements from an anonymous inland wind farm to study the impact of atmospheric turbulence characteristics on the wake behavior. Measurements were collected from 30 September 2021 to 20 December 2022. Figure 4.4 shows the layout of part of the wind farm around the reference wind turbines T3 and T10. Wind sectors in which T3 is in freestream and T10 is only shadowed by the wake from T3 are used for the analysis. The turbines in the wind farm have a rotor diameter of 62 m, a hub height of 49 m, and a rated power of 1.3 MW. The wind turbines' active power, yaw angle (relative to the north), yaw error, and turbines' status were recorded in the SCADA system.
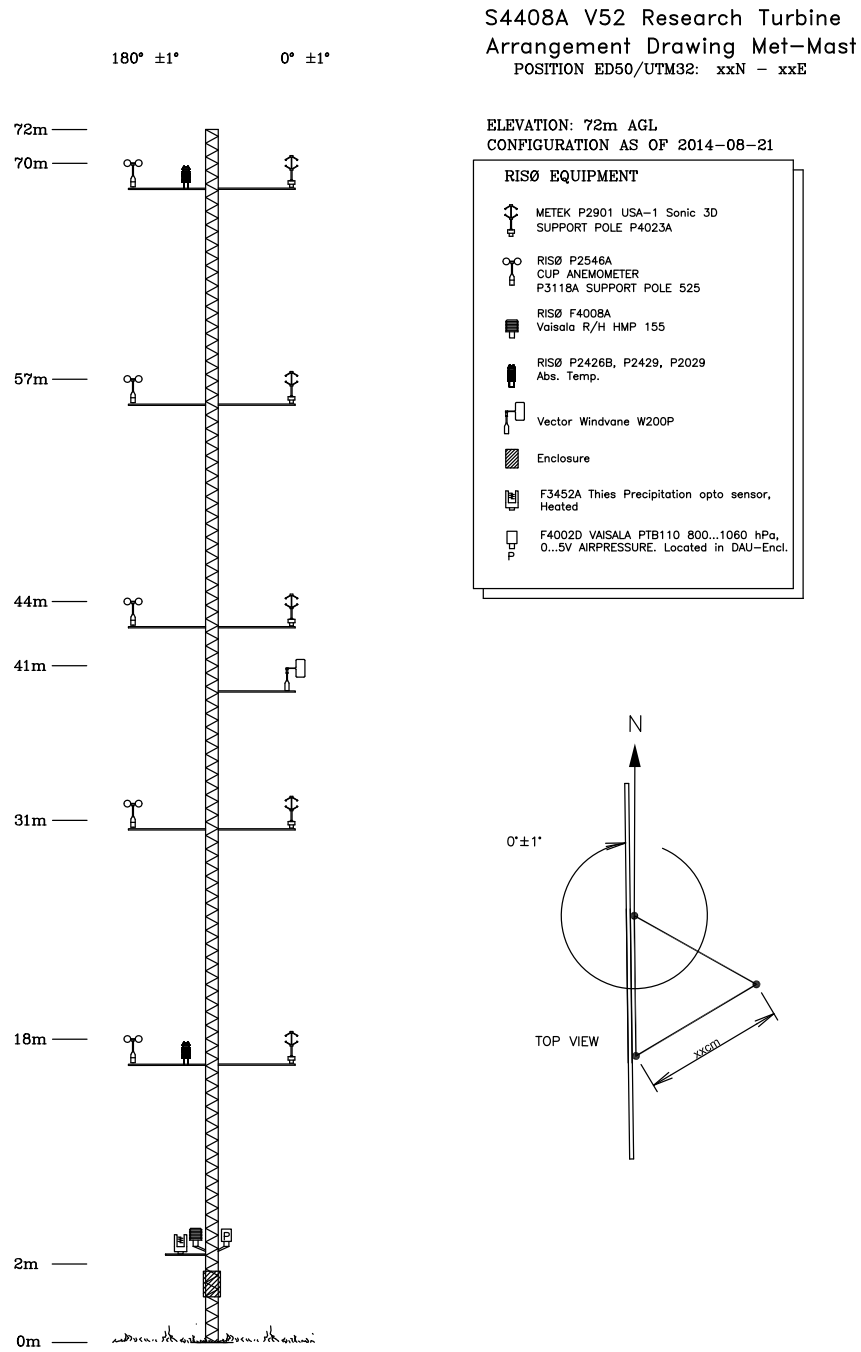
Figure 4.3: A sketch of the V52 met mast and the equipped sensors at Risø test site (DTU Wind Energy, 2014).

A single-beam CW lidar measures the flow horizontally in a staring mode on the nacelle of T3. The focus distance is 80 m. The dataset contains lidar Doppler spectra of radial velocities and the system-reported wind data, including the radial velocities, the turbulence intensity, the spectra-averaged turbulence intensity, which is equivalent to the 'unfiltered' TI, the spectral spreads, which is the width of the spectrum indicating the amount of turbulence or flow complexity within the probe volume, and the backscatter, which is a measure of lidar signal-to-noise ratio.
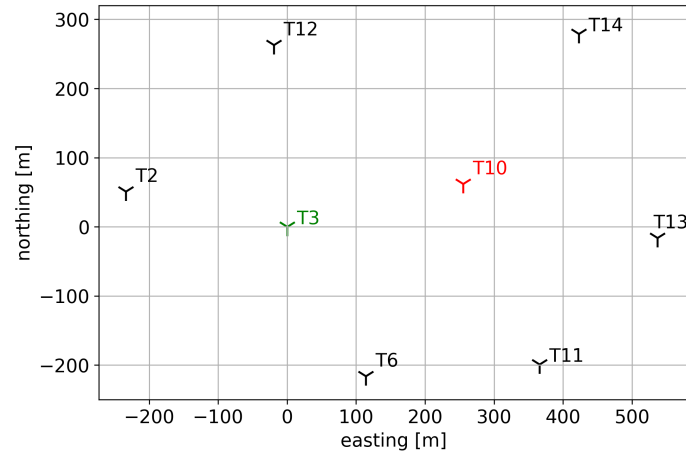
Figure 4.4: Layout of the wind farm, in which the wake effect of T3 (upstream, marked in green) on T10 (downstream, marked in red) is studied in **Paper V**. The coordinates of wind turbines are relative to the location of T3.

5 | PhD contribution

This chapter summarizes the major findings from the scientific works regards to the defined thesis objectives, formulated hypotheses, and raised research questions. The scientific works are attached in the Appendix, in which details of the data analysis and more results are shown.

5.1 Methodology to characterize atmospheric turbulence

Paper I-III investigate the turbulence characterization methods using nacelle lidars. The main difference between the three paper is that **Paper I** uses the 2- and 4-beam CW lidars, and the SpinnerLidar, while **Paper II-III** include lidars in other different scanning configurations.

Paper I first evaluates the mean along-wind velocity estimated from three different nacelle lidars and shows the radial statistics of the SpinnerLidar (Fig 5.1), which reveals the possible cross-contamination effect on the turbulence estimation when combining radial measurements in different beam directions. A good estimation of the along-wind variance could be obtained for the wrong reason sometimes, e.g., when the cross-contamination effect cancels out the probe volume averaging effect.
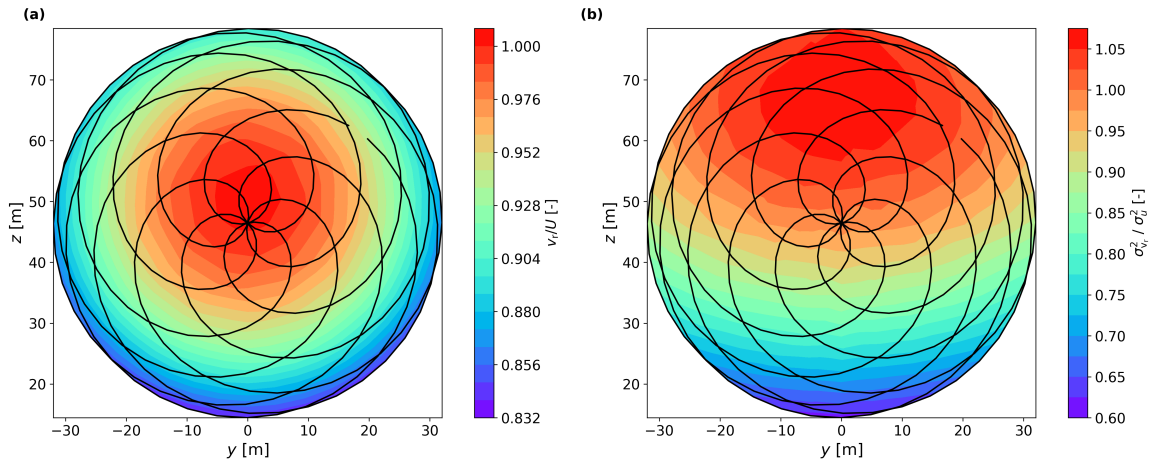
Figure 5.1: Ideal contour plots of (a) the radial velocities and (b) the unfiltered radial variances, which are both normalized by the along-wind statistics of a sonic anemometer at hub height. Results are the mean value from virtual SpinnerLidar measurements simulated using 30 wind field realizations. Source: reproduced from **Paper I**.

Moreover, **Paper I** studies the impacts of different radial velocity estimation methods (the

centroid, median and maximum) on turbulence estimation. Since these methods use the dominant frequency of the Doppler shift, none of these methods uses all fluctuations detected in the lidar probe volume. Variances computed from the estimated radial velocities are 'filtered'. Among the three methods, the centroid method is most affected by the probe volume, while the maximum method mitigates best the turbulence attenuation.

The use of the ensemble-averaged Doppler spectrum of radial velocities can efficiently eliminate the probe volume averaging effect. **Paper I** shows that the 'unfiltered' variance of the SpinnerLidar central beam has recovered by 10% compared to the 'filtered' variance from the centroid radial velocities. The successful estimation of the 'unfiltered' variance relies on 'clean' Doppler spectra, in which the noises are eliminated and the signals left are contributed by turbulence. In field measurements, the possible source of the signal noises includes reflections from optical lenses, hard targets, moving objectives (turbine blades, clouds, passing vehicles, birds), precipitations, etc. Therefore, **Paper I** put substantial efforts to process each instantaneous Doppler spectrum of the SpinnerLidar before using them to compute the 'unfiltered' variance.

The least-square procedure uses radial measurements and the unit vectors of the beams in all available directions over a full scan to compute the Reynolds stress tensor. Results in **Paper I-III** demonstrate that if the nacelle lidar has more than six beams and at least two different opening angles, e.g. the 6-beam, 51-beam lidars, and the SpinnerLidar, all six components in the Reynolds stress tensor can be well estimated using Eq. (3.49). The along-wind variance estimated by those lidars is as accurate as the one from the sonic anemometer, whereas estimates of other components have larger uncertainties than those from the sonic anemometer.

Furthermore, results from different nacelle lidars in **Paper I-III** show that, when Eq.(3.49) can not be fully solved, the *'LSP-IEC'* assumption (in Section 3.6) is the fairest procedure to estimate the along-wind variance because it assumes the relations of the Reynolds stresses closest to what can be observed in the atmospheric surface layer. It is a universal procedure that works for all lidars in the study including the 6-, 51-beam lidars and the SpinnerLidar. When the Doppler spectra of radial velocities can be used to derive the 'unfiltered' variance, the *'LSP-IEC'* assumption gives accurate σ_u^2 using all considered lidars. Particularly, the staring beam performs just like a sonic anemometer in measuring the along-wind variance.

The *'LSP-σ_u^2'* assumption can systematically overestimate σ_u^2 when the lidar scanning pattern is symmetric and the beams have only one opening angle because Eq.(3.49) can be simplified to $\sigma_u^2 = \sum \sigma_{v_r}^2 / \sum \cos^2 \phi$, where $\sum \cos^2 \phi < 1$. Nevertheless, the overestimation can sometimes counterweigh the turbulence attenuation by the probe volume, as shown in **Paper I**. Coincidentally, we get the best along-wind variance estimates using *'LSP-σ_u^2'* assumption from W4 and W2 measurements.

The least-square procedure used in this work assumes turbulence homogeneity over the lidar scanning area, which can be violated in complex terrains or inside wind turbine wakes. Therefore, new methodologies to characterize turbulence under inhomogeneous inflow conditions need to be investigated, such as using the constrained turbulent flow (Dimitrov et al., 2016; Rinker, 2018), physics-informed machine learning approach (Zhang et al., 2021) or proper orthogonal decomposition method (Saranyasoontorn et al., 2005).

5.2 Impact of nacelle lidar scanning strategies on turbulence characterization

Paper II and **Paper III** apply the least-square procedure to more lidars and investigate how the lidar scanning strategies affect the accuracy and the uncertainty of the Reynolds stress estimations. The main features of the scanning strategies are considered, i.e., the number of measurement points, the beam opening angles, the focus distances, and the type of lidar systems. **Paper II** is based on numerical simulations, while **Paper III** reuses the SpinnerLidar dataset in **Paper I** to verify our findings from the simulations. The SpinnerLidar measurements at different scanning locations are carefully selected to mimic lidars with different numbers of beams or different opening angles.

As mentioned in Section 5.1, the number of beams and the number of opening angles determine if the nacelle lidar can estimate all six Reynolds stresses following the least-square procedure. Additionally, **Paper II-III** show that using the multi-plane measurements along the same beam directions does not improve the accuracy of Reynolds stress estimations; it only reduces slightly the estimation uncertainty of the transverse Reynolds stress components.

Furthermore, using the 6-beam lidar, **Paper II-III** show that increasing the beam opening angle improves the estimation of the transverse Reynolds stress components. Since the 6-beam lidar has a central beam that aligns with the along-wind component, increasing the opening angle does not sacrifice the along-wind variance estimation, which in principle could happen to the 2-, 4-beam, and circular-scanning lidars. When $\phi = 45°$, the 6-beam lidar even outperforms the SpinnerLidar, despite having much fewer beams.

The lidar probe volume has to be considered when studying the impact of the focus distance on the Reynolds stress estimations. The estimation bias and uncertainty increases with the focus distance. Therefore, for both CW and pulsed lidars, measuring close to the rotor is beneficial for Reynolds stress estimations.

To summarize, a 6-beam nacelle lidar measuring at a close distance with a large opening angle is the best scanning strategy in our study for characterizing the Reynolds stress tensor. The central beam of the 6-beam lidar guarantees that the along-wind component can be well measured when enlarging the opening angle for a better view of the lateral and vertical components, which are important for wind directions, turbulence kinetic energy, etc. The best opening angle and the focus distance of the 6-beam lidar need to be determined by further studies and experiments for different applications.

5.3 Application of a single-beam lidar for wind turbine feedforward control

Feedforward collective pitch control is one of the most promising lidar-assisted control techniques since significant improvements in rotor speed regulations and fatigue load reductions can be achieved (Canet et al., 2021; Schlipf et al., 2014; Schlipf, Simley, et al., 2015; Scholbrock et al., 2013). The feedforward controller uses the preview information of the approaching wind to help the conventional feedback controller react before the aerodynamic impact on the turbine's structure has occurred. To achieve control benefits, the wind preview signal should be well correlated with the wind that interacts with the wind turbine rotor plane, which is usually

represented as the REWS. The lidar scanning strategy is one of the key factors that impact the benefits of feedforward pitch control. Other factors include the turbine size, the wind conditions, the lidar data processing, and the controller design (Schlipf et al., 2014).

A single-beam lidar is flexible and low in cost. From **Paper III**, it can be seen that a staring lidar that measures horizontally gives the best along-wind statistics. For control applications, however, measurement at a single point is not a good representative of the inflow interacting with the wind turbine rotor. To make the best use of a single-beam lidar for control, **Paper IV** simulates the lidar in the spinner of an IEA 15-MW reference wind turbine (Gaertner et al., 2020). With an opening angle between the beam and the turbine's horizontal axis, the spinner-based lidar is able to scan the inflow in a circular pattern during turbine operations.

In **Paper IV**, the lidar beams' opening angles and measurement distance are optimized for the best wind preview quality evaluated by the REWS coherence. An additional constraint for the lidar optimization is the buffer time, which is used to synchronize the blade pitch actuation with the wind reaching the rotor plane. The buffer time has to be positive to ensure the wind preview signal reaches the turbine before the wind.

Results indicate that both the CW and pulsed single-beam lidar based in the spinner can provide a much better coherence compared to the same lidar based on the nacelle. The optimum scanning configurations of CW and pulsed lidars are different, but both result in a lidar scan radius of approximately 0.6 of the rotor radius. The CW lidar should measure at a closer distance with a wider opening angle compared to the pulsed lidar since the probe volume of CW lidars becomes very influential at large distances. The study also discusses how wind evolution influences the measurement coherence bandwidth and the optimum lidar configurations.

The optimized configurations of the single-beam lidars in the spinner are applied for feedforward pitch control. The control performances, i.e., the regulation of rotor speed fluctuations and the reduction of tower and blade damage equivalent loads, are evaluated by aero-elastic simulations using OpenFAST (National Renewable Energy Laboratory, 2022). Results show that the spinner-based single-beam lidar achieves much higher control benefits compared to the nacelle-based ones, which are at the same level as a four-beam CW nacelle lidar.

The findings in **Paper IV** are limited in several aspects. First, only a mean wind speed at $18\,\mathrm{ms}^{-1}$ is considered. The wind speed affects not only the optimum lidar measurement range due to its impact on the buffer time but also the control benefits (Guo et al., 2023; Schlipf, 2016; Schlipf et al., 2018). Second, the paper considers only a neutral turbulence condition. The control benefits can be higher in unstable conditions and lower in stable conditions (Guo et al., 2023). Furthermore, the study uses the default parameters for the feedback controller. Higher fatigue load reductions can be gained by optimizing the controller gains (Schlipf et al., 2018). In addition, multiple measurement planes should be considered for the pulsed lidar so that a larger scan area can be covered with the same number of beams, which improves the REWS coherence.

In the future, one could potentially use more than one single-beam lidar in the spinner so that multi-range measurements can be achieved even with CW lidar systems. Using multiple single-beam lidars in the spinner can reduce the lidar full scan time and increase the system redundancy. The wind shear can be derived from the circular pattern of the single-beam lidar, which can be used for individual pitch control.

5.4   Application of a single-beam lidar for wake studies

Wind turbine wake is characterized by a reduced wind speed and a more complex flow structure, which gradually recovers while the wake travels downstream. The velocity deficit has a direct impact on the power output of the downstream wind turbine. Previous studies found that the atmospheric stability and ambient turbulence intensity impact the wake recovery (Breton et al., 2014; Hansen et al., 2012; Maeda et al., 2011; Peña et al., 2014; Troldborg et al., 2011).

Paper V investigates the influence of the ambient flow turbulence intensity on the wake losses using a single-beam nacelle lidar. Measurements from an inland wind farm are analyzed. The wake losses are represented by the power deficits between a pair of wind turbines in the wind farm. The turbulence intensity is measured by the single-beam nacelle lidar on the upstream wind turbine. Results in **Paper V** show that when two turbines are both facing the undisturbed inflow, the ratio of their power outputs is almost constant with the changing ambient turbulence intensity. When the downstream wind turbine is affected by the wake, we see a clear trend that the wake-induced power deficit decreases with the increasing turbulence intensity of the ambient flow. The trend indicates that the wake recovers faster when the ambient flow is more turbulent. These findings demonstrate the potential of using a single-beam nacelle lidar for wake studies.

In addition, **Paper V** attempts to estimate the turbulence length scale and dissipation rate from the single-beam nacelle lidar measurements based on the Mann turbulence model. The length scale is related to the atmospheric conditions and the dissipation rate acts as a scaling factor on the turbulence intensity. Therefore, both parameters are important for studying the interactions between atmospheric flow and wind turbine wakes. We propose two methods to estimate the length scale and dissipation rate using the radial velocity spectrum. One method uses the amount of turbulence attenuation by the lidar probe volume, which is represented by the ratio of the 'filtered' to 'unfiltered' radial velocity variances. The other method estimates both parameters simultaneously by fitting the modelled radial velocity spectrum to the one computed from the measurements. Both methods assume a fixed turbulence anisotropy. So far, we found that the estimates from two methods do not agree with each other sometimes. The noises in the high-frequency range of the radial velocity spectra are disturbing the fitting procedures. Therefore, we are planning to optimize the algorithm by log-binning the spectrum and dropping a part of the signals in the high-frequency range of the spectrum. This work is still in progress.

6 | Conclusion and outlook

6.1 Conclusion

The main objectives of this thesis were (1) to investigate methodologies to characterize atmospheric turbulence using nacelle lidars, (2) to study the dependence of turbulence estimations on the scanning strategies of nacelle lidars, and (3) to make the best use of a flexible single-beam lidar for wind turbine feedforward control and wake studies. The research objectives are achieved using virtual and field measurements of nacelle lidars, measurements inside a wind farm as well as aero-elastic wind turbine simulations.

We found that nacelle lidars with more than six beams and two different beam opening angles are able to retrieve all six components of the Reynolds stress tensor following a least-square procedure. If the Doppler spectra of radial velocities are used to account for the probe volume spatial averaging effect, nacelle lidars in several different scanning configurations can estimate the along-wind variance as well as a sonic anemometer. Other lidar-estimated Reynolds stresses have larger uncertainties than those from a sonic anemometer.

Enlarging the beam opening angle improves the estimation of transverse Reynolds stress components. Increasing the lidar focus distance has negative effects on the estimation of the Reynolds stress tensor. We obtained the best estimation of the Reynolds stress tensor from a 6-beam nacelle lidar measuring at a close focus distance with a large opening angle. The 6-beam lidar has five beams forming a circular pattern and a central horizontal beam. Therefore, measuring with a large opening angle using the 6-beam lidar does not sacrifice the estimation of the along-wind variance.

Using a single-beam lidar in the wind turbine spinner, the lidar scans the inflow in a circular pattern during turbine operations. It was found that the spinner-based single-beam lidar brings much more control benefits in terms of rotor speed regulations and fatigue load reductions compared to the same lidar based on the nacelle. The spinner-based single-beam lidar achieved similar control benefits as a four-beam nacelle lidar. Furthermore, we showed that the wake-induced power deficit of the downstream wind turbine is inversely proportional to the ambient turbulence intensity, which is measured by a single-beam lidar on the nacelle of the upstream wind turbine. These results demonstrated the potential of using a simple single-beam lidar for wind turbine control and wake studies.

6.2 Industrial applications

The research findings have the potential to be highly valuable within the wind energy and meteorology industries. The methods of estimating Reynolds stress components are very use-

ful for lidar users to obtain accurate and detailed turbulence characteristics, which benefit wind turbine power performance assessments and optimizations, load validations and wind turbine design, and wind resource assessments in met-ocean applications. We proved the usefulness of the methods using field measurements of commercial nacelle lidars provided by IEA Wind Task 32 for a round-robin on "turbulence estimation using nacelle-mounted lidar systems" (Riechert et al., 2022). The least-square procedure was implemented as an algorithm in Python, which can be published on GitHub as a stand-alone algorithm to assist the application in the wind energy industry. The study on lidar scanning strategy provides insights and guidance on designing and utilizing nacelle lidars for turbulence characterization.

The research findings on the low-cost and robust single-beam lidar open various possibilities for wind energy industries. Using one or several single-beam lidars in the spinner, or combining a spinner-based and a nacelle-based single-beam lidar have great potential to benefit lidar-assisted control and turbulence characterization. The single-beam lidar can also be used for estimating the wake losses to help make decisions on wind turbine control. Those applications can optimize wind turbine power outputs and mitigate fatigue loads on the turbine structural components, which eventually reduces the levelized cost of wind energy.

6.3 Outlook

While summarizing the findings of this thesis, we found some unsolved questions for future research. First of all, the least-square procedure for turbulence characterization assumes homogeneity among the lidar scanning area. This worked for a wind turbine with a relatively small rotor size. However, the inflow turbulence can be highly spatially heterogeneous for wind turbines with large rotor spans or turbines operating in complex terrains. Methodologies such as constrained simulations, proper orthogonal decomposition, or physics-informed machine learning methods can be useful to reconstruct inhomogeneous wind fields.

Second, we found that enlarging the half-cone opening angle of the lidar beams improves turbulence estimations. But how large is the best opening angle? The answer can vary with the main turbulence features of interest and the wind turbine size. Therefore, future studies and experiments are needed to investigate the most useful and robust 6-beam configuration for different applications.

Furthermore, there are a lot of opportunities for optimizing the scanning strategies of the spinner-based single-beam lidar. More than one single-beam lidar in the spinner could be used to achieve multi-plane measurements, increase the scanning rate of a full scan, and improve the system's redundancy. The spinner-based lidar could work together with a nacelle-based single-beam lidar, which guarantees a good sight in the along-wind direction. The study of using a single-beam lidar in the spinner for control is based on simulations. Field measurements are valuable to test the idea and demonstrate the control benefits. Lastly, the relation between the ambient turbulence intensity and the wind turbine power deficit can be used to improve the existing wake loss models.

Bibliography

Angelou, N., & Sjöholm, M. (2022). Data Reliability Enhancement for Wind-Turbine-Mounted Lidars. *Remote Sensing 2022, Vol. 14, Page 3225*, *14*(13), 3225. https://doi.org/10.3390/RS14133225

Angelou, N., Sjöholm, M., & Papetta, A. (2015). *UniTTe WP3/MC1: Measuring the inflow towards a Nordtank 500 kW turbine using three short-range WindScanners and one SpinnerLidar* (tech. rep. DTU Wind Energy E-0093). DTU Wind Energy.

Berg, J., Kelly, M., Mann, J., & Nielsen, M. (2022). *Dtu 46100: Introduction to micrometeorology for wind energy*. DTU Wind Energy.

Borraccino, A., Schlipf, D., Haizmann, F., & Wagner, R. (2017). Wind field reconstruction from nacelle-mounted lidar short-range measurements. *Wind Energy Science*, *2*(1), 269–283. https://doi.org/10.5194/wes-2-269-2017

Bossanyi, E. A., Kumar, A., & Hugues-Salas, O. (2012). Wind turbine control applications of turbine-mounted lidar. *Journal of Physics: Conference Series*, *555*(1), 012011. https://doi.org/10.1088/1742-6596/555/1/012011

Branlard, E., Pedersen, A. T., Mann, J., Angelou, N., Fischer, A., Mikkelsen, T., Harris, M., Slinger, C., & Montes, B. F. (2013). Retrieving wind statistics from average spectrum of continuous-wave lidar. *Atmospheric Measurement Techniques*, *6*, 1673–1683. https://doi.org/10.5194/amt-6-1673-2013

Breton, S. P., Nilsson, K., Olivares-Espinosa, H., Masson, C., Dufresne, L., & Ivanell, S. (2014). Study of the influence of imposed turbulence on the asymptotic wake deficit in a very long line of wind turbines. *Renewable Energy*, *70*, 153–163. https://doi.org/10.1016/j.renene.2014.05.009

Canet, H., Loew, S., & Bottasso, C. L. (2021). What are the benefits of lidar-assisted control in the design of a wind turbine? *Wind Energy Science*, *6*(5), 1325–1340. https://doi.org/10.5194/wes-6-1325-2021

Cheynet, E., Jakobsen, J. B., & Snæbjörnsson, J. (2016). Buffeting response of a suspension bridge in complex terrain. *Engineering Structures*, *128*, 474–487. https://doi.org/10.1016/j.engstruct.2016.09.060

Conti, D., Pettas, V., Dimitrov, N., & Peña, A. (2021). Wind turbine load validation in wakes using wind field reconstruction techniques and nacelle lidar wind retrievals. *Wind Energy Science*, *6*(3), 841–866. https://doi.org/10.5194/wes-6-841-2021

Conti, D., Dimitrov, N., & Peña, A. (2020). Aeroelastic load validation in wake conditions using nacelle-mounted lidar measurements. *Wind Energy Science*, *5*(3), 1129–1154. https://doi.org/10.5194/wes-5-1129-2020

Dimitrov, N., Borraccino, A., Peña, A., Natarajan, A., & Mann, J. (2019). Wind turbine load validation using lidar-based wind retrievals. *Wind Energy*, *22*(11), 1512–1533. https://doi.org/10.1002/we.2385

Dimitrov, N., & Natarajan, A. (2016). Application of simulated lidar scanning patterns to constrained gaussian turbulence fields for load validation. *Wind Energy*, *20*(1), 79–95. https://doi.org/10.1002/we.1992

DTU Wind Energy. (2014). V52 research turbine arrangement drawing met-mast.

Eberhard, W. L., Cupp, R. E., & Healy, K. R. (1989). Doppler lidar measurement of profiles of turbulence and momentum flux. *Journal of Atmospheric and Oceanic Technology*, *6*(5), 809–819. https://doi.org/10.1175/1520-0426(1989)006<0809:DLMOPO>2.0.CO;2

Fu, W., Peña, A., & Mann, J. (2022). Turbulence statistics from three different nacelle lidars. *Wind Energy Science*, *7*(2), 831–848. https://doi.org/10.5194/wes-7-831-2022

Fu, W., Sebastiani, A., Peña, A., & Mann, J. (2022a). Dependence of turbulence estimations on nacelle-lidar scanning strategies. *Wind Energy Science Discussions*, *2022*, 1–21. https://doi.org/10.5194/wes-2022-85

Fu, W., Sebastiani, A., Peña, A., & Mann, J. (2022b). Influence of nacelle-lidar scanning patterns on inflow turbulence characterization. *Journal of Physics: Conference Series*, *2265*, 022016. https://doi.org/10.1088/1742-6596/2265/2/022016

Gaertner, E., Rinker, J., Sethuraman, L., Zahle, F., Anderson, B., Barter, G. E., Abbas, N. J., Meng, F., Bortolotti, P., Skrzypinski, W., Scott, G. N., Feil, R., Bredmose, H., Dykes, K., Shields, M., Allen, C., & Viselli, A. (2020). Iea wind tcp task 37: Definition of the iea 15-megawatt offshore reference wind turbine. https://doi.org/10.2172/1603478

Global Wind Energy Council. (2022). Global Wind Report 2022. Retrieved January 7, 2023, from https://gwec.net/global-wind-report-2022/

Gottschall, J., & Peinke, J. (2008). How to improve the estimation of power curves for wind turbines. *Environmental Research Letters*, *3*(1), 015005. https://doi.org/10.1088/1748-9326/3/1/015005

Guo, F., Schlipf, D., & Cheng, P. W. (2023). Evaluation of lidar-assisted wind turbine control under various turbulence characteristics. *Wind Energy Science*, *8*(2), 149–171. https://doi.org/10.5194/wes-8-149-2023

Guo, F., Mann, J., Peña, A., Schlipf, D., & Cheng, P. W. (2022). The space-time structure of turbulence for lidar-assisted wind turbine control. *Renewable Energy*, *195*, 293–310. https://doi.org/10.1016/J.RENENE.2022.05.133

Guo, F., Schlipf, D., Zhu, H., Platt, A., Cheng, P. W., & Thomas, F. (2022). Updates on the openfast lidar simulator. *Journal of Physics: Conference Series*, *2265*(4), 042030. https://doi.org/10.1088/1742-6596/2265/4/042030

Hansen, K. S., Barthelmie, R. J., Jensen, L. E., & Sommer, A. (2012). The impact of turbulence intensity and atmospheric stability on power deficits due to wind turbine wakes at Horns Rev wind farm. *Wind Energy*, *15*(1), 183–196. https://doi.org/10.1002/WE.512

Harris, M., Bryce, D. J., Coffey, A. S., Smith, D. A., Birkemeyer, J., & Knopf, U. (2007). Advance measurement of gusts by laser anemometry. *Journal of Wind Engineering and Industrial Aerodynamics*, *95*(12), 1637–1647. https://doi.org/10.1016/J.JWEIA.2007.02.029

Held, D. P., & Mann, J. (2018). Comparison of methods to derive radial wind speed from a continuous-wave coherent lidar Doppler spectrum. *Atmospheric Measurement Techniques*, *11*, 6339–6350. https://doi.org/10.5194/amt-11-6339-2018

Held, D. P., & Mann, J. (2019). Lidar estimation of rotor-effective wind speed – an experimental comparison. *Wind Energy Science, 4*(3), 421–438. https://doi.org/10.5194/wes-4-421-2019

International Electrotechnical Commission. (2019). *IEC 61400-1. Wind turbines – Part 1: design guidelines* (International Standard). Geneva, Switzerland. https://standards.iteh.ai/catalog/standards/sist/3454e370-7ef2-468e-a074-7a5c1c6cb693/iec-61400-1-2019

Kaimal, J. C., Wyngaard, J. C., Izumi, Y., & Coté, O. R. (1972). Spectral characteristics of surface-layer turbulence. *Quarterly Journal of the Royal Meteorological Society, 98*(417), 563–589. https://doi.org/10.1002/QJ.49709841707

Kelberlau, F., & Mann, J. (2020). Cross-contamination effect on turbulence spectra from doppler beam swinging wind lidar. *Wind Energy Science, 5*(2), 519–541. https://doi.org/10.5194/wes-5-519-2020

Kristensen, L., Lenschow, D. H., Kirkegaard, P., & Courtney, M. (1989). The spectral velocity tensor for homogeneous boundary-layer turbulence. *Boundary-Layer Meteorology, 47,* 149–193. https://doi.org/10.1007/BF00122327

Kumer, V.-M., Reuder, J., Dorninger, M., Zauner, R., & Grubišić, V. (2016). Turbulent kinetic energy estimates from profiling wind lidar measurements and their potential for wind energy applications. *Renewable Energy, 99,* 898–910. https://doi.org/10.1016/j.renene.2016.07.014

Laks, J., Simley, E., & Pao, L. (2013). A spectral model for evaluating the effect of wind evolution on wind turbine preview control. *Proceedings of the American Control Conference,* 3673–3679. https://doi.org/10.1109/ACC.2013.6580400

Maeda, T., Kamada, Y., Murata, J., Yonekura, S., Ito, T., Okawa, A., & Kogaki, T. (2011). Wind tunnel study on wind and turbulence intensity profiles in wind turbine wake. *Journal of Thermal Science, 20*(2), 127–132. https://doi.org/10.1007/s11630-011-0446-9

Mann, J. (1994). The spatial structure of neutral atmospheric surface-layer turbulence. *Journal of Fluid Mechanics, 273,* 141–168. https://doi.org/10.1017/S0022112094001886

Mann, J. (1998). Wind field simulation. *Probabilistic Engineering Mechanics, 13,* 269–282. https://doi.org/10.1016/S0266-8920(97)00036-2

Mann, J., Peña, A., Bingöl, F., Wagner, R., & Courtney, M. S. (2010). Lidar scanning of momentum flux in and above the surface layer. *Journal of Atmospheric and Oceanic Technology, 27,* 959–976. https://doi.org/10.1175/2010JTECHA1389.1

Mann, J., Cariou, J.-P. C., Parmentier, R. M., Wagner, R., Lindelöw, P., Sjöholm, M., & Enevoldsen, K. (2009). Comparison of 3d turbulence measurements using three staring wind lidars and a sonic anemometer. *Meteorologische Zeitschrift, 18*(2), 135–140. https://doi.org/10.1127/0941-2948/2009/0370

Meyer Forsting, A. R., Troldborg, N., & Borraccino, A. (2017). Modelling lidar volume-averaging and its significance to wind turbine wake measurements. *Journal of Physics: Conference Series, 854,* 012014. https://doi.org/10.1088/1742-6596/854/1/012014

Mikkelsen, T., Angelou, N., Hansen, K., Sjöholm, M., Harris, M., Slinger, C., Hadley, P., Scullion, R., Ellis, G., & Vives, G. (2013). A spinner-integrated wind lidar for enhanced wind turbine control. *Wind Energy, 16*(4), 625–643. https://doi.org/10.1002/we.1564

National Renewable Energy Laboratory. (2022). *Openfast documentation.* Retrieved November 21, 2022, from https://openfast.readthedocs.io/en/main/

Peña, A., Mann, J., & Dimitrov, N. (2017). Turbulence characterization from a forward-looking nacelle lidar. *Wind Energy Science*, *2*(1), 133–152. https://doi.org/10.5194/wes-2-133-2017

Peña, A., Mann, J., & Thorsen, G. (2019). *Spinnerlidar measurements for the ccav52* (tech. rep. DTU Wind Energy E Vol. 0177). DTU Wind Energy.

Peña, A. (2009). *Sensing the wind profile* (Doctoral dissertation 45(EN)) [Risø-PhD-45(EN)]. Risø National Laboratory.

Peña, A., Floors, R., Sathe, A., Gryning, S. E., Wagner, R., Courtney, M. S., Larsén, X. G., Hahmann, A. N., & Hasager, C. B. (2016). Ten Years of Boundary-Layer and Wind-Power Meteorology at Høvsøre, Denmark. *Boundary-Layer Meteorology*, *158*(1), 1–26. https://doi.org/10.1007/s10546-015-0079-8

Peña, A., Hasager, C., Badger, M., Barthelmie, R., Bingöl, F., Cariou, J.-P., Emeis, S., Frandsen, S., Harris, M., Karagali, I., Larsen, S., Mann, J., Mikkelsen, T., Pitter, M., Pryor, S., Sathe, A., Schlipf, D., Slinger, C., & Wagner, R. (2015). *Remote sensing for wind energy*. DTU Wind Energy.

Peña, A., Réthoré, P. E., & Rathmann, O. (2014). Modeling large offshore wind farms under different atmospheric stability regimes with the Park wake model. *Renewable Energy*, *70*, 164–171. https://doi.org/10.1016/j.renene.2014.02.019

Riechert, J., von Eisenhart Rothe, J., Menke, R., & Schlipf, D. (2022). (IEA Wind Task 32/52) Round Robin on turbulence estimates from nacelle mounted Lidar systems - Project overview and intermediate results. https://doi.org/10.5281/zenodo.6815532

Rinker, J. M. (2018). PyConTurb: an open-source constrained turbulence generator. *Journal of Physics: Conference Series*, *1037*(6), 062032. https://doi.org/10.1088/1742-6596/1037/6/062032

Saranyasoontorn, K., & Manuel, L. (2005). Low-Dimensional Representations of Inflow Turbulence and Wind Turbine Response Using Proper Orthogonal Decomposition. *Journal of Solar Energy Engineering*, *127*(4), 553–562. https://doi.org/10.1115/1.2037108

Sathe, A., & Mann, J. (2013). A review of turbulence measurements using ground-based wind lidars. *Atmospheric Measurement Techniques*, *6*, 3147–3167. https://doi.org/10.5194/amt-6-3147-2013

Sathe, A., Banta, R., Pauscher, L., Vogstad, K., Schlipf, D., & Wylie, S. (2015). *Estimating turbulence statistics and parameters from ground- and nacelle-based lidar measurements: Iea wind expert report* [Grant no: 0602-02486B]. DTU Wind Energy.

Sathe, A., Mann, J., Barlas, T., Bierbooms, W., & van Bussel, G. (2013). Influence of atmospheric stability on wind turbine loads. *Wind Energy*, *16*. https://doi.org/10.1002/we.1528

Sathe, A., Mann, J., Vasiljevic, N., & Lea, G. (2015). A six-beam method to measure turbulence statistics using ground-based wind lidars. *Atmospheric Measurement Techniques*, *8*(2), 729–740. https://doi.org/10.5194/amt-8-729-2015

Schlipf, D. (2016). *Lidar-Assisted Control Concepts for Wind Turbines* (Doctoral dissertation June 2015). https://doi.org/10.18419/opus-8796

Schlipf, D., Cheng, P., & Mann, J. (2013). Model of the correlation between lidar systems and wind turbines for lidar-assisted control. *Journal of Atmospheric and Oceanic Technology*, *30*(10), 2233–2240. https://doi.org/10.1175/JTECH-D-13-00077.1

Schlipf, D., Fleming, P., Haizmann, F., Scholbrock, A., Hofsäß, M., Wright, A., & Cheng, P. W. (2014). Field testing of feedforward collective pitch control on the CART2 using a nacelle-

based lidar scanner. *Journal of Physics: Conference Series, 555,* 012090. https://doi.org/10.1088/1742-6596/555/1/012090

Schlipf, D., Fürst, H., Raach, S., & Haizmann, F. (2018). Systems engineering for lidar-assisted control: A sequential approach. *Journal of Physics: Conference Series, 1102,* 012014. https://doi.org/10.1088/1742-6596/1102/1/012014

Schlipf, D., Haizmann, F., Cosack, N., Siebers, T., & Cheng, P. W. (2015). Detection of wind evolution and lidar trajectory optimization for lidar-assisted wind turbine control. *Meteorologische Zeitschrift, 24*(6), 565–579. https://doi.org/10.1127/metz/2015/0634

Schlipf, D., Simley, E., Lemmer, F., Pao, L., & Cheng, P. W. (2015). Collective pitch feedforward control of floating wind turbines using lidar. *Journal of Ocean and Wind Energy, 2.* https://doi.org/10.17736/jowe.2015.arr04

Schlipf, D., Trabucchi, D., Bischoff, O., Hofsäß, M., Mann, J., Mikkelsen, T., Rettenmeier, A., Trujillo, J. J., & Kühn, M. J. (2011). Testing of frozen turbulence hypothesis for wind turbine applications with a scanning lidar system. *International Symposium for the Advancement of Boundary Layer Remote Sensing.* https://doi.org/10.18419/opus-3915

Scholbrock, A., Fleming, P., Fingersh, L., Wright, A., Schlipf, D., Haizmann, F., & Belen, F. (2013). Field testing LIDAR-based feed-forward controls on the NREL controls advanced research turbine. American Institute of Aeronautics; Astronautics Inc. https://doi.org/10.2514/6.2013-818

Simley, E., Angelou, N., Mikkelsen, T., Sjöholm, M., Mann, J., & Pao, L. Y. (2016). Characterization of wind velocities in the upstream induction zone of a wind turbine using scanning continuous-wave lidars. *Journal of Renewable and Sustainable Energy, 8.* https://doi.org/10.1063/1.4940025

Simley, E. (2015). *Wind Speed Preview Measurement and Estimation for Feedforward Control of Wind Turbines* (Doctoral dissertation). University of Colorado.

Simley, E., Fürst, H., Haizmann, F., & Schlipf, D. (2018). Optimizing lidars for wind turbine control applications-Results from the IEA Wind Task 32 workshop. *Remote Sensing, 10*(6). https://doi.org/10.3390/rs10060863

Simley, E., Pao, L. Y., Kelley, N., Jonkman, B., & Frehlich, R. (2012). Lidar wind speed measurements of evolving wind fields. https://www.osti.gov/biblio/1047950

Sjöholm, M., Mikkelsen, T., Mann, J., Enevoldsen, K., & Courtney, M. (2009). Spatial averaging-effects on turbulence measured by a continuous-wave coherent lidar. *Meteorologische Zeitschrift, 18,* 281–287. https://doi.org/10.1127/0941-2948/2009/0379

Sonnenschein, C. M., & Horrigan, F. A. (1971). Signal-to-noise relationships for coaxial systems that heterodyne backscatter from the atmosphere. *Applied Optics, 10,* 1600–1604. https://doi.org/10.1364/AO.10.001600

Troldborg, N., Larsen, G. C., Madsen, H. A., Hansen, K. S., Sørensen, J. N., Mikkelsen, & Robert. (2011). Numerical simulations of wake interaction between two wind turbines at various infl ow conditions. *Wind Energy.* https://doi.org/10.1002/we.433

Veers, P. S. (1988). Three-dimensional wind simulation. https://www.osti.gov/biblio/7102613

Vestas. (2022). V236-15.0 MW™. Retrieved March 28, 2023, from https://www.vestas.com/en/products/offshore/V236-15MW

Wagner, R., Courtney, M., Pedersen, T. F., & Davoust, S. (2015). Uncertainty of power curve measurement with a two-beam nacelle mounted lidar. *Wind Energy, 19,* 1269–1287. https://doi.org/10.1002/we.1897

Wagner, R., Pedersen, T. F., Courtney, M., Antoniou, I., Davoust, S., & Rivera, R. L. (2014). Power curve measurement with a nacelle mounted lidar. *Wind Energy*, *17*, 1441–1453. https://doi.org/10.1002/we.1643

Wang, S., De Roo, F., Thobois, L., & Reuder, J. (2022). Characterization of terrain-induced turbulence by large-eddy simulation for air safety considerations in airport siting. *Atmosphere*, *13*(6). https://doi.org/10.3390/atmos13060952

Windar Photonics. (2020). *Book of lidar*. https://www.windarphotonics.com/f/f1/Book_of_Lidar_Windar_Photonics.pdf

WindEurope. (2023). Wind energy in Europe: 2022 Statistics and the outlook for 2023-2027. https://windeurope.org/intelligence-platform/product/wind-energy-in-europe-2022-statistics-and-the-outlook-for-2023-2027/

Wyngaard, J. C. (2010). *Turbulence in the atmosphere*. Cambridge University Press. https://doi.org/10.1017/CBO9780511840524

Zhang, J., & Zhao, X. (2021). Three-dimensional spatiotemporal wind field reconstruction based on physics-informed deep learning. *Applied Energy*, *300*, 117390. https://doi.org/10.1016/J.APENERGY.2021.117390

Part II

Appendix

A | Scientific manuscripts

A.1 Turbulence statistics from three different nacelle lidars

Fu, W., Peña, A., and Mann, J.: Turbulence statistics from three different nacelle lidars, Wind Energy Science, 7, 831–848, https://doi.org/10.5194/wes-7-831-2022.

WIND ENERGY SCIENCE

Open Access

Turbulence statistics from three different nacelle lidars

Wei Fu, Alfredo Peña, and Jakob Mann

Department of Wind Energy, Technical University of Denmark, Frederiksborgvej 399, 4000 Roskilde, Denmark

Correspondence: Wei Fu (weif@dtu.dk)

Abstract. Atmospheric turbulence can be characterized by the Reynolds stress tensor, which consists of the second-order moments of the wind field components. Most of the commercial nacelle lidars cannot estimate all components of the Reynolds stress tensor due to their limited number of beams; most can estimate the along-wind velocity variance relatively well. Other components are however also important to understand the behavior of, e.g., the vertical wind profile and meandering of wakes. The SpinnerLidar, a research lidar with multiple beams and a very high sampling frequency, was deployed together with two commercial lidars in a forward-looking mode on the nacelle of a Vestas V52 turbine to scan the inflow. Here, we compare the lidar-derived turbulence estimates with those from a sonic anemometer using both numerical simulations and measurements from a nearby mast. We show that from these lidars, the SpinnerLidar is the only one able to retrieve all Reynolds stress components. For the two- and four-beam lidars, we study different methods to compute the along-wind velocity variance. By using the SpinnerLidar's Doppler spectra of the radial velocity, we can partly compensate for the lidar's probe volume averaging effect and thus reduce the systematic error of turbulence estimates. We find that the variances of the radial velocities estimated from the maximum of the Doppler spectrum are less affected by the lidar probe volume compared to those estimated from the median or the centroid of the Doppler spectrum.

1 Introduction

Understanding and measuring atmospheric turbulence are essential for the effective use of wind energy, to assess wind turbine site conditions, and for the assessment of the structural integrity of wind turbines. Traditionally, in situ anemometers installed on meteorological (met) masts are used to measure turbulence. However, with the increasing size of modern wind turbines, installing and operating a met mast that reaches the top of the rotor disk are becoming more and more expensive and infeasible. Nacelle lidars are compact and portable. They yaw with the wind turbine and scan over an area comparable to the rotor plane.

The Reynolds stress tensor is one of the most important turbulence statistics used in the wind energy industry. It consists of the second-order moments (variances and covariances) of the wind field components. One of the Reynolds stress components, the along-wind velocity variance, is used in the definition of turbulence intensity (IEC, 2019) and ap-

plied in different aspects of wind energy. Other components are also essential in wind energy and boundary-layer meteorology. For example, the vertical wind shear is connected to the friction velocity (Wyngaard, 2010), which can be computed using the momentum fluxes (two covariances); the momentum fluxes can also be used to crudely estimate the height of the boundary layer (Stull, 1988). The turbulence kinetic energy, expressed as half the sum of the three velocity components' variances, is a key parameter for investigating the turbulence structure in, e.g., wind turbine wakes (Kumer et al., 2016).

The main objective of this study is to investigate the benefit of using multiple-beam nacelle lidars for measuring inflow turbulence. Most commercial nacelle lidars are not able to estimate all components of the Reynolds stress tensor due to the limited number of beams and the scanning configuration. The SpinnerLidar is a research continuous-wave (CW) Doppler nacelle lidar. It scans at 400 positions at a high sampling frequency, which enables characterizing the inflow in detail. We

evaluate and compare the turbulence characterization performance of a two- and a four-beam commercial lidar, and the SpinnerLidar through both numerical simulations and measurements inter-comparisons with in situ anemometers. For the latter, we deployed the three lidars in a forward-looking mode on the nacelle of a V52 wind turbine. Measurements from sonic anemometers on a met mast are used as reference for evaluation of the lidar-derived turbulence characteristics.

Assuming statistical homogeneity, we estimate the Reynolds stress components by fitting lidar radial velocity variances from the beams over the scanning pattern using a least-squares-based method. To determine the six components of the Reynolds stress tensor, we require at least six radial velocity variances measured in different beam orientations in analogy to the method by Eberhard et al. (1989). Here, we discuss the limitations of using different methods and assumptions to estimate the along-wind velocity variance with fewer than six radial velocity variances. We focus on this variance because it is a key parameter for load validation (Dimitrov et al., 2019; Conti et al., 2021), power performance assessment (Wagner et al., 2014, 2015; Borracino et al., 2017) and wind turbine control (Schlipf et al., 2014, 2020).

Measurements of turbulence by lidars are affected by spatial average filtering effects caused by the lidar probe volume and cross-contamination effects from combining line-of-sight velocities at different locations assuming instantaneous homogeneity and not only statistical homogeneity (Sathe and Mann, 2013; Kelberlau and Mann, 2020). Both effects contribute to the systematic error of turbulence estimation using lidars. As a consequence of the first effect, a lidar estimates turbulence essentially through a low-pass filter and cannot detect high-frequency variations, which yields the so-called "filtered variances". Held and Mann (2018) showed that different methods of deriving the radial velocity from the lidar Doppler spectrum influence the degree of the turbulence attenuation. We explore the ability of these methods for turbulence estimation with the SpinnerLidar measurements. We also compensate for the probe volume filtering effect and compute "unfiltered variances" of the radial velocity using Doppler radial velocity spectra from the SpinnerLidar measurements. Peña et al. (2017) used Doppler radial velocity spectra and showed that the along-wind unfiltered variance from a conically scanning lidar agreed well with the one from a cup anemometer on a met mast. However, other lidar-derived estimates of velocity-component variances were largely biased due to the lidar scanning configuration.

This paper is organized as follows. Section 2 describes the turbulence spectral model, the maximum, median and centroid methods to derive the lidar radial velocities from the Doppler spectrum, the filtered and the unfiltered radial velocity variances, the least-squares method to compute the Reynolds stress tensor, and the numerical lidar simulations. Section 3 provides information on the measurement campaign and the employed nacelle lidars. Section 4 describes how we filter and post-process the high-frequency lidar radial velocities and the Doppler radial velocity spectra. Section 5 shows the inter-comparison of turbulence characteristics between three nacelle lidars and a mast-mounted sonic anemometer at turbine hub height. Discussions and conclusions are given in Sects. 6 and 7, respectively.

2 Methodology

2.1 Turbulence spectral model

Assuming Taylor's frozen turbulence hypothesis (Taylor, 1938), the wind field can be described by a vector field $\boldsymbol{u}(\boldsymbol{x}) = (u, v, w) = (u_1, u_2, u_3)$, where u is the horizontal along-wind component, v the horizontal lateral component, w the vertical component, and $\boldsymbol{x} = (x, y, z)$ the position vector defined in a right-handed coordinate system. The mean value of the homogeneous velocity field is $\langle \boldsymbol{u}(\boldsymbol{x}) \rangle = (U, 0, 0)$, so the coordinate x is in the mean wind direction. The turbulence spectral properties of the three-dimensional homogeneous wind field are described by the spectral velocity tensor $\Phi_{ij}(\boldsymbol{k})$ (Kristensen et al., 1989):

$$\Phi_{ij}(\boldsymbol{k}) = \frac{1}{(2\pi)^3} \int R_{ij}(\boldsymbol{x}) \exp(-i\boldsymbol{k} \cdot \boldsymbol{x}) \mathrm{d}\boldsymbol{x}, \tag{1}$$

which is the Fourier transform of the covariance tensor $R_{ij}(\boldsymbol{x}) \equiv \langle u_i'(\boldsymbol{x}) u_j'(\boldsymbol{x} + \boldsymbol{r}) \rangle$, where $\langle \ \rangle$ denotes ensemble averaging, $\boldsymbol{r}$ is the separation vector, u_i' are the fluctuations around the mean and $\boldsymbol{k} = (k_1, k_2, k_3)$ is the wave vector in the (x, y, z) directions.

We assume that the spectral velocity tensor $\Phi_{ij}(\boldsymbol{k})$ can be described by the model of Mann (1994) (hereafter the Mann model), which, besides $\boldsymbol{k}$, only contains three parameters (known as Mann parameters): $\alpha\varepsilon^{2/3}$ is a product of the spectral Kolmogorov constant α and the turbulent energy dissipation rate ε to the two-thirds power, L is a length scale related to the size of the energy-containing eddies, and Γ is a parameter describing the anisotropy of the turbulence. From the spectral tensor, the one-point spectra of velocity fluctuations are calculated by

$$F_{ij}(k_1) = \iint \Phi_{ij}(\boldsymbol{k}) \mathrm{d}k_2 \mathrm{d}k_3. \tag{2}$$

The wind velocity components have the three auto-spectra $F_{11} (= F_u)$, F_{22}, and F_{33}. The auto-spectra can be evaluated using Eq. (2). The variances of the velocity components are

$$\sigma_{u,v,w}^2 = \int\limits_{-\infty}^{\infty} F_{u,v,w}(k_1) \mathrm{d}k_1, \tag{3}$$

and these, together with the covariances, are the components of the Reynolds stress tensor:

$$
\boldsymbol{R} = \begin{bmatrix} \sigma_u^2 & \langle u'v' \rangle & \langle u'w' \rangle \\ \langle v'u' \rangle & \sigma_v^2 & \langle v'w' \rangle \\ \langle w'u' \rangle & \langle w'v' \rangle & \sigma_w^2 \end{bmatrix}. \tag{4}
$$

2.2 Nacelle lidar

The unit vector $\boldsymbol{n}$ describing the beam orientation of a nacelle lidar can be expressed as (Peña et al., 2017)

$$
\boldsymbol{n}(\phi, \theta) = (-\cos\phi, \cos\theta\sin\phi, \sin\theta\sin\phi), \tag{5}
$$

where θ is the angle between the y axis and $\boldsymbol{n}$ projected onto the y–z plane and ϕ is the angle between the beam and the negative x axis (hereafter half-cone opening angle). As with any other Doppler lidar, nacelle lidars only measure the radial velocity (also known as the line-of-sight velocity) along the laser beam. Thus, the radial velocity can be expressed as (Mann et al., 2010)

$$
v_{\mathrm{r}}(\phi, \theta) = \int_{-\infty}^{\infty} \varphi(s)\boldsymbol{n}(\phi, \theta) \cdot \boldsymbol{u}[\boldsymbol{n}(\phi, \theta)(f_d + s)]\mathrm{d}s, \tag{6}
$$

where φ is the lidar weighting function that considers the probe volume, s is the distance from the focus point along the beam and f_d is the focus distance. This equation assumes that v_{r} is determined from the Doppler spectrum by the centroid or center of gravity method. For the case of the investigated CW lidars, their weighting functions are assumed to be of the Lorentzian form (Sonnenschein and Horrigan, 1971):

$$
\varphi(s) = \frac{1}{\pi} \frac{z_{\mathrm{R}}}{z_{\mathrm{R}}^2 + s^2}, \tag{7}
$$

where z_{R} is the Rayleigh length that can be estimated as

$$
z_{\mathrm{R}} = \frac{\lambda f_d^2}{\pi r_{\mathrm{b}}^2}, \tag{8}
$$

where λ is the laser wavelength and r_{b} the beam radius at the output lens.

If we assume that the lidars measure at a point, instead of over a probe volume, and that u, v and w do not change over the scanned area, the radial velocity in Eq. (6) can be estimated as the sum of the projection of the three-dimensional wind components on the beam pointing direction:

$$
v_{\mathrm{r}}(\phi, \theta) = -u\cos\phi + v\cos\theta\sin\phi + w\sin\theta\sin\phi. \tag{9}
$$

The variance of the radial velocity $\sigma_{v_{\mathrm{r}}}^2$ can be derived by taking the variance of Eq. (9) (Eberhard et al., 1989):

$$
\begin{aligned}
\sigma_{v_{\mathrm{r}},\mathrm{unf}}^2(\phi, \theta) = {}& \sigma_u^2\cos^2\phi + \sigma_v^2\cos^2\theta\sin^2\phi + \sigma_w^2\sin^2\theta\sin^2\phi \\
& - 2\langle u'v' \rangle\cos\phi\cos\theta\sin\phi \\
& - 2\langle u'w' \rangle\cos\phi\sin\theta\sin\phi \\
& + 2\langle v'w' \rangle\sin^2\phi\cos\theta\sin\theta.
\end{aligned} \tag{10}
$$

Equation (10) provides accurate velocity-component variance and covariance estimates if the radial velocity variance is unfiltered, i.e., if we are able to account for the lidar probe volume. In practice, if the Doppler radial velocity spectrum is available, we have means to estimate the unfiltered radial velocity variance. This will be described in Sect. 2.4.

2.3 Estimation of the radial velocity and the filtered radial velocity variance

Three methods are used here to determine the dominant frequency from the Doppler radial velocity spectrum to compute the radial velocity. The centroid method computes the characteristic frequency f in the Doppler radial velocity spectrum $p(f)$ as

$$
f_{\mathrm{cen}} = \frac{\int f p(f)\mathrm{d}f}{\int p(f)\mathrm{d}f}. \tag{11}
$$

The maximum method finds the frequency bin where the maximum peak in the Doppler spectrum occurs. The median method treats the Doppler spectrum as a probability distribution and finds the frequency bin that corresponds to the median value. These frequencies are then converted to radial velocity estimates according to the sampling frequency of the digitizer, the length of the fast Fourier transform, and the lidar's laser wavelength. Since none of these methods considers the whole Doppler radial velocity spectrum, turbulence statistics computed from these radial velocities are filtered. Therefore, we use the term-filtered radial velocity variance $\sigma_{v_{\mathrm{r}},\mathrm{filt}}^2$.

2.4 Estimation of the unfiltered radial velocity variance

Here, we use the Doppler radial velocity spectrum to estimate the unfiltered radial velocity variance $\sigma_{v_{\mathrm{r}},\mathrm{unf}}^2$ of the lidar beams. Since the investigated nacelle lidars measure at small opening angles over a relatively homogeneous inflow, the effect of the radial velocity gradient within the probe volume is negligible (see Mann et al., 2010, for a detailed discussion). Therefore, $\sigma_{v_{\mathrm{r}},\mathrm{unf}}^2$ can be estimated as the second central statistical moment of the ensemble-average Doppler spectrum of the radial velocity. The mean radial velocity can be estimated from the area-normalized mean Doppler spectrum $p(v_{\mathrm{r}})$ as

$$
\mu_{v_{\mathrm{r}}} = \int_{-\infty}^{\infty} v_{\mathrm{r}} p(v_{\mathrm{r}})\mathrm{d}v_{\mathrm{r}}, \tag{12}
$$

and its variance as

$$\sigma_{v_r}^2 = \int\limits_{-\infty}^{\infty} (v_r - \mu_{v_r})^2 p(v_r) \mathrm{d}v_r. \tag{13}$$

Assuming all radial velocity contributions to the Doppler spectrum are due to turbulence, $\sigma_{v_r}^2$ in Eq. (13) provides an estimate of $\sigma_{v_r, \mathrm{unf}}^2$. This can be used to extract the velocity variances using Eq. (10), which gives the components of the Reynolds stress tensor.

2.5 Estimation of the mean wind velocity

Radial velocity measurements from different beam directions can be combined to reconstruct the mean wind. In the following sections, we show that different approaches are used for different lidars.

2.5.1 First approach

A least-squares formulation is used to find the mean wind vector $\boldsymbol{U} = (U, V, W)$ over all beam positions. Here, we minimize the sum of squared differences between the beam-projected wind and the measured radial velocities:

$$\Delta^2 = \int (\boldsymbol{n} \cdot \boldsymbol{U} - v_r)^2 \mathrm{d}\mu. \tag{14}$$

The integral $\int \mathrm{d}\mu$ could be an area-weighted average of the beam measurements. In practice, the integral could simply be the sum over all pairs of radial velocity v_r and the corresponding beam unit vectors $\boldsymbol{n}$ among the scanning area. The vector $\boldsymbol{U}$ that minimizes the integral must fulfill

$$\frac{\partial \Delta^2}{\partial U_i} = 0 \Rightarrow \int (\boldsymbol{n} \cdot \boldsymbol{U} - v_r) n_i \mathrm{d}\mu = 0, \quad \text{for } i = 1, 2, 3. \tag{15}$$

Expanding the integral and isolating $\boldsymbol{U}$ we get

$$U_i = (M^{-1})_{ij} \int v_r n_i \mathrm{d}\mu, \quad \text{where } M_{ij} = \int n_i n_j \mathrm{d}\mu. \tag{16}$$

This approach assumes wind homogeneity over the scanning area. To get the three mean wind components, we need at least three values of v_r measured in different orientations. This approach is used for deriving the mean wind vector from SpinnerLidar multi-beam measurements.

2.5.2 Second approach

Assuming that the inflow wind is horizontal, i.e., $w = 0 \, \mathrm{m \, s^{-1}}$, Eq. (9) can here be reduced to

$$v_r(\phi, \theta) = u \cos \phi + v \sin \phi \cos \theta. \tag{17}$$

To compute the mean wind components, we need at least two radial velocities measurements and the corresponding beam

positions (ϕ and θ) assuming that u and v are identical at the focus points of a pair of beams. Therefore, a two-beam nacelle lidar can compute u and v:

$$u = \frac{v_{r,\mathrm{left}} + v_{r,\mathrm{right}}}{2 \cos \phi},$$
$$v = \frac{v_{r,\mathrm{right}} - v_{r,\mathrm{left}}}{2 \sin \phi}. \tag{18}$$

A similar approach can be used for a four-beam nacelle lidar. The two upper beams and two lower beams are used separately (Larvol, 2016) to estimate u and v at two different heights. Here, we average the estimates at the two heights to represent the mean inflow velocity.

2.5.3 Induction correction

Due to the presence of the wind turbine, the wind slows down as it approaches the rotor. We perform the correction of the slowdown in speed (also referred as the induction correction) to the estimates of lidars and the sonic anemometer using the method in Simley et al. (2016):

$$\frac{U}{U_\infty} = 1 - a \left(1 + \frac{2x}{D} \left(1 + \left(\frac{2x}{D} \right)^2 \right)^{-\frac{1}{2}} \right), \tag{19}$$

where U_∞ is the undisturbed free stream wind speed, x is the distance between the lidar scanning plane and the rotor, and a is the axial induction factor. The induction factor a is determined using the same procedure as the one in Held and Mann (2019) assuming the effect of the induction is constant over a 10 min period. A steady-state thrust curve of the V52 turbine and the 10 min mean wind speeds measured by the cup anemometer at 44 m are used to look up the thrust coefficient C_t. Then, we compute the induction factor using axial momentum theory, i.e., $C_t = 4a(1-a)$.

2.6 Estimation of the Reynolds stress tensor

We assume that the Reynolds stresses $R_{ij} \equiv \langle u_i u_j \rangle$ are homogeneous over the rotor plane irrespective of the mean wind field. We apply a least-squares fit to the radial velocity variances and the corresponding beam unit vectors to estimate the Reynolds stresses:

$$\Delta^2 = \int \left(\boldsymbol{n} \cdot \boldsymbol{Rn} - \sigma_{v_r}^2 \right)^2 \mathrm{d}\mu. \tag{20}$$

The matrix $\boldsymbol{R}$ that minimizes the integral must fulfill

$$\frac{\partial \Delta^2}{\partial R_{ij}} = 0 \Rightarrow \int \left(\boldsymbol{n} \cdot \boldsymbol{Rn} - \sigma_{v_r}^2 \right) n_i n_j \mathrm{d}\mu = 0. \tag{21}$$

This can be written as

$$R_{kl} \int n_k n_l n_i n_j \mathrm{d}\mu = \int \sigma_{v_r}^2 n_i n_j \mathrm{d}\mu. \tag{22}$$

The right side of Eq. (22) is written as a vector having the length of six using the six combinations of indices $(i, j) = (1, 1), (1, 2), (1, 3), (2, 2), (2, 3), (3, 3)$ with $n_1 = -\cos\phi$, $n_2 = \cos\theta\sin\phi$ and $n_3 = \sin\theta\sin\phi$ (as given in Eq. 5). Similarly, on the left side of Eq. (22), R_{kl} is rearranged to a length six vector, where $\int n_k n_l n_i n_j \mathrm{d}\mu$ is a 6-by-6 matrix with both (k, l) and (i, j) going through the same combinations of indices:

$$
\begin{bmatrix}
\sum n_1^4 & \sum n_1^2 n_2^2 & \sum n_1^2 n_3^2 & \sum 2n_1^3 n_2 & \sum 2n_1^3 n_3 & \sum 2n_1^2 n_2 n_3 \\
\cdots & \sum n_2^4 & \cdots & \cdots & \cdots & \cdots \\
\cdots & \cdots & \sum n_3^4 & \cdots & \cdots & \cdots \\
\cdots & \cdots & \cdots & \sum 2n_1^2 n_2^2 & \cdots & \cdots \\
\cdots & \cdots & \cdots & \cdots & \sum 2n_1^2 n_3^2 & \cdots \\
\cdots & \cdots & \cdots & \cdots & \cdots & \sum 2n_2^2 n_3^2
\end{bmatrix}
$$
$$
\times
\begin{bmatrix}
R_{uu} \\
R_{vv} \\
R_{ww} \\
R_{uv} \\
R_{uw} \\
R_{vw}
\end{bmatrix}
=
\begin{bmatrix}
\sum \sigma_{v_r}^2 n_1^2 \\
\sum \sigma_{v_r}^2 n_2^2 \\
\sum \sigma_{v_r}^2 n_3^2 \\
\sum \sigma_{v_r}^2 n_1 n_2 \\
\sum \sigma_{v_r}^2 n_1 n_3 \\
\sum \sigma_{v_r}^2 n_2 n_3
\end{bmatrix}.
\tag{23}
$$

To compute the six Reynolds stresses, we need at least six radial velocity variances from different beam directions to ensure that the large matrix in Eq. (23) is not degenerate (i.e., its determinant is not zero) (Sathe et al., 2015). If fewer than six variances of the radial velocity are available, we have fewer knowns than unknowns. If the nacelle lidar beams have only one opening angle ϕ, the equations will be linearly dependent, and so the determinant will be zero and Eq. (23) will have infinite solutions. In those cases, only σ_u^2 can be well determined, and the stresses involving the lateral component will be more noisy (Peña et al., 2019). In this study, we use all radial velocity variances from the SpinnerLidar to calculate the six Reynolds stresses.

2.7 Numerical simulations

We generate three-dimensional random turbulence fields using the Mann model (Mann, 1998) with typical values of the model parameters: $\alpha\varepsilon^{2/3} = 0.05\,\mathrm{m}^{4/3}\,\mathrm{s}^{-1}$, $L = 61\,\mathrm{m}$ and $\Gamma = 3.2$. We furthermore assume Taylor's frozen turbulence hypothesis:

$$
\boldsymbol{u}(x, y, z, t = 0) = \boldsymbol{u}(x + Ut, y, z, t),
\tag{24}
$$

so the wind field at any given time can be obtained by translating the wind field at time $t = 0$. The turbulence boxes are 18 km long in the along-wind and 128 m long in both the vertical and lateral directions. The number of grid points in the simulation in the three directions is $(N_x, N_y, N_z) = (8192, 64, 64)$. A total of 100 turbulence boxes with the same Mann parameters but different seeds were generated. For simulating lidar measurements, we add a mean wind U and a linear vertical shear $\mathrm{d}U/\mathrm{d}z$ to the along-wind velocity com-
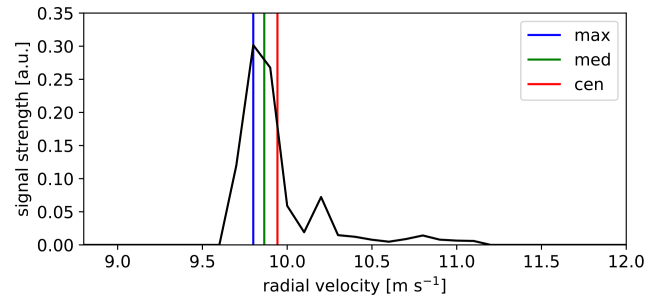

Figure 1. Example of a Doppler radial velocity spectrum simulated in a turbulence box, including the radial velocity estimates using the maximum (max), the median (med) and the centroid (cen) methods.

ponent u in each box:

$$
u = U + \frac{\mathrm{d}U}{\mathrm{d}z}(z - z_{\mathrm{rotor}}) + u',
\tag{25}
$$

where $U = 10\,\mathrm{m}\,\mathrm{s}^{-1}$, $\mathrm{d}U/\mathrm{d}z = 0.0288\,\mathrm{s}^{-1}$, z_{rotor} is the turbine hub height in the turbulence box, i.e., the middle grid point in the z coordinate, and u' is the fluctuation around the mean from the turbulence box.

We also account for the lidar probe volume. The lidar Doppler spectrum $S(v_r, t)$ is (Held and Mann, 2018)

$$
S(v_r, t) = \int_{-M}^{M} \varphi(s)\delta(v_r - \boldsymbol{u}(s) \cdot \boldsymbol{n})\mathrm{d}s,
\tag{26}
$$

where δ is the Dirac delta function and M is the distance along the beam that we use to truncate the integral due to the finite length of the turbulence boxes. Figure 1 shows an example of an instantaneous Doppler radial velocity spectrum simulated in a turbulence box for one arbitrary beam of the SpinnerLidar, in which the radial velocity is determined by the three methods introduced in Sect. 2.3. The velocity bin resolution is $0.1\,\mathrm{m}\,\mathrm{s}^{-1}\,\mathrm{bin}^{-1}$ and $M = 8z_R$, which is hereafter always used.

3 Experiment setup

3.1 Measurement campaign

A measurement campaign on a Vestas V52 wind turbine was conducted at DTU Risø campus in Roskilde, Denmark. Figure 2 shows a layout of the test site on a digital surface elevation model. The terrain is slightly hilly and the surface is characterized by a mix of cropland, grassland and coast. A row of wind turbines stands ≈ 200–300 m south-east of the Roskilde fjord. The V52 wind turbine (marked as a red circle) is located at the northernmost position. It has a rotor diameter D of 52 m, a hub height of 44 m and a nominal power of 850 kW. The rotor speed is within the range of 14–31 rpm with a nominal value of 26 rpm. The cut-in, rated and
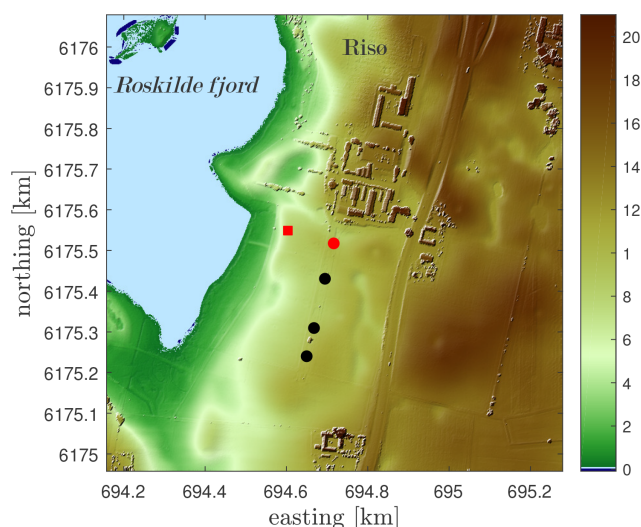
Figure 2. The Risø test site in Roskilde, Denmark, on a digital surface elevation model (UTM32 WGS84). The V52 meteorological mast is shown in a red square. The wind turbines are shown in circles (in red the reference V52 wind turbine). The color bar indicates the height above mean sea level in meters.

Figure 3. Three lidars sitting on the nacelle of the V52 wind turbine at DTU Risø campus: SpinnerLidar (top), WindVision (middle) and WindEye (bottom).

cut-out wind speeds are 4, 14 and 25 m s^{-1}, respectively. A meteorological mast (marked as a red square) was mounted at 291° (from the north) at a distance of 120 m (2.3D) upstream from the turbine. The mast is 72 m high and instrumented with anemometers at 18, 31, 44, 57 and 70 m above the ground level (Peña et al., 2019): Metek USA-1 3D sonic anemometers are on the northern side of the booms and Risø cup anemometers on the southern side of the booms. In addition, there is a wind vane at 41 m and Risø absolute temperature sensors at 18 and 70 m. There are also a Thies precipitation opto-sensor and a Vaisala pressure sensor at 2 m (DTU Wind Energy, 2014). Three continuous-wave lidars were mounted on the nacelle of the V52 wind turbine, as shown in Fig. 3: the SpinnerLidar (on the top), a four-beam WindVision (in the middle) and a two-beam WindEye (at the bottom). The vertical displacement between the scan head of the SpinnerLidar, WindVision, WindEye and the wind turbine rotation axis is 2.47, 2 and 1.64 m, respectively. More information about the three lidars is given in Sect. 3.2.

3.2 Nacelle lidars

Three forward-looking nacelle lidars are investigated here. All lidars are based on a CW system and they all were scanning at a single plane (see Fig. 4). The specifications for three nacelle lidars can be found in Table 1. The SpinnerLidar (Peña et al., 2019) scans in a rosette-curve pattern and generates 400 radial velocities in one full scan. For this measurement campaign, the SpinnerLidar was set up to perform a full scan every 2 s at a focus distance of 62 m. The system also recorded the instantaneous Doppler spectrum of the

radial velocity, which is used here both to derive the radial velocity using different methods and to estimate the unfiltered radial velocity variance. The SpinnerLidar streams out average Doppler spectra at a rate of 200 Hz. Each Doppler spectrum is represented in 256 frequency bins with a spectral resolution of 195.3 kHz corresponding to a radial velocity resolution of 0.1528 m s^{-1} per bin. In addition, it recorded the signal strength (here called "power") of the instantaneous spectrum. We also use the inclination and the azimuthal positions from the SpinnerLidar sensors to correct the scanned locations.

The two-beam WindEye (hereafter W2) and the four-beam WindVision (hereafter W4) are two commercial lidars from Windar Photonics A/S (Windar Photonics, 2020). W2 measured at 37 m and has similar width of the probe volume (indicated by the Rayleigh length) as the SpinnerLidar. Note that the largest probe volume and the smallest half-cone opening angle are those of the four-beam system. The azimuthal angle in Table 1 refers to the position of the beams on the scanning cone surface (from the top of the cone). The two beams from W2 are aligned horizontally, while the four beams from W4 focuses at each quadrant of the rotor area. Both systems complete a scan in 1 s.

4 Data analysis

4.1 Data selection and filtering

The measurements were collected between 1 October 2020 and 30 April 2021. We analyze the time series of all data and their statistics within 10 min periods (in total 30 492 periods of 10 min). There are three types of measurements: the supervisory control and data acquisition of the wind turbine, the mast measurements and the measurements from three lidars. We concentrate our analysis on the wind sectors, which are relatively aligned with the mast-turbine direction (291°) to exclude the influence of the wakes from the nearby wind turbines to the greatest extent. We select 10 min periods for the analysis using the following criteria:
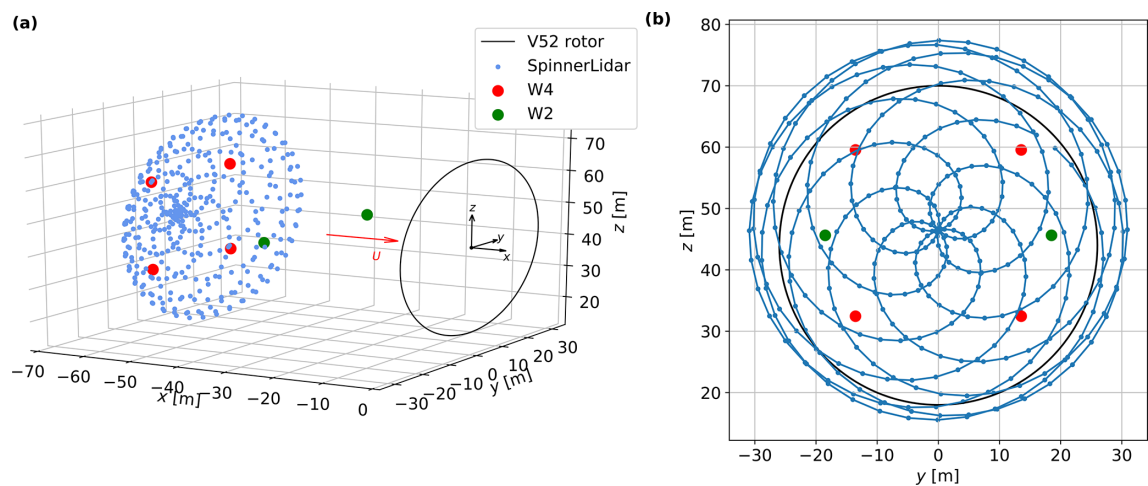
Figure 4. (a) The scanning trajectory of the nacelle lidars. **(b)** An upwind view of the theoretical scanning pattern performed by the W2, W4 and the SpinnerLidar.

Table 1. Specifications of the nacelle lidars for the measurement campaign.

		SpinnerLidar	WindVision (W4)	WindEye (W2)
Number of beams	[–]	400	4	2
Focus distance f_d	[m]	62	62	37
Rayleigh length z_R	[m]	2.44	7.18	2.42
Half-cone opening angle ϕ	[°]	0–30	18	30
Beam azimuth angle θ	[°]	0–360	45, 135, 225, 315	90, 270
Time for a full scan	[s]	2	1	1

– All lidars and the V52 turbine should be concurrently operating. The turbine status is indicated by the rotor speed, which should be higher than 14 rpm. This leaves us 19 190 periods of 10 min.

– The wind direction measured by the wind vane and the yaw angle of the turbine are both between 261–321°. The absolute difference between these two directions is lower than 5°. Since the dominant wind direction at this site is west and south-west, we have 2457 periods of 10 min left after applying this filter.

– The wind speed measured by the cup anemometer at the turbine hub height is higher than $3\,\mathrm{m\,s^{-1}}$.

– No precipitation is detected during the 10 min period.

After filtering, the number of the 10 min periods for the analysis is 2348.

4.2 SpinnerLidar measurements

4.2.1 Data filtering

We process the SpinnerLidar measurements for the selected 2348 periods of 10 min. The SpinnerLidar measurements are

further filtered based on both the system-reported radial velocity, which is the median estimate from the raw Doppler radial velocity spectrum, and the power of the spectrum. The following criteria are applied (Fig. 5 shows an example of results of the SpinnerLidar filtering within an arbitrary 10 min period):

– We filter out all measurements with system-reported radial velocity estimates below $3.2\,\mathrm{m\,s^{-1}}$, which is the reference minimal detectable radial velocity by the SpinnerLidar due to the interference of the turbine blades (Karen Enevoldsen, personal communication, 2021).

– We simulate the radial velocity of all possible blade returns as (Angelou et al., 2015)

$$v_r = |\Omega S_y h_{SL}|, \qquad (27)$$

where Ω is the 10 min mean rotor speed, S_y is the lateral component of the unit vector with reference to the SpinnerLidar in the y–z plane, and h_{SL} is the vertical displacement between the SpinnerLidar scan head and the wind turbine rotation axis. Equation (27) does not consider the misalignment between the SpinnerLidar and the nacelle, which is negligible (below 0.5°) in the measurement campaign. The simulated blade signals are
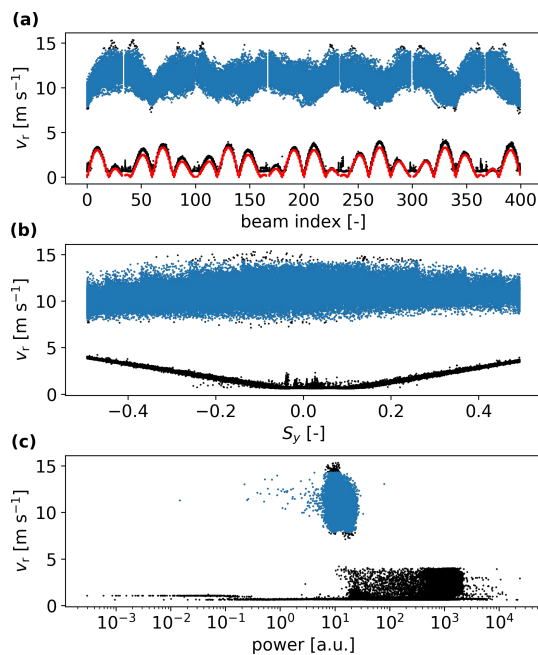
Figure 5. Radial velocity as function of **(a)** index of the 400 beams in each full scan, **(b)** the lateral component of the unit vector S_y and **(c)** power for an arbitrary 10 min period. Filtered data are shown in black and data left after filtering in blue. The red color in the top panel represents the simulated radial velocity from the possible blade returns.

marked in red in Fig. 5. We discriminate the wind speed signal from the blade return signal from Eq. (27) when the difference between them is above $0.2\,\mathrm{m\,s^{-1}}$.

– We filter out all measurements exceeding power values above 100 (Peña et al., 2019) (this signal strength has arbitrary units). We can see from Fig. 6 that some measurements close to the middle of the pattern are filtered out with this criterion.

– Finally, we filter out radial velocities exceeding its mean $\pm$ 3 times its standard deviation within the 10 min period.

Further, there should be at least half of the raw measurements left for the analysis to consider a 10 min period of SpinnerLidar measurements, which leaves us 1605 periods of 10 min for the later post-processing.

4.2.2   Gridding the scans

We estimate the lidar scan locations using the average azimuthal and inclination angles of the SpinnerLidar within the 10 min period, i.e., the system-reported coordinates are rotated along the longitudinal and lateral axis of the SpinnerLidar scanhead, respectively. Figure 6a shows the scan locations in blue and the non-rotated locations in orange within a 10 min period (26 February 2021 at 14:10:00), where the

average inclination angle is $3.15°$ and the average azimuthal angle is $0.34°$.

Due to the turbine movement and SpinnerLidar slack, we aggregate the azimuthal- and inclination-corrected scan locations within a grid of 1 m resolution in the y–z plane, as shown in Fig. 6b. The coordinates of the grid cells, which are marked in light grey, are given by the resolution and extension of the grid. The "gridded" rosette pattern is shown in black (some are covered by red color as explained later). All radial velocity spectra for the scans lying within each grid cell in the given 10 min period are accumulated. We use only grid cells, where there are more than 30 instantaneous Doppler radial velocity spectra. In Fig. 6b, we show in red the grid cells satisfying this criterion. Finally, we only use those 10 min periods in which we have 900 grid cells satisfying the criterion.

4.2.3   Doppler spectra processing and usage

Figure 7 shows an example of the processing of the Doppler radial velocity spectra from the accumulated measurements within a grid cell close to the middle of the scan. The raw Doppler radial velocity spectra within that grid cell are shown in Fig. 7a. For this 10 min period (26 February 2021 at 14:10:00), the vane measures a wind direction of $291.6°$ and the yaw angle is $291.0°$. The lidar unit vector pointing onto this grid cell is almost parallel to the terrain (ϕ is around $1.4°$), thus close to the main wind direction. As shown in Fig. 7a, high spectral values "contaminate" the spectra in the first few velocity bins due to, e.g., optical reflections from the bore point (i.e., the beam hitting the telescope lens perpendicularly) or few left blade signals. To ease the spectra processing, we define a threshold for each individual spectrum, which defines the limit above which a Doppler spectrum is considered to be caused by the wind. The calculation of the threshold is based on the mean value (μ) plus a number of standard deviations (σ) within a frequency range where no radial velocity signals are anticipated. Angelou et al. (2012) showed that a systematic selection of the threshold level should take into account the shape of the Doppler spectrum relative to the variation of the spectrum noise level. The number of standard deviations is thus different for the case of a wide Doppler velocity spectrum (high turbulence level) and a narrow one (low turbulence level). An overestimation of the threshold removes low-intensity fluctuations and, subsequently, biases the estimation of the radial velocity and reduces its variance. Here, we select a threshold of $\mu+3\sigma$ of the spectral values in the last 50 frequency bins. After thresholding, we remove the spectral values up to the bin corresponding to $2.3\,\mathrm{m\,s^{-1}}$, which filters out the high spectral peaks in unrealistic low-velocity bins (Fig. 7b).

Each "cleaned" spectrum is then area-normalized. Figure 7c shows the ensemble-average Doppler radial velocity spectrum from all normalized, thresholded and cleaned spectra. We also show the normalized distribution of sonic mea-
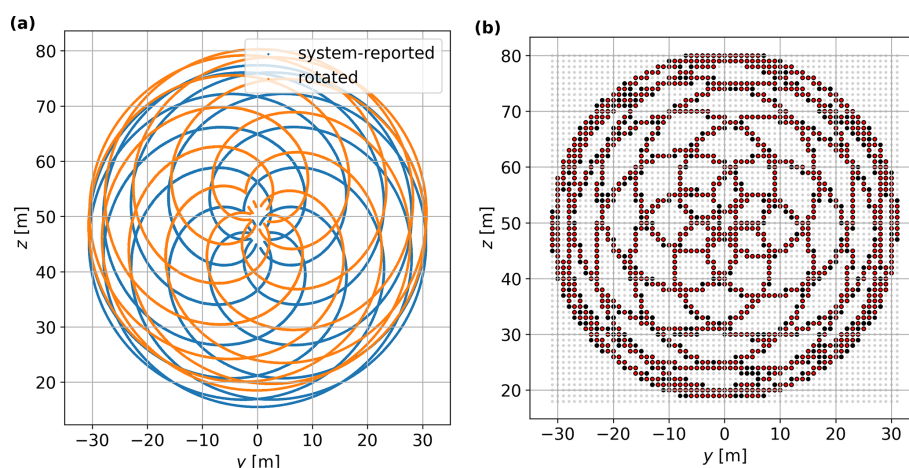
Figure 6. (a) Scan locations (before and after rotation) in an arbitrary 10 min period. **(b)** Gridding of the scans within the same 10 min period. Grid cells with more than 30 radial velocity spectra are marked in red. Other details are given in the text.
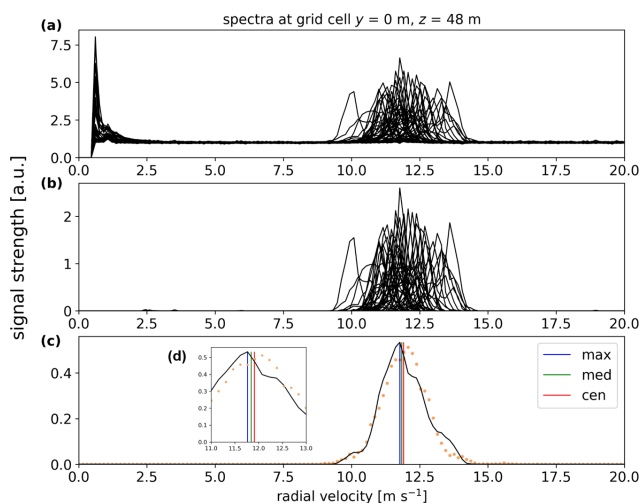

Figure 7. An example of Doppler radial velocity spectra analysis within a 10 min period (26 February 2021 at 14:10:00). The location of the grid cell $y = 0$ m, $z = 48$ m is shown in the scanning pattern in Fig. 6b. **(a)** Raw and scaled Doppler radial velocity spectra. **(b)** Cleaned and normalized Doppler spectra. **(c)** The average Doppler spectrum (black), the distribution of the sonic measurements at hub height (orange) and the three radial velocity estimates, which can be clearly seen in the inset **(d)**.

surements at hub height within the same 10 min period projected to the direction of the grid cell unit vector, which as illustrated are in good agreement with the ensemble-average Doppler radial velocity spectrum. We use the ensemble-averaged Doppler radial velocity spectrum to derive both the unfiltered radial velocity variance and the radial velocity estimates (maximum, centroid and median), which are later used for the reconstruction of the mean wind.

All grid cells with at least 900 Doppler radial velocity spectra within each 10 min period are considered for the re-

construction of the mean wind and the Reynolds stresses. The three-dimensional mean wind vector is computed from the median-, maximum- and centroid-radial velocities, using the approach in Sect. 2.5.1. Figure 8a shows a contour map of the median-derived radial velocity for an arbitrary 10 min period of SpinnerLidar measurements. As expected, the highest radial velocities are found in the middle-top part of the scan. This radial velocity contour map shows a similar pattern as that from the average of SpinnerLidar simulations using 30 turbulence boxes (Fig. 8b).

4.3 Windar measurements

4.3.1 Data filtering

The measurements for the W2 and W4 nacelle lidars are processed at 2 and 4 Hz, respectively. Therefore, within a 10 min period, the optimal amount of radial velocities per beam for W2 is 1200 and for W4 is 2400. We remove outliers of radial velocities and apply the same blade filtering using the method described in Sect. 4.2. We set a criterion that there should be at least 90 % of the optimal amount of data left after the filtering for a 10 min period. We do not account for the radial velocities of a full scan when data from any beam are missing. This leaves us 1499 periods of 10 min for the intercomparison.

4.3.2 Methods to compute the along-wind velocity variance

The along-wind and lateral velocities are reconstructed for each scan (i.e., for every 1 s) using the approach described in Sect. 2.5.2, and we compute 10 min statistics from these velocities. Due to the limited number of beams and the unavailability of Doppler radial velocity spectra, we only compute the filtered along-wind variance using two methods. We can compute the wind speed variance directly from the
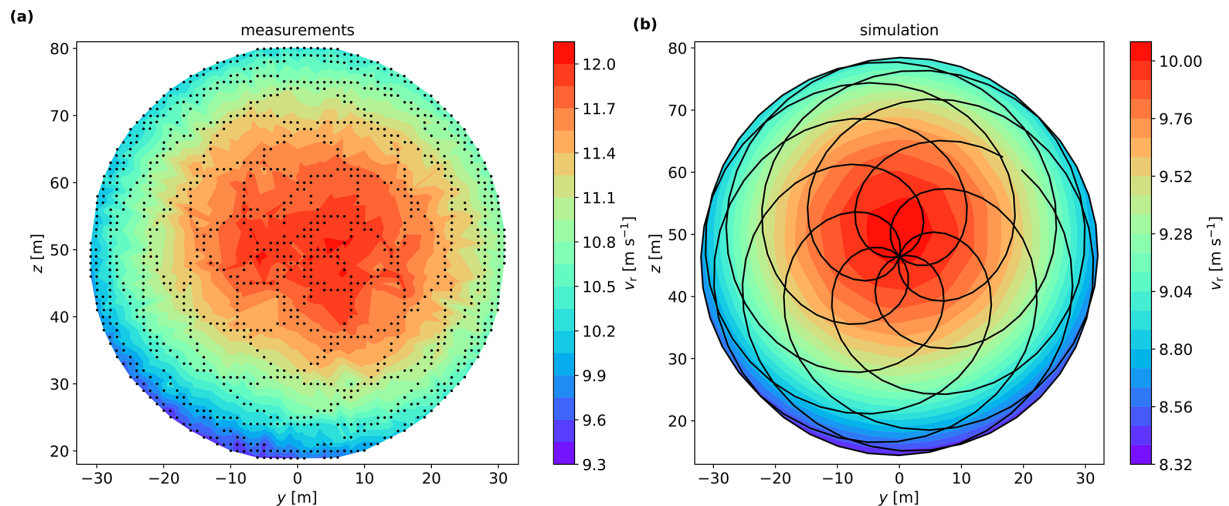
Figure 8. (a) Contour map of the median-derived radial velocity from the ensemble-average Doppler spectra in a 10 min period. Black dots indicate the location of the grid cells with more than 30 Doppler spectra. **(b)** Contour map of the average median-derived radial velocity from SpinnerLidar simulations using 30 turbulence boxes.

time series of reconstructed along-wind velocity U within the 10 min periods (hereafter denoted as the "U-variance" method). We can also compute σ_u^2 using Eq. (23) with some assumptions and three are investigated here. The first is to assume that all Reynolds stress components apart from σ_u^2 are zero (hereafter denoted as the "LSP-σ_u^2" method). This basically means that Eq. (23) becomes

$$\sigma_u^2 = \frac{\sigma_{v_{\rm r}}^2}{\cos^2\phi}. \tag{28}$$

Since the half-cone opening angle of nacelle lidars is usually small, this method tends to overestimate σ_u^2. The second is to assume turbulence isotropy; i.e., the auto-variance of the three velocity components is the same and they are uncorrelated (hereafter denoted as the "LSP-isotropy" method). From Eq. (23), this means that σ_u^2 is then the average of the radial velocity variances of the lidar beams. The third option is to assume that $\sigma_v = 0.7\sigma_u$ and $\sigma_w = 0.5\sigma_u$, as suggested in IEC (2019) (hereafter denoted as the "LSP-IEC" method).

4.4 Sonic measurements

We use the 20 Hz raw sonic measurements at hub height (44 m) to calculate the mean horizontal wind speed and its variance for all selected 10 min periods. Figure 9a shows that the horizontal speed measured by the cup and the sonic anemometer is nearly the same. When looking at the computed variance in Fig. 9b, a bias of 3.4 % is found. We rotate the sonic-measured 3-D wind components, which are defined in the main wind coordinate system, to the coordinate system fixed with the wind turbine so that the sonic u velocity is aligned with the rotation axis of the turbine. We use the velocity and the variance of the rotated sonic-measured mean

wind components as the reference for the comparison with the estimates from the nacelle lidars.

5 Results

5.1 Mean wind speed

We perform comparisons of the 1499 10 min mean along-wind velocity component reconstructed from the lidar measurements with that from sonic measurements at 44 m (see Fig. 10). The estimates from lidars and the sonic anemometer are corrected for the induction using the method in Sect. 2.5.3. The lidar-derived estimate is a rotor-effective mean velocity since measurements at all scanning positions are considered. As illustrated, there is a high correlation for all nacelle lidars, as expected. The W2 and the SpinnerLidar estimates are slightly higher than that from the sonic anemometer while the estimate of W4 is 2.6 % lower. From the numerical simulation with 30 turbulence boxes, we found that all nacelle lidars are able to estimate the along-wind velocity well (not shown here); the uncertainties in the mean wind obtained from lidar are as large as those from the sonic anemometer.

5.2 Radial velocity variance

Figure 11a shows the simulated ratio of the unfiltered radial velocity variance to the u-velocity variance of the sonic anemometer among the scanning area. As the simulated wind field is based on the Mann model, the major source of cross-contamination on the radial velocity comes from the spectral tensor components involving w. As seen from the plot, the ratio is higher than one above the center and lower than one beneath it, which is due to the positive and negative contribu-
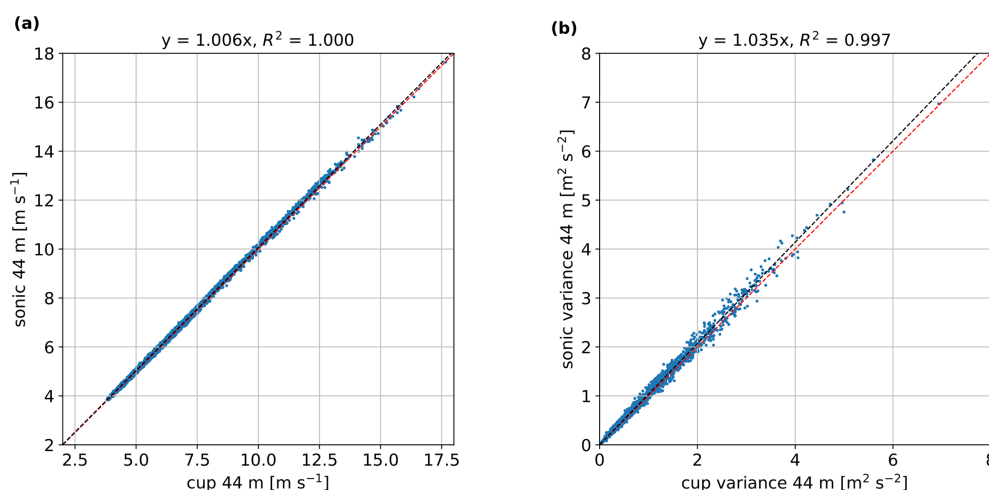
Figure 9. Comparison of the 10 min mean horizontal **(a)** wind speed and **(b)** variance between the sonic and the cup anemometers at 44 m. Each 10 min is shown in blue markers, a 1 : 1 relation is shown in the red dashed line, and a linear regression fit to origin in the black dashed line (results of the regression are given on the top of the plot, where R^2 is the coefficient of determination).
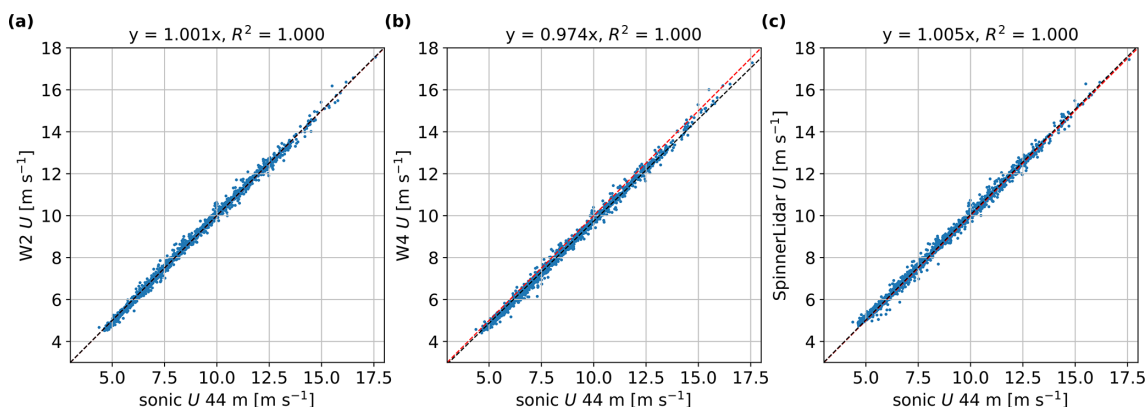

Figure 10. Comparison between the reconstructed along-wind mean velocity from the sonic anemometer at 44 m and **(a)** W2, **(b)** W4 and **(c)** SpinnerLidar. All estimates are corrected for the induction. Features regarding the red and black dashed lines as in Fig. 9.

tion of $\langle u'w' \rangle$, respectively, to the beam radial variance. Figure 11b shows the result from the measurement campaign as a scatter plot between the unfiltered radial velocity variance of the central grid cell ($y = 0$ m, $z = 48$ m) from the SpinnerLidar to the u variance of the sonic anemometer measurements at 44 m. From the measurements, the unfiltered radial velocity variance of the central beam reaches 91.5 % of the sonic variance, whereas the simulations show a zero bias for that central beam. We attribute this difference to our rather conservative method to clean Doppler radial velocity spectra, which attempts to eliminate any possible noise. However, this might lead to reduction of true turbulence contained in the Doppler radial velocity spectrum.

In Fig. 12a, we show the probe volume filtering effect on the scanning pattern by plotting the ratio of the filtered to the unfiltered radial velocity variance from the simulations. Here, the filtered radial velocity variance is computed from the centroid-derived radial velocity, because the cen-

troid method experiences the most turbulence attenuation caused by the probe volume (Held and Mann, 2018). The filtering effect due to probe volume is very similar throughout the pattern. The highest ratios are found around the center of the pattern, where the beam aligns with the along-wind velocity component. As the beam moves from the center, the ratio decreases because the beam's opening angle increases and the cross-contamination from other velocity components increases. The amount of the cross-contamination depends highly on the anisotropy of turbulence Γ. Our simulation was conducted with a set of typical Mann parameters (see Sect. 2.7), so the degree of simulated filtering can be different from that of measurements. Figure 12b shows the comparison between the filtered and unfiltered radial velocity variance at the grid cell ($y = 0$ m, $z = 48$ m) from the measurement campaign. The correlation is very high, as expected, and the unfiltered radial velocity variance is around 9 % higher than the centroid-derived filtered one.
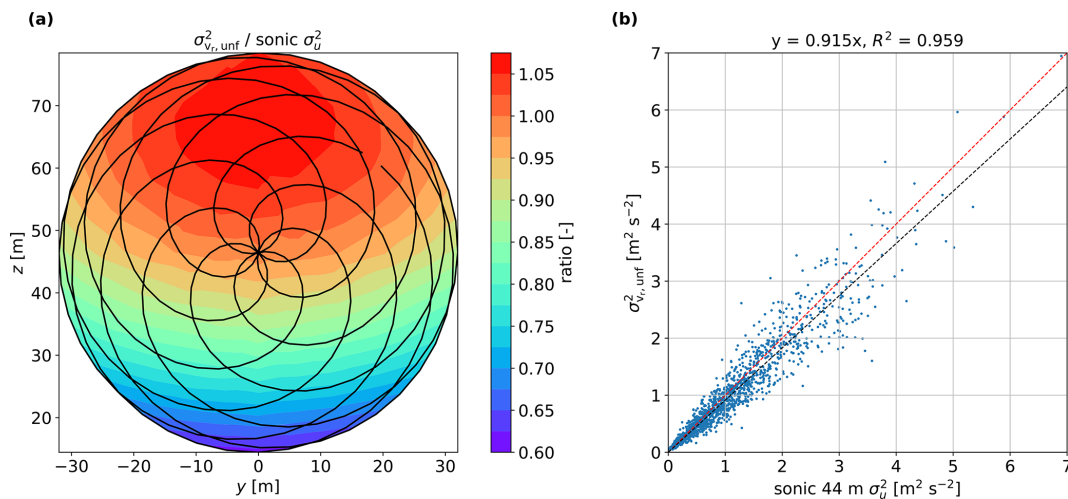
Figure 11. (a) Ratio of the unfiltered radial velocity variance to the u-velocity variance of the sonic anemometer from the simulations (30 turbulence boxes are used). **(b)** Comparison between the unfiltered radial velocity variance at the central grid cell ($y = 0$ m, $z = 48$ m) and the u variance of the sonic anemometer at 44 m from the measurements. Features regarding the red and black dashed lines as in Fig. 9.
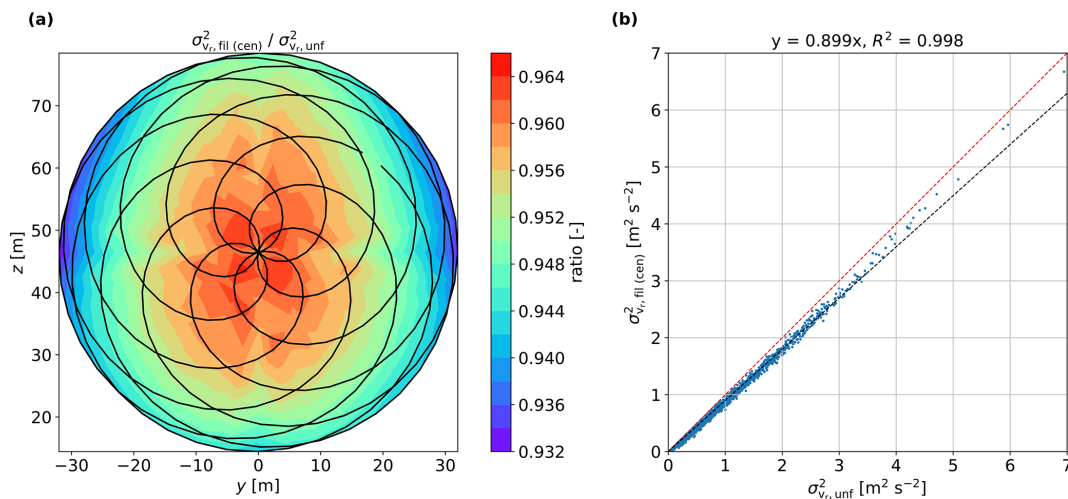

Figure 12. (a) Ratio of the filtered to the unfiltered radial velocity variance from simulations (30 turbulence boxes are used). **(b)** Comparison between the SpinnerLidar filtered and unfiltered radial velocity variance at the central grid cell ($y = 0$ m, $z = 48$ m) from the measurements. Features regarding the red and black dashed lines as in Fig. 9.

5.3 Turbulence estimates

Using the methodology described in Sect. 2.6, we estimate the six components of the Reynolds stress tensor from the SpinnerLidar unfiltered radial velocity variances and compare them against the computed components from the sonic anemometer measurements at 44 m for the 1499 periods of 10 min. Figure 13 shows the inter-comparison for σ_u^2. From the simulation with 30 turbulence boxes, we get a nearly perfect correlation and a bias of 1.4 %, whereas from the measurements the bias is 8.9 %. The bias is higher in the measurements mainly because we cannot guarantee that some variance of the radial velocity is lost when processing the Doppler radial velocity spectra.

We perform the comparison of all Reynolds stresses computed from the SpinnerLidar scans with those from the sonic anemometer at 44 m in Fig. 14. The Reynolds stresses from the measurement campaign are normalized by U^2 with which they are roughly proportional. The unfiltered variances from simulations were derived by the same method (see Sect. 2.4) as for the measurements. The numerical simulations show that we can accurately estimate all components of the Reynolds stress tensor using the SpinnerLidar compared to the sonic anemometer. The SpinnerLidar uncertainties of $\langle u'u' \rangle$ are not very different from those of the sonic anemometer, while the uncertainties of other components are larger. This is mainly because all other components where
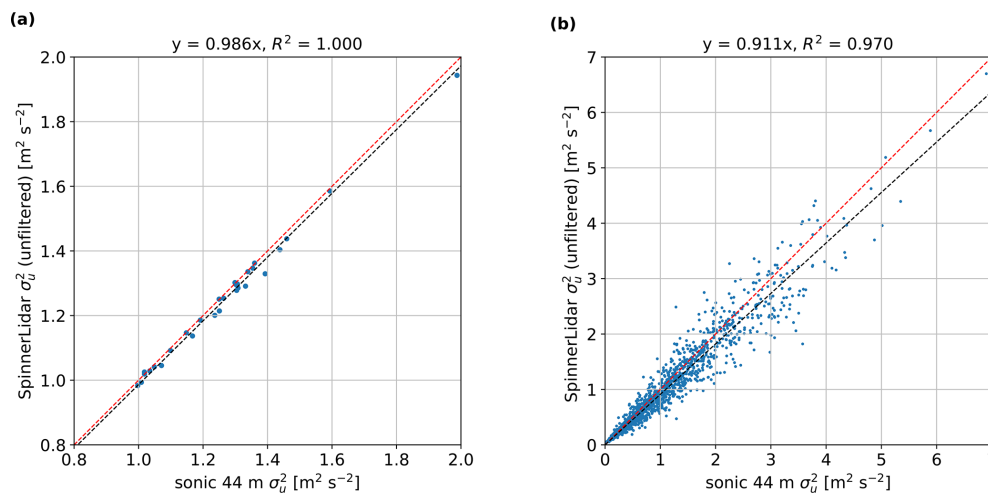
Figure 13. Comparison of the unfiltered variance of the along-wind velocity component between the SpinnerLidar and the sonic anemometer at 44 m from **(a)** numerical simulation using 30 turbulence boxes and **(b)** measurement campaign.

u fluctuations are not included are driven by fluctuations of components largely misaligned with the beams. Results from the measurements show that all Reynolds stress components estimated from SpinnerLidar are close to those from the sonic anemometer but biased. We even observe negative values for $\langle v'v' \rangle$ and $\langle w'w' \rangle$. This is discussed in Sect. 6.2.

Figure 15 shows the comparison of the SpinnerLidar estimations of the maximum-, median- and centroid-derived filtered variances of the along-wind velocity component with those from the 44 m sonic measurements. Results from both the simulations using 30 turbulence boxes and the measurements indicate that turbulence attenuation is most severe using the centroid method from the Doppler radial velocity spectrum, while the maximum method gives the closest value, as expected (Held and Mann, 2018).

Figure 16 shows the comparison of the Windar lidar reconstructed filtered σ_u^2 using different methods against σ_u^2 values from the 44 m sonic anemometer. As illustrated, about 37 % of the variance is filtered out for both W4 and W2, when the variance is computed by taking the statistics of the reconstructed U time series. This is still the common practice in the wind energy community. The degree of filtering is similar for both lidars although W4 has a larger probe volume. From Eq. (28), we note that by using the "LSP-σ_u^2" method, we can overestimate the along-wind variance when all beams are scanning horizontally (or close to). Estimates using the "LSP-isotropy" method take the average of all beam variances. When the scanning geometry is symmetrical in the two-dimensional y–z plane (like in the W4 case), the contributions from $\langle u'w' \rangle$ might (nearly) cancel out. The method "LSP-IEC" is perhaps a fairer procedure when compared to the other methods, as it assumes relations between velocity components' variances that are close to those we can observe within the atmospheric surface layer. Estimates from the "LSP-IEC" and "LSP-isotropy" methods

can be computed by scaling those from method "LSP-σ_u^2"; that explains the same correlations in Fig. 16a–c and e–g. All inter-comparison results of the estimated along-wind components are summarized in Table 2.

6 Discussion

6.1 Influence of spectra processing on the unfiltered variances

The way we process the Doppler radial velocity spectra influences the unfiltered variance estimates. Therefore, we investigate the sensitivity of using a more rigorous method to further alleviate the contamination of the Doppler spectra from, e.g., noise. This method first determines the peak of the Doppler signal and then moves forwards and backwards in the vicinity of the peak velocity bin to find the two locations (velocity bins) where the Doppler signal reaches zero. Only Doppler signals between these two velocity bins are used to compute the variance. The unfiltered along-wind velocity variance estimated from the SpinnerLidar measurements shows a bias reduction of ≈ 3.0 % using the more rigorous spectra-processing when compared to the relatively "moderate" method, which is used in Sect. 4.2.3. The coefficient of the determination reduces from 97 % to 96.6 %.

6.2 Negative SpinnerLidar-derived variances

Negative variances might result when using SpinnerLidar measurements to estimate the Reynolds stress tensor. We find randomly occurring negative values of σ_v^2 in 7 % and of σ_w^2 in 15 % of the 10 min periods that are used for the inter-comparison. We investigate the conditions in which this occurs by simulating measurements of a nacelle lidar with 30 beams such that they cover the extent of rotor at hub height
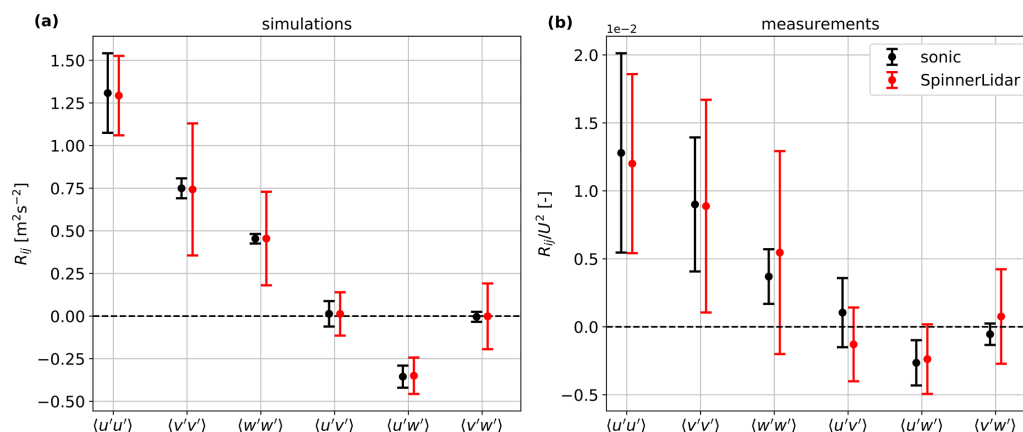
Figure 14. Reynolds stresses derived from the SpinnerLidar and sonic anemometer, **(a)** numerical simulations using 100 turbulence boxes and **(b)** measurements. The markers are the means and the error bars are ± 1 standard deviation.
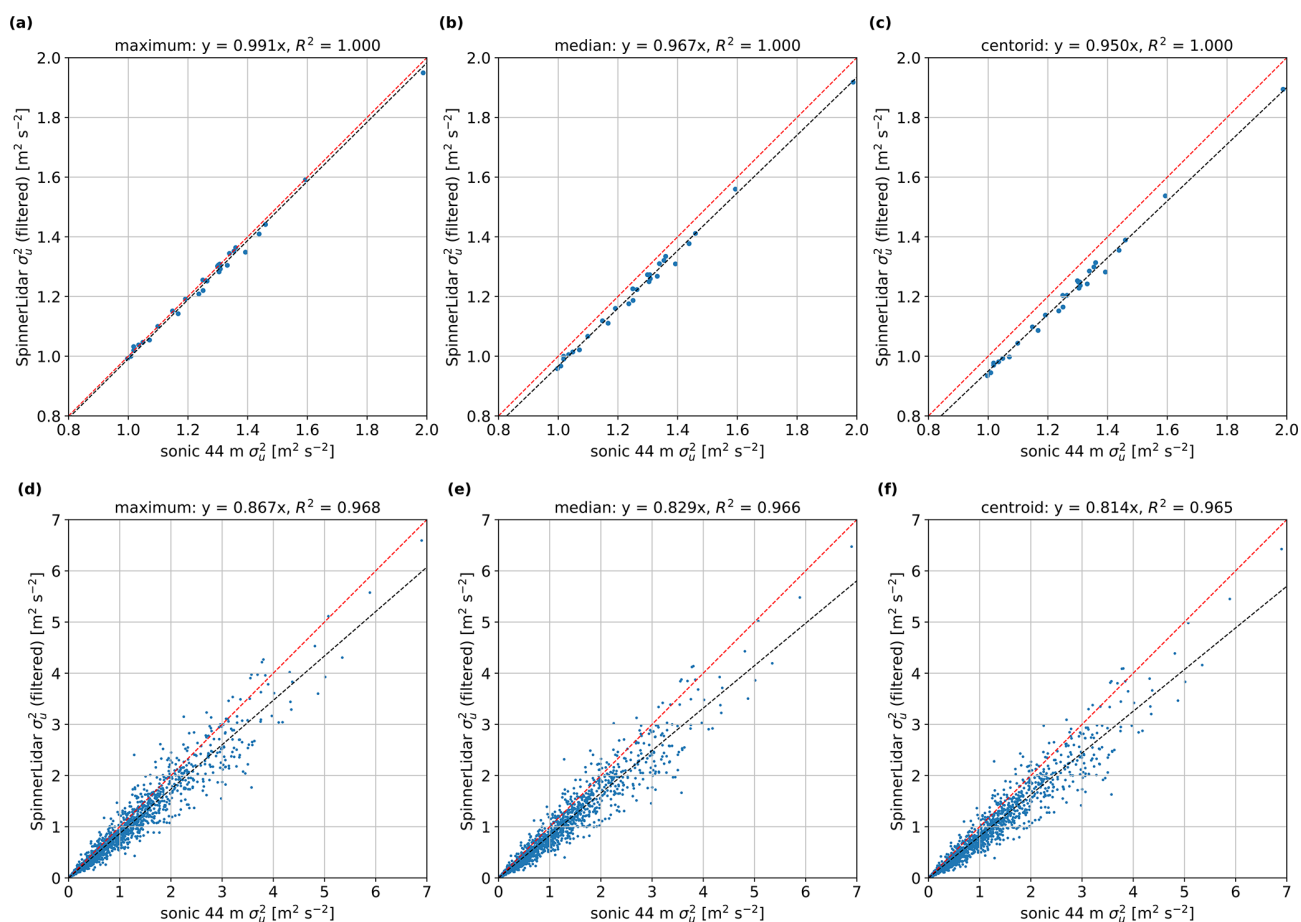

Figure 15. Comparison of the filtered variance of the along-wind velocity component between the SpinnerLidar and the sonic anemometer at 44 m. **(a–c)** Numerical simulations using 30 turbulence boxes. **(d–f)** Measurement campaign.
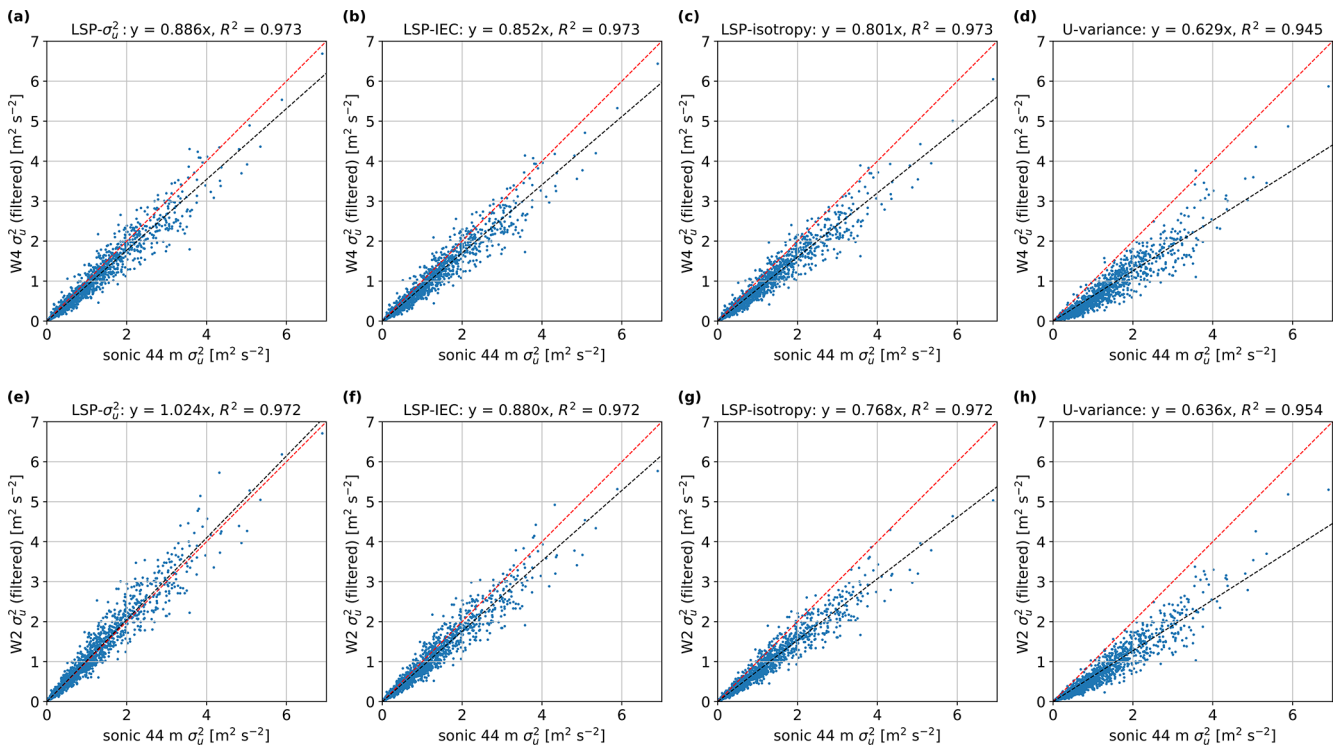
Figure 16. Comparison of the filtered variance of the along-wind velocity component between the Windar lidars and the sonic anemometer at 44 m. **(a–d)** W4. **(e–h)** W2.

Table 2. Bias and coefficient of determination between the lidar-derived along-wind velocity variance using different lidars and methods and that from the sonic anemometer at 44 m.

Lidars	Methods	Bias [%]	Coefficient of the determination [%]
SpinnerLidar	unfiltered	−8.9	97.0
	filtered (max)	−13.3	96.8
	filtered (med)	−17.1	96.6
	filtered (cen)	−18.6	96.5
W4	filtered (LSP-σ_u^2)	−11.4	97.3
	filtered (LSP-IEC)	−14.8	97.3
	filtered (LSP-isotropy)	−19.9	97.3
	filtered (U-variance)	−37.1	94.5
W2	filtered (LSP-σ_u^2)	+2.4	97.2
	filtered (LSP-IEC)	−12.0	97.2
	filtered (LSP-isotropy)	−22.6	97.2
	filtered (U-variance)	−36.4	95.4

(see Fig. 17a). Figure 17b shows the simulated radial velocity variances (marked in blue) of the beams across the rotor. Each point corresponds to the average radial velocity variance from five turbulence fields. With increasing opening angle, the simulated radial velocity variance decreases. By using the method in Sect. 2.6 to derive the velocity variances, we obtain positive values of all velocity components and $\sigma_u^2 \gg \sigma_v^2$, as expected. We obtain negative σ_v^2 values when the radial velocity variances highly decrease with increasing

opening angle (high decrease marked in green in Fig. 17b). In this case, the turbulence homogeneity assumption is not satisfied. Further, we find $\sigma_u^2 \approx \sigma_v^2$ when $\sigma_{v_r}^2$ slowly decreases with increasing opening angle (low decrease). Figure 18a shows the pattern of unfiltered radial velocity variances in one of the 10 min periods where we estimate negative σ_v^2 and σ_w^2 variances. As illustrated, the pattern shows a strong decrease of $\sigma_{v_r}^2$ particularly around the right side of the scans. Figure 18b corresponds to another 10 min period where $\sigma_u^2 \approx$
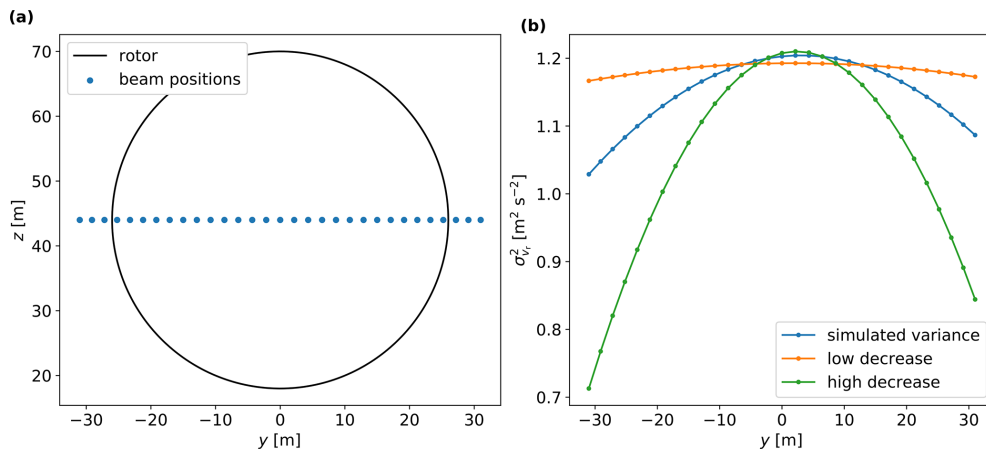
Figure 17. (a) Scanning pattern of a nacelle lidar with beams across the rotor. **(b)** The radial velocity variances of the beams across the rotor from simulations using five turbulence boxes.
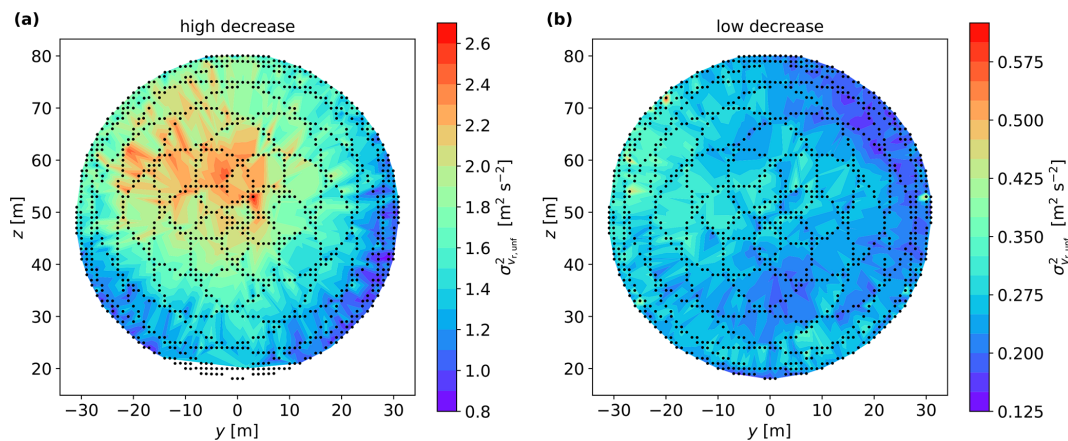

Figure 18. Contour plots of the radial velocity variance over the SpinnerLidar scanning pattern during two 10 min periods, **(a)** a case with negative σ_v^2 and σ_w^2 values, **(b)** a case with $\sigma_u^2 \approx \sigma_v^2 > \sigma_w^2$.

$\sigma_v^2 > \sigma_w^2$. The occurrence of the negative variances is less frequent in our measurements when we perform the turbulence estimation every 30 min, as expected.

7 Conclusions

In this study, we analyzed measurements of three forward-looking nacelle lidars with different scanning configurations to investigate the benefit of multi-beam nacelle lidars for turbulence characterization. For the first time, the Spinner-Lidar measurements were compared with those of commercial nacelle lidars. We focused our analysis on wind sectors, in which the inflow is relatively homogeneous. The inflow characteristics estimated by three lidars were compared with those from a nearby sonic anemometer at hub height.

Our results from the analysis of numerical simulations and measurements showed that all lidars were able to estimate the mean wind velocity well compared to the sonic anemome-

ter. We also found that the SpinnerLidar was the only one out of the three nacelle lidars that is able to measure the six Reynolds stress components accurately. This is due to both its multi-beam capability and its ability to measure unfiltered radial velocity variances.

By using the information from the Doppler radial velocity spectrum, one can partly compensate for the probe volume averaging effect and reduce the error of turbulence estimation. We showed that using maximum-derived radial velocities to compute the along-wind velocity variance mitigates best the turbulence attenuation caused by the lidar probe volume.

For the commercial lidars, one can estimate the along-wind velocity variance using three different methods: scaling the radial velocity variance with a factor of $\cos^2\phi$, assuming $\sigma_v = 0.7\sigma_u$ and $\sigma_w = 0.5\sigma_u$, or assuming isotropic turbulence. We found the smallest bias in the estimates using the first method when compared to the sonic anemometer values. However, the first method can overestimate the along-wind

variance when all beams are scanning horizontally. The second method is the fairest procedure among the three methods. All methods showed smaller bias when compared to computing the variance from the reconstructed along-wind velocity values in the time series.

Author contributions. WF, AP and JM participated in the conceptualization and design of the work. AP was responsible for the acquisition of the dataset. WF performed the numerical simulations, conducted the data analysis and wrote the draft manuscript. AP and JM supported the whole analysis and reviewed and edited the manuscript.

Competing interests. At least one of the (co-)authors is a member of the editorial board of *Wind Energy Science*. The peer-review process was guided by an independent editor, and the authors also have no other competing interests to declare.

Disclaimer. Publisher's note: Copernicus Publications remains neutral with regard to jurisdictional claims in published maps and institutional affiliations.

Review statement. This paper was edited by Sandrine Aubrun and reviewed by Wim Bierbooms and one anonymous referee.

References

Angelou, N., Abari, F. F., Mann, J., Mikkelsen, T. K., and Sjöholm, M.: Challenges in noise removal from Doppler spectra acquired by a continous-wave lidar, in: Proceedings of the 26th International Laser Radar Conference, Greece, Porto Heli, S5P-01, 25–29 June 2012.

Angelou, N., Sjoholm, M., and Papetta, A.: UniTTe WP3/MC1: Measuring the inflow towards a Nordtank 500 kW turbine using three short-range WindScanners and one SpinnerLidar, Tech. Rep. DTU Wind Energy E-0093, DTU Wind Energy, ISBN 978-87-93278-49-3, https://backend.orbit.dtu.dk/ws/portalfiles/portal/120952277/UniTTe_WP3_MC1.pdf (last access: 1 April 2022), 2015.

Borraccino, A., Schlipf, D., Haizmann, F., and Wagner, R.: Wind field reconstruction from nacelle-mounted lidar short-range measurements, Wind Energ. Sci., 2, 269–283, https://doi.org/10.5194/wes-2-269-2017, 2017.

Conti, D., Pettas, V., Dimitrov, N., and Peña, A.: Wind turbine load validation in wakes using wind field reconstruction techniques and nacelle lidar wind retrievals, Wind Energ. Sci., 6, 841–866, https://doi.org/10.5194/wes-6-841-2021, 2021.

Dimitrov, N., Borraccino, A., Peña, A., Natarajan, A., and Mann, J.: Wind turbine load validation using lidar-based wind retrivals, Wind Energy, 22, 1512–1533, 2019.

DTU Wind Energy: V52 Research turbine arrangement drawing met-mast, 2014.

Eberhard, W. L., Cupp, R. E., and Healy, K. R.: Doppler lidar measurement of profiles of turbulence and momentum flux, J. Atmos. Ocean. Tech., 6, 809–819, 1989.

Held, D. P. and Mann, J.: Comparison of methods to derive radial wind speed from a continuous-wave coherent lidar Doppler spectrum, Atmos. Meas. Tech., 11, 6339–6350, https://doi.org/10.5194/amt-11-6339-2018, 2018.

Held, D. P. and Mann, J.: Lidar estimation of rotor-effective wind speed – an experimental comparison, Wind Energ. Sci., 4, 421–438, https://doi.org/10.5194/wes-4-421-2019, 2019.

IEC: IEC 61400-1. Wind turbines – Part 1: design guidelines, International standard, International Electrotechnical Commission, Geneva, Switzerland, https://standards.iteh.ai/catalog/standards/sist/3454e370-7ef2-468e-a074-7a5c1c6cb693/iec-61400-1-2019 (last access: 1 April 2022), 2019.

Kelberlau, F. and Mann, J.: Cross-contamination effect on turbulence spectra from Doppler beam swinging wind lidar, Wind Energ. Sci., 5, 519–541, https://doi.org/10.5194/wes-5-519-2020, 2020.

Kristensen, L., Lenschow, D. H., Kirkegaard, P., and Courtney, M.: The spectral velocity tensor for homogeneous boundary-layer turbulence, Bound.-Lay. Meteorol., 47, 149–193, 1989.

Kumer, V.-M., Reuder, J., Dorninger, M., Zauner, R., and Grubišić, V.: Turbulent kinetic energy estimates from profiling wind LiDAR measurements and their potential for wind energy applications, Renew. Energ., 99, 898–910, 2016.

Larvol, A.: WindVision setup and measurement capabilities, Tech. rep., Windar Photonics A/S, 2016.

Mann, J.: The spatial structure of neutral atmospheric surface-layer turbulence, J. Fluid Mech., 273, 141–168, 1994.

Mann, J.: Wind field simulation, Probabilist. Eng. Mech., 13, 269–282, 1998.

Mann, J., Peña, A., Bingöl, F., Wagner, R., and Courtney, M. S.: Lidar scanning of momentum flux in and above the surface layer, J. Atmos. Ocean. Tech., 27, 959–976, 2010.

Peña, A., Mann, J., and Dimitrov, N.: Turbulence characterization from a forward-looking nacelle lidar, Wind Energ. Sci., 2, 133–152, https://doi.org/10.5194/wes-2-133-2017, 2017.

Peña, A., Mann, J., and Thorsen, G.: SpinnerLidar measurements for the CCAV52, Tech. Rep. DTU Wind Energy E Vol. 0177, DTU Wind Energy, ISBN 978-87-93549-45-6, https://backend.orbit.dtu.dk/ws/portalfiles/portal/193377980/Report_with_cover.pdf (last access: 1 April 2022), 2019.

Sathe, A. and Mann, J.: A review of turbulence measurements using ground-based wind lidars, Atmos. Meas. Tech., 6, 3147–3167, https://doi.org/10.5194/amt-6-3147-2013, 2013.

Sathe, A., Mann, J., Vasiljevic, N., and Lea, G.: A six-beam method to measure turbulence statistics using ground-based wind lidars, Atmos. Meas. Tech., 8, 729–740, https://doi.org/10.5194/amt-8-729-2015, 2015.

Schlipf, D., Fleming, P., Haizmann, F., Scholbrock, A., Hofsäß, M., Wright, A., and Cheng, P. W.: Field testing of feedforward collective pitch control on the CART2 using a nacelle-based lidar scanner, J. Phys. Conf. Ser., 555, 012090, https://doi.org/10.1088/1742-6596/555/1/012090, 2014.

Schlipf, D., Guo, F., and Raach, S.: Lidar-based estimation of turbulence intensity for controller scheduling, J. Phys. Conf. Ser., 1618, 032053, https://doi.org/10.1088/1742-6596/1618/3/032053, 2020.

Simley, E., Angelou, N., Mikkelsen, T., Sjöholm, M., Mann, J., and Pao, L. Y.: Characterization of wind velocities in the upstream induction zone of a wind turbine using scanning continuous-wave lidars, J. Renew. Sustain. Ener., 8, https://doi.org/10.1063/1.4940025, 2016.

Sonnenschein, C. M. and Horrigan, F. A.: Signal-to-noise relationships for coaxial systems that heterodyne backscatter from the atmosphere, Appl. Opt., 10, 1600–1604, 1971.

Stull, R. B.: An introduction to boundary layer Meteorology, 1 edn., Springer, Dordrecht, ISBN 978-90-277-2769-5, https://link.springer.com/book/10.1007/978-94-009-3027-8 (last access: 1 April 2022), 1988.

Taylor, G. I.: The spectrum of turbulence, P. Roy. Soc. Lond. A-Mat., 164, 476–490, 1938.

Wagner, R., Pedersen, T. F., Courtney, M., Antoniou, I., Davoust, S., and Rivera, R. L.: Power curve measurement with a nacelle mounted lidar, Wind Energy, 17, 1441–1453, 2014.

Wagner, R., Courtney, M., Pedersen, T. F., and Davoust, S.: Uncertainty of power curve measurement with a two-beam nacelle mounted lidar, Wind Energy, 19, 1269–1287, 2015.

Windar Photonics: Book of lidar, 2020.

Wyngaard, J.: Turbulence in the Atmosphere, Cambridge University Press, ISBN 9780511840524, https://doi.org/10.1017/CBO9780511840524, 2010.

A.2 Influence of nacelle-lidar scanning patterns on inflow turbulence characterization

Fu, W., Sebastiani, A., Peña, A., and Mann, J.: Influence of nacelle-lidar scanning patterns on inflow turbulence characterization, Journal of Physics: Conference Series, 2265, 022 016, https://doi.org/10.1088/1742-6596/2265/2/022016.

Influence of nacelle-lidar scanning patterns on inflow turbulence characterization

To cite this article: Wei Fu *et al* 2022 *J. Phys.: Conf. Ser.* **2265** 022016

View the article online for updates and enhancements.

Influence of nacelle-lidar scanning patterns on inflow turbulence characterization

Wei Fu, Alessandro Sebastiani, Alfredo Peña, Jakob Mann

Department of Wind Energy, Technical University of Denmark, Frederiksborgvej 399, 4000 Roskilde, Denmark

E-mail: `weif@dtu.dk`

Abstract. Nacelle lidars with different number of beams, scanning configurations and focus distances are simulated for characterizing the inflow turbulence. Lidar measurements are simulated within 100 turbulence wind fields described by the Mann model. The reference wind turbine has a rotor diameter of 52 m. We assume homogeneous frozen turbulence over the lidar scanning area. The lidar-derived Reynolds stresses are computed from a least-square procedure that uses radial velocity variances of each of the beams and compared with those from a simulated sonic anemometer at turbine hub height. Results show that at least six beams, including one beam with a different opening angle, are needed to estimate all Reynolds stresses. Enlarging the beam opening angle improves the accuracy and uncertainty in turbulence estimation more than increasing the number of beams. All simulated lidars can estimate the along-wind variance accurately. This work provides guidance on designing and utilizing nacelle lidars for inflow turbulence characterization.

1. Introduction

Characteristics of inflow turbulence are crucial for wind turbine load validation [1], power performance assessment [2] and wind turbine control [3]. In-situ anemometers installed on meteorological masts, such as cup and sonic anemometers, have been used to measure inflow turbulence. Nevertheless, with the increasing size of modern wind turbines, installing a meteorological mast that reaches the height of the blade tips has becoming more and more unaffordable, especially in offshore conditions. In recent years, lidars of different types and configurations have been mounted on the nacelle of wind turbines to scan the inflow [2; 4]. These forward-looking nacelle lidars have the advantage that they yaw with the wind turbine and scan towards the main wind direction. Compared to the point-wise anemometers, lidars measure over an area in front of the rotor, which gives the possibility to derive rotor-averaged turbulence characteristics.

Turbulence can be characterized by the second-order moments (variances and covariances) of the wind field components u, v and w in typically 10 min or 30 min assuming statistical stationarity. A matrix containing these six second-order moments $\langle u_i' u_j' \rangle$ is known as the Reynolds stress tensor, which is frequently used to describe atmospheric flow. The along-wind variance is widely used in wind energy as it is part of the definition of the turbulence intensity, which is an important turbulence parameter for turbine structural loads [5]. The momentum fluxes (i.e., two covariances $\langle u'w' \rangle$ and $\langle v'w' \rangle$) are used to calculate the friction velocity, which is closely connected to the vertical wind profile [6; 7]. The turbulence kinetic energy, i.e., half

the sum of the variances of the three velocity components, is a key parameter for studying wind turbine wake structure [8]. The Reynolds stresses are also useful for evaluating the three-dimensional turbulence models for e.g., load simulations.

Compared to turbulence estimates from sonic anemometers, lidar-derived turbulence characteristics can be biased due to the lidar scanning patterns, the spatial and temporal resolutions intrinsic to the lidar systems and the characteristics of atmospheric turbulence. [1; 9] studied the application of lidar measurements from different scanning patterns for load validation. [10] optimized the scanning trajectory of nacelle lidars based on a coherence model for the rotor-effective wind speed for control applications. Only a few works have investigated the influence of lidar scanning pattern on turbulence characterization. [11] proposed an optimized six-beam configuration using an objective function for a ground-based lidar to minimize the sum of the random errors of the Reynolds stresses. [12] showed that turbulence estimates from ground-based lidars can be improved by using the variance from the vertical beam.

Here, we compare the estimates of the Reynolds stress tensor from nacelle lidars with different scanning patterns through numerical simulations. The Reynolds stresses are computed via a least-square procedure that uses radial velocity variances for each of the lidars' beams without the need to reconstruct the wind components. We summarize how the number of beams, the half-cone opening angle and focus distance influence the accuracy and the uncertainty of turbulence estimates. This work provides guidance on designing and utilizing nacelle lidars for inflow turbulence characterization.

This paper is organized as follows. Section 2 describes the simulated turbulence wind fields and the methodology to estimate the Reynolds stresses. Section 3 provides information on the simulated lidar scanning patterns and the simulation setup. Section 4 shows the comparison of Reynolds stress estimation between the virtual lidars and sonic anemometer. Conclusion and outlook are given in Section 5.

2. Methodology

2.1. Turbulence wind fields

Assuming homogeneous frozen turbulence [13], the wind fields can be described by a vector field $\boldsymbol{u}(\boldsymbol{x}) = (u, v, w)$, where u is the horizontal along-wind component, v the horizontal lateral component, w the vertical component, and $\boldsymbol{x} = (x, y, z)$ the position vector defined in a right-handed coordinate system. The mean value of the homogeneous velocity field is $\langle \boldsymbol{u}(\boldsymbol{x}) \rangle = (U, 0, 0)$, so the coordinate x is in the mean wind direction. We simulate lidar measurements on the nacelle of a wind turbine with a rotor diameter (D) of 52 m using 100 randomly generated turbulence fields described by the Mann model [14; 15]. The wind fields have typical values of the model parameters: $\alpha\varepsilon^{2/3} = 0.05$ m$^{4/3}$ s^{-1}, which is related to the turbulent energy dissipation rate; $L = 61$ m, which is a turbulent length scale; and $\Gamma = 3.2$, which describes the anisotropy of the turbulence. The turbulence boxes have lengths of 30 min in the along-wind direction assuming a mean wind $U = 10$ m s^{-1}. We add a linear shear $dU/dz = 0.0288$ s^{-1} to the u components in each box. The lengths are 128 m both in the vertical and lateral directions. The number of grid points in the three directions are $(N_x, N_y, N_z) = (8192, 64, 64)$. Sonic anemometer statistics are taken at the location of the turbine rotor (i.e., center of the turbulence boxes) as the reference for evaluation of the lidar-derived turbulence characteristics.

2.2. Estimation of the Reynolds stresses

The Reynolds stress tensor $R_{ij}(\boldsymbol{x}) \equiv \langle u'_i u'_j \rangle$, where u_i are the fluctuations around the mean, contains the variances $\sigma^2_{u,v,w}$ and the covariances of the velocity components:

$$\boldsymbol{R} = \begin{bmatrix} \sigma^2_u & \langle u'v' \rangle & \langle u'w' \rangle \\ \langle v'u' \rangle & \sigma^2_v & \langle v'w' \rangle \\ \langle w'u' \rangle & \langle w'v' \rangle & \sigma^2_w \end{bmatrix}. \tag{1}$$

The unit vector $\boldsymbol{n}$ describing the beam orientation of a nacelle lidar can be expressed as [4]:

$$\boldsymbol{n}(\phi, \theta) = (-\cos\phi, \cos\theta\sin\phi, \sin\theta\sin\phi), \tag{2}$$

where θ is the angle between the y axis and $\boldsymbol{n}$ projected onto the y-z plane and ϕ is the angle between the beam and the negative x-axis (the half-cone opening angle). If we assume the lidar probe volume can be negligible and $u, v,$ and w do not change over the scanned area, the radial velocity can be expressed as

$$v_{\mathrm{r}}(\phi, \theta) = -u\cos\phi + v\cos\theta\sin\phi + w\sin\theta\sin\phi. \tag{3}$$

The radial velocity variance can be derived by taking the variance of Eq. (3), as shown in [16]:

$$\sigma^2_{v_{\mathrm{r}}}(\phi, \theta) = \sigma^2_u \cos^2\phi + \sigma^2_v \cos^2\theta\sin^2\phi + \sigma^2_w \sin^2\theta\sin^2\phi - 2\langle u'v' \rangle \cos\phi\cos\theta\sin\phi$$
$$- 2\langle u'w' \rangle \cos\phi\sin\theta\sin\phi + 2\langle v'w' \rangle \sin^2\phi\cos\theta\sin\theta. \tag{4}$$

To compute the Reynolds stress tensor $\boldsymbol{R}$, we use the simulated lidar radial velocity variance from all beams over the scanning pattern. Assuming statistical homogeneity, we apply a least-square fit to all radial velocity variances $\sigma^2_{v_{\mathrm{r}}}$ and the beam unit vectors $\boldsymbol{n}$:

$$\Delta^2 = \int (\boldsymbol{n} \cdot \boldsymbol{R}\boldsymbol{n} - \sigma^2_{v_{\mathrm{r}}})^2 \mathrm{d}\mu. \tag{5}$$

The matrix $\boldsymbol{R}_{ij}$ that minimizes the integral must fulfill

$$\frac{\partial \Delta^2}{\partial R_{ij}} = 0 \Rightarrow \int (\boldsymbol{n} \cdot \boldsymbol{R}\boldsymbol{n} - \sigma^2_{v_{\mathrm{r}}})n_i n_j \mathrm{d}\mu = 0. \tag{6}$$

This can be written as

$$R_{kl} \int n_k n_l n_i n_j \mathrm{d}\mu = \int \sigma^2_{v_{\mathrm{r}}} n_i n_j \mathrm{d}\mu, \tag{7}$$

where (k, l) and (i, j) go through the six combinations of indices. More details are given in [17].

Equation (7) implies that we need at least six radial velocity variances from different beam directions to compute the six Reynolds stresses. If the nacelle lidar has fewer than six beams, only σ^2_u (R_{uu}) can be determined well and the stresses involving the lateral component will be more noisy [18]. For lidars that have fewer than six beams, we use another two ways to retrieve only σ^2_u from the simulated measurements under different assumptions. The first is to correct all radial velocity variances $\sigma^2_{v_{\mathrm{r}}}$ with a factor of $\cos^2\phi$, which is the same as solving Eq. (4) assuming that all Reynolds stresses apart from σ^2_u are zero (denoted as 'σ^2_u-LSP' method). The second is to assume that turbulence is isotropic, which gives σ^2_u as the mean of all $\sigma^2_{v_{\mathrm{r}}}$ (denoted as 'σ^2_u-isotropy' method).

3. Lidar scanning patterns

Figure 1 shows the considered lidar scanning patterns. The SpinnerLidar (SL in short) scans in a rosette-curve pattern and generates 400 radial velocities in one full scan. In practice, the SpinnerLidar streams out radial velocities at a rate of 200 Hz so it takes 2 s to finish one full scan. It has half-cone opening angles between $0-30°$ and measures with a focus distance $f_d = 52$ m ($1D$) in front of the rotor. Other lidars have $\phi = 15°$ and measure further away (at the focus distance of 98 m) to cover the whole rotor plane. Furthermore, we simulate all considered lidars with multiple measurement planes at $f_d = 49, 72, 98, 121$ and 142 m. We use the simulated radial velocity variances at all measurement levels to compute the turbulence statistics. Figure 2 illustrates the scanning trajectories of the 4-beam and 50-beam lidars with multiple planes as examples. To investigate the influences of the lidar opening angle and the focus distance on turbulence estimation, we simulate the 6-beam configuration [11] with a fixed focus distance of 52 m and increasing opening angles (Fig. 3(a)), and a fixed opening angle of $15°$ and increasing focus distances (Fig. 3(b)). We neglect the lidar probe volume and assume that the lidar can measure at a point in the simulation.
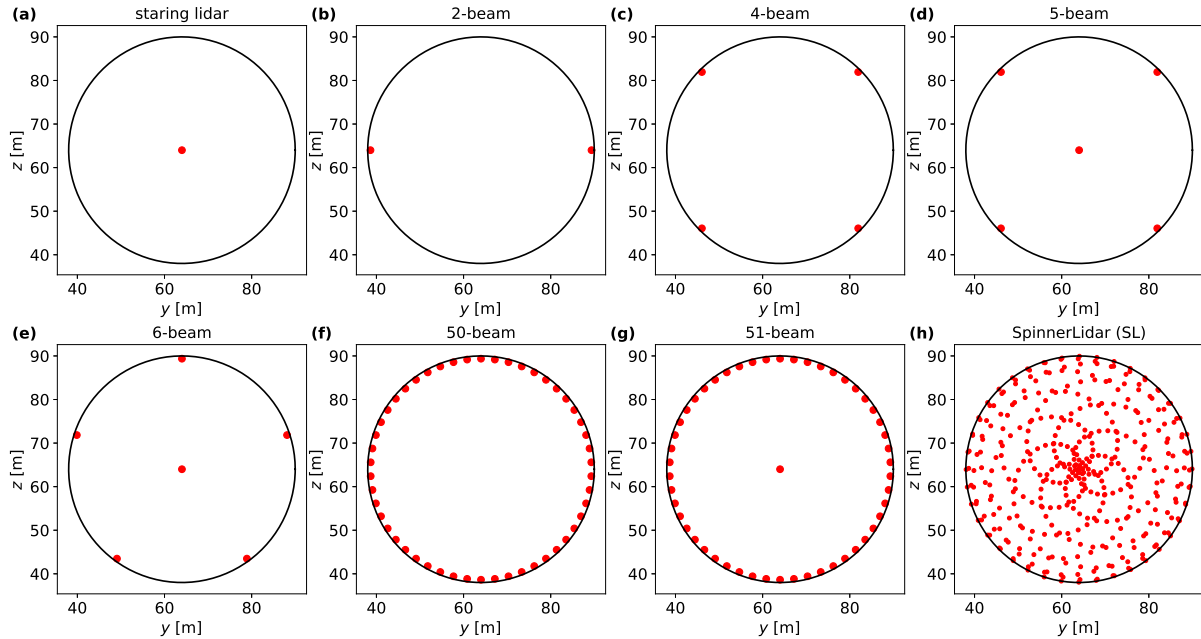

Figure 1: Scanning patterns of the simulated lidars. The SpinnerLidar (h) has $\phi = 0-30°$ and scans at $f_d = 52$ m, while other lidars (a-g) have $\phi = 15°$ and scan at $f_d = 98$ m to cover the whole rotor plane. Red dots represent the lidar beam scanning locations. The wind turbine rotor is indicated in a black circle.

4. Results

We compare the six Reynolds stresses computed from the simulated measurements of lidars, which have more than six beams and measure with a single plane, with those from a sonic anemometer at hub height, as shown in Fig. 4. The SpinnerLidar gives the best estimation for all six components, which is closely related to the maximum ϕ of the lidar. The 6-beam and 51-beam lidar provide very similar results, with larger errors and higher uncertainties than the SpinnerLidar. However, the 50-beam configuration cannot estimate the v- and w-variances accurately. This is because the least-squares problem can lead to infinite solutions if we have
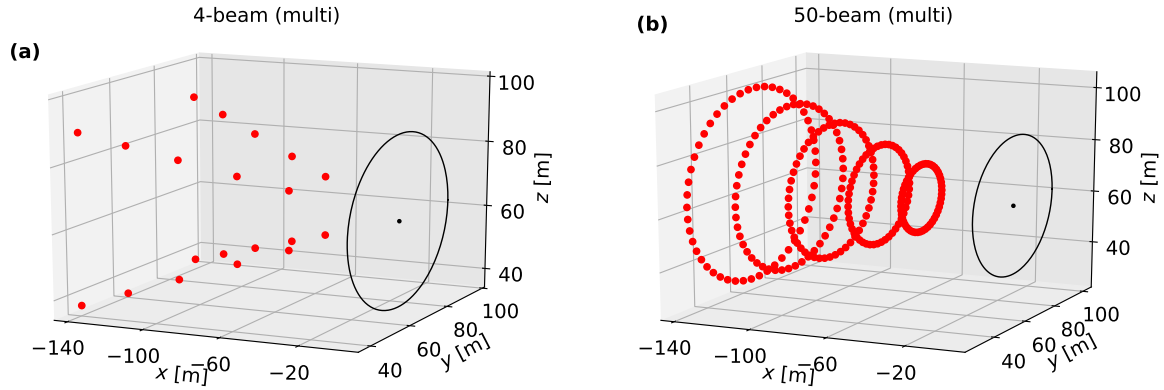
Figure 2: Scanning trajectories of the 4-beam and the 50-beam lidars with multiple measurement planes at $f_d = 49, 72, 98, 121$ and 142 m. Red dots represent the lidar beam scanning locations. The wind turbine rotor is indicated in a black circle. The turbine nacelle is marked in a black dot on the rotor plane.
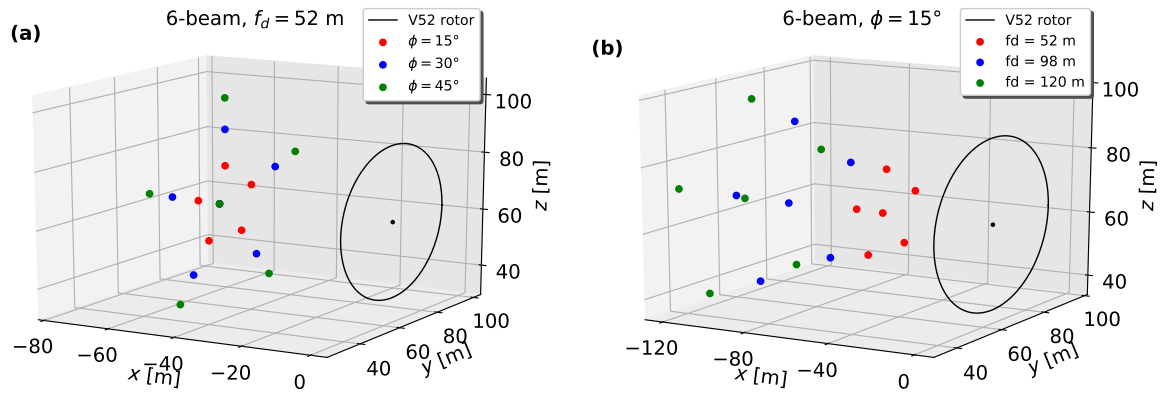

Figure 3: Scanning patterns of the 6-beam lidar with (a) a fixed focus distance and various half-cone opening angles, and (b) a fixed half-cone opening angle and various focus distances. The wind turbine rotor is indicated in a black circle. The turbine nacelle is marked in a black dot on the rotor plane.

only one ϕ value. Comparing the results from 50-beam and 51-beam lidar, we can see that adding one central beam is very beneficial for measuring all variances.

We show the performances of 50-beam and 51-beam lidar with multiple measurement planes on the Reynolds stresses estimation in Fig. 5, where the estimates using a single plane (marked in green and blue) are the same as those in Fig. 4. The comparison shows that if the measurements at a single plane are not sufficient to retrieve all Reynolds stresses, measuring at multiple planes with the same beam configuration does not help in the turbulence reconstruction. Results from the 51-beam lidar suggest that using multiple measurement planes does not improve the results much in our simulations; it only reduces slightly the uncertainty of the estimations.

Figure 6 shows the four Reynolds stresses retrieved from the 4-beam and 5-beam lidars assuming that the $\langle u'v' \rangle$ and $\langle v'w' \rangle$ covariances are negligible in Eq. (7). The Reynolds stress estimates are very noisy so that some of them are out of the limit of the axis. In all cases, the determinants of the matrix that results when expanding Eq. (7) are close to zero, which
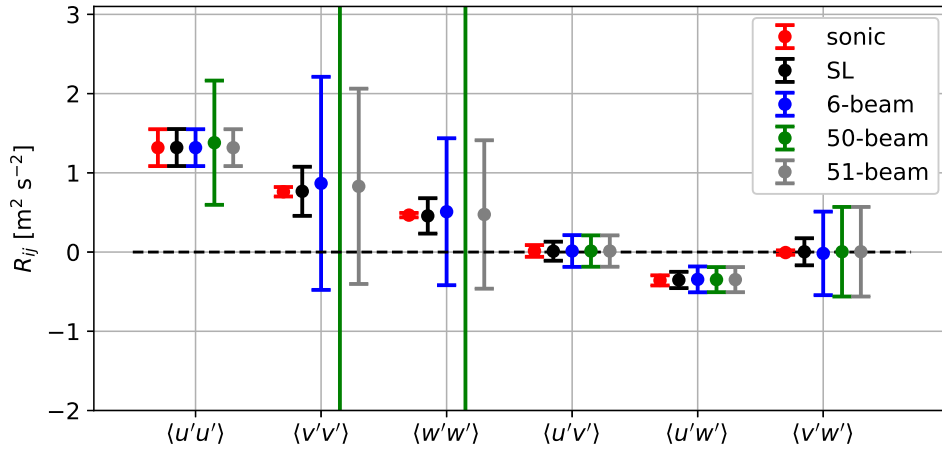
Figure 4: Reynolds stresses derived from the virtual sonic anemometer and lidars, which have more than six beams and measure at a single distance, from 100 simulated wind fields. The markers are the means and the error bars are $\pm$ one standard deviation.
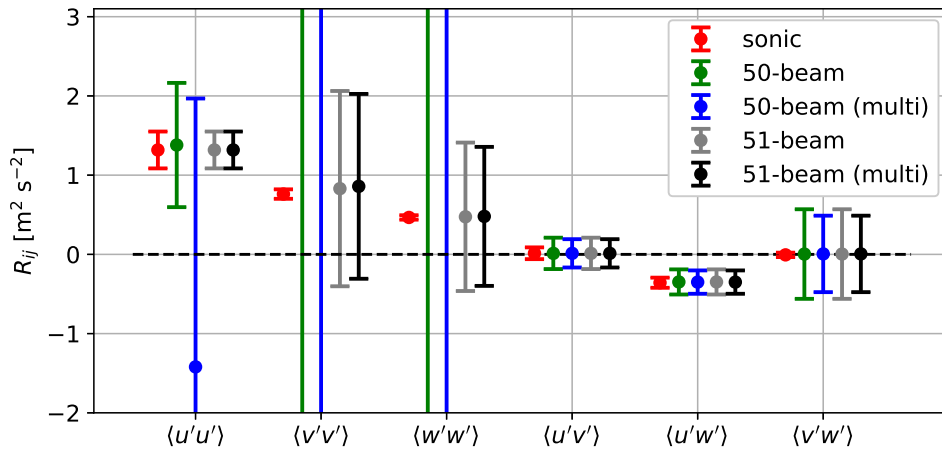

Figure 5: Reynolds stresses derived from the virtual sonic anemometer, the 50-beam and 51-beam lidars measuring at a single plane and at multiple planes from 100 simulated wind fields. The markers are the means and the error bars are $\pm$ one standard deviation.

indicates that the four Reynolds stresses cannot be estimated accurately using the least-square procedure with the 4-beam and 5-beam configurations. Again, the comparison suggests that using multiple measurement planes does not improve the results much in our simulations.

In Fig. 7, we analyze how the accuracy and the uncertainty of the Reynolds stresses estimation change when increasing ϕ and f_d of the 6-beam lidar. We compare them with those from the sonic anemometer and the SpinnerLidar. Both the error and the uncertainty decrease as the opening angle increases. Specifically, for $\phi = 45°$, the six-beams configuration provides lower uncertainty than the SpinnerLidar despite having much fewer beams. Increasing the focus distance has an opposite effect as increasing the beams' opening angles due to the random error on the variances of the radial velocity. The radial velocity variances of the beams are less correlated when the lidar scans over a larger area. We performed the same analysis with the 51-beam lidar and observed the same trends (not shown here).
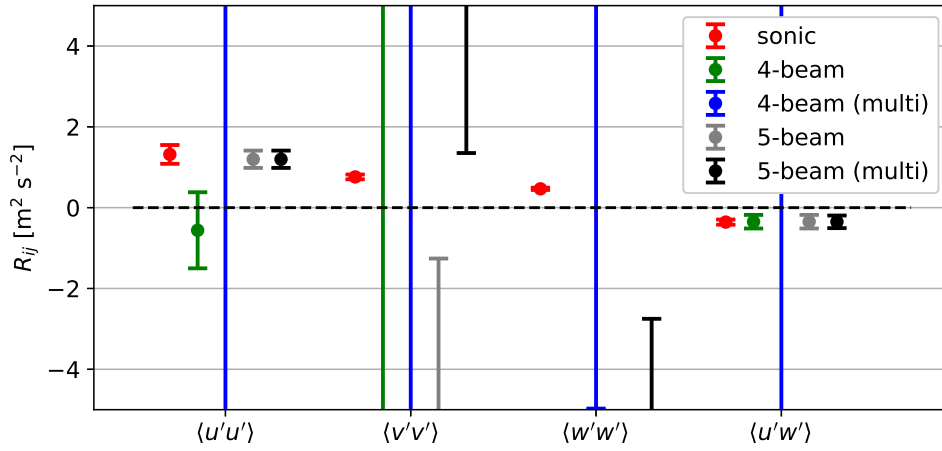
Figure 6: Reynolds stresses derived from the virtual sonic anemometer, the 4-beam and 5-beam lidars measuring at a single plane and at multiple planes from 100 simulated wind fields. The markers are the means and the error bars are $\pm$ one standard deviation.
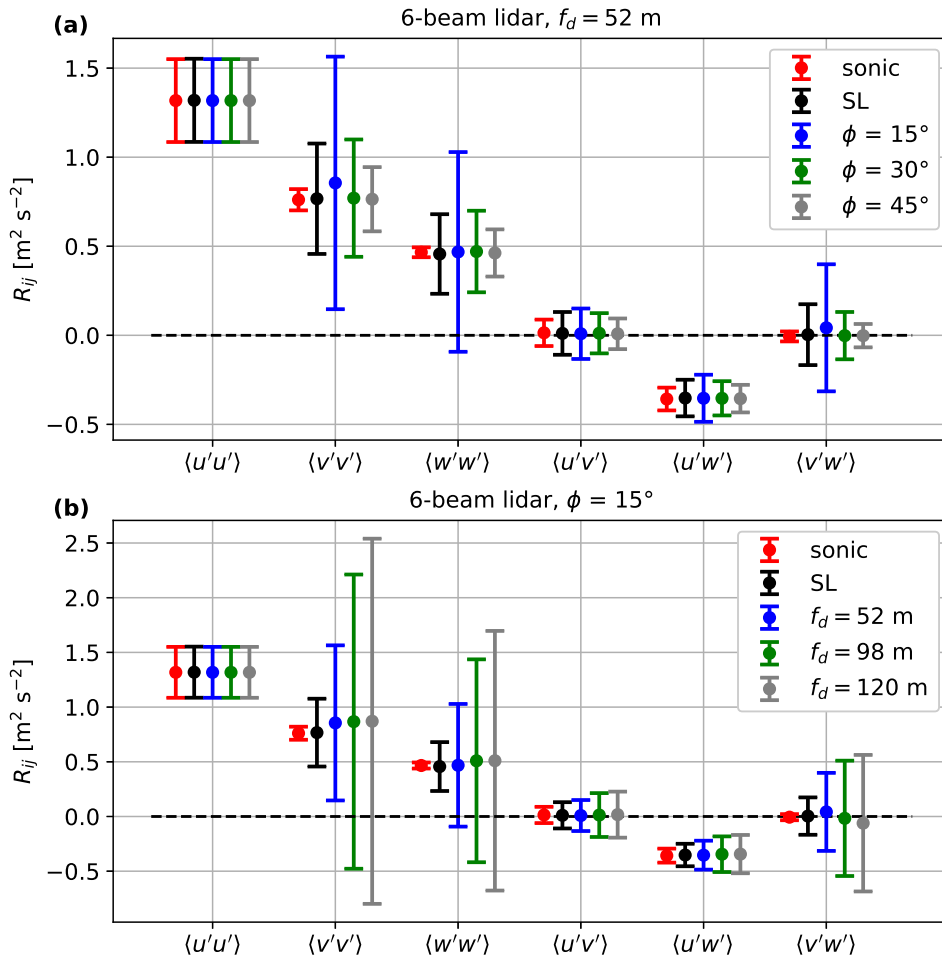
Figure 7: Influence of increasing opening angle ϕ and focus distance f_d on the Reynolds stresses estimation for the virtual sonic anemometer, the SpinnerLidar, and all 6-beam lidar configurations from 100 simulated wind fields.

We also simulate the nacelle lidars with all considered scanning patterns at the five measurement planes mentioned above, and retrieve the along-wind variance using the 'σ_u^2-LSP' and 'σ_u^2-isotropy' methods, respectively. The results are shown in Fig. 8. Table 1 summarizes the relative errors of the lidar-derived estimates compared to the one from the sonic anemometer. The results in first row are computed solving Eq. (7), from which we get perfect estimations of the along-wind variance using lidars with more than six beams. Furthermore, we find as an overall trend that lidar-derived σ_u^2 are overestimated using the 'LSP' method, when compared to the estimate from the sonic anemometer, while they are slightly underestimated using the 'isotropy' method. The biases are in general smaller when σ_u^2 are computed using the 'isotropy' method. Overall, all simulated lidars are able to estimate σ_u^2 well, despite of their different number of beams. The staring lidar acts like a sonic anemometer in our simulation and achieves zero relative error since no probe volume is considered and the beam is perfectly aligned with the along-wind component.
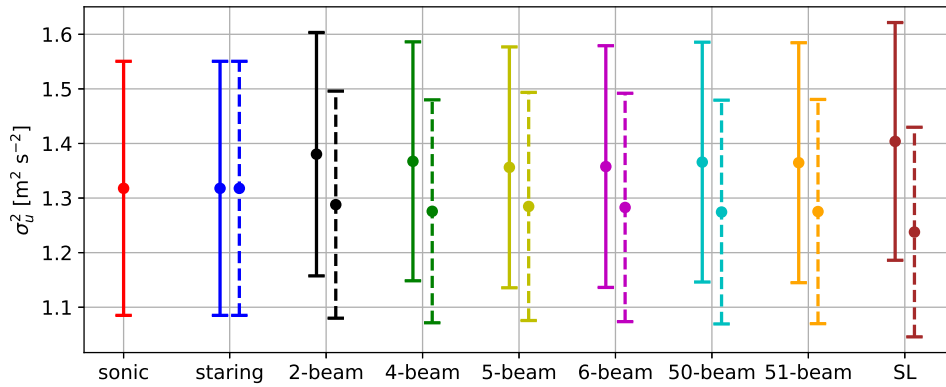

Figure 8: The along-wind variance derived from simulated lidars using the 'σ_u^2-LSP' method (in solid lines) and 'σ_u^2-isotropy' method (in dashed lines). All lidars measure at multiple planes.

Table 1: Relative error of the mean value of the lidar-derived along-wind variance using 100 simulated wind fields, when compared to the one from the sonic anemometer. All lidars measure at multiple planes. Negative values indicate that the along-wind variance is underestimated.

	staring	2-beam	4-beam	5-beam	6-beam	50-beam	51-beam	SL
$\langle u'u' \rangle$ [%]	—	—	—	—	0.00	—	0.00	0.17
σ_u^2-LSP [%]	0	4.75	3.76	2.92	3.03	3.65	3.56	6.53
σ_u^2-isotropy [%]	0	-2.27	-3.91	-2.52	-2.66	-3.30	-3.23	-6.07

5. Conclusion and Outlook
Our results show that at least six beams, including one beam with a different opening angle, are needed to estimate all the six Reynolds stresses accurately. The accuracy and uncertainty in turbulence characterization are better improved by enlarging the opening angle than by increasing the number of beams. Enlarging the measurement area of the nacelle lidars with the same beam orientation reduces the accuracy and increases the uncertainty. Compared to the point-wise sonic anemometer, all considered lidars can estimate the along-wind variance with

a relative error lower than 7%. All in all, the lidar with a 6-beam configuration and a large opening angle gives the best estimates of all Reynolds stresses.

This study should be extended by modelling the lidar probe volume in the simulation, which can cause turbulence attenuation. For continuous-wave lidar, the focus distance is closely related to the impact of the probe volume. Further studies on the lidar scanning pattern should also consider the inhomogeneity of the inflow. Modern wind turbines are often operating inside a wind farm or have large vertical span among the rotor area. Under those conditions, the turbulence homogeneity assumption is violated. Therefore, there is a need to investigate the scanning strategy for characterizing inhomogeneous inflows.

References

[1] Conti D, Pettas V, Dimitrov N and Peña A 2021 *Wind Energy Science* **6** 841–866

[2] Wagner R, Courtney M, Pedersen T F and Davoust S 2015 *Wind Energy* **19** 1269–1287

[3] Schlipf D, Guo F and Raach S 2020 *Journal of Physics: Conference Series* **1618** 032053

[4] Peña A, Mann J and Dimitrov N 2017 *Wind Energy Science* **2** 133–152

[5] IEC 2019 IEC 61400-1. Wind turbines – Part 1: Design guidelines International standard International Electrotechnical Commission Geneva, Switzerland

[6] Wyngaard J 2010 *Turbulence in the Atmosphere* (Cambridge University Press) ISBN 9781139485524

[7] Peña A, Floors R, Sathe A, Gryning S E, Wagner R, Courtney M S, Larsén X G, Hahmann A N and Hasager C B 2016 *Boundary-Layer Meteorology* **158** 1–26

[8] Kumer V M, Reuder J, Dorninger M, Zauner R and Grubišić V 2016 *Renewable Energy* **99** 898–910

[9] Dimitrov N and Natarajan A 2017 *Wind Energy* **20** 79–95

[10] Schlipf D, Fürst H, Raach S and Haizmann F 2018 *Journal of Physics: Conference Series* **1102** 012014

[11] Sathe A, Mann J, Vasiljevic N and Lea G 2015 *Atmospheric Measurement Techniques* **8** 729–740

[12] Newman J F, Klein P M, Wharton S, Sathe A, Bonin T A, Chilson P B and Muschinski A 2016 *Atmospheric Measurement Techniques* **9** 1993–2013

[13] Taylor G I 1938 *Proceedings of the Royal Society of London. Series A - Mathematical and Physical Sciences* **164** 476–490

[14] Mann J 1994 *Journal of Fluid Mechanics* **273** 141–168

[15] Mann J 1998 *Probabilistic Engineering Mechanics* **13** 269–282

[16] Eberhard W L, Cupp R E and Healy K R 1989 *Journal of Atmospheric and Oceanic Technology* **6** 809–819

[17] Fu W, Peña A and Mann J 2021 *Wind Energy Science Discussions* **2021** 1–29 URL https://wes.copernicus.org/preprints/wes-2021-149/

[18] Peña A, Mann J and Thorsen G 2019 Spinnerlidar measurements for the ccav52 Tech. Rep. DTU Wind Energy E Vol. 0177 DTU Wind Energy

A.3 Dependence of turbulence estimations on nacelle-lidar scanning strategies

Fu, W., Sebastiani, A., Peña, A., and Mann, J.: Dependence of turbulence estimations on nacelle-lidar scanning strategies, Wind Energ. Sci. Discuss. [preprint], https://doi.org/10.5194/wes-2022-85.

The revised version (attached below) of the manuscript is under review in the journal Wind Energy Science.

Dependence of turbulence estimations on nacelle-lidar scanning strategies

Wei Fu, Alessandro Sebastiani, Alfredo Peña, and Jakob Mann

Department of Wind and Energy Systems, Technical University of Denmark, Frederiksborgvej 399, 4000 Roskilde, Denmark

Correspondence: Wei Fu (weif@dtu.dk)

Abstract. Through numerical simulations and the analysis of field measurements, we investigate the dependence of the accuracy and uncertainty of turbulence estimations on the main features of the nacelle lidars' scanning strategy, i.e., the number of measurement points, the half-cone opening angle, the focus distance and the type of the lidar system. We assume homogeneous turbulence over the lidar scanning area in front of a Vestas V52 wind turbine. The Reynolds stresses are computed via a least-squares procedure that uses the radial velocity variances of each lidar beam without the need to reconstruct the wind components. The lidar-retrieved Reynolds stresses are compared with those from a sonic anemometer at turbine hub height. Our findings from the analysis of both simulations and measurements demonstrate that to estimate the six Reynolds stresses accurately, a nacelle lidar system with at least six beams is required. Further, one of the beams of this system should have a different opening angle. Adding one central beam improves the estimations of the velocity components' variances. Assuming the relations of the velocity components' variances as suggested in the IEC standard, all considered lidars can estimate the along-wind variance accurately using the least-squares procedure and the Doppler radial velocity spectra. Increasing the opening angle increases the accuracy and reduces the uncertainty on the transverse components, while enlarging the measurement distance has opposite effects. All in all, a 6-beam continuous-wave lidar measuring at a close distance with a large opening angle provides the best estimations of all Reynolds stresses. This work gives insights on designing and utilizing nacelle lidars for inflow turbulence characterization.

1 Introduction

Inflow turbulence characteristics are important for wind turbine load validation (Conti et al., 2021), power performance assessment (Gottschall and Peinke, 2008; Wagner et al., 2014) and wind turbine control (Dong et al., 2021). The traditional way to measure inflow turbulence uses the in-situ anemometers installed on meteorological masts, such as cup and sonic anemometers. However, rotor planes of the modern wind turbines have large vertical span that can reach 250 m above the ground. It is more and more costly to install a meteorological mast that reaches the height of the blade tips, especially under offshore conditions. Recently, nacelle lidars of different types and configurations have been used to scan the inflow (Harris et al., 2006; Mikkelsen et al., 2013; Wagner et al., 2015; Peña et al., 2017; Fu et al., 2022a). Compared to the point-wise, mast-mounted anemometers, forward-looking nacelle lidars yaw with the wind turbine and measure at different points in front of the rotor, which can potentially better characterize the inflow that actually interacts with the wind turbine.

Assuming statistical stationarity, turbulence can be represented by the variances and covariances of the wind field components u, v and w (u_1, u_2, u_3) averaged typically over 10 or 30 min. The homogeneous velocity field can be decomposed into the mean U_i and the fluctuating part u_i'. The Reynolds stress tensor, a matrix containing the six second-order moments $\langle u_i' u_j' \rangle$, describes the variability of the atmospheric flow in some detail. The terms in the Reynolds stress tensor are frequently used in wind energy and meteorology. The square root of the along-wind variance is a part of the definition in the turbulence intensity, which is a key turbulence parameter for the structural loads assessment and the design of wind turbines (IEC, 2019). However, this is not the only component that is important for loads (Petersen et al., 1994). The two covariances $\langle u' w' \rangle$ and $\langle v' w' \rangle$ form the momentum fluxes, which are used to calculate the friction velocity and are closely connected to the vertical wind profile (Wyngaard, 2010; Peña et al., 2016). The half the sum of the variances of the three velocity components is the turbulence kinetic energy, which is an important parameter for investigating wind turbine wake structures (Kumer et al., 2016). Also, the Reynolds stresses are needed to determine the parameters of the three-dimensional turbulence models for, e.g., load simulations (Mann, 1994).

Compared to turbulence estimates from traditional anemometry, the accuracy and the uncertainty of lidar-derived turbulence characteristics can be affected by not only the spatial and temporal resolutions intrinsic to the lidar systems and the characteristics of atmospheric turbulence but also the lidar scanning strategies (Sathe et al., 2011; Smalikho and Banakh, 2017). Dimitrov and Natarajan (2017) and Conti et al. (2021) applied lidar measurements using different scanning strategies for load validation. Schlipf et al. (2018) optimized the scanning trajectory of nacelle lidars based on a coherence model for the rotor-effective wind speed to improve control performance. Only a few works investigated the dependence of turbulence estimations on lidar scanning strategies. Sathe et al. (2015) explained that at least six radial velocity variances are needed to compute all six Reynolds stresses, and proposed for a ground-based lidar an optimized six-beam configuration using an objective function which minimizes the sum of the random errors of the Reynolds stresses. Newman et al. (2016) showed that using the variance from the vertical beam improves the turbulence estimates from ground-based lidars. Fu et al. (2022a) investigated the benefit of using multiple-beam nacelle lidars by comparing the accuracy of turbulence estimations from a SpinnerLidar (a lidar measuring the inflow at 400 positions) with two- and four-beam lidars.

Lidars measure the radial velocity (also known as the line-of-sight velocity) along the laser beam. Sathe and Mann (2013) and Fu et al. (2022a) showed that the variance along a single beam can be higher or lower than the u-variance measured by sonic anemometers depending on the beam orientation. This is due to the correlation between different velocity components, which can be described in the three-dimensional spectral velocity tensor model by Mann (1994) (hereafter Mann model). We need to assume homogeneity when combining the radial velocity variances along different laser beam directions to reconstruct the Reynolds stresses. Compared to the in-situ anemometers, the lidar's measurement volume is generally larger, which leads to turbulence attenuation.

There are two main types of nacelle lidar systems, namely continuous-wave (CW) and pulsed. They mainly differ on the working principle and the way they probe the atmosphere within their measurement volume. The probe volume of a CW system increases with the square of the focus distance, while the one of a pulsed system remains constant with measurement range (Peña et al., 2015). The 'unfiltered' radial velocity variances (in which the volume-averaging effect is compensated) can be

retrieved from the Doppler radial velocity spectra, which are normally available in CW systems (Mann et al., 2010; Branlard et al., 2013).

This work investigates the dependence of the accuracy and the uncertainty of the turbulence estimations on the main features of the nacelle lidars' scanning strategy, i.e., the number of measurement positions within a full scan, the half-cone opening angle, the focus distance and the type of the lidar system. We select eight scanning patterns, which are commonly known or widely used in the wind energy industry. Homogeneous frozen turbulence is assumed throughout our analysis. The Reynolds stresses are estimated via a least-squares procedure using radial velocity variances instead of computing from the reconstructed mean wind velocities. Estimates from a sonic anemometer at turbine hub height are used as reference. Compared to Fu et al. (2022b), here we study the topic using not only numerical simulations with turbulence boxes but also the SpinnerLidar measurements collected at DTU Risø test site. We select measurements at certain beam scanning locations of the SpinnerLidar to imitate lidars with different scanning configurations. Another main difference to Fu et al. (2022b) is that we consider the probe volume of both a CW and a pulsed lidar system in our simulations, which plays an important role, especially when studying the influence of the focus distance on the turbulence estimation.

This paper is organized as follows. Section 2 introduces the turbulence spectral model and the modeling of nacelle lidars. Section 3 describes how the unfiltered radial velocity variance and the Reynolds stresses are estimated. It also gives details about the setup of the numerical simulations, the considered lidar scanning strategies and the field experiment. Section 4 compares the Reynolds stress estimations between the lidars and the sonic anemometer at turbine hub height from both numerical simulations and measurements. Discussions are given in Section 5. Section 6 concludes the work and provides the outlook.

2 Theoretical background

2.1 Turbulence spectral model

Assuming Taylor's frozen turbulence (Taylor, 1938), the wind field can be described by $\boldsymbol{u}(\boldsymbol{x}) = (u, v, w)$, where $\boldsymbol{x} = (x, y, z)$ is the position vector defined in a right-handed coordinate system, u the horizontal along-wind component, v the horizontal lateral component, and w the vertical component. The homogeneous wind field $\boldsymbol{u}(\boldsymbol{x})$ can be decomposed into the mean value $\langle \boldsymbol{u}(\boldsymbol{x}) \rangle = (U, 0, 0)$, where $\langle \ \rangle$ denotes ensemble averaging, and the fluctuating part $\boldsymbol{u}'(\boldsymbol{x}) = (u', v', w')$. U is the mean wind velocity along the x-direction. The one-dimensional single point (co-)spectra of any component of the wind field are given as (Mann, 1994)

$$F_{ij}(k_1) = \frac{1}{(2\pi)} \int\limits_{-\infty}^{\infty} R_{ij}(x_1, 0, 0) \exp(-ik_1 \cdot x_1) \mathrm{d}x_1, \tag{1}$$

where k_1 is the first component of the wave vector $\boldsymbol{k}$, $R_{ij}(\boldsymbol{r}) \equiv \langle u_i'(\boldsymbol{x}) u_j'(\boldsymbol{x} + \boldsymbol{r}) \rangle$ is the Reynolds stress tensor, $\boldsymbol{r}$ is the separation vector, and u_i' are the fluctuations around the mean of the wind field. The wave number can, via Taylor's hypothesis, be related to the frequency f through $k_1 = 2\pi f / U$. The auto-spectra of the three wind components $F_{u,v,w} (= F_{11,22,33})$ can

be evaluated using Eq. (1). The velocity components' variances are

$$\sigma^2_{u,v,w} = \int_{-\infty}^{\infty} F_{u,v,w}(k_1) \mathrm{d}k_1. \tag{2}$$

We assume that the Mann model well describes the spatial structure of the turbulent flow. Besides k_1 and the other two components of the wave vector $\boldsymbol{k}$, the Mann model contains three parameters: $\alpha\varepsilon^{2/3}$, which is related to the turbulent energy dissipation rate, L to a turbulence length scale, and Γ to the anisotropy of turbulence. This model is chosen because it describes the correlations between different velocity components, which play an important role in deriving turbulence statistics from measurements of multiple-beam lidars pointing at different directions.

2.2 Nacelle lidar and modeling of the probe volume

The unit vector $\boldsymbol{n}$ describes the beam orientation of a nacelle lidar, which can be expressed as (Peña et al., 2017):

$$\boldsymbol{n}(\phi, \theta) = (-\cos\phi, \cos\theta\sin\phi, \sin\theta\sin\phi), \tag{3}$$

where θ is the angle between the y axis and $\boldsymbol{n}$ projected onto the y-z plane and ϕ the angle between the beam and the negative x-axis (also known as the half-cone opening angle), as shown in Fig.1.
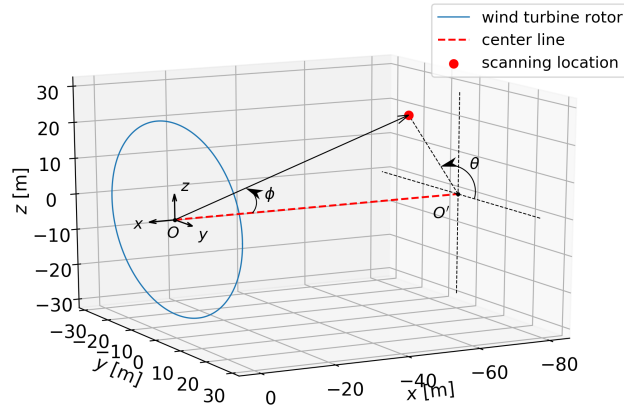
Figure 1. Definition of the coordinate system and beam angles for nacelle lidar modeling.

The radial velocity of a lidar can be written as the convolution of the weighting function φ and the radial velocity sampled along the beam in the probe volume (Mann et al., 2010):

$$v_\mathrm{r}(\phi, \theta) = \int_{-\infty}^{\infty} \varphi(s)\boldsymbol{n}(\phi, \theta) \cdot \boldsymbol{u}[\boldsymbol{n}(\phi, \theta)(f_d + s)]\mathrm{d}s, \tag{4}$$

4

where s is the distance from the focus point along the beam and f_d the focus or measurement distance. The relation assumes that the velocity is determined from the Doppler spectrum as the center of gravity, see Held and Mann (2018). We use the following weighting functions to approximate the probe volume of different types of lidar:

– CW lidar (Sonnenschein and Horrigan, 1971):

$$\varphi(s) = \frac{1}{\pi} \frac{z_{\mathrm{R}}}{z_{\mathrm{R}}^2 + s^2} \quad \text{with } z_{\mathrm{R}} = \frac{\lambda f_d^2}{\pi r_{\mathrm{b}}^2}, \tag{5}$$

where z_{R} is the Rayleigh length, λ the laser wavelength and r_{b} the beam radius at the output lens.

– pulsed lidar (Meyer Forsting et al., 2017):

$$\varphi(s) = \frac{1}{2\Delta p} \left\{ \mathrm{Erf}\left[\frac{s + \Delta p/2}{r_p}\right] - \mathrm{Erf}\left[\frac{s - \Delta p/2}{r_p}\right] \right\}$$

with the error function $\mathrm{Erf}(x) = \frac{2}{\sqrt{\pi}} \int\limits_0^x \exp(-t^2)\mathrm{d}t \quad \text{and} \quad r_p = \frac{\Delta l}{2\sqrt{\ln(2)}}, \tag{6}$

where Δp is the range-gate length and Δl the Gaussian lidar pulse Full Width at Half Maximum (FWHM).

Variances calculated from the centroid-derived radial velocities are attenuated by the lidar probe volume, which acts like a low-pass filter to the wind velocity fluctuations. Therefore, we refer to them as the 'filtered' radial velocity variances. If we assume that the lidar probe volume can be negligible and that u, v, and w are constant over the scanned area, the radial velocity can be expressed as

$$v_{\mathrm{r}}(\phi, \theta) = -u\cos\phi + v\cos\theta\sin\phi + w\sin\theta\sin\phi. \tag{7}$$

The 'unfiltered' radial velocity variance can be derived by taking the variance of Eq. (7), as shown in Eberhard et al. (1989):

$$\sigma_{v_{\mathrm{r}},\mathrm{unf}}^2(\phi, \theta) = \sigma_u^2 \cos^2\phi + \sigma_v^2 \cos^2\theta\sin^2\phi + \sigma_w^2 \sin^2\theta\sin^2\phi - 2\langle u'v'\rangle\cos\phi\cos\theta\sin\phi$$
$$- 2\langle u'w'\rangle\cos\phi\sin\theta\sin\phi + 2\langle v'w'\rangle\sin^2\phi\cos\theta\sin\theta. \tag{8}$$

3 Methodology

3.1 Estimation of the unfiltered radial velocity variance

In practice, the unfiltered radial velocity variance $\sigma_{v_{\mathrm{r}},\mathrm{unf}}^2$ in Eq. (8) can be estimated from the Doppler radial velocity spectrum. When the nacelle lidar measures at a small opening angle over a relatively homogeneous inflow and the wind shear is not very strong, the effect of radial velocity gradient within the lidar probe volume can be negligible (see Mann et al., 2010, for a detailed discussion). In this case, one can estimate $\sigma_{v_{\mathrm{r}},\mathrm{unf}}^2$ as the second central statistical moment of the ensemble-averaged Doppler spectrum of the radial velocity within typically a 10- or 30-min period. Each Doppler spectrum is area-normalized

before computing the ensemble-averaged Doppler spectrum $p(v_\mathrm{r})$. The mean radial velocity can be estimated as

$$\mu_{v_\mathrm{r}} = \int_{-\infty}^{\infty} v_\mathrm{r} p(v_\mathrm{r}) \mathrm{d}v_\mathrm{r}, \tag{9}$$

and its variance as

$$\sigma_{v_\mathrm{r}}^2 = \int_{-\infty}^{\infty} (v_\mathrm{r} - \mu_{v_\mathrm{r}})^2 p(v_\mathrm{r}) \mathrm{d}v_\mathrm{r}. \tag{10}$$

Assuming that all contributions of the radial velocity to the Doppler spectrum are because of turbulence, $\sigma_{v_\mathrm{r}}^2$ in Eq. (10) provides an estimate of $\sigma_{v_\mathrm{r},\mathrm{unf}}^2$. This assumption is reasonable when beams are close to horizontal.

3.2 Estimation of the Reynolds stresses

The Reynolds stress tensor $\boldsymbol{R} \equiv \boldsymbol{R}(\boldsymbol{x} = \boldsymbol{0})$ contains the variances and covariances of the velocity components:

$$\boldsymbol{R} = \begin{bmatrix} \sigma_u^2 & \langle u'v' \rangle & \langle u'w' \rangle \\ \langle v'u' \rangle & \sigma_v^2 & \langle v'w' \rangle \\ \langle w'u' \rangle & \langle w'v' \rangle & \sigma_w^2 \end{bmatrix}. \tag{11}$$

To compute $\boldsymbol{R}$, we use the radial velocity variances from all beams over the lidar scanning trajectory. Assuming spatial homogeneity, we apply a least-squares fit to the radial velocity variances $\sigma_{v_\mathrm{r}}^2$. This can be done since the variance in any direction $\boldsymbol{n}$ can be written as $\boldsymbol{n} \cdot \boldsymbol{R}\boldsymbol{n}$ or $n_i R_{ij} n_j$ using the index notation and assuming summation over repeated indices. We then sum the squared differences between the measured radial variances $\sigma_{v_\mathrm{r}}^2$ and $\boldsymbol{n} \cdot \boldsymbol{R}\boldsymbol{n}$ for any given Reynolds stress tensor $\boldsymbol{R}$. In order to avoid too many indices, we express this sum as integral $\int \mathrm{d}\mu$ such that the sum we are going to minimize can be written as

$$\Delta^2 = \int (\boldsymbol{n} \cdot \boldsymbol{R}\boldsymbol{n} - \sigma_{v_\mathrm{r}}^2)^2 \mathrm{d}\mu. \tag{12}$$

The matrix R_{ij} that minimizes the integral must fulfill

$$\frac{\partial \Delta^2}{\partial R_{ij}} = 0 \Rightarrow 2 \int (\boldsymbol{n} \cdot \boldsymbol{R}\boldsymbol{n} - \sigma_{v_\mathrm{r}}^2) n_i n_j \mathrm{d}\mu = 0. \tag{13}$$

This can be written as

$$R_{kl} \int n_k n_l n_i n_j \mathrm{d}\mu = \int \sigma_{v_\mathrm{r}}^2 n_i n_j \mathrm{d}\mu, \tag{14}$$

where (k,l) and (i,j) are each of the indices combinations $(1,1), (1,2), (1,3), (2,2), (2,3), (3,3)$, $n_1 = -\cos\phi$, $n_2 = \cos\theta\sin\phi$ and $n_3 = \sin\theta\sin\phi$ (as given in Eq. 3), i.e. Fu et al. (2022a),:

$$\begin{bmatrix} \sum n_1^4 & \sum n_1^2 n_2^2 & \sum n_1^2 n_3^2 & \sum 2n_1^3 n_2 & \sum 2n_1^3 n_3 & \sum 2n_1^2 n_2 n_3 \\ \sum n_1^2 n_2^2 & \sum n_2^4 & \sum n_2^2 n_3^2 & \sum 2n_1 n_2^3 & \sum 2n_1 n_2^2 n_3 & \sum 2n_2^3 n_3 \\ \sum n_1^2 n_3^2 & \sum n_2^2 n_3^2 & \sum n_3^4 & \sum 2n_1 n_2 n_3^2 & \sum 2n_1 n_3^3 & \sum 2n_2 n_3^3 \\ \sum n_1^3 n_2 & \sum n_1 n_2^3 & \sum n_1 n_2 n_3^2 & \sum 2n_1^2 n_2^2 & \sum 2n_1^2 n_2 n_3 & \sum 2n_1 n_2^2 n_3 \\ \sum n_1^3 n_3 & \sum n_1 n_2^2 n_3 & \sum n_1 n_3^3 & \sum 2n_1^2 n_2 n_3 & \sum 2n_1^2 n_3^2 & \sum 2n_1 n_2 n_3^2 \\ \sum n_1^2 n_2 n_3 & \sum n_2^3 n_3 & \sum n_2 n_3^3 & \sum 2n_1 n_2^2 n_3 & \sum 2n_1 n_2 n_3^2 & \sum 2n_2^2 n_3^2 \end{bmatrix} \begin{bmatrix} R_{uu} \\ R_{vv} \\ R_{ww} \\ R_{uv} \\ R_{uw} \\ R_{vw} \end{bmatrix} = \begin{bmatrix} \sum n_1^2 \sigma_{v_\mathrm{r}}^2 \\ \sum n_2^2 \sigma_{v_\mathrm{r}}^2 \\ \sum n_3^2 \sigma_{v_\mathrm{r}}^2 \\ \sum n_1 n_2 \sigma_{v_\mathrm{r}}^2 \\ \sum n_1 n_3 \sigma_{v_\mathrm{r}}^2 \\ \sum n_2 n_3 \sigma_{v_\mathrm{r}}^2 \end{bmatrix}. \tag{15}$$

To solve the six Reynolds stresses from Eq. (15), two requirements of the nacelle lidar scanning pattern need to be fulfilled (see Sathe et al., 2015, for a detailed discussion):

– the lidar has at least six beams or measures at six different locations within one full scan;

– the lidar beams have at least two different opening angles.

If a lidar has less than six beams, or the opening angles of all beams are identical and some of the six equations are linearly dependent, we have fewer knowns than unknowns in Eq. (15), which leads to infinite solutions. In those cases, only the along-wind variance σ_u^2 can be estimated well (Peña et al., 2019). To solve σ_u^2 from Eq. (15), assumptions of some Reynolds stresses terms are needed to reduce the number of unknowns. Here, we use three different assumptions, as introduced in Fu et al. (2022a):

– All Reynolds stresses apart from σ_u^2 are zero (denoted as 'LSP-σ_u^2' method). For lidars with only one half-cone opening angle, this means $\sigma_u^2 = \sum \sigma_{v_r}^2 / \sum \cos^2 \phi$.

– Turbulence is isotropic, i.e., $\sigma_u^2 = \sigma_v^2 = \sigma_w^2$ and that other terms are negligible (denoted as 'LSP-isotropy' method). This method is the same for lidars with only one half-cone opening angle as taking the mean of all radial velocity variances.

– The relations between velocity components' standard deviation $\sigma_v = 0.7\sigma_u$ and $\sigma_w = 0.5\sigma_u$, as recommended in IEC (2019), and all covariances are negligible (denoted as 'LSP-IEC' method).

3.3 Numerical simulations

We simulate lidar measurements on the nacelle of a wind turbine with a rotor diameter (D) of 52 m using 100 randomly generated turbulence boxes. The boxes contain the fluctuations of the three wind components. The turbulence boxes are described by the Mann model with typical values of the model parameters $\alpha\varepsilon^{2/3} = 0.05$ m$^{4/3}$ s^{-1}, $L = 61$ m and $\Gamma = 3.2$. The selected three parameters are adopted from Mann (1994) and characterize a neutral atmospheric stratification on a typical offshore site. The dissipation rate $\alpha\varepsilon^{2/3}$ is a scaling factor on the turbulence intensity. The number of grid points in the three directions are $(N_x, N_y, N_z) = (8192, 64, 64)$. The lengths of the turbulence boxes in the vertical and lateral directions are both 128 m. The boxes have lengths of 30 min in the along-wind direction assuming a mean wind $U = 10$ m s^{-1}. We add a linear shear $\mathrm{d}U/\mathrm{d}z = 0.0288$ s^{-1} on top of the along-wind velocity component u in each box:

$$u = U + \frac{\mathrm{d}U}{\mathrm{d}z}(z - z_{\text{rotor}}) + u', \tag{16}$$

where z_{rotor} is the turbine hub height in the turbulence box, i.e., the middle grid point in the z-coordinate.

We simulate eight lidars with different scanning patterns, as shown in Fig. 2. Statistics of the sonic anemometer are taken at the location of the turbine rotor center (which is also the center of the turbulence boxes) as the reference for evaluating the lidar-derived turbulence characteristics. The SpinnerLidar scans in a rosette-curve pattern and has half-cone opening angles in the range $0 - 30°$. It generates 400 radial velocities in one full scan. The SpinnerLidar is simulated with a focus distance of

7

52 m ($1D$) in front of the rotor, while other lidars are simulated with the focus distance of 98 m due to their smaller opening angles ($\phi = 15°$) to cover the whole rotor plane. We also simulate all considered lidars with multiple measurement planes at $f_d = 49$, 72, 98, 121 and 142 m, which are arbitrarily selected. As examples, Fig. 3 shows the scanning trajectories of the 4-beam and 50-beam lidars measuring at the five planes. We then use the radial velocity variances at all measurement levels

185 to compute the turbulence statistics. Furthermore, to study the dependence of the turbulence estimations on the opening angle and the focus distance, we simulate the 6-beam configuration, proposed by Sathe et al. (2015), with extra setups: a fixed focus distance of 52 m and increasing opening angles (see Fig. 4(a)), as well as a fixed opening angle of 15° and increasing focus distances (see Fig. 4(b)).
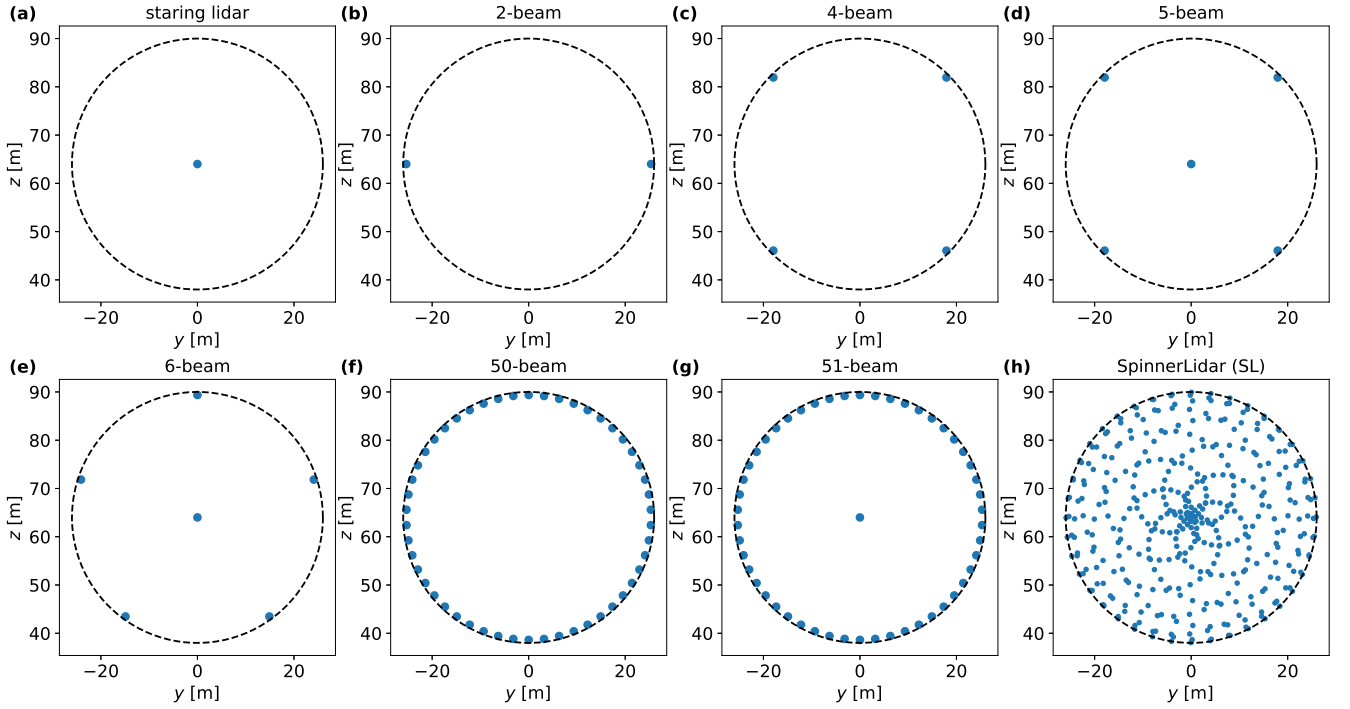

Figure 2. Selected lidar scanning patterns for numerical simulations. The SpinnerLidar (h) has $\phi = 0 - 30°$ and scans at $f_d = 52$ m, while other lidars (a-g) have $\phi = 15°$ and scan at $f_d = 98$ m to cover the whole rotor plane. The lidar beam scanning locations are marked in blue dots. The wind turbine rotor is represented in a black dashed circle.

We consider the lidar probe volume when we investigate the dependence of the Reynolds stresses estimation on ϕ and f_d.

190 The Doppler radial velocity spectrum $S(v_r, t)$ is simulated as (Held and Mann, 2018)

$$S(v_r, t) = \int_{-M}^{M} \varphi(s)\delta(v_r - \boldsymbol{u}(\boldsymbol{n}s - \boldsymbol{U}t) \cdot \boldsymbol{n})\mathrm{d}s, \tag{17}$$
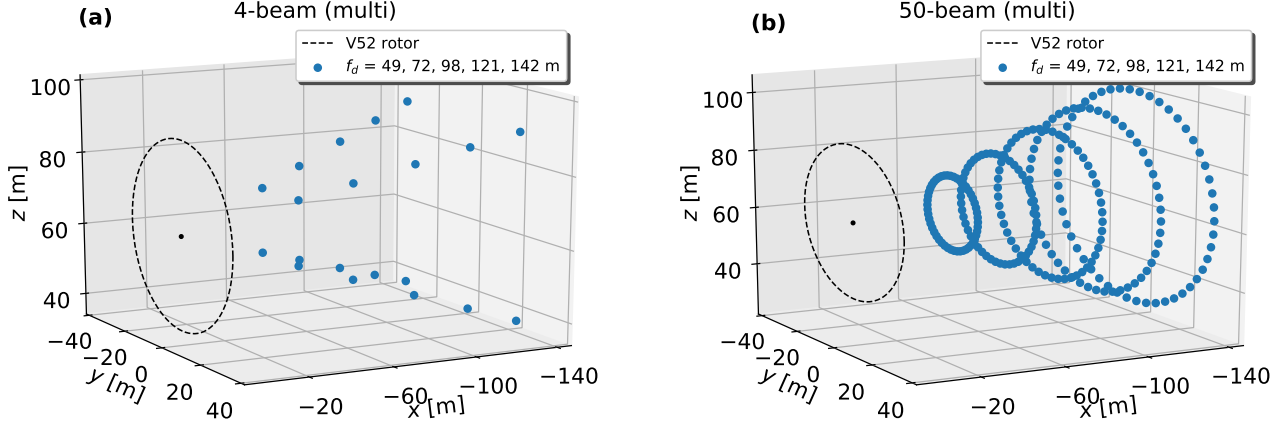
Figure 3. Scanning trajectories of the 4-beam and the 50-beam lidars measuring at $f_d = 49, 72, 98, 121$ and 142 m. Features regarding the blue dots and the dashed circle as in Fig. 2. The turbine nacelle is marked in a black dot on the rotor plane.
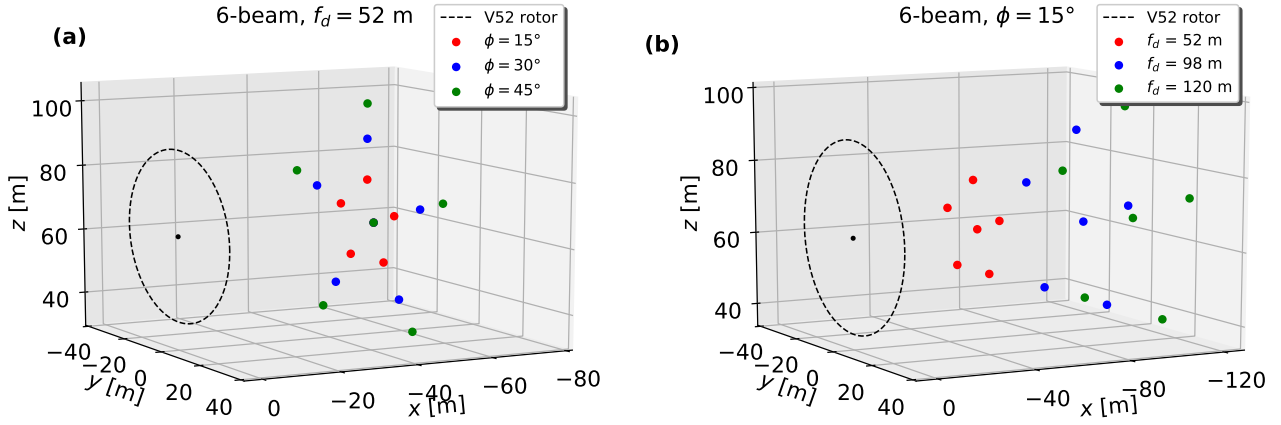

Figure 4. Scanning strategies of the 6-beam lidar with (a) a fixed focus distance and various half-cone opening angles, and (b) a fixed half-cone opening angle and various focus distances. Features regarding the dashed circle and the black dot as in Fig.3.

where δ represents the Dirac delta function, the integral is truncated with the distance M along the beam, and $\varphi(s)$ can be described by Eq. (5) or (6) depending on the type of the lidar system. The resolution of the Doppler radial velocity spectrum is 0.1 m s^{-1} per velocity bin, which is hereafter always used. Parameters used for modelling the probe volume are summarized in Table 1 (Meyer Forsting et al., 2017). We select M as shown in Table 1 so that 95% of the area under both weighting functions is covered. Figure 5 compares the modelled lidar probe volume for CW and pulsed lidars at focus distances $f_d = 52$, 98 and 120 m. The size of the probe volume for CW lidars increases with the square of the focus distance (see Eq. 5), while it remains the same for pulsed lidars.

	$\lambda = 1.565 \times 10^{-6}\text{m}$
CW	$r_b = 2.8 \times 10^{-2}$ m
	$M = 8z_\text{R}$
	$\Delta l = 24.75$ m
pulsed	$\Delta p = 38.4$ m
	$M = 1.2\Delta l$

Table 1. Parameters for modelling the CW and pulsed lidar probe volume in numerical simulations.
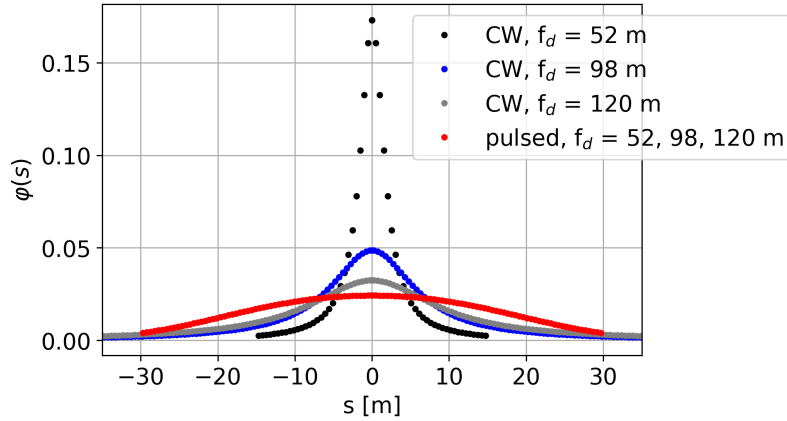

Figure 5. Comparison of the modelled lidar probe volume for CW and pulsed lidars at three different focus distances.

The time lag between each measurement within a full scan is not considered but assumed that measurements are taken at the same time. In the numerical simulations neglecting lidar probe volume (see results in Sections 4.1 and 4.2), the time resolution of the wind field is used as the lidar scan rate, i.e., lidars complete one full scan in $dt = dx/U = 0.22$ s. In the simulations considering lidar probe volume (see results in Section 4.3), the lidars are assumed to finish a full scan in 2 s.

3.4 Field measurements

During the period from 1 October 2020 to 30 April 2021, a SpinnerLidar was deployed on the nacelle of a Vestas V52 wind
turbine at DTU Risø campus in Roskilde, Denmark, measuring the flow in front of the turbine. The V52 wind turbine has a
rotor diameter of 52 m and a hub height of 44 m. Between the scan head of the SpinnerLidar and the turbine rotation axis, there
is a vertical displacement of 2.47 m. A test site layout is shown on a digital surface elevation model in Fig. 6. The terrain is
slightly hilly and its surface is characterized by a mix of cropland, grassland and coast. The dominant wind directions during
this period at this site are west and south-west. The V52 wind turbine (marked with a red circle) stands at the northernmost
position of a row of wind turbines (marked in black circles). There is also a meteorological mast (marked as a red square)
mounted at 120 m ($\approx$ 2.3D) upstream from the V52 wind turbine at 291° from the north. One of the Metek USA-1 3D sonic
anemometers on the mast is located at 44 m above the ground, and its turbulence statistics is used as references to be compared
with the estimations from the nacelle-based lidars. A cup anemometer is located at the same height as the sonic anemometer
on the mast. There are also a wind vane at 41 m and a Thies precipitation opto sensor at 2 m on the mast.
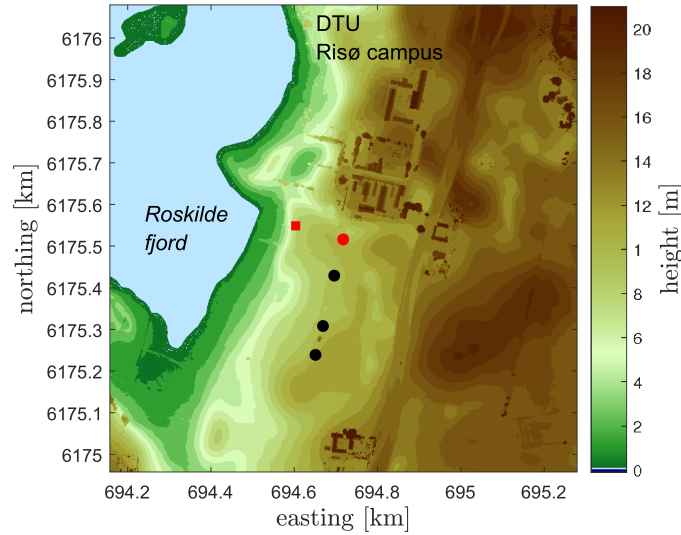

Figure 6. A digital surface elevation model (UTM32 WGS84) showing the Risø test site in Roskilde, Denmark. The height above the mean
sea level is indicated by the color bar (in meters). A row of wind turbines are marked in circles (in red the reference V52 wind turbine). The
meteorological mast is shown in a red square.

The SpinnerLidar (Peña et al., 2019) is based on a CW system and it was set up to scan the inflow at a focus distance of 62
m ($\approx 1.2D$, see Fig. 7). The Rayleigh length z_R of the SpinnerLidar at this focused distance is 2.44 m. It reported 400 radial
velocities at a rate of 200 Hz, so it took 2 s to finish one full scan. The system also stored the instantaneous Doppler spectrum
of the radial velocity, which allows us to estimate the unfiltered radial velocity variance.

The measurements used for the analysis are from the wind sectors, which are relatively aligned with the mast-turbine direc-
tion (i.e., the 10-min averaged wind direction measured by the vane is within 291° $\pm$ 30°). The yaw misalignment of the V52
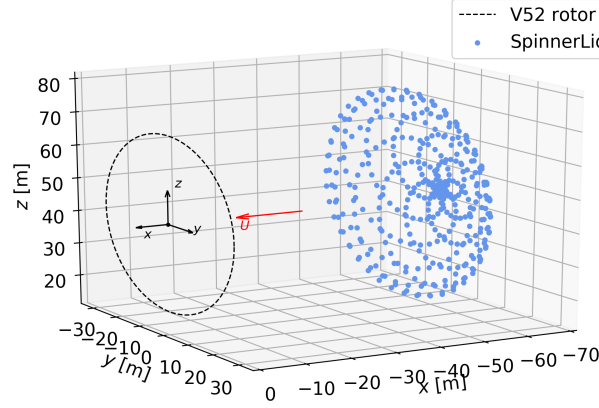
11

Figure 7. The scanning trajectory of the SpinnerLidar in the measurement campaign.

turbine is below $5°$, thereby minimizing the influence of nearby wind turbine wakes. We use a 10-min period, when the lidar and the V52 wind turbine are concurrently operating, and the averaged wind speed from the cup anemometer at 44 m is higher than 3 m s^{-1}. No precipitation was detected during the analyzed 10-min periods. After filtering, 2348 10-min periods are used for the analysis.

225   The SpinnerLidar measurements are post-processed to remove the signals reflected by the wind turbine blades, the telescope lens (the beam can hit the lens perpendicularly) or other hard targets. Such a procedure filters out some measurements close to the middle of the pattern. To compensate for the nacelle movement, we rotate the system-reported beam scanning coordinates using the 10-min averaged azimuthal and inclination angles of the SpinnerLidar, which are typically around $0.3°$ and $3°$, respectively. Taking the motion of the turbine and the slack of the SpinnerLidar into consideration, we divide the y–z plane

230   into grids of 1-m resolution to aggregate the corrected scan locations. In the given 10-min, all Doppler radial velocity spectra lying within each grid cell are accumulated, and only measurements within the grid cells, where there are more than 30 instantaneous Doppler spectra, are used for the reconstruction. At least 900 grid cells should satisfy the criterion in the 10-min periods for our analysis. The light-grey dots in Figs. 8 and 9 represent the grid cells (for this particular case we have 1127 grid cells) satisfying the criterion in one arbitrary 10-min period. Other details about the measurement campaign and how the

235   SpinnerLidar measurements are selected, filtered and processed can be found in Fu et al. (2022a). The post-processing of the measurements leaves us 1294 time periods for the final comparison.

     To imitate lidars with different scanning strategies, we select SpinnerLidar measurements at certain grid cells to estimate the Reynolds stresses, as marked in red in Fig. 8. Due to the rotation of the system-reported lidar unit vectors, the corresponding half-cone opening angles of the grid cells are typically higher in the upper circle than those in the lower circle of the pattern,

240   e.g., the ϕ of the top beam reaches $32°$ while the ϕ of the bottom beam is $27°$. To mimic the simulation setup of the 6-beam lidar in Fig. 4(a), we select 6 grid cells with different levels of opening angle (see Fig. 9), in which the central grid is always used. The mean half-cone opening angles of the 5 grid cells forming the circles are $12°$, $19°$ and $30°$, respectively. We estimate

the unfiltered radial velocity variance $\sigma^2_{v_r,\text{unf}}$ using the Doppler radial velocity spectra collected in each selected grid cell. The Doppler spectra processing and usage are described in detail in Fu et al. (2022a).
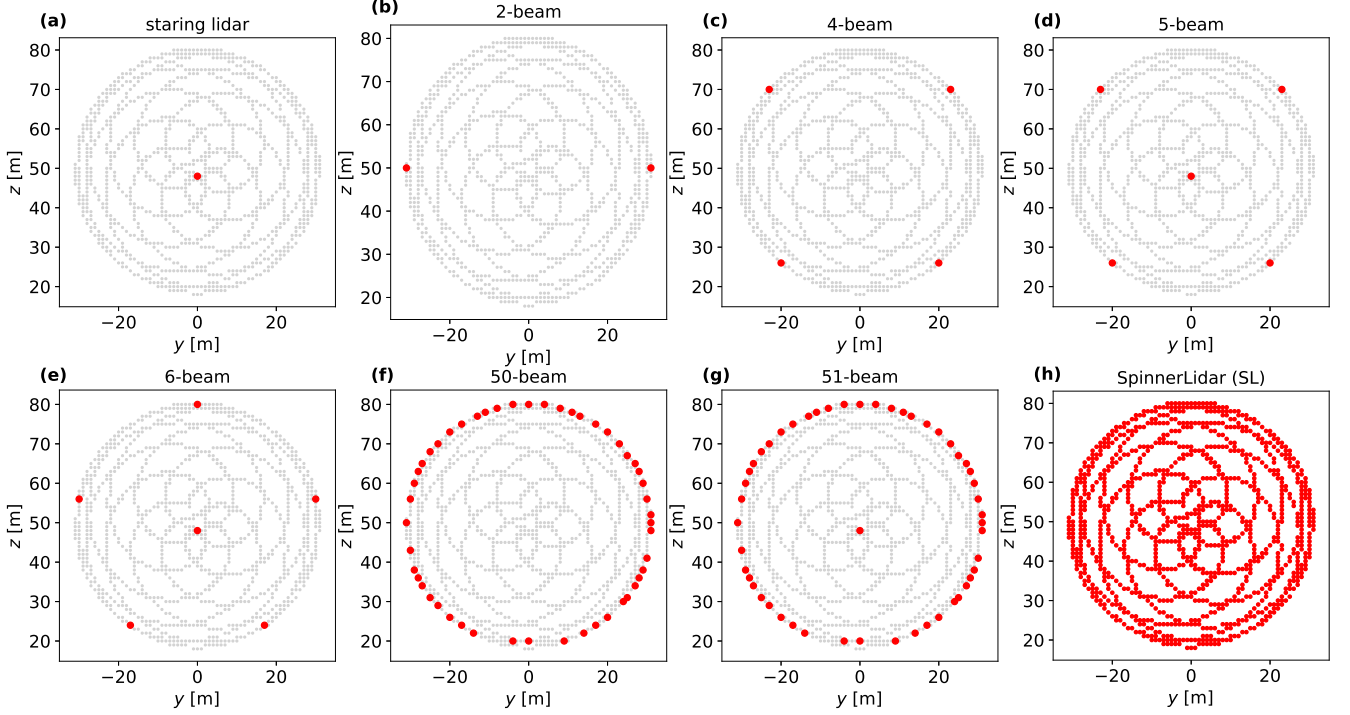

Figure 8. Selected lidar scanning patterns (in red) from the gridded SpinnerLidar scans (in light grey), which are at the focus distance of 62 m.

4 Results

In this section, we show comparisons of the Reynolds stresses computed from the considered lidars against those from the sonic anemometer at turbine hub height in bar plots. In the plots, markers correspond to the means of the estimations from 100 turbulence fields and the error bars are $\pm$ one standard deviation indicating the uncertainty of the estimation. The Reynolds stresses estimated from the measurements are normalized by the square of the mean along-wind velocity estimated by the lidar U^2 as we analyze a wide range of observed turbulence conditions. The mean wind velocity is computed by applying a least-square fit to the lidar radial velocities from all beams (Fu et al., 2022a). Results in Sections 4.1 and 4.2 neglect the lidars' probe volumes to study the influence of the number of beams. Nevertheless, for the CW lidar system, the probe volume increases with the square of the focus distance. Also, for pulsed lidar systems, the probe volume effect cannot be easily compensated since the Doppler spectra are usually not accessible. Therefore, the probe volumes are considered in Section 4.3 to show how different factors are altogether influencing the turbulence estimations.
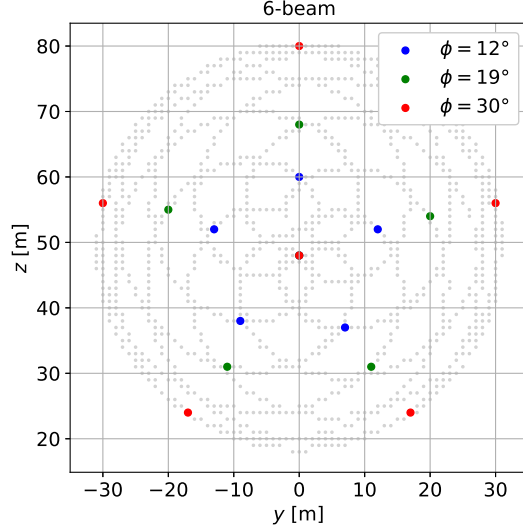
13

Figure 9. Selected grid cells for the 6-beam lidar with three different levels of the half-cone opening angle. The central grid coincides in the three cases. The gridded SpinnerLidar scans are shown in light grey.

4.1 Estimation of Reynolds stresses by multiple-beam lidars

We show in Fig. 10 the estimations of the six Reynolds stresses by the lidars, which have more than six beams and measure at a single plane, as well as those of the sonic anemometer. Results in Fig. 10(a) are from simulations that assume the lidars measure at the focus point only, i.e., no probe-volume averaging is accounted for. Results from both the simulations and the measurements show that the SpinnerLidar gives the best estimation for all six components. The results for the 6-beam and 51-beam lidars are very similar with larger errors and higher uncertainties than those of the SpinnerLidar. The 50-beam lidar can estimate the covariances accurately, while it shows large errors and uncertainties for $\langle v'v' \rangle$ and $\langle w'w' \rangle$; these are so noisy that some of them are out of the limit of the figure's axis. This is because the least-squares problem as formulated in Eq. (14) can lead to infinite solutions if we have only one opening angle ϕ. By comparing the results from the 50- and 51-beam lidar, we can see that the addition of a central beam is very beneficial for the computation of the variances of the velocity components, because the central beam provides an additional opening angle to the 50-beam lidar making the matrix on the left side of Eq. (15) not singular. In principle, adding an extra beam in any different opening angle than the others in the 50-beam scanning pattern will improve the estimations. The central beam is the best option for improving the estimation of the $\langle u'u' \rangle$ since the beam aligns with the along-wind velocity component and can fully capture its variation when the probe volume is neglected.

Results in Fig. 10 (a) indicate that nacelle lidars are able to characterize inflow turbulence as accurate as the sonic anemometer with reasonable uncertainties, when the lidar has at least six beams and two different opening angles. We see the similar trends from the measurements shown in Fig. 10 (b). The unfiltered Reynolds stresses estimated from all lidar measurements

14

are generally close to those from the sonic anemometer but biased. What unexpected and rare are the negative values of $\langle v'v'\rangle$ and $\langle w'w'\rangle$ observed in some periods of the measurements, as shown and discussed in Fu et al. (2022a).
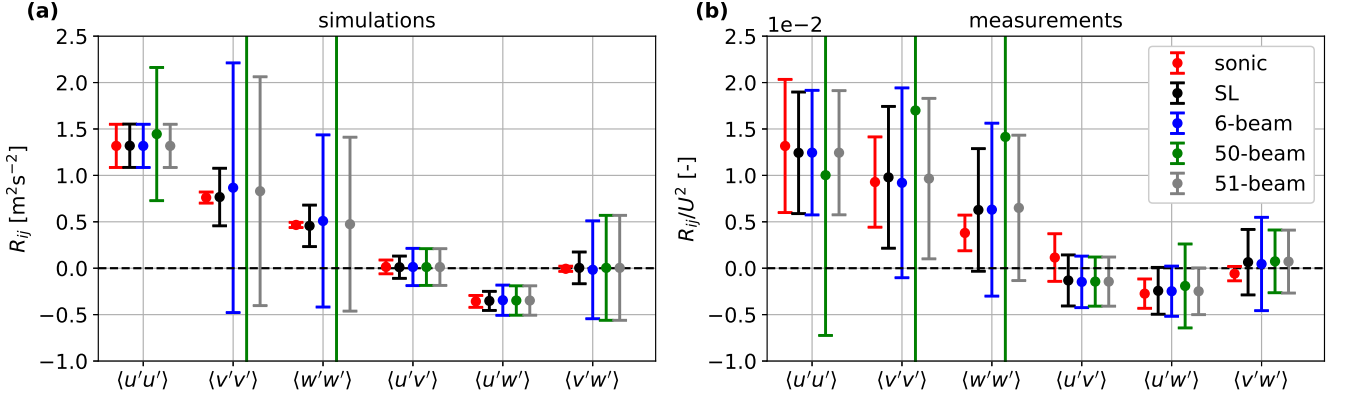

Figure 10. Reynolds stresses derived from the sonic anemometer and lidars, which have more than six beams and measure at a single distance. (a) simulated with 100 virtual wind fields. The lidars' probe volumes are neglected. (b) computed from the unfiltered radial velocity variance of the measurements. The markers are the means and the error bars are $\pm$ one standard deviation indicating the uncertainty of the estimation.

Figure 11 shows four of the Reynolds stresses retrieved from the 4- and 5-beam lidars. $\langle u'v'\rangle$ and $\langle v'w'\rangle$ are neglected in Eq. (15). In all cases, the determinants of the matrix in Eq. (15) are close to zero, which indicate that the 4- and 5-beam configurations cannot estimate these four Reynolds stresses accurately using the least-square procedure. Results from multiple-plane cases show that measuring at several planes with the same beam orientations does not aid much in the Reynolds stress reconstruction, as the determinant of the matrix in Eq. (15) does not change. For the 5-beam lidar, adding measurement planes only slightly reduces the uncertainty of the $\langle u'u'\rangle$ and $\langle u'w'\rangle$ components. This lack of sensitivity is partly due to Taylor's frozen hypothesis, as we do not account for evolution in the turbulence fields. We observe the same trend by comparing the estimation of these stresses from a 50-beam lidar measuring at a single and multiple planes (not shown here).

4.2 Estimation of the along-wind variance by all considered lidars

In case the nacelle lidar has fewer than six beams, not all six Reynolds stresses can be solved from Eq. (15). We focus our estimations on the along-wind variance and retrieve σ_u^2 from all considered lidars using the 'LSP-σ_u^2', 'LSP-isotropy' and 'LSP-IEC' methods, respectively, as introduced in Section 3.2. Results are shown in Fig. 12. All lidars are simulated to measure at a single plane (same as in Fig. 2) without accounting for the probe volume. Results from measurements are computed using the unfiltered radial velocity variances.

Both simulation and measurement results show, as a general trend, that lidar-derived σ_u^2 values are overestimated using the 'LSP-σ_u^2' method when compared to those from the sonic anemometer, while they are underestimated using the 'LSP-isotropy' method. The 'LSP-IEC' method gives the most accurate estimates among the three methods, as it assumes relations between the
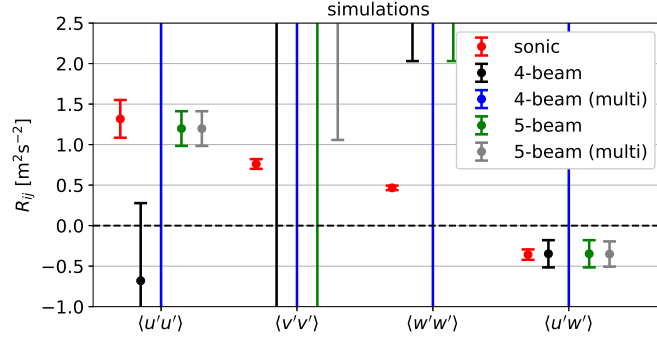
Figure 11. Reynolds stresses derived from the virtual sonic anemometer, the 4- and 5-beam lidars measuring at a single and multiple (multi) planes from 100 simulated wind fields. The lidars' probe volumes are neglected.

variances of the velocity components that might be close to those we can find within the atmospheric surface layer. The staring lidar performs like a sonic anemometer in our simulations as the beam is perfectly aligned with the along-wind component and the effect of lidar probe volume is not considered. Overall, all considered lidars are able to estimate σ_u^2 very well, despite of their different number of beams.

Table 2 summarizes the relative errors of the means of lidar-derived estimates compared to the one from the sonic anemometer. A negative value indicates that the along-wind variance is underestimated and vice-versa. The results in the first row of the table are computed solving the full matrix of Eq. (15) (same as $\langle u'u' \rangle$ showed in Fig. 10, here denoted as 'LSP-6Re' method), from which we get perfect estimations of σ_u^2 using the 6- and the 51-beam lidars, and the SpinnerLidar without the effect of the probe volume in the simulations. Furthermore, for lidars that have at least six beams and two different opening angles, the method 'LSP-6Re' is the best option to compute σ_u^2 among others, because it does not assume any relations between the six Reynolds stresses. While for lidars with fewer than six beams or only one opening angle, the 'LSP-6Re' does not work well and the 'LSP-IEC' gives the best estimation of σ_u^2. These results are aligned with one of the main findings in Fu et al. (2022a). In this work, the 'LSP-IEC' gives even smaller errors because we are able to compensate for the probe volume effect and use the 'unfiltered' radial velocity variances. In addition, comparing the relative errors between the 4- and 5-beam lidars, and those between the 50- and 51-beam lidars, we find again that the addition of a central beam can sometimes improve the estimation of the along-wind variance.

4.3 Dependence of Reynolds stresses estimations on the opening angle, focus distances and the type of lidar

The results shown in this section include the averaging effect of the lidar probe volume. In Fig. 13, we analyze how the accuracy and the uncertainty of the Reynolds stresses estimations change when increasing the half-cone opening angle ϕ for the 6-beam lidar. The simulation setup has been shown in Fig. 4(a). We compare these estimations with those from the sonic anemometer and the SpinnerLidar. The lidar probe volumes are modelled as in a CW system. Simulation and measurement results show that both the error and the uncertainty decrease as the opening angle increases. Specifically, the 6-beam lidar with $\phi = 45°$
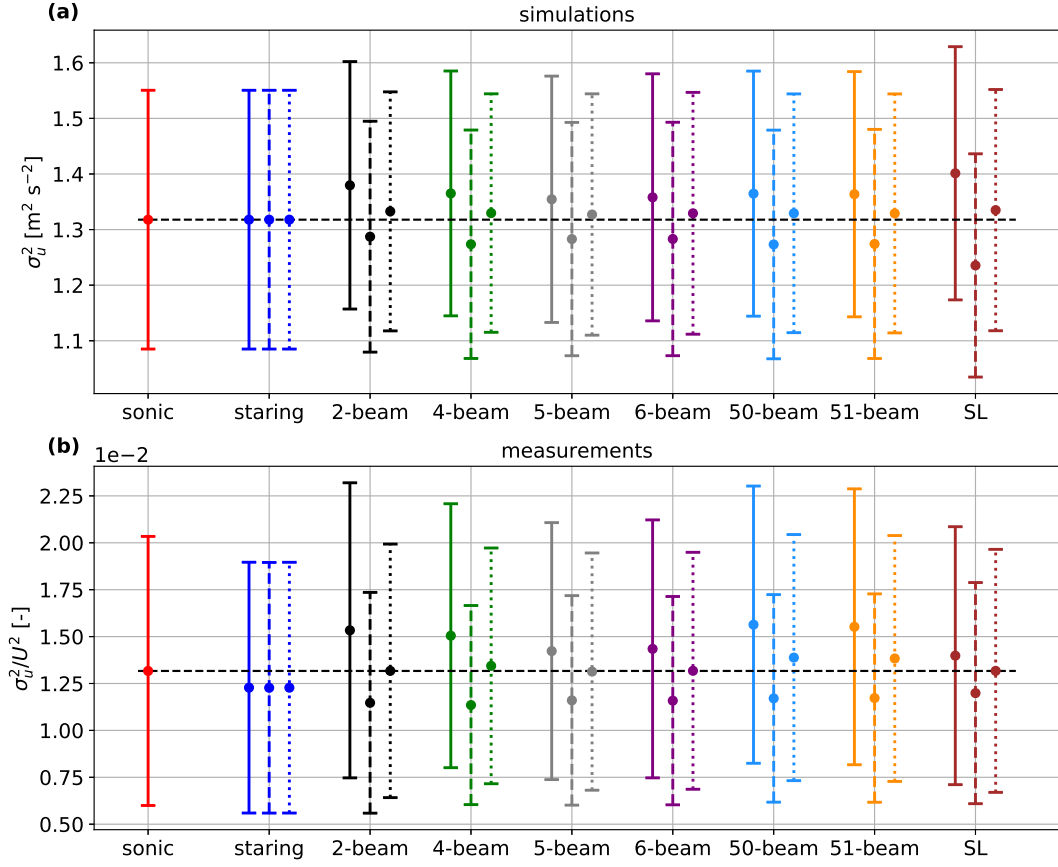
Figure 12. The along-wind variance derived from all considered lidars using the 'LSP-σ_u^2' method (solid lines), 'LSP-isotropy' method (dashed lines) and 'LSP-IEC' method (dotted lines). All lidars from simulations are assumed to have no probe volume and they measure at a single plane (Fig. 2).

in the simulations provides lower uncertainty than the SpinnerLidar despite having much fewer beams, as the SpinnerLidar's maximum opening angle is $\phi = 30°$. We observe the same trend when simulating the probe volume with a 6-beam pulsed system (not shown here). Possible reasons for the positive bias of the v- and w-variances seen from the simulation results are discussed in Section 5.

We study the dependence of the Reynolds stresses estimations on the increasing focus distance f_d for the 6-beam lidar based on numerical simulations. The setup has been shown in Fig. 4(b). We assume the lidar systems to be continuous-wave and pulsed, as shown in Fig. 14(a) and (b), respectively. All Reynolds stresses are computed using the centroid-derived radial velocity variances. Therefore, the estimated variances are attenuated by the probe volume and in general smaller than those from the sonic anemometer. For both types of lidar, we see that increasing the focus distance has negative effects on the estimation of all Reynolds stresses. The uncertainty increases due to the random error on the variances of the radial velocity;

17

	methods	staring	2-beam	4-beam	5-beam	6-beam	50-beam	51-beam	SL
	LSP-6Re	—	—	—	—	0	9.7	0	0.1
simulations	LSP-σ_u^2	0	4.7	3.6	2.8	3.0	3.6	3.5	6.3
(without probe volume)	LSP-isotropy	0	-2.3	-3.4	-2.6	-2.6	-3.4	-3.3	-6.2
	LSP-IEC	0	1.1	0.9	0.7	0.9	0.9	0.9	1.3
	LSP-6Re	—	—	—	—	-5.4	-23.9	-5.5	-5.6
measurements	LSP-σ_u^2	-6.8	16.4	14.3	8.0	8.9	18.7	17.9	6.2
(unfiltered variance)	LSP-isotropy	-6.8	-12.9	-13.8	-11.9	-12.0	-11.1	-11.0	-9.0
	LSP-IEC	-6.8	0	2.1	-0.3	0.1	5.4	5.0	0

Table 2. Relative error [%] of the mean values of the lidar-derived along-wind variance to the one from the sonic anemometer. The lidars' probe volumes are neglected in the simulations. Results from the simulations are computed using measurements at a single plane (same set up as Fig. 2). A negative value indicates that the along-wind variance is underestimated and vice-versa.
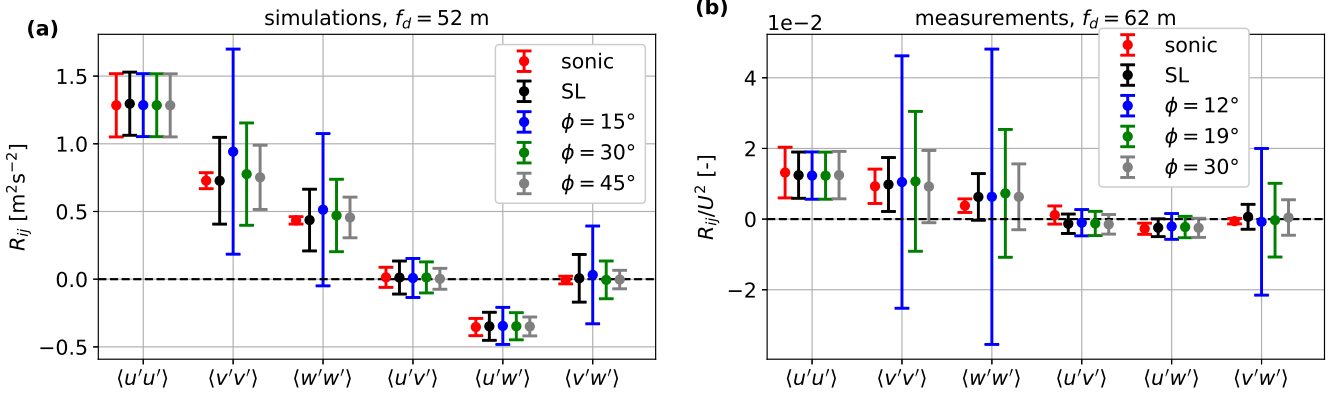

Figure 13. Dependence of the Reynolds stresses estimations on the increasing half-cone opening angle ϕ for the 6-beam lidar (single plane), the sonic anemometer and the SpinnerLidar ($\phi = 0$–$30°$). The probe volume in the simulations is assumed to be as in CW systems. All Reynolds stresses are computed using the unfiltered radial velocity variances.

they are less correlated when the lidar scans over a larger area. In the case of the CW system, the bias for the estimations increases with f_d due to its growing probe volume, while the bias is almost constant for the pulsed system, as expected. For the closest focus distance $f_d = 52$ m, the bias of the estimations from the pulsed system is evidently larger than those from the CW system, where the later system gives accurate estimations of all Reynolds stresses. We perform the same analysis with the 51-beam lidar and observe the same trends (not shown here).
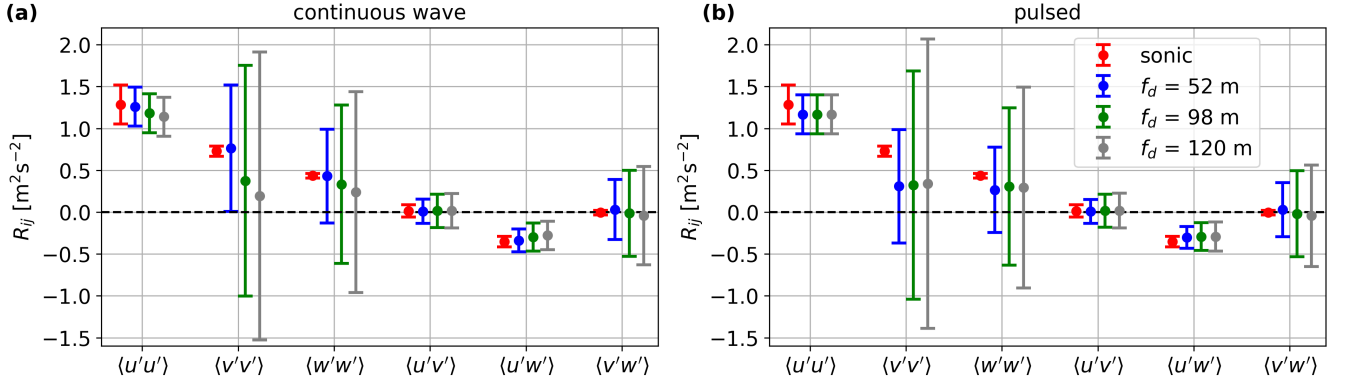

Figure 14. Dependence of the Reynolds stresses estimations on the increasing focus distance f_d for the 6-beam lidar (single plane, $\phi = 15°$), compared to those from the sonic anemometer. The probe volume in the simulations are assumed to be as in (a) a CW system, and (b) a pulsed system. All Reynolds stresses are computed using the centroid-derived (filtered) radial velocity variances.

5 Discussion

Results shown in Fig. 13 are from simulations that consider the CW lidar probe volume to mimic the lidar's behavior in the reality. Then, the Doppler radial velocity spectra are used to compute the 'unfiltered' velocity variances for both simulations and measurements. Compared to the estimations from the sonic anemometer, we observe positive biases of the lidar-retrieved v- and w- variances. The biases decreas with increasing the half-cone opening angle ϕ. The reason is that although the large matrix on the left side of Eq. (15) is not degenerate (i.e., its determinant is not zero) for a 6-beam lidar, the coefficients for R_{vv} and R_{ww} are very small (in the order of 10^{-3}) for $\phi = 15°$; the equation system is only balanced by overestimating both terms R_{vv} and R_{ww}. The coefficients are proportional to the value of the opening angle ϕ, so they increase to 10^{-2} in the case of $\phi = 30°$, and to 10^{-1} in the case of $\phi = 45°$, which explains why the biases are reduced with larger opening angles. The positive biases for R_{vv} and R_{ww} are slightly more evident in the simulations with probe volume compared to the case in which the probe volume is neglected (see Fig. 10 (a)), because the simulated radial velocity variances are different in the two scenarios.

As shown in Fig. 13, increasing the lidar opening angle improves the accuracy and uncertainty of R_{vv} and R_{ww} estimations. The uncertainty of σ_u^2 is not much influenced if the lidar has a central beam that always aligns with the mean wind, e.g. the six-, 51-beam lidars, and the SpinnerLidar. For nacelle lidars without a central beam, enlarging the opening angle brings higher

uncertainty to σ_u^2 estimation, which is a key parameter for assessing wind turbine loads (IEC, 2019). Therefore, the optimum
opening angle for turbulence estimations depends on which Reynolds stress is of interest. In addition, for control applications,
the large opening angle is beneficial for measuring wind directions, but sacrifices the accuracy of rotor-effective wind speed
and wind shear estimations (Simley et al., 2018). The optimum opening angle is also very much relevant to the turbine's size.

In this work, we characterize turbulence in front of a small wind turbine at $1D$ and $1.2D$ in the simulations and the field
experiment, respectively. Taylor's frozen turbulence hypothesis (and homogeneity) is assumed throughout our numerical sim-
ulations, because the wind evolution is not very relevant to turbulence statistics, but more to the rotor-effective wind speed
estimations (Chen et al., 2021). Mann et al. (2018) showed that turbulence is slightly affected by the stagnation in front of
the wind turbine rotor as it goes through the induction zone. The change of the low-frequency wind variation is related to the
thrust coefficient of the wind turbine, but the main turbulence statistics do not change. In addition, the yaw misalignment of the
wind turbine is not considered in this work. A small yaw misalignment (below 20°) does not affect much σ_u^2 estimations but
increases the uncertainty of R_{vv} and R_{ww} estimations. For modern wind turbines with very large rotor disks, the single-point
turbulence statistics do not represent well the inflow turbulence affecting the wind turbine. The least-square procedure cannot
be used to characterize the inhomogeneous inflow. New methodologies, e.g., constrained simulations (Dimitrov and Natarajan,
2017; Conti et al., 2021), are needed to reconstruct the inhomogeneous wind field.

We show from both simulations and measurements that all six Reynolds stress components can be estimated accurately
when using a nacelle multi-beam lidar. Although the spectral turbulence model used here (the Mann model), which is the
basis of our simulated turbulence fields, assumes two of these components to be zero, namely $\langle u'v' \rangle$ and $\langle v'w' \rangle$, the methods
and techniques introduced in this work enable us to estimate all components accurately. This is advantageous for the study of
atmospheric flow over complex terrain and, particularly, in offshore conditions, where turbulence measurements are scarce and
expensive, and where we rely very much on models to assess the site conditions that impact wind turbines. These models often
assume relations between the turbulence components and/or use parametrizations of stresses/fluxes that are invalid due to the
nature of the flow phenomena and the interaction between the waves and the wind field. For example, surface stresses over
long-lasting waves can be highly misaligned with the vertical gradient of the horizontal wind; most parametrizations of the
air-sea interaction assume such an alignment to estimate momentum fluxes within the marine boundary layer. Offshore nacelle
lidars can therefore help us understanding phenomena that are otherwise difficult to assess with traditional anemometry used
for offshore wind power development.

6 Conclusion and Outlook

This study investigated the dependence of the Reynolds stresses estimations on different number of beams, half-cone opening
angles, focus distances, single or multiple measurement planes, and different types of the Doppler wind nacelle lidars using
both numerical simulations and measurements. The considered lidar scanning patterns included the staring lidar (single beam),
the 2-, 4-, 5-, 6-, 50-, 51-beam lidars and the SpinnerLidar, which reports 400 radial velocities with one scan. We assumed a
homogeneous inflow turbulence (both for the simulations and measurements) and the Taylor's frozen turbulence (for the simu-

lations). The lidar-retrieved turbulence estimations were compared with those from a sonic anemometer at turbine hub height. Analysis of both numerical simulations and measurements showed that to estimate all the six Reynolds stresses accurately, a nacelle lidar system with at least six beams is required. Also, one of the beams of this system should have a different opening angle. Adding one central beam improves the estimations of the velocity components' variances. Measuring at multiple planes with the same beam orientations only reduces the uncertainty but not the bias in the reconstruction, if Taylor's frozen turbulence hypothesis is applied. All considered lidars can estimate the along-wind variance accurately by using the least-squares procedure and the assumption that the relations of the velocity components' variances are as suggested in the IEC standard. Also, the Doppler radial velocity spectra are needed for the accurate estimations. For both CW and pulsed lidars, increasing the opening angle reduces both the error and uncertainty of the estimations, while increasing the focus distance has opposite effects. In short, from all tested scanning strategies, a 6-beam CW lidar measuring at a close distance with a large opening angle gives the best estimations of all Reynolds stresses. The optimum value of the opening angle depends on the Reynolds stress term of interest and also the wind turbines' size. Further studies or experiments are needed to study the best opening angle of the 6-beam lidar for different applications.

In this work, the single-point turbulence statistics are estimated using the least-square procedure, which assumes homogeneity over the lidar scanning area. Wind turbines nowadays are often operating inside a wind farm or have large spans over the swept area. The assumption of homogeneous turbulence can be violated under those conditions. Therefore, further studies on the optimized lidar scanning strategy for turbulence estimation should consider the inhomogeneity of the inflow. Additionally, the proposed nacelle lidar scanning strategies can be used to study the wind evolution, the spatial correlations of turbulence and estimate multi-point statistics, which better characterize the inflow that interacts with the turbine than the hub height ones. The wind field reconstruction of the inhomogeneous wind fields can benefit from constrained simulations, which incorporate lidar measurements into three-dimensional turbulence wind fields. Future works could also consider the non-Gaussianity of turbulence (Liu et al., 2010; Schottler et al., 2017) and the scale-dependent anisotropy of wind fluctuations (Syed et al., 2023).

21

References

410   Branlard, E., Pedersen, A. T., Mann, J., Angelou, N., Fischer, A., Mikkelsen, T., Harris, M., Slinger, C., and Montes, B. F.: Retrieving wind statistics from average spectrum of continuous-wave lidar, Atmospheric Measurement Techniques, 6, 1673–1683, https://doi.org/10.5194/amt-6-1673-2013, 2013.

Chen, Y., Schlipf, D., and Cheng, P. W.: Parameterization of wind evolution using lidar, Wind Energy Science, 6, 61–91, https://doi.org/10.5194/wes-6-61-2021, 2021.

415   Conti, D., Pettas, V., Dimitrov, N., and Peña, A.: Wind turbine load validation in wakes using wind field reconstruction techniques and nacelle lidar wind retrievals, Wind Energy Science, 6, 841–866, https://doi.org/10.5194/wes-6-841-2021, 2021.

Dimitrov, N. and Natarajan, A.: Application of simulated lidar scanning patterns to constrained Gaussian turbulence fields for load validation, Wind Energy, 20, 79–95, https://doi.org/10.1002/we.1992, 2017.

Dong, L., Lio, W. H., and Simley, E.: On turbulence models and lidar measurements for wind turbine control, Wind Energy Science, 6,
420   1491–1500, https://doi.org/10.5194/wes-6-1491-2021, 2021.

Eberhard, W. L., Cupp, R. E., and Healy, K. R.: Doppler lidar measurement of profiles of turbulence and momentum flux, Journal of Atmospheric and Oceanic Technology, 6, 809–819, https://doi.org/10.1175/1520-0426(1989)006<0809:DLMOPO>2.0.CO;2, 1989.

Fu, W., Peña, A., and Mann, J.: Turbulence statistics from three different nacelle lidars, Wind Energy Science, 7, 831–848, https://doi.org/10.5194/wes-7-831-2022, 2022a.

425   Fu, W., Sebastiani, A., Peña, A., and Mann, J.: Influence of nacelle-lidar scanning patterns on inflow turbulence characterization, Journal of Physics: Conference Series, 2265, 022 016, https://doi.org/10.1088/1742-6596/2265/2/022016, 2022b.

Gottschall, J. and Peinke, J.: How to improve the estimation of power curves for wind turbines, Environ. Res. Lett, 3, 15 005–7, https://doi.org/10.1088/1748-9326/3/1/015005, 2008.

Harris, M., Hand, M., and Wright, A.: Lidar for turbine control, National Renewable Energy Laboratory, Golden, CO, Report No. NREL/TP-
430   500-39154, https://www.nrel.gov/docs/fy06osti/39154.pdf, 2006.

Held, D. P. and Mann, J.: Comparison of methods to derive radial wind speed from a continuous-wave coherent lidar Doppler spectrum, Atmospheric Measurement Techniques, 11, 6339–6350, https://doi.org/10.5194/amt-11-6339-2018, 2018.

IEC: IEC 61400-1. Wind turbines – Part 1: design guidelines, International standard, International Electrotechnical Commission, Geneva, Switzerland, https://standards.iteh.ai/catalog/standards/sist/3454e370-7ef2-468e-a074-7a5c1c6cb693/iec-61400-1-2019, 2019.

435   Kumer, V.-M., Reuder, J., Dorninger, M., Zauner, R., and Grubišić, V.: Turbulent kinetic energy estimates from profiling wind LiDAR measurements and their potential for wind energy applications, Renewable Energy, 99, 898–910, https://doi.org/10.1016/j.renene.2016.07.014, 2016.

Liu, L., Hu, F., Cheng, X. L., and Song, L. L.: Probability density functions of velocity increments in the atmospheric boundary layer, Boundary-Layer Meteorology, 134, 243–255, https://doi.org/10.1007/S10546-009-9441-Z/METRICS, 2010.

440   Mann, J.: The spatial structure of neutral atmospheric surface-layer turbulence, Journal of Fluid Mechanics, 273, 141–168, https://doi.org/10.1017/S0022112094001886, 1994.

Mann, J., Peña, A., Bingöl, F., Wagner, R., and Courtney, M. S.: Lidar scanning of momentum flux in and above the surface layer, Journal of Atmospheric and Oceanic Technology, 27, 959–976, https://doi.org/10.1175/2010JTECHA1389.1, 2010.

Mann, J., Penã, A., Troldborg, N., and Andersen, S. J.: How does turbulence change approaching a rotor?, Wind Energy Science, 3, 293–300,
445   https://doi.org/10.5194/wes-3-293-2018, 2018.

Meyer Forsting, A. R., Troldborg, N., and Borraccino, A.: Modelling lidar volume-averaging and its significance to wind turbine wake measurements, Journal of Physics: Conference Series, 854, 012 014, https://doi.org/10.1088/1742-6596/854/1/012014, 2017.

Mikkelsen, T., Angelou, N., Hansen, K., Sjöholm, M., Harris, M., Slinger, C., Hadley, P., Scullion, R., Ellis, G., and Vives, G.: A spinner-integrated wind lidar for enhanced wind turbine control, Wind Energy, 16, 625–643, https://doi.org/10.1002/we.1564, 2013.

450 Newman, J. F., Klein, P. M., Wharton, S., Sathe, A., Bonin, T. A., Chilson, P. B., and Muschinski, A.: Evaluation of three lidar scanning strategies for turbulence measurements, Atmospheric Measurement Techniques, 9, 1993–2013, https://doi.org/10.5194/amt-9-1993-2016, 2016.

Peña, A., Hasager, C., Bay, Badger, M., Barthelmie, R. J., Bingöl, F., Cariou, J.-P., Emeis, S., Frandsen, S., Tronaes, Harris, M., and Karagali, I.: Remote Sensing for Wind Energy, DTU Wind Energy, 2015.

455 Peña, A., Floors, R., Sathe, A., Gryning, S. E., Wagner, R., Courtney, M. S., Larsén, X. G., Hahmann, A. N., and Hasager, C. B.: Ten Years of Boundary-Layer and Wind-Power Meteorology at Høvsøre, Denmark, Boundary-Layer Meteorology, 158, 1–26, https://doi.org/10.1007/s10546-015-0079-8, 2016.

Peña, A., Mann, J., and Dimitrov, N.: Turbulence characterization from a forward-looking nacelle lidar, Wind Energy Science, 2, 133–152, https://doi.org/10.5194/wes-2-133-2017, 2017.

460 Peña, A., Mann, J., and Thorsen, G.: SpinnerLidar measurements for the CCAV52, Tech. Rep. DTU Wind Energy E Vol. 0177, DTU Wind Energy, 2019.

Petersen, J. T., Kretz, A., and Mann, J.: Influence of transversal turbulence on lifetime predictions for a HAWT, in: Contributions from the Department of Meteorology and Wind Energy to the EWEC'94 Conference in Thessaloniki, Greece, p. 72, 1994.

Sathe, A. and Mann, J.: A review of turbulence measurements using ground-based wind lidars, Atmospheric Measurement Techniques, 6, 465 3147–3167, https://doi.org/10.5194/amt-6-3147-2013, 2013.

Sathe, A., Mann, J., Gottschall, J., and Courtney, M. S.: Can wind lidars measure turbulence?, Journal of Atmospheric and Oceanic Technology, 28, 853–868, https://doi.org/10.1175/JTECH-D-10-05004.1, 2011.

Sathe, A., Mann, J., Vasiljevic, N., and Lea, G.: A six-beam method to measure turbulence statistics using ground-based wind lidars, Atmospheric Measurement Techniques, 8, 729–740, https://doi.org/10.5194/amt-8-729-2015, 2015.

470 Schlipf, D., Fürst, H., Raach, S., and Haizmann, F.: Systems Engineering for Lidar-Assisted Control: A Sequential Approach, Journal of Physics: Conference Series, 1102, 012 014, https://doi.org/10.1088/1742-6596/1102/1/012014, 2018.

Schottler, J., Reinke, N., Hölling, A., Whale, J., Peinke, J., and Hölling, M.: On the impact of non-Gaussian wind statistics on wind turbines – an experimental approach, Wind Energy Science, 2, 1–13, https://doi.org/10.5194/wes-2-1-2017, 2017.

Simley, E., Fürst, H., Haizmann, F., and Schlipf, D.: Optimizing lidars for wind turbine control applications-Results from the IEA Wind Task 475 32 workshop, Remote Sensing, 10, https://doi.org/10.3390/rs10060863, 2018.

Smalikho, I. N. and Banakh, V. A.: Measurements of wind turbulence parameters by a conically scanning coherent Doppler lidar in the atmospheric boundary layer, Atmospheric Measurement Techniques, 10, 4191–4208, https://doi.org/10.5194/amt-10-4191-2017, 2017.

Sonnenschein, C. M. and Horrigan, F. A.: Signal-to-noise relationships for coaxial systems that heterodyne backscatter from the atmosphere, Applied Optics, 10, 1600–1604, https://doi.org/10.1364/AO.10.001600, 1971.

480 Syed, A. H., Mann, J., Platis, A., and Bange, J.: Turbulence structures and entrainment length scales in large offshore wind farms, Wind Energy Science, 8, 125–139, https://doi.org/10.5194/WES-8-125-2023, 2023.

Taylor, G. I.: The spectrum of turbulence, Proceedings of the Royal Society of London. Series A - Mathematical and Physical Sciences, 164, 476–490, https://doi.org/10.1098/rspa.1938.0032, 1938.

Wagner, R., Pedersen, T. F., Courtney, M., Antoniou, I., Davoust, S., and Rivera, R. L.: Power curve measurement with a nacelle mounted
    lidar, Wind Energy, 17, 1441–1453, https://doi.org/10.1002/we.1643, 2014.

Wagner, R., Courtney, M., Pedersen, T. F., and Davoust, S.: Uncertainty of power curve measurement with a two-beam nacelle mounted lidar,
    Wind Energy, 19, 1269–1287, https://doi.org/10.1002/we.1897, 2015.

Wyngaard, J.: Turbulence in the Atmosphere, Cambridge University Press, 2010.

485

A.4 Feedforward control for a 15-MW wind turbine using a spinner-mounted single-beam lidar

Fu, W., Guo, F., Schlipf, D., and Peña, A.: Feedforward control for a 15-MW wind turbine using a spinner-mounted single-beam lidar.

This manuscript is under review in the journal Applied Energy.

Feedforward pitch control for a 15-MW wind turbine using a spinner-mounted single-beam lidar

Wei Fu[1], Feng Guo[2], David Schlipf[2], and Alfredo Peña[1]

[1]Department of Wind and Energy Systems, Technical University of Denmark, Frederiksborgvej 399, 4000 Roskilde, Denmark
[2]Wind Energy Technology Institute, Flensburg University of Applied Sciences, Kanzleistraße 91-93, 24943 Flensburg, Germany

Correspondence: Wei Fu (weif@dtu.dk)

Abstract. Feedforward blade pitch control is one of the most promising lidar-assisted control strategies due to its significant improvement in rotor speed regulation and fatigue load reduction. A high-quality preview of the rotor-effective wind speed is a key element to control benefits. In this work, a single-beam continuous-wave or a pulsed lidar system is simulated in the spinner of a bottom-fixed IEA 15 MW wind turbine. The single-beam lidar can rotate with the wind turbine rotor and scan the

5   inflow with a circular pattern, which mimics a multiple-beam nacelle lidar at a lower cost. Also, the spinner-based lidar has an unimpeded view of the inflow without intermittent blockage from the rotating blade. The focus distance and the cone angle of the spinner-based single-beam lidar are optimized for the best wind preview quality based on a rotor-effective wind speed coherence model. Then, the control benefits of using the optimized spinner-based lidar are evaluated for an above-rated wind speed in OpenFAST with an embedded lidar simulator and virtual four-dimensional Mann turbulence fields considering the

10   wind evolution. Results are compared against those from a single-beam nacelle-based lidar. Furthermore, this work attempts to study the correlations between the fatigue loads of the tower and blades with different turbulence parameters. The optimum scanning configurations of both CW and pulsed lidars lead to a lidar scan radius of 0.6 of the rotor radius. Results show that a single-beam lidar mounted in the spinner brings much more control benefits than the one based on the nacelle, and it can be as helpful as a 4-beam CW nacelle lidar for feedforward control.

15   ## 1 Introduction

In the past decade, lidar-assisted wind turbine control (LAC) is of growing interest in the wind energy community. Among different control strategies, blade pitch feedforward control is one of the most promising LAC techniques, due to the significant improvement in the regulation of the rotor speed and the reduction of the fatigue loads (Canet et al., 2021). Whereas the conventional feedback controller reacts to the wind disturbance after the effect of turbulent wind on the structure has occurred,

20   the feedforward controller is able to utilize the preview information of the approaching wind provided by, e.g., lidars, which helps the turbine to react in advance. The collective pitch control, in which the blades are controlled all together, uses the rotor-effective wind speed (REWS) as a key input to the feedforward controller.

    In 2022, the installed prototype of the world's biggest wind turbine had a rated power of 15 MW. It has reached over 200 m in height and the rotor-swept area is equivalent to four soccer fields (Venditti, 2022). The inflow to wind turbines of such size

cannot be measured by anemometers installed on a meteorological mast. As remote sensing devices, forward-looking lidars mounted on the nacelle or the spinner of the wind turbines have a better sight of the wind approaching the rotor, and they can provide a high-quality wind preview. They are aligned with the wind turbine rotor and always track the incoming wind. Also, nacelle lidars can measure the inflow remotely at different locations over the rotor-swept area. The REWS estimated from a lidar system by combining the radial measurements over a full scan might more closely resemble the true REWS, which is the spatial average of the longitudinal wind velocities across the rotor disk (Schlipf et al., 2015a), than a point-wise anemometer. Therefore, they have the potential to deliver inflow characteristics that are better correlated with turbine signals (rotor speed, fatigue loads, etc.) than those derived from point-wise anemometers, e.g., cup and sonic anemometers.

Two types of nacelle lidar systems have been tested for wind turbine control, namely the continuous-wave (CW) and pulsed systems. The CW lidars usually measure at one range gate at a time with adjustable focus distance at a high sampling rate. Pulsed lidars are able to collect backscattered signals from several range gates according to the response time, but they require typically long sampling periods. Both lidars have been reported useful for LAC (Mikkelsen et al., 2013; Kumar et al., 2015). Schlipf et al. (2014) found a decrease in the rotor speed variation during the above-rated operation of the CART2 using feedforward pitch control and a circularly-scanning pulsed lidar. Scholbrock et al. (2013) showed the mitigation on tower fore-aft loads using measurements from a three-beam pulsed lidar for the feedforward controller on the CART3. Scholbrock et al. (2015) achieved a reduction in yaw error using the circularly-scanning CW lidar replacing the turbine-based wind vane, etc. Although many other relevant studies are based on aero-elastic simulations (Harris et al., 2006a; Bossanyi et al., 2012; Simley et al., 2014), the results from the above experiments demonstrate control improvements when using LAC (Simley et al., 2018).

The benefit of LAC needs to be balanced with the investment in using nacelle lidars. The simplest basic option is a single-beam staring lidar system. It is also robust and flexible. As the first field test of a nacelle-mounted lidar, Harris et al. (2006b) demonstrated that a single-beam CW lidar measuring at hub height is able to detect the fluctuations of the longitudinal velocity at 200 m upstream of a Nordex N90 wind turbine. Nevertheless, the measurement at a single location is not a good representative of the REWS interacting with the turbine rotor.

Compared to the staring lidar mounted on the wind turbine nacelle, the single-beam lidar in the spinner can rotate with the rotor during turbine operation, scan a good portion of the inflow coming to the rotor disk, and reduce the cost of nacelle lidars relying on complex scanning patterns. Another advantage of using a spinner-based lidar, over a nacelle-mounted system, is the unimpeded view of the inflow without intermittent signal blockage by the blades, which increases data availability. A proof-of-concept field experiment was conducted by Mikkelsen et al. (2013), in which a ZephIR single-beam lidar system was deployed in the spinner of a NM80 2.3 MW wind turbine. They showed that the system is capable of measuring the upcoming wind and turbulence structure in real time. Based on a simulation study of the spinner-based CW lidar on the NREL 5 MW wind turbine, Simley et al. (2014) examined the accuracy of different measurement scenarios and found a minimum root-mean-square error of the along-wind component at a scan radius of 75% blade span, while at 69% blade span the lidar provides lowest blade-effective wind speed error.

This work aims at demonstrating the usefulness of a single-beam lidar for wind turbine feedforward control if the lidar is mounted in the spinner compared to a nacelle-based system. Our reference wind turbine is the bottom-fixed variable-speed

collective-pitch-controlled IEA 15-MW turbine (design class 1B) with a rotor diameter of 240 m and a hub height of 150 m (National Renewable Energy Laboratory, 2020). We consider both continuous-wave and pulsed Doppler lidars. Based on the four-dimensional (4D) Mann turbulence model that considers wind evolution (Guo et al., 2022a), we optimize the focus distance and the cone angle of the spinner-mounted single-beam lidar to achieve the highest coherence between the rotor- and the lidar-estimated REWS. Then, through time-domain simulations using the 4D Mann turbulence fields with typical turbulence parameters of near-neutral atmospheric stability conditions, the performance of the feedforward control using the optimized lidar is evaluated. The ROSCO controller (Abbas et al., 2022) is used as the reference feedback controller. The simulations are conducted in the open-source aero-elastic tool OpenFAST (National Renewable Energy Laboratory, 2022), and the results are compared against those using a single-beam nacelle-based lidar.

This paper is organized as follows. Section 2 describes the background for this work including the turbulence spectral model, the modeling of the wind evolution, the spinner-based lidar, and the wind preview quality. Section 3 introduces the set-up of time-domain simulations. Section 4 shows the results of the lidar configuration optimization, which is followed by Section 5, where we evaluate the performance of the feedforward control. Discussions are given in Section 6. Section 7 concludes the work and provides the outlook.

2 Background

2.1 Mann turbulence spectral model

The three-dimensional wind field can be described by a vector field $\boldsymbol{u}(\boldsymbol{x}, t_0) = (u, v, w) = (u_1, u_2, u_3)$ at a given time t_0, where u, v, w are the horizontal along-wind, the horizontal lateral and the vertical wind components, respectively. The vector $\boldsymbol{x} = (x, y, z)$ is the position vector defined in the right-handed Cartesian coordinate system. Using Reynolds decomposition, the wind field can be decomposed into the mean wind speed $\boldsymbol{U} = \langle \boldsymbol{u}(x, 0, 0) \rangle = (U, 0, 0)$, where $\langle \ \rangle$ denotes ensemble averaging, and the fluctuating parts (u', v', w'). Assuming Taylor's frozen hypothesis (Taylor, 1938), the velocity fluctuations do not propagate with time. Therefore, the wind field after a given time Δt can be derived as

$$\boldsymbol{u}(x, y, z, t_0 + \Delta t) = \boldsymbol{u}(x - U\Delta t, y, z, t_0). \tag{1}$$

The wind field can also be expressed in the wavenumber domain using the three-dimensional Fourier transform

$$\boldsymbol{u}(\boldsymbol{k}, t_0) = \frac{1}{(2\pi)^3} \int \boldsymbol{u}(\boldsymbol{x}, t_0) \exp(-i\boldsymbol{k} \cdot \boldsymbol{x}) d\boldsymbol{x}, \tag{2}$$

where $\boldsymbol{k} = (k_1, k_2, k_3)$ and $\int d\boldsymbol{x} \equiv \int_{-\infty}^{\infty} \int_{-\infty}^{\infty} \int_{-\infty}^{\infty} dx dy dz$. Denoting complex conjugate by * and the three velocity components by indices $i, j = 1, 2, 3$, the ensemble average of the Fourier coefficients is the spectral velocity tensor:

$$\langle u_i^*(\boldsymbol{k}, t_0) u_j(\boldsymbol{k'}, t_0) \rangle = \Phi_{ij}(\boldsymbol{k}) \delta(\boldsymbol{k} - \boldsymbol{k'}). \tag{3}$$

With the Dirac delta function $\delta(.)$, Eq. (3) implies the homogeneity of the stochastic wind field, i.e., $\langle u_i^*(\boldsymbol{k}) u_j(\boldsymbol{k'}) \rangle$ is zero for $\boldsymbol{k} \neq \boldsymbol{k'}$. Here, we assume that the spectral tensor $\Phi_{ij}(\boldsymbol{k})$ can be described by the Mann model (Mann, 1994), in which,

besides the wave number k, three adjustable parameters are used: $\alpha\varepsilon^{2/3}$, where α is the spectral Kolmogorov constant and ε the turbulent energy dissipation rate, L, which is a length scale describing the size of the most energy-containing eddies, and Γ, which represents the turbulence anisotropy and distortion of the eddies from the vertical velocity shear in the atmospheric surface layer. The characteristics of the Mann model permit the modeling of three-dimensional spectra and coherence. The model is also recommended by the IEC 61400-1 standard IEC (2019) for the calculation of wind turbine loads.

2.2 Temporal evolution of turbulence

Turbulence structures evolve when they approach the rotor. To consider the temporal evolution of turbulence, we assume that the stochastic field travels with the mean wind speed U in the along-wind direction. However, we assume the turbulent eddies decay exponentially with time. The spectral velocity tensor Φ_{ij} then becomes space-time tensor Θ_{ij} (Guo et al., 2022a)

$$\Theta_{ij}(\boldsymbol{k}, \Delta t) = \exp\left(\frac{-\Delta t}{\tau_e(\boldsymbol{k})}\right)\Phi_{ij}(\boldsymbol{k}), \tag{4}$$

with

$$\langle u_i^*(\boldsymbol{k}, t_0)u_j(\boldsymbol{k'}, t_0 + \Delta t)\rangle = \Theta_{ij}(\boldsymbol{k}, \Delta t)\delta(\boldsymbol{k} - \boldsymbol{k'}), \tag{5}$$

where τ_e is a new eddy lifetime that considers the temporal evolution. We also assume this eddy lifetime as in (Guo et al., 2022a)

$$\tau_e(\boldsymbol{k}) = \gamma\left[a(|\boldsymbol{k}|L)^{-1}\left((|\boldsymbol{k}|L)^{10} + 1\right)^{-\frac{2}{15}}\right], \tag{6}$$

where γ is a coefficient that determines the strength of turbulence evolution. Guo et al. (2022a) and Guo et al. (2023) considered $\gamma \approx 400$ for near-neutral atmospheric stability conditions, and $\gamma \approx 200$ for stable atmospheric conditions.

The one-dimensional cross-spectra of all velocity fluctuations with separations Δy and Δz that consider evolution is then

$$F_{ij}(k_1, \Delta t, \Delta y, \Delta z) = \int \Theta_{ij}(\boldsymbol{k}, \Delta t)\exp(\mathrm{i}(k_2\Delta y + k_3\Delta z))\mathrm{d}\boldsymbol{k}_\perp, \tag{7}$$

where $\int \mathrm{d}\boldsymbol{k}_\perp \equiv \int_{-\infty}^{\infty}\int_{-\infty}^{\infty}\mathrm{d}k_2\mathrm{d}k_3$. The one-point cross-spectra and auto-spectra of the velocity components can be obtained when the separations Δy and Δz are zero, and $i = j$ in Eq. (7). The magnitude squared coherence of all velocity components is

$$\mathrm{coh}_{ij}^2(k_1, \Delta t, \Delta y, \Delta z) = \frac{|F_{ij}(k_1, \Delta t, \Delta y, \Delta z)|^2}{F_{ii}(k_1, \Delta t = 0)F_{jj}(k_1, \Delta t = 0)}, \tag{8}$$

where

$$F_{ii}(k_1, \Delta t = 0) = \int \Phi_{ii}(\boldsymbol{k})\mathrm{d}\boldsymbol{k}_\perp. \tag{9}$$

2.3 Spinner-mounted single-beam lidar

A single-beam lidar system mounted in the wind turbine spinner is simulated. With an angle between the beam and the turbine's horizontal axis, the spinner-based lidar is able to scan the inflow in a circular pattern without signal blockage from the turbine

blades or the nacelle, which is otherwise an issue in nacelle-mounted lidars. The beam orientation $\boldsymbol{n}$ can be expressed as

$$\boldsymbol{n}(\phi,\theta) = (n_1, n_2, n_3) = (-\cos\phi, \cos\theta\sin\phi, \sin\theta\sin\phi), \tag{10}$$

where ϕ is the half-cone opening angle, θ is the angle between the y-axis and the beam direction projected on the y-z plane. The beam unit vector can also be expressed with the beam azimuth α and elevation angle β, which is used in the OpenFAST lidar simulator (Guo et al., 2022b)

$$\boldsymbol{n}(\alpha,\beta) = (-\cos\alpha\cos\beta, \sin\alpha\cos\beta, \sin\beta). \tag{11}$$

The four angles are marked in Figure 1. The rotor shaft of the reference wind turbine has a tilt angle of $6°$. Therefore, the lidar beam unit vector is rotated around the y-axis. The red circles in Figure 1 indicate the scanning locations of the single-beam lidar before the rotation around the y-axis.
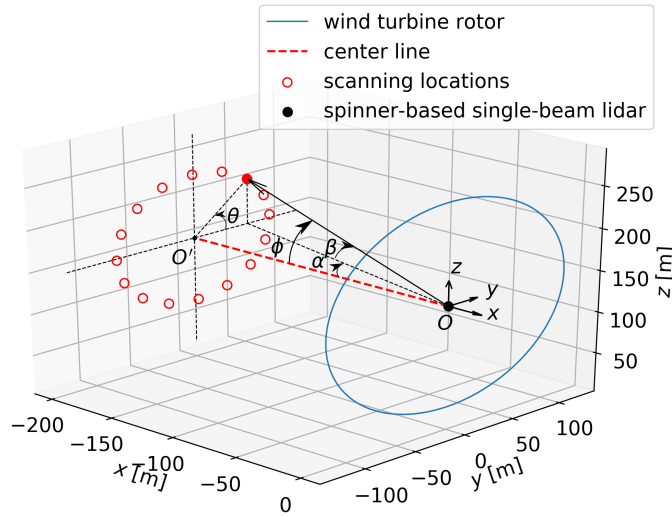

Figure 1. Scanning trajectory of the single-beam lidar in the spinner of the IEA 15-MW wind turbine. The used lidar angles are marked.

Since the typical feedforward collective pitch controller is active beyond rated wind speeds only, the rotational speed of the wind turbine has reached its rated value. For the reference wind turbine, the rated wind speed is $v_R = 10.59$ ms^{-1} and the rated rotor speed is $\Omega_R = 7.56$ rpm. The turbine is controlled to maintain its rotor speed close to the rated value. Therefore, the single-beam lidar needs ≈ 8 s to complete a full scan. Assuming that the rotor speed is almost constant and the beam scanning locations are fixed with a sampling frequency $f_s = 4$ Hz, the spinner-based lidar can measure 32 radial velocities in one circular scan. Therefore, θ can be modelled as

$$\theta = \frac{2\pi}{60}\Omega_R i/f_s, \tag{12}$$

where $i = 1, 2, ..., 32$ is the beam index.

5

Assuming that the dominant radial velocity v_r in the Doppler spectrum of radial velocities within the probe volume can be determined by the centroid method (Held and Mann, 2018; Fu et al., 2022), v_r is the convolution of the lidar weighting function due to its probe volume $\varphi(s)$ and the wind components along the beam

$$v_r(\phi, \theta) = \int\limits_{-\infty}^{\infty} \varphi(s)\boldsymbol{n}(\phi, \theta) \cdot \boldsymbol{u}[\boldsymbol{n}(\phi, \theta)(f_d + s)]\mathrm{d}s. \tag{13}$$

The weighting function of a CW lidar system is approximated by a Lorentzian function (Sonnenschein and Horrigan, 1971)

$$\varphi(s) = \frac{1}{\pi}\frac{z_R}{z_R^2 + s^2}, \text{ and its Fourier transform is } \hat{\varphi}(\boldsymbol{k}, \boldsymbol{n}) = \exp(-|\boldsymbol{k} \cdot \boldsymbol{n}|z_R) \quad \text{with } z_R = \frac{\lambda f_d^2}{\pi r_b^2}, \tag{14}$$

where s is the distance to the beam focus and z_R is the Rayleigh length determined by the focus distance f_d, the laser wavelength λ, and the transmitted beam radius at the exit of the optical lens r_b. For pulsed systems, we assume the weighting function has a Gaussian-shape parameterized by a standard deviation σ_L (Cariou, 2013)

$$\varphi(s) = \frac{1}{\sigma_L\sqrt{2\pi}}\exp\left(-\frac{s^2}{2\sigma_L^2}\right), \text{ and its Fourier transform is } \hat{\varphi}(\boldsymbol{k}, \boldsymbol{n}) = |\boldsymbol{k} \cdot \boldsymbol{n}|\exp\left(-|\boldsymbol{k} \cdot \boldsymbol{n}|^2\frac{\sigma_L^2}{2}\right) \quad \text{with } \sigma_L = \frac{W_L}{2\sqrt{2\ln 2}}, \tag{15}$$

where W_L is the Full-Width at Half Maximum (FWHM). The probe volume of CW lidars increases with the square of the focus distance, whereas it is constant at any range for pulsed systems. In our study, we assume $\lambda = 1.565~\mu$m, $r_b = 28$ mm and $W_L = 30$ m (Peña et al., 2016).

The weighting functions need to be truncated to simulate lidar measurements in turbulence boxes of finite length. We discretize Eq. (14) with a resolution of $\Delta s = 0.1z_R$ and consider $s_{max} = 6z_R$ and $s_{min} = -6z_R$. Similarly, we use $s_{max} = 1.5W_L$ and $s_{min} = -1.5W_L$ with a resolution of $\Delta s = 2.5$ m ($\approx 0.08W_L$) for Eq. (15). The discretized weights are normalized to have the sum one. Since $W_L = 2z_R$, the pulsed lidar probe volume is more compact and centralized than that of the CW. Figure 2 compares the truncated theoretical weighting functions of the two lidar systems measuring at different ranges. To illustrate the two types of weighting functions, the weights in Figure 2 are normalized by the maximum values. In our case, the pulsed lidar has a similar FWHM with the CW lidar focusing at 155 m.

The amount of truncation needs to be balanced between a realistic probe volume and the limited size of the virtual wind fields. The truncation and discretization influence the amount of the turbulence attenuation by the probe volume. However, the small turbulent eddies do not greatly impact the coherence of the REWS, since the spatial averaging by the rotor disk has a similar filtering effect on the true REWS.

2.4 Lidar wind preview quality

2.4.1 Rotor-effective wind speed from the wind turbine

If the yaw misalignment is neglected, the true REWS is the spatial average of the longitudinal velocities u across the rotor-swept area defined by the rotor radius R (Schlipf et al., 2015a):

$$u_{RR}(x) = \frac{1}{\pi R^2}\iint\limits_{\text{rotor}} u(\boldsymbol{x})\mathrm{d}y\mathrm{d}z. \tag{16}$$
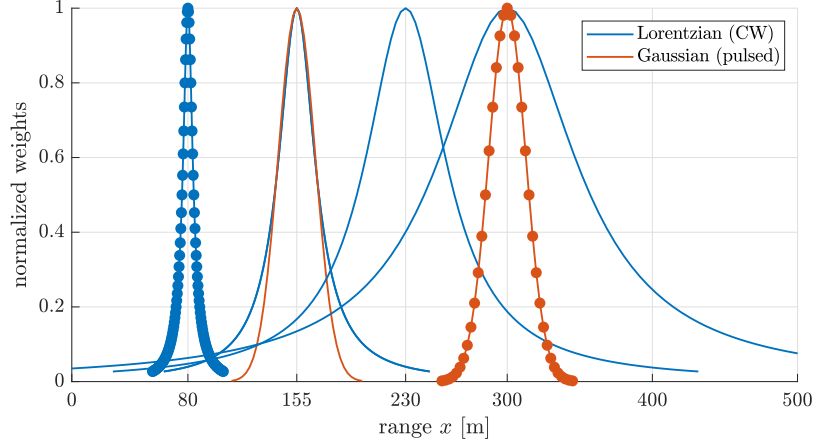
Figure 2. Weighting functions of the CW lidar measuring at 80 m, 155 m, 230 m, 300 m and the one of the pulsed lidar measuring at 155 m, 300 m. The weights are normalized by the maximum values for illustration purposes. The blue and red markers indicate the discretization of the functions.

Held and Mann (2019) demonstrated that this REWS can be rewritten as

$$u_{\mathrm{RR}}(x) = \int u(\boldsymbol{k})e^{ik_1 x_1} \frac{2J_1(\kappa R)}{\kappa R} \mathrm{d}\boldsymbol{k}, \tag{17}$$

where $\kappa = \sqrt{k_2^2 + k_3^2}$ and J_1 is the Bessel function of the first kind. Held and Mann (2019) also showed that the auto-spectrum of u_{RR} is

$$S_{\mathrm{RR}}(k_1) = \int\limits_{-\infty}^{\infty} \Phi_{11}(\boldsymbol{k}) \frac{4J_1^2(\kappa R)}{\kappa^2 R^2} \mathrm{d}\boldsymbol{k}_\perp. \tag{18}$$

2.4.2 Rotor-effective wind speed estimated by the lidar

Assuming that the turbine yaw misalignment is negligible, the center line of the lidar scanning trajectory is well aligned with the turbine rotation axis, and v and w are considered to be zero, the u component can be estimated directly from the radial velocity. The lidar-estimated REWS is the mean of the along-wind component retrieved from the radial velocities:

$$u_{\mathrm{LL}}(t) = \sum_{i=1}^{N_b} \frac{1}{N_b n_{i1}} v_{\mathrm{r},i}(t), \tag{19}$$

where N_b is the number of measurements over a full scan and n_{i1} is the first element in the unit vector of the ith measurement.

Because the longitudinal wind evolution is the most important factor for control, and the considered lidars in this work only measure at a single plane, the wind evolution between each measurement in a full scan is not considered, which should have only a marginal effect on our optimization. The auto-spectrum of the lidar-estimated REWS is (Guo et al., 2022a)

$$S_{\mathrm{LL}}(k_1) = \sum_{i,j=1}^{N_b} \sum_{l,m=1}^{3} \frac{1}{N_b^2 n_{i1} n_{j1}} \int n_{il} n_{jm} \Phi_{lm} \exp(\mathrm{i}\boldsymbol{k}\cdot(\boldsymbol{x}_i - \boldsymbol{x}_j))\hat{\varphi}(\boldsymbol{k}\cdot\boldsymbol{n}_i)\hat{\varphi}(\boldsymbol{k}\cdot\boldsymbol{n}_j)\mathrm{d}\boldsymbol{k}_\perp, \tag{20}$$

7

where $\boldsymbol{x}_i$ denotes the position vector of the lidar measurement, n_{il} stands for the lth element in the unit vector $\boldsymbol{n}$ of the ith measurement.

For control purposes, the lidar scanning strategy is considered optimal, if it provides REWS estimates that correlate the best with the true REWS sensed by the rotor disk. Considering the turbulence evolution from lidar measurement planes to the rotor plane, the cross-spectrum between u_{RR} and u_{LL} can be expressed as (Guo et al., 2022a)

$$S_{\text{RL}}(k_1) = \sum_{i=1}^{N_b} \sum_{l=1}^{3} \frac{1}{N_b n_{i1}} \int n_{il} \Theta_{l1}(\boldsymbol{k}, \Delta t_i) \hat{\varphi}(\boldsymbol{k} \cdot \boldsymbol{n}_i) \exp(\text{i}(k_2 x_{i2} + k_3 x_{i3})) \frac{2J_1(\kappa R)}{\kappa R} \text{d}\boldsymbol{k}_\perp, \tag{21}$$

where Δt_i denotes the time needed for the turbulence field to travel from a lidar plane to the rotor plane, given a good estimation by their longitudinal separation divided by the mean along-wind speed, i.e., $\Delta t_i = |\Delta x_{iR}|/U$.

2.4.3 Rotor-effective wind speed coherence

The wind preview quality can be evaluated by the magnitude squared lidar-rotor REWS coherence (Schlipf, 2016; Simley et al., 2018)

$$\gamma_{\text{RL}}^2(k_1) = \frac{|S_{\text{RL}}(k_1)|^2}{S_{\text{RR}}(k_1) S_{\text{LL}}(k_1)}, \tag{22}$$

which is a value between 0 and 1. The measurement coherence bandwidth (MCB) is defined as the wave number $k_{0.5}$ where γ_{RL}^2 drops below 0.5. The corresponding frequency can be calculated by $f_{0.5} = k_{0.5} U/(2\pi)$. The larger the MCB, the better the wind preview quality. Therefore, maximizing the MCB is the goal of lidar trajectory optimization.

To evaluate the lidar wind preview quality, the so-called 'smallest detectable eddy size' $d_{\text{eddy,min}}$ is used by control engineers, which is the size of the eddies that can still be detectable by the lidar with the 50% coherence assuming turbulence isotropy (Schlipf et al., 2018)

$$d_{\text{eddy,min}} = \frac{2\pi}{k_{0.5}}. \tag{23}$$

The smallest detectable eddy size is inversely proportional to the MCB. To have a measure that is independent of the rotor size, the $d_{\text{eddy,min}}$ can be normalized by the rotor diameter of the reference wind turbine. A normalized $d_{\text{eddy,min}}$ close to $1D$ indicates a very good lidar for fatigue load reduction, while a value between $1.5D$ and $2D$ is satisfying.

The wind preview quality of the considered lidar configurations is directly calculated for the reference wind turbine in the frequency domain using Eqs. (18), (20) and (21) instead of using time-domain simulations, which greatly reduces the computational effort and provides a clear MCB value compared to that estimated from simulated spectra of coherence in time domain. Then, the controller performance using the optimal lidar is evaluated with time domain aero-elastic simulations using Mann turbulent wind fields with the same turbulence characteristics.

3 Time-domain simulation set-up

3.1 Simulation environment

The time-domain aero-elastic simulations are performed for the IEA 15-MW wind turbine using the open-source tool Open-FAST (National Renewable Energy Laboratory, 2022), in which a lidar simulator is embedded. Using the latest version of the OpenFAST lidar simulator (see Guo et al., 2022b, for more details), the probe volume, the turbine nacelle motion, and the turbulence evolution are included. The weighting function of the probe volume is given in discrete points as explained in Section 2.3.

The four-dimensional stochastic turbulence fields are generated by the 4D Mann turbulence generator developed by Guo et al. (2022a). The turbulence fields have model parameters $\alpha\varepsilon^{2/3} = 0.2882$ m$^{4/3}$ s^{-2}, $L = 49$ m and $\Gamma = 3.1$, which are typical of near-neutral atmospheric conditions and corresponding to the IEC class 1B with a turbulence intensity of $\approx 15\%$ at the mean wind speed of 18 ms^{-1}. The mean wind field $\boldsymbol{U} = (U_{\mathrm{ref}}, 0, 0)$ at the turbine hub height and a power law shear profile with a shear exponent of 0.14, i.e., $U(z) = U_{\mathrm{ref}}\left(\frac{z}{z_{\mathrm{HH}}}\right)^{0.14}$, is added upon the turbulence boxes, where z_{HH} is the turbine hub height. The turbulence box has dimensions of $4096\times64\times64$ grid points in the x, y, and z directions, respectively. The grid size in y and z directions are both 4.5 m to cover the whole rotor disk and the tower in the vertical direction, while the resolution in the x direction is $\Delta x = (0.5\ \mathrm{s})U_{\mathrm{ref}}$. All simulations are performed for a single wind speed of $U_{\mathrm{ref}} = 18$ ms^{-1}. The blade, tower and generator degree of freedoms (DOFs) are enabled.
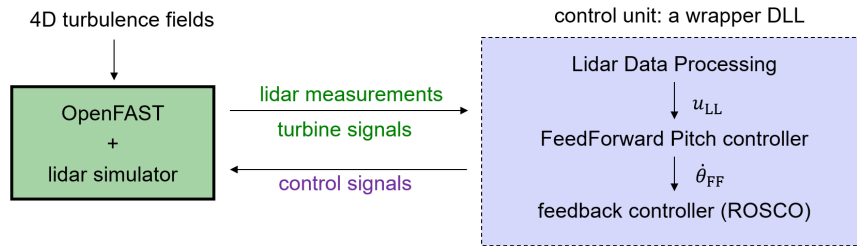

Figure 3. Structure of the communication interface between the OpenFAST and the controller dynamic-link library chain.

As illustrated in Figure 3, the turbulent wind acts as a disturbance to the turbine. The turbine-lidar unit delivers lidar radial velocities and simultaneous turbine signals (generator speed and pitch angle) to the control unit, which then sends control signals (generator torque and demanded pitch angle) back to the turbine to demand control actions. Therefore, without the feedforward controller that relies on the wind preview, the feedback controller calculates control demands based on the past turbine signals and reacts to the disturbance only after the aerodynamic impact on the turbine's structure has occurred. The feedforward controller can utilize the lidar-estimated preview information and assists the feedback controller to react in advance. Since OpenFAST can only refer to a single dynamic-link library (DLL) as the control unit, a wrapper DLL is configured to encapsulate and call the lidar data processing, feedforward pitch controller and feedback controller (ROSCO; Abbas et al.

230 2022) sequentially in order to exchange signals with OpenFAST (Guo et al., 2023). The three subunits are introduced in the following subsections.

3.2 Lidar data processing

The simulated spinner-based lidar completes a full scan in approximately 8 s with a sampling frequency of 4 Hz. Therefore, the latest 32 measurements are collected to reconstruct the REWS using Eq. (19), and the reconstructed REWS is updated every
235 0.25 s. In frequency-domain optimization, the beam scanning locations in the circular pattern are assumed to be fixed, while in time-domain simulation, the beam scanning locations depend on the rotor azimuth positions and nacelle motions in real-time.

In practice, the REWS estimated from the lidar measurements is not perfectly correlated with the real one sensed by the rotor. Therefore, a filter needs to be applied to the lidar-estimated REWS before using it for the feedforward controller to avoid unnecessary and harmful reactions from the pitch actuator. Here, a first-order Butterworth low-pass filter is applied

240 $$G_{\text{filter}}(s) = \frac{\omega_{\text{cutoff}}}{s + \omega_{\text{cutoff}}},$$ (24)

with a cutoff angular frequency $\omega_{\text{cutoff}} = 2\pi f_{\text{cutoff}} = k_{\text{cutoff}} U_{\text{ref}}$, which is calculated from the cut-off wavenumber k_{cutoff} where the theoretical REWS measurement transfer function drops at -3 dB (Schlipf, 2016; Guo et al., 2023) and s is the complex frequency. The theoretical REWS transfer function is calculated from Eqs. (21) and (20)

$$G_{\text{RL}} = \frac{|S_{\text{RL}}(f)|}{S_{\text{LL}}(f)}.$$ (25)

245 The low pass filtering usually delays a signal due to the frequency-depending phase shift. For the first-order filter, the consumed time T_{filter} is approximated by

$$T_{\text{filter}} = \frac{\arctan\left(\frac{f_{\text{delay}}}{f_{\text{cutoff}}}\right)}{2\pi f_{\text{delay}}},$$ (26)

where f_{delay} is the interested frequency (in our case 0.025 Hz), in which the simulated rotor speed spectrum by the feedback-only control has its highest energy. Therefore, the higher the cutoff frequency, the more useful information is available in the
250 lidar-estimated REWS signals, and less time is needed for filtering the signal.

3.3 Feedforward controller

The feedforward controller is designed to stabilize the rotational speed in the changing inflow wind speed by demanding an additional pitch angle θ_{FF} before the disturbance hits the rotor. In this way, the rotor speed acceleration $\dot{\Omega}$ caused by the wind speed fluctuations can be compensated by the additional pitch angle.
255 The design of the feedforward controller follows the methodology given in Schlipf (2016) and Guo et al. (2023). Considering a reduced wind turbine model with a single rotor rotation DOF:

$$J\dot{\Omega} = M_a(u_{\text{RR}}, \Omega, \theta_{\text{p}}) - M_{\text{G}}, \quad \text{with} \quad M_a = \frac{1}{2}\rho\pi R^2 \frac{c_{\text{P}(\lambda,\theta_{\text{p}})}}{\Omega} u_{\text{RR}}^3 \text{ and } \lambda = \frac{\Omega R}{u_{\text{RR}}},$$ (27)

10

where J is the rotor inertia, θ_p is the blade pitch angle, c_P is the turbine power coefficient, λ is the tip speed ratio, M_a is the aerodynamic torque and M_G is the generator torque. The aerodynamic effect on the rotational speed change can be canceled out if $M_a(u_{\mathrm{RR}}, \Omega, \theta_p) = M_G$. Therefore, by changing the pitch angle, the aerodynamic torque is adjusted to be close to the rated value of the generator torque. The feedforward pitch angle θ_{FF} should follow the static pitch curve $\theta_{\mathrm{FF}} = \theta_{p,ss}(u)$, which can be obtained by steady-state simulations with a feedback controller and the uniform and constant wind of all speeds between cut-in and cut-off, as shown in Figure 4. At the cut-in wind speed, the blades have an initial pitch angle. The pitch angle first decreases to make the best use of the incoming wind, and increases after reaching the rated wind speed of $10.59\,\mathrm{ms^{-1}}$. Thus, a feedforward pitch rate $\dot{\theta}_{\mathrm{FF}}$ can be calculated using the derivation of the static pitch curve (see Schlipf, 2016, Chapter 6.1.1 for more details), which is delivered to the integrator included in the feedback controller.
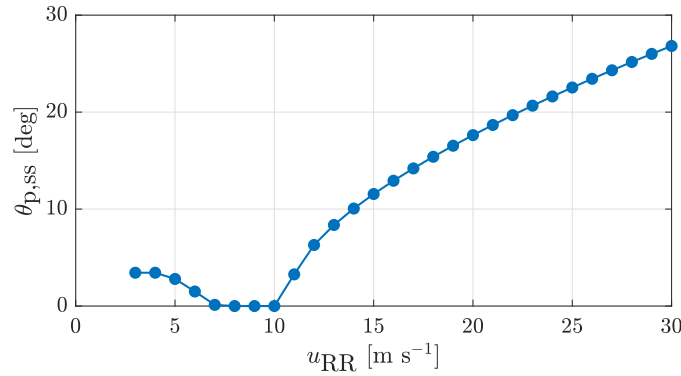

Figure 4. Static pitch curve of the bottom-fixed IEA 15-MW wind turbine performed with ROSCO in OpenFAST.

3.4 Feedback controller

The modular Reference Open-Source COntroller (ROSCO) developed by Abbas et al. (2022) for fixed and floating wind turbines is used as the feedback controller in this work. The feedback controller contains two parts: a torque controller, which mainly regulates the generator torque M_G to maximize the energy yield in below-rated wind speeds and keeps the power steady in above-rated wind speeds, and a collective blade pitch controller, which maintains the rated generator speed in the fluctuating wind by changing the blade pitch angle.

The baseline collective blade pitch controller is achieved by a proportional-integral controller described in Jonkman et al. (2009). Therefore, the calculated pitch angle is

$$\theta_{\mathrm{FB}} = k_p \Delta\Omega + K_I \int_0^t \Delta\Omega \, \mathrm{d}t, \tag{28}$$

where k_p is the proportional gain, K_I the integral gain, $\Delta\Omega = \Omega_{\mathrm{G,rated}} - \Omega_G$ the difference between the contemporary generator speed and its rated value, and s the complex frequency. The default values of the feedback controller gains are used in this study.

The integral block of the feedback controller uses the feedforward pitch rate $\dot\theta$ passed by the feedforward controller. This gives the total demanded pitch angle θ_c as

$$\theta_c = \theta_{\text{FB}} + \int_0^t \dot\theta_{\text{FF}} \, \mathrm{d}t. \tag{29}$$

Then, the pitch actuator moves the blades according to the demanded pitch angle. The pitch actuator is modelled as a second-order damper system with the cut-off frequency of $1.5708 \, \mathrm{rad \, s^{-1}}$ and the damping ratio of 0.707 (Abbas et al., 2022), so the pitch actuation takes $T_{\text{pitch}} \approx 0.9 \, \mathrm{s}$ for frequencies lower than $0.04 \, \mathrm{Hz}$ for the reference wind turbine.

3.5 Buffer time of REWS signal

To synchronize the pitch actuation with the REWS interacting with the turbine, the preview signal is usually buffered with a suitable time T_{buffer}. T_{buffer} contains the advection time of the wind field from the lidar measurement plane to the rotor plane $T_{\text{lead}} = \frac{\Delta x}{U_{\text{ref}}}$, the averaging time of the lidar raw measurement (half of a full scan time T_{scan}), the time consumed by the low-pass filter T_{filter}, and the pitch actuator delay T_{pitch} (Schlipf, 2016):

$$T_{\text{buffer}} = T_{\text{lead}} - \frac{1}{2}T_{\text{scan}} - T_{\text{filter}} - T_{\text{pitch}}. \tag{30}$$

To ensure the controllers have enough time to react to the wind disturbance before the wind hits the rotor, T_{buffer} has to be larger than zero. Since T_{lead} and T_{filter} are influenced by the lidar scanning trajectory, $T_{\text{buffer}} > 0 \, \mathrm{s}$ is a constraint to select the optimal configuration.

4 Optimization of lidar configuration for wind preview quality

The measurement range along the x-direction and the half-cone opening angle ϕ of the spinner-based single-beam lidar is optimized. The focus distance can be calculated from the measurement range by $f_\mathrm{d} = x/\cos\phi$. The optimization is done in the frequency domain based on the coherence model given in Section 2.4. The lidar configuration is considered to be optimal when the highest MCB (also written as $k_{0.5}$) is achieved. In our optimization, only a single measurement range is considered for both CW and pulsed lidars.

The optimization is done at a mean wind speed of $18 \, \mathrm{ms^{-1}}$. With the same turbulence characteristics, the mean wind speed value does not affect much the optimization results, only slightly the general level of wind evolution (Guo et al., 2023). As shown in Figure 5(a) and (c), both CW and pulsed spinner-based lidars can achieve a maximum $k_{0.5}$ more than $0.014 \, \mathrm{m^{-1}}$ corresponding to a $d_{\text{eddy,min}}$ smaller than $1.87D$, while the nacelle-based single-beam lidar achieves only approximately $0.005 \, \mathrm{m^{-1}}$ (the single-point measurements provide $k_{0.5}$ that are almost constant but slightly reduce with further measurement ranges). The best scanning configurations of CW and pulsed lidars are different, but the best range-opening angle combinations both result in a scan radius at approximately $72 \, \mathrm{m}$ $(0.6R)$ (see Figure 5(b) and (d)). Due to the rotor shaft tilt angle, the lidar scanning area is at the middle-top part of the rotor plane. Also, the results indicate that the CW lidar gives better REWS coherence
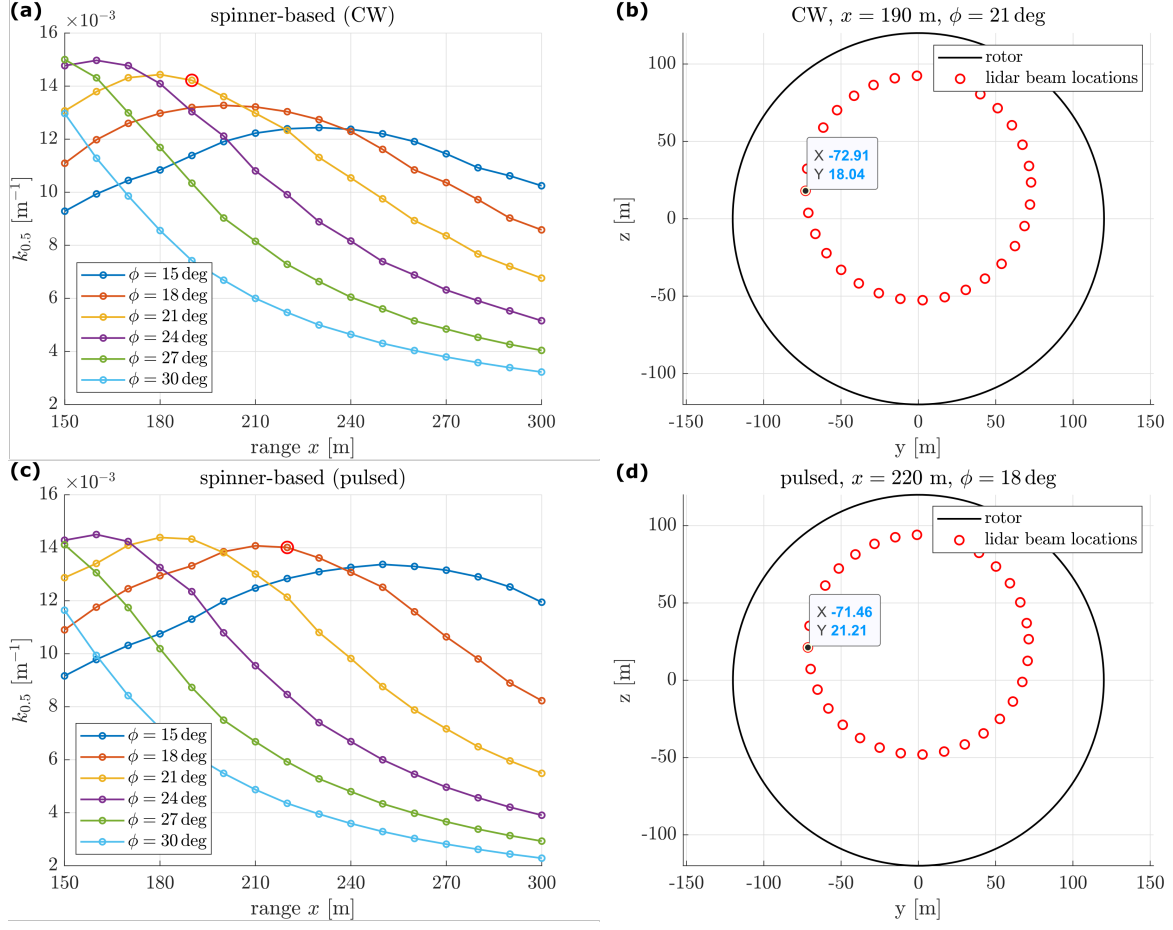
Figure 5. Left: optimization of the range x and half-cone opening angle ϕ of the spinner-based lidar based on coherence model. The selected optimum configurations at a mean wind speed of $18 \, \mathrm{ms}^{-1}$ are marked in a red circle. Right: The scanning pattern of the selected optimum configurations.

when it measures closer to the rotor with a wider angle compared to the pulsed lidar. This is expected since the probe volume filtering effect becomes more influential for CW lidars the further the measurement range. However, when measuring at $190 \, \mathrm{m}$ and $\phi = 21°$ with a CW lidar, the filtered REWS signal has a very short buffer time ($0.7 \, \mathrm{s}$); this distance will be too close for controllers to react if the wind speed is higher than $19 \, \mathrm{ms}^{-1}$. Although measuring at $160 \, \mathrm{m}$ and $\phi = 24°$ with a CW lidar provides the highest MCB in our optimization, it is not usable due to a negative buffer time. Measuring at $220 \, \mathrm{m}$ and $\phi = 18°$ with a pulsed lidar gives a buffer time of $1.62 \, \mathrm{s}$, and the controller would have enough time to react for a mean wind speed below $20 \, \mathrm{ms}^{-1}$. A larger measurement range should be selected for both types of lidars if the full wind speed range (up to the wind turbine cut-off wind speed) is considered. When the measurement range increases from the optimum point, the MCB could decrease and the low-pass filter will have a lower cut-off frequency and need a longer time to process the lidar measure-

13

ment. Therefore, it is essential to estimate the REWS coherence for the selected scanning pattern and design the feedforward controller accordingly.

Time domain simulations were executed in OpenFAST with the embedded lidar simulator, the optimal configurations of both lidars given in Figure 5(b)(d), the feedforward-feedback combined controller and 4D Mann turbulence fields with a mean wind speed of $18\,\mathrm{ms}^{-1}$. To ensure statistical convergence of 10-min simulations, 21 realizations (seeds) of the same turbulence fields are used (Liew and Larsen, 2022). The filtered REWS u_{LL} time series is collected, and the real REWS u_{RR} is calculated from the virtual turbulence fields by averaging the along-wind time series among the rotor swept area. Simulations with similar set-ups are performed using the nacelle-based lidar. The nacelle-based CW lidar is simulated at a measurement range of $200\,\mathrm{m}$ so that the controller has enough time to react to the turbulent wind with a mean wind speed of $18\,\mathrm{ms}^{-1}$ (it takes longer to filter the REWS signal estimated from the nacelle-based than the spinner-based lidar due to the low MCB). Figure 6 compares the REWS coherence and transfer functions from time-domain simulations and those calculated in the frequency domain using the method presented in Section 2.4. Results of the CW and pulsed types of lidar are shown in the upper and lower panels, respectively.

Comparing the left plots (spinner-based) with the right plots (nacelle-based) in Figure 6, we see that the coherence in terms of the $k_{0.5}$ has been improved a lot by using the optimized lidar in the spinner. Overall, the simulated REWS coherence fits with the analytical models, which indicates that the scanning configurations optimized in the frequency domain are also providing the best wind preview in the time domain. Some noise appears at high frequencies due to the spectra estimation process.

5 Feedforward control benefits

The benefits of using the feedforward pitch controller are evaluated in this section. Time-domain simulations are performed using the optimized lidar in the spinner and on the nacelle, respectively, first with the feedback controller only, and then with the feedforward-feedback combined controller. Simulations in each scenario are executed using turbulence fields with the same turbulence characteristics for 21 different seeds (Liew and Larsen, 2022). Therefore, for lidar in CW and pulsed systems, respectively, $2 \times 2 \times 21$ simulations are carried out. All DOFs of the 15-MW reference wind turbine are enabled and no wave are simulated. The simulation time is $640\,\mathrm{s}$ in total, in which the first $40\,\mathrm{s}$ is the transient and excluded from the analysis. Then, the spectra of the rotor speed, the tower base bending moment and the blade root bending moment are calculated from the simulated time series. Here, only results of CW lidars are shown, since similar results are found for pulsed lidars.

The analytical spectrum of the rotor speed using feedforward control is modelled as

$$S_{\Omega\Omega} = |G_{\Omega u_{\mathrm{LL}}}|^2 S_{\mathrm{RR}}(1 - \gamma_{\mathrm{RL}}^2), \tag{31}$$

where $G_{\Omega u_{\mathrm{LL}}}$ is the closed-loop transfer function from the REWS to the rotor speed, which consists of the linearized wind turbine model, the pitch actuator, the control units and the generator torque controller (Schlipf et al., 2015b).

Results are shown in Figure 7, in which the left panels are from spinner-based lidar and the right panels are from the nacelle-based lidar. The benefits of using feedforward control (FBFF) compared to the feedback-only (FB-only) case are well visible
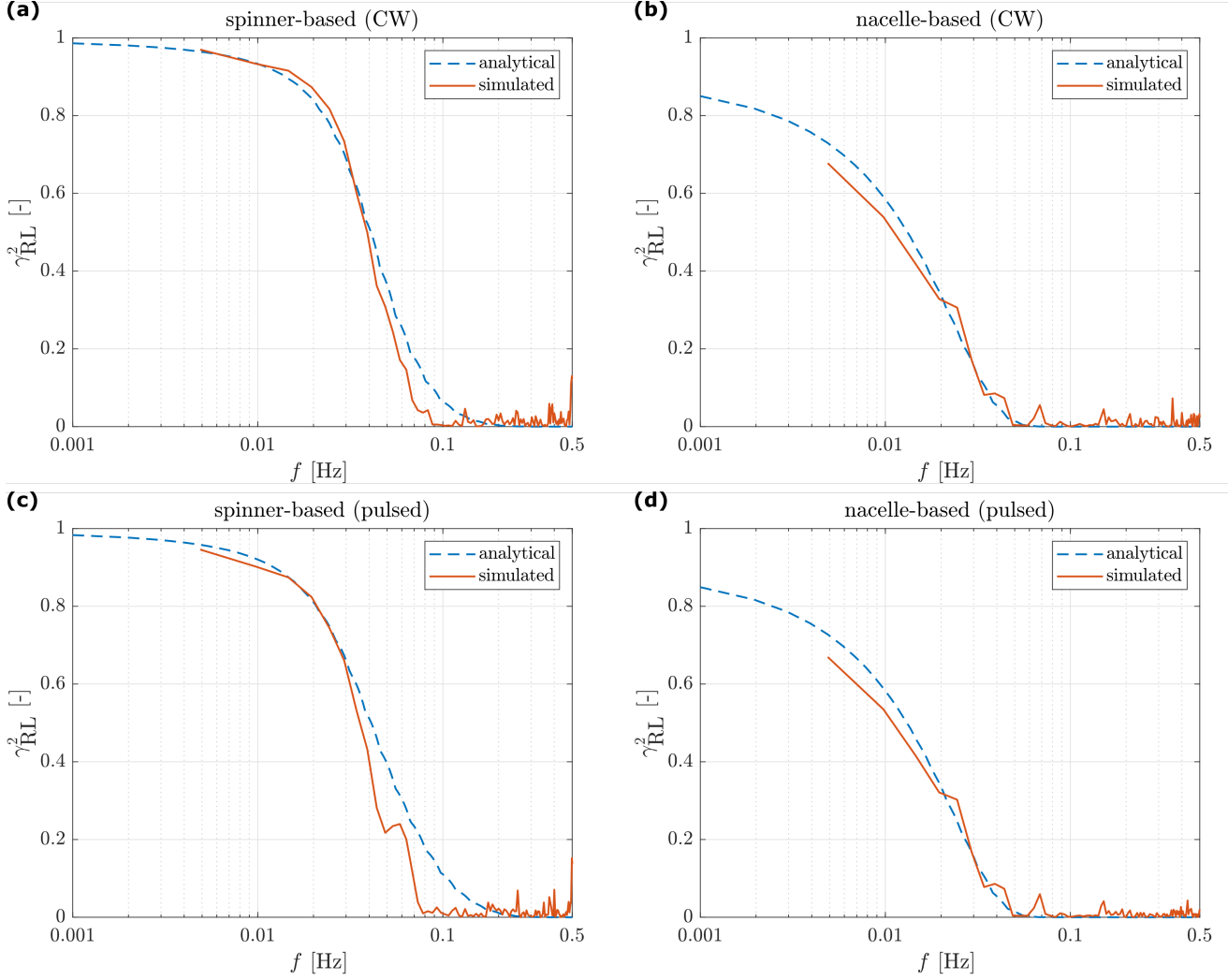
14

Figure 6. Coherence of the REWS using the optimal single-beam lidar (a)(c) in the spinner and (b)(d) on the nacelle. Upper panel for CW lidars, lower panel for pulsed lidars. Simulation results are averaged from 21 wind field realizations.

mainly at low frequencies. This is expected since the low-frequency range is where the lidar wind preview signal correlates well with the real REWS. In Figure 7(a) and (b), the simulated rotor speed spectra fit well with the analytical one for the frequency range below 0.2 Hz (below the 1P of the turbine). Significant reductions of the rotor speed variations are achieved using the spinner-based configuration compared to the nacelle-based one. Furthermore, within the low-frequency range, higher load reductions on the tower-base fore-aft (below 0.07 Hz) and blade-root flap-wise directions (below 0.1 Hz) can be seen using the spinner-based lidar.

The standard deviation of the rotor speed and the fatigue loads, i.e., damage equivalent loads (DELs) of the tower-base and blade-root bending moments are calculated from the time series. To estimate the DELs, the rain flow counting method introduced by Matsuichi and Endo (1968) is applied. The DELs are based on a reference number of cycles of 2×10^6 and a turbine lifetime of 20 years. Wöhler exponents of 4 and 10 are used for the tower-base fore-aft and blade-root flap-wise bending moments, respectively (Schlipf, 2016). Statistically, by using FBFF with the single-beam CW lidar in the spinner instead of on the nacelle, the reduction of the mean rotor speed standard deviation is improved from 13.8% to 47.4%, and the reduction of the tower-base fore-aft bending moment DEL increases from 1.0% to 4.3%. The strategy also brings 3.1% reduction to the blade-root flap-wise moment DEL. Since the default feedback controller parameters are adopted, the DEL reductions can be further improved by optimizing the controller gains (Schlipf et al., 2018).

Similar results and trends are seen from the simulations using the pulsed lidar, which are summarized in Table 1. We have also optimized the scanning pattern of a 4-beam CW nacelle lidar, which provides a MCB around 0.011 m^{-1} measuring at 220 m with $\phi = 15°$. The optimized 4-beam nacelle lidar is applied and simulated with 21 realizations of the same turbulence fields. Results in Table 1 show that the control benefits gained using the spinner-based single-beam lidar are larger than those we can achieve using the same lidar on the nacelle, and that the benefits using a spinner-beam single-lidar are of a similar level to those using a 4-beam system.

reductions	spinner (CW)	nacelle (CW)	spinner (pulsed)	nacelle (pulsed)	4-beam nacelle (CW)
rotor speed standard deviation	-47.4%	-13.8%	-44.0%	-14.1%	-44.6%
tower-base fore-aft DEL	-4.3%	-1.0%	-4.1%	-1.1%	-4.3%
blade-root flap-wise DEL	-3.1%	0.4%	-2.7%	0.2%	-2.9%

Table 1. Control benefits of feedforward-feedback combined controllers relative to using feedback-only controllers for: a single-beam lidar in the spinner and on the nacelle both using a CW and a pulsed system, and a 4-beam CW lidar on the nacelle at a mean wind speed of 18 ms^{-1}.

6 Discussions

The goal of this study is to demonstrate that a single-beam lidar mounted in the spinner brings much more benefit of feedforward control compared to the single-beam lidar based on the nacelle. The study optimizes the lidar scanning configurations for
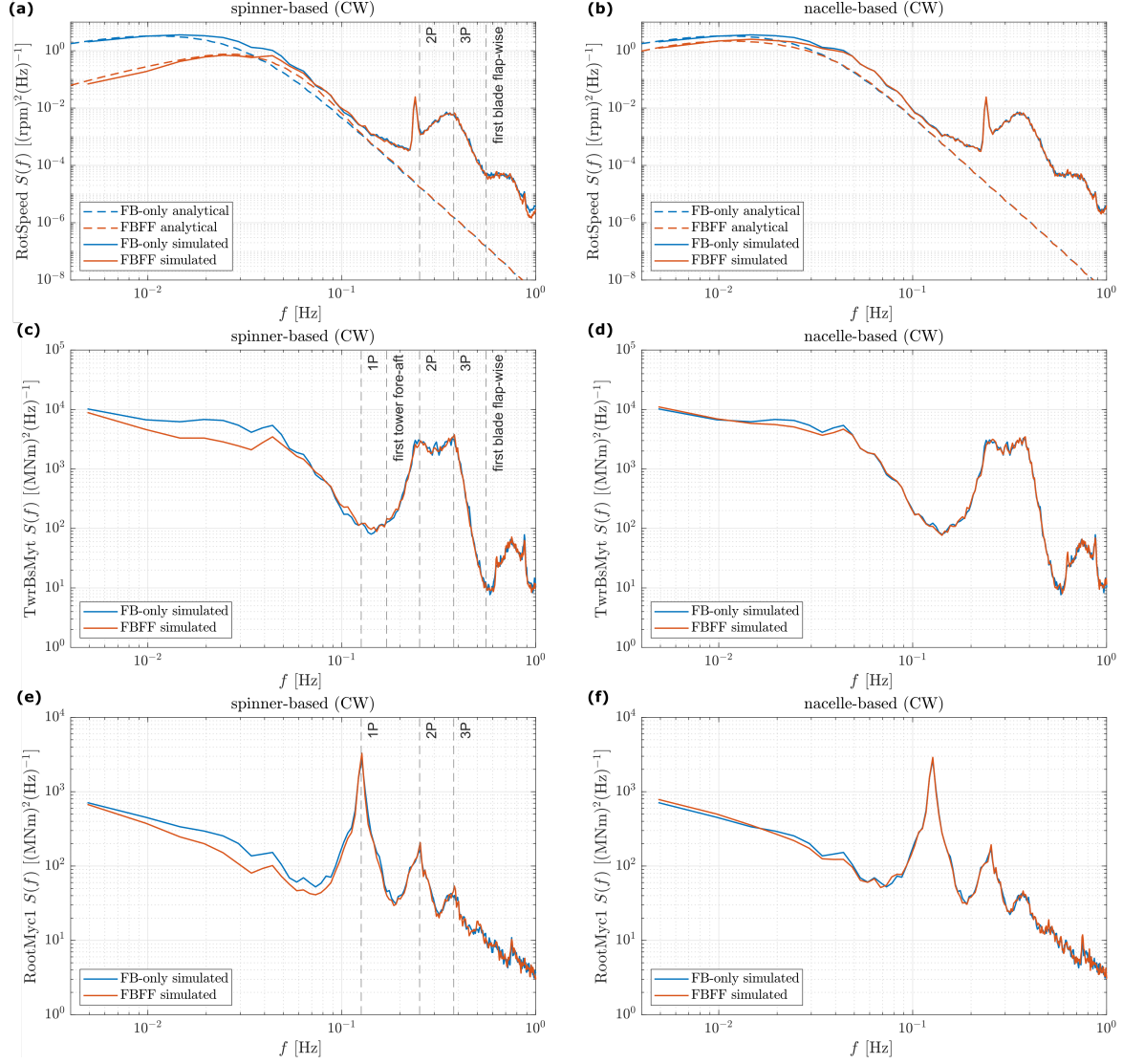
Figure 7. Spectra of the rotor speed (RotSpeed), tower-base fore-aft (TwBsMyt) and blade-root flap-wise bending moments (RootMyc1) with feedback-only and the feedforward-feedback combined controller using the optimal single-beam CW lidar (a)(c)(e) in the spinner and (b)(d)(f) on the nacelle at a mean wind speed of 18 ms^{-1}. Simulation results are averaged from 21 wind field realizations. Some relevant structural frequencies are marked.

the best wind preview quality considering the longitudinal wind evolution in the wind field. The optimum configurations for both CW and pulsed lidars are selected for a mean wind speed of $18\,\mathrm{ms}^{-1}$.

375   The strength of wind evolution is one of the factors that affect the optimal lidar scanning strategy. Other factors include the number and the location of measurements, the turbulence spectra, and the severity of contamination by the transverse velocity components, which is affected by the lidar beam directions (Guo et al., 2022a). The smaller the beam opening angle, the smaller the contribution of the transverse velocity components to the radial velocity. To reveal the impact of turbulence evolution, Figure 8 shows the optimization results of the CW and pulsed lidars if the evolution is neglected. The maximum

380 achievable MCBs of both lidars are overestimated, compared to those shown in Figure 5. In addition, for the CW lidar, assuming frozen turbulence does not change the shape of the MCB curve. This is expected because the probe volume of a CW lidar increases quadratically with the focus distance, which plays a more important role in determining the MCBs than the turbulence evolution. As for the pulsed lidar whose probe volume does not change with the measurement range, the highest MCB is reached with a different configuration compared to the one in Figure 5. The new optimum configuration has a smaller opening

385 angle $\phi = 15°$ and a further measurement distance at $x = 270$ m due to the disregard of wind evolution. The resulting lidar scan radius remains at $\approx 0.6R$. Owing to the rotor shaft tilt angle, measuring too far away from the rotor causes the lidar scanning area to be easily out of the rotor swept area. Therefore, the MCB decreases from the optimum point when the lidar measures at $x = 270$ m with a wider opening angle or with $\phi = 15°$ at a further measurement distance. In summary, it is essential to consider wind evolution for the optimization of lidar scanning configuration and for the estimation of a realistic MCB.
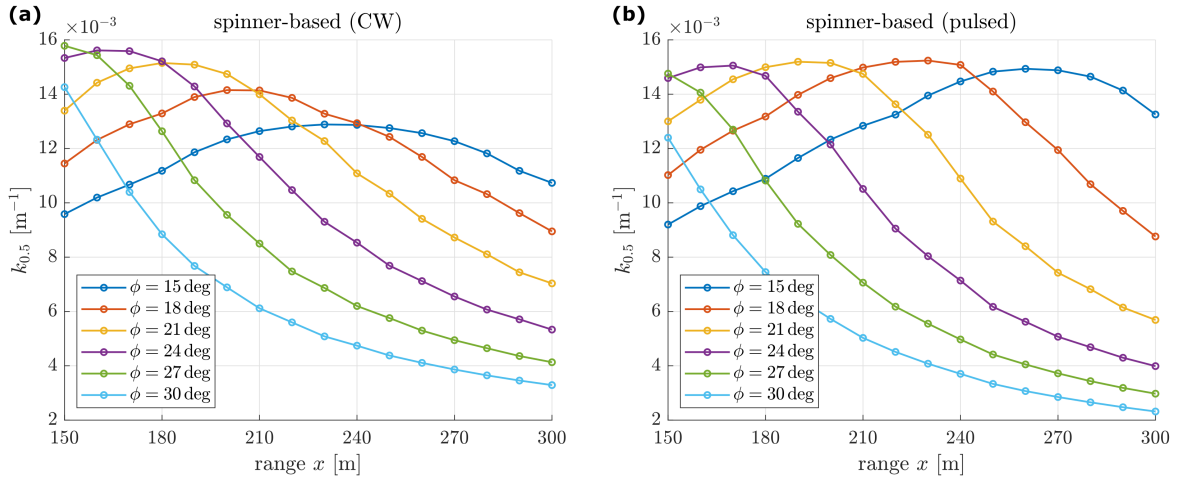

Figure 8. Optimization of the range x and half-cone opening angle ϕ of the spinner-based lidar when wind evolution is neglected.

390   As mentioned in Section 4, for higher wind speeds, larger measurement ranges are needed for both CW and pulsed lidars so that the controllers have enough time to react to the wind disturbance. Further work needs to be done with the full wind speed range to decide the best scanning configuration of the single-beam lidar in the spinner. Also, the controller performances can

be influenced by turbulence conditions. Only neutral atmospheric stability is considered in this work. Guo et al. (2023) showed that the control benefit is at its highest in unstable, middle in neutral, and lowest in stable turbulence conditions.

7 Conclusion and Outlook

A single-beam Doppler lidar is flexible and low in cost. Using the single-beam lidar in the spinner, the lidar can rotate with the rotor at an almost steady rotational speed in the turbine's above-rated operations and scans a good portion of the inflow to the rotor disk. Also, the spinner-based lidar can have an impeded view of the inflow without periodic blockage by the running blades, which improves the lidar data availability.

Based on a coherence model of the lidar-rotor REWS using 4D Mann turbulence model, this work optimizes the measurement range and the half-cone opening angle of the spinner-mounted single-beam lidar based on a CW and a pulsed system, respectively, at a single wind speed of $18 \mathrm{~ms}^{-1}$ for the bottom-fixed IEA 15-MW wind turbine. The optimum configurations of the two types of lidars are different due to the spatial averaging effect of their probe volumes, but they both result in a scan radius of approximately 0.6 of the turbine radius. The optimum configurations of both types of lidars give a MCB of around $0.014 \mathrm{~m}^{-1}$, which corresponds to the smallest detectable eddy size of $1.87D$. Large lidar measurement ranges are needed to ensure the turbine controllers have enough time to react to the wind disturbance over the full wind speed range, which slightly reduces the MCB.

Using time-domain simulations and 4D Mann turbulence wind fields in the neutral condition, the benefits of regulating rotor speed variation and reducing fatigue loads on the tower and blades using the feedforward controller and the spinner-based single-beam lidar are evaluated for the reference turbine at a single wind speed of $18 \mathrm{~ms}^{-1}$. Results are compared against a single-beam and a 4-beam nacelle-based lidar. The control benefits using the optimized spinner-based configurations of both CW and pulsed lidars are much higher than the single-beam nacelle lidar, and they are on a similar level to the 4-beam nacelle lidar.

For future work, full wind speed ranges up to the wind turbine cut-off wind speed should be considered to select the optimum scanning trajectory of the spinner-based single-beam lidar for the IEA 15-MW wind turbine. The pulsed lidar could potentially deliver a better wind preview signal than the one shown in this work when measurements at multiple range gates are combined. In addition, more reductions in fatigue loads could be achieved by optimizing the parameters of the feedback controller. In the future, more than one single-beam lidar can be used in the spinner to add redundancy to the system, meanwhile, having the possibility to achieve a shorter full scan time or multi-plane measurements even with a CW lidar system.

20

References

Abbas, N. J., Zalkind, D. S., Pao, L., and Wright, A.: A reference open-source controller for fixed and floating offshore wind turbines, Wind Energy Science, 7, 53–73, https://doi.org/10.5194/wes-7-53-2022, 2022.

435 Bossanyi, E. A., Kumar, A., and Hugues-Salas, O.: Wind turbine control applications of turbine-mounted LIDAR, Journal of Physics: Conference Series, 555, 012 011, https://doi.org/10.1088/1742-6596/555/1/012011, 2012.

Canet, H., Loew, S., and Bottasso, C. L.: What are the benefits of lidar-assisted control in the design of a wind turbine?, Wind Energy Science, 6, 1325–1340, https://doi.org/10.5194/wes-6-1325-2021, 2021.

Cariou, J.-P.: Pulsed lidar, in: Remote Sensing for Wind Energy, chap. 5, pp. 104–121, DTU Wind Energy-E-Report-0029(EN), 2013.

440 Fu, W., Peña, A., and Mann, J.: Turbulence statistics from three different nacelle lidars, Wind Energy Science, 7, 831–848, https://doi.org/10.5194/wes-7-831-2022, 2022.

Guo, F., Mann, J., Peña, A., Schlipf, D., and Cheng, P. W.: The space-time structure of turbulence for lidar-assisted wind turbine control, Renewable Energy, 195, 293–310, https://doi.org/10.1016/J.RENENE.2022.05.133, 2022a.

Guo, F., Schlipf, D., Zhu, H., Platt, A., Cheng, P. W., and Thomas, F.: Updates on the OpenFAST Lidar Simulator, Journal of Physics:
445 Conference Series, 2265, 042 030, https://doi.org/10.1088/1742-6596/2265/4/042030, 2022b.

Guo, F., Schlipf, D., and Cheng, P. W.: Evaluation of lidar-assisted wind turbine control under various turbulence characteristics, Wind Energy Science, 8, 149–171, https://doi.org/10.5194/wes-8-149-2023, 2023.

Harris, M., Hand, M., and Wright, A.: Lidar for Turbine Control: March 1, 2005 - November 30, 2005, Tech. rep., https://doi.org/10.2172/881478, 2006a.

450 Harris, M., Hand, M., and Wright, A.: Lidar for turbine control, National Renewable Energy Laboratory, Golden, CO, Report No. NREL/TP-500-39154, https://www.nrel.gov/docs/fy06osti/39154.pdf, 2006b.

Held, D. P. and Mann, J.: Comparison of methods to derive radial wind speed from a continuous-wave coherent lidar Doppler spectrum, Atmospheric Measurement Techniques, 11, 6339–6350, https://doi.org/10.5194/amt-11-6339-2018, 2018.

Held, D. P. and Mann, J.: Lidar estimation of rotor-effective wind speed - An experimental comparison, Wind Energy Science, 4, 421–438,
455 2019.

IEC: IEC 61400-1. Wind turbines – Part 1: design guidelines, International standard, International Electrotechnical Commission, Geneva, Switzerland, https://standards.iteh.ai/catalog/standards/sist/3454e370-7ef2-468e-a074-7a5c1c6cb693/iec-61400-1-2019, 2019.

Jonkman, J., Butterfield, S., Musial, W., and Scott, G.: Definition of a 5-MW Reference Wind Turbine for Offshore System Development, https://doi.org/10.2172/947422, 2009.

460 Kumar, A., Bossanyi, E., Scholbrock, A., Fleming, P., Boquet, M., and Krishnamurthy, R.: Field Testing of LIDAR Assisted Feedforward Control Algorithms for Improved Speed Control and Fatigue Load Reduction on a 600 kW Wind Turbine, in: European Wind Energy Association Annual Event, Paris, https://www.researchgate.net/publication/305637934_Field_Testing_of_LIDAR_Assisted_Feedforward_Control_Algorithms_for_Improved_Speed_Control_and_Fatigue_Load_Reduction_on_a_600_kW_Wind_Turbine, 2015.

Liew, J. and Larsen, G. C.: How does the quantity, resolution, and scaling of turbulence boxes affect aeroelastic simulation convergence?,
465 Journal of Physics: Conference Series, 2265, https://doi.org/10.1088/1742-6596/2265/3/032049, 2022.

Mann, J.: The spatial structure of neutral atmospheric surface-layer turbulence, Journal of Fluid Mechanics, 273, 141–168, https://doi.org/10.1017/S0022112094001886, 1994.

Matsuichi, M. and Endo, T.: Fatigue of metals subjected to varying stress, https://www.semanticscholar.org/paper/Fatigue-of-metals-subjected-to-varying-stress-Matsuichi-Endo/467c88ec1feaa61400ab05fbe8b9f69046e59260, 1968.

470 Mikkelsen, T., Angelou, N., Hansen, K., Sjöholm, M., Harris, M., Slinger, C., Hadley, P., Scullion, R., Ellis, G., and Vives, G.: A spinner-integrated wind lidar for enhanced wind turbine control, Wind Energy, 16, 625–643, https://doi.org/10.1002/WE.1564, 2013.

National Renewable Energy Laboratory: Definition of the IEA Wind 15-Megawatt Offshore Reference Wind Turbine, Tech. rep., IEA Wind TCP Task 37, https://www.nrel.gov/docs/fy20osti/75698.pdf, 2020.

National Renewable Energy Laboratory: OpenFAST Documentation, https://openfast.readthedocs.io/en/main/, 2022.

475 Peña, A., Floors, R., Sathe, A., Gryning, S. E., Wagner, R., Courtney, M. S., Larsén, X. G., Hahmann, A. N., and Hasager, C. B.: Ten Years of Boundary-Layer and Wind-Power Meteorology at Høvsøre, Denmark, Boundary-Layer Meteorology, 158, 1–26, https://doi.org/10.1007/s10546-015-0079-8, 2016.

Schlipf, D.: Lidar-Assisted Control Concepts for Wind Turbines, Ph.D. thesis, https://doi.org/10.18419/opus-8796, 2016.

Schlipf, D., Fleming, P., Haizmann, F., Scholbrock, A., Hofsäß, M., Wright, A., and Cheng, P. W.: Field testing of feedforward
480 collective pitch control on the CART2 using a nacelle-based lidar scanner, Journal of Physics: Conference Series, 555, 012 090, https://doi.org/10.1088/1742-6596/555/1/012090, 2014.

Schlipf, D., Haizmann, F., Cosack, N., Siebers, T., and Cheng, P. W.: Detection of wind evolution and lidar trajectory optimization for lidar-assisted wind turbine control, Meteorologische Zeitschrift, 24, 565–579, 2015a.

Schlipf, D., Simley, E., Lemmer, F., Pao, L., and Cheng, P. W.: Collective Pitch Feedforward Control of Floating Wind Turbines Using Lidar,
485 Journal of Ocean and Wind Energy, 2, https://doi.org/10.17736/jowe.2015.arr04, 2015b.

Schlipf, D., Fürst, H., Raach, S., and Haizmann, F.: Systems Engineering for Lidar-Assisted Control: A Sequential Approach, Journal of Physics: Conference Series, 1102, 012 014, https://doi.org/10.1088/1742-6596/1102/1/012014, 2018.

Scholbrock, A., Fleming, P., Fingersh, L., Wright, A., Schlipf, D., Haizmann, F., and Belen, F.: Field testing LIDAR-based feed-forward controls on the NREL controls advanced research turbine, 51st AIAA Aerospace Sciences Meeting including the New Horizons Forum
490 and Aerospace Exposition 2013, https://doi.org/10.2514/6.2013-818, 2013.

Scholbrock, A., Fleming, P., Wright, A., Slinger, C., Medley, J., and Harris, M.: Field test results from lidar measured yaw control for improved yaw alignment with the NREL controls advanced research turbine, Tech. rep., https://www.nrel.gov/docs/fy15osti/63202.pdf, 2015.

Simley, E., Pao, L. Y., Frehlich, R., Jonkman, B., and Kelley, N.: Analysis of light detection and ranging wind speed measurements for wind
495 turbine control, Wind Energy, 17, 413–433, https://doi.org/10.1002/WE.1584, 2014.

Simley, E., Fürst, H., Haizmann, F., and Schlipf, D.: Optimizing lidars for wind turbine control applications-Results from the IEA Wind Task 32 workshop, Remote Sensing, 10, https://doi.org/10.3390/rs10060863, 2018.

Sonnenschein, C. M. and Horrigan, F. A.: Signal-to-noise relationships for coaxial systems that heterodyne backscatter from the atmosphere, Applied Optics, 10, 1600–1604, https://doi.org/10.1364/AO.10.001600, 1971.

500 Taylor, G. I.: The spectrum of turbulence, Proceedings of the Royal Society of London. Series A - Mathematical and Physical Sciences, 164, 476–490, https://doi.org/10.1098/rspa.1938.0032, 1938.

Venditti, B.: Animation: The World's Biggest Wind Turbines, https://www.visualcapitalist.com/visualizing-the-worlds-biggest-wind-turbines/, 2022.

A.5 Impact of the lidar-measured ambient flow turbulence intensity on the wake losses

Fu, W., Peña, A., Mann, J., and Young, T.: Impact of the lidar-measured ambient flow turbulence intensity on the wake losses.

This manuscript is under preparation.

Impact of the lidar-measured ambient flow turbulence intensity on the wake losses

Wei Fu[1], Alfredo Peña[1], Jakob Mann[1], and Tom Young[2]

[1]Department of Wind and Energy Systems, Technical University of Denmark, Frederiksborgvej 399, 4000 Roskilde, Denmark
[2]Renewable Energy Systems, Third Floor STV, Pacific Quay, Glasgow G51 1PQ, UK

Correspondence: Wei Fu (weif@dtu.dk)

Abstract. The power outputs of a pair of wind turbines inside an inland wind farm are analyzed. The power deficits are studied in different ambient turbulence intensity levels, which are measured by a single-beam nacelle lidar on the upstream wind turbine. Results show a clear trend that the power deficit decreases with increasing ambient turbulence intensity, which indicates that the wake recovers faster when the ambient flow is more turbulent. Furthermore, we attempt to estimate the turbulence length scale and dissipation rate from the radial velocity spectra of the single-beam lidar, and study the impact of length scale and dissipation rate on the wake losses. This part of work is still in progress. Overall, this work demonstrates the potential of using a single-beam nacelle lidar for wake studies.

1 Introduction

As a wind turbine extract kinetic energy from the incoming wind, the flow behind the rotor is characterized to have a reduced wind speed and a more complex turbulence structure, which gradually recovers with the downwind distance (Aitken et al., 2014). Previous studies showed that the ambient turbulence intensity and atmospheric stability conditions, the later ones are usually classified based on the turbulence length scale, have evident effects on the wake behavior (Maeda et al., 2011; Troldborg et al., 2011; Hansen et al., 2012; Breton et al., 2014; Peña et al., 2014). Particularly, it was found that the velocity deficit in the wind turbine wakes recovers faster when the turbulence intensity of the ambient flow is higher (Wu and Porté-Agel, 2012; Troldborg et al., 2011). This effect has a direct impact on the power production of the downstream wind turbine. By analyzing measurements in the Horns Rev offshore wind farm, Hansen et al. (2012) showed that the maximum power deficit of two turbines decreases from 0.5 to less than 0.4 when turbulence intensity increases from 4% to 12%. Those studies highlighted the importance of characterizing atmospheric turbulence of the ambient flow for estimating wind turbine wake losses.

Coherent Doppler lidars measure the wind velocity by detecting the dominant Doppler shift between the emitted coherence light beam and the signals backscattered from the aerosols in the atmosphere. Now lidar is a cost-effective alternative to meteorological masts and sometimes is the only option to access the wind resources around wind turbines and wind farms, especially in offshore conditions. Lidars mounted on the wind turbine nacelle (hereafter nacelle lidars) have the advantage that they yaw with the wind turbines and always track the inflow. Thus, they can potentially better measure the flow that interacts with the wind turbine than mast-mounted anemometers.

Due to the probe volume, lidar radial velocities are the weighted average of wind velocities sampled along the beam. The probe volume acts like a low-pass filter, and the high-frequency wind fluctuations cannot be fully detected by lidars. Thus, the second-order statistics derived from the radial velocities are attenuated and called the 'filtered' variances. The Doppler radial velocity spectrum, which is the raw lidar data and represents the distribution of wind velocities sampled in the probe volume, can be used to compensate for the spatial averaging effect and to estimate the 'unfiltered' second-order statistics, which approximate those measured by a sonic anemometer (Mann et al., 2010; Branlard et al., 2013). The degree of turbulence attenuation, i.e., the ratio of the 'filtered' to 'unfiltered' second-order statistics, varies with the size of the probe volume relative to the turbulence length scale Mann et al. (2010).

By using the Doppler spectrum, nacelle lidars in different configurations were shown to be able to accurately measure turbulence statistics of homogeneous flow (Peña et al., 2017, 2019; Fu et al., 2022a, b), among which a single-beam lidar operating in the staring mode is the simplest measurement configuration. Being the first field test of a nacelle-based lidar, Harris et al. (2006) presented that a single-beam continuous-wave (CW) lidar measuring horizontally can detect the along-wind fluctuations. Fu et al. (2022b) showed that the same single-beam nacelle lidar is able to measure the along-wind variance as well as a mast-mounted sonic anemometer. In addition, the single-beam lidar was used to understand the probe volume averaging effect through its radial velocity spectrum (Sjöholm et al., 2009).

For the first time, measurements of a single-beam CW nacelle lidar are analyzed for wake studies. In this work, the lidar scans the flow on the upstream wind turbine in an inland wind farm. We study the relations of the lidar-measured ambient turbulence intensity with the power deficit of the downstream wind turbine. Also, we try to estimate the turbulence length scale and dissipation rate from the single-beam lidar measurements and relate them with the power deficit. The turbulence kinetic energy dissipation rate indicates the strength of turbulence and acts as a scaling factor on the turbulence intensity. It also describes the rate of energy transfer into small eddies in the inertial subrange and thus influences the wake mixing with the ambient flow. Banakh et al. (1999) estimated the dissipation rate using the width of the Doppler spectrum. But the method can be used only when the lidar probe volume is much smaller than the length scale. The dissipation rate can also be estimated using the radial velocity structure function (Banakh et al., 1999), which needs two-point statistics and this cannot be obtained from the single-beam lidar. In this work, the turbulence length scale and dissipation rate are estimated using the lidar radial velocity spectrum. One method estimates the length scale based on the ratio of the 'filtered' to 'unfiltered' radial velocity variance and then computes the dissipation rate by fitting the theoretical spectrum described by the Mann turbulence spectral model (Mann, 1994) to the measured one. The other method estimates the length scale and dissipation rate simultaneously by fitting the model to the measured spectrum. This part of study is still in progress.

This paper is organized as follows. Section 2 introduces turbulence background, the modelling of lidar radial velocity spectrum, the methods to estimate radial velocity variances, turbulence length scale and dissipation rate. Section 3 describes the test site and used datasets. Section 4 studies the impact of the ambient turbulence intensity on the wake shape. Section 5 shows the estimation of the turbulence length scale and dissipation rate. Some shortcomings and possible future work of the study are discussed in Section 6. Section 7 concludes the work.

2 Methodology

2.1 Turbulence background

The three-dimensional wind field can be represented by the vector field $\boldsymbol{u}(\boldsymbol{x}) = (u,v,w) = (u_1,u_2,u_3)$, where the position vector $\boldsymbol{x} = (x,y,z)$ is defined in a right-handed Cartesian coordinate system, and u,v,w are the along-wind, lateral and vertical component, respectively. Assuming Taylor's frozen hypothesis (Taylor, 1938), the fluctuating part of the homogeneous wind field is time-independent and is transferred by the mean wind speed $\boldsymbol{U} = \langle \boldsymbol{u}(x,0,0)\rangle = (U,0,0)$. The mean wind direction is along the x-axis. The wind field can also be written in the wave-number domain as a Fourier integral,

$$\boldsymbol{u}(\boldsymbol{k}) = \frac{1}{(2\pi)^3}\int \boldsymbol{u}(\boldsymbol{x})\exp(-\mathrm{i}\boldsymbol{k}\cdot\boldsymbol{x})\mathrm{d}\boldsymbol{x}, \tag{1}$$

where $\boldsymbol{k} = (k_1,k_2,k_3)$ is the wave vector. For the homogeneous wind field, the ensemble-averaged absolute squared Fourier coefficients form the three-dimensional spectral tensor $\Phi_{ij}(\boldsymbol{k})$:

$$\langle u_i^*(\boldsymbol{k})u_j(\boldsymbol{k'})\rangle = \Phi_{ij}(\boldsymbol{k})\delta(\boldsymbol{k}-\boldsymbol{k'}), \tag{2}$$

where $\delta(.)$ is the Dirac delta function, * denotes complex conjugate, and $i,j = 1,2,3$ implies the three velocity components. We assume that the spectral velocity tensor $\Phi_{ij}(\boldsymbol{k})$ is described by the Mann turbulence model (Mann, 1994), which contains three tunable model parameters: $\alpha\varepsilon^{2/3}$ is the multiplication of the spectral Kolmogorov constant and the turbulent kinetic energy dissipation rate ε to its two-third power, L is the length scale describing the size of the most energetic eddies, and Γ describes the turbulence anisotropy.

The one-point spectra of the velocity components can be calculated from the spectral tensor by

$$F_{ij}(k_1) = \iint \Phi_{ij}(\boldsymbol{k})\mathrm{d}k_2\mathrm{d}k_3. \tag{3}$$

Thus, the auto-spectrum of the along-wind component is $F_u = F_{11}$. The along-wind variance is calculated as the integral of the auto-spectrum

$$\sigma_u^2 = \int\limits_{-\infty}^{\infty} F_u(k_1)\mathrm{d}k_1, \tag{4}$$

The turbulence intensity (TI) can be calculated from the standard deviation of the along-wind component σ_u and the mean wind, i.e., σ_u/U.

2.2 Theoretical lidar radial velocity spectrum

The radial velocity measured by lidar is the convolution of the lidar weighting function that approximates the probe volume and the wind components projected in the beam direction (Sjöholm et al., 2009)

$$v_\mathrm{r}(\boldsymbol{n},f_d) = \int\limits_{-\infty}^{\infty} \varphi(s)\boldsymbol{n}\cdot\boldsymbol{u}[\boldsymbol{n}(f_d+s)]\mathrm{d}s, \tag{5}$$

where $\boldsymbol{n}$ is the beam unit vector, f_d is the beam's focus distance, $\varphi(s)$ is the weighting function and s is the distance to the beam focus in the radial direction. Equation (5) assumes that the radial velocity is estimated from the Doppler spectrum by the center of gravity (centroid) method. Another method to estimate the radial velocity is the median method (Held and Mann, 2018), which uses the Doppler spectrum as a probability distribution of the radial velocities and finds the frequency bin that

90   corresponds to the median value.

The beam unit vector for a single-beam nacelle lidar that aligns with mean wind direction is

$$\boldsymbol{n} = (n_1, n_2, n_3) = (-1, 0, 0), \tag{6}$$

in which n_1 is negative since the beam is pointing upwind. The weighting function of a CW lidar is approximated by a Lorentzian function (Sonnenschein and Horrigan, 1971; Sjöholm et al., 2009)

95   $$\varphi(s) = \frac{1}{\pi} \frac{z_{\mathrm{R}}}{z_{\mathrm{R}}^2 + s^2}, \tag{7}$$

where z_{R} is the Rayleigh length (half of the full-width half maximum of the distribution). At a given focus distance, the Rayleigh length can be estimated by the laser wavelength λ and the transmitted beam radius at the output lens r_{b}

$$z_{\mathrm{R}} = \frac{\lambda f_d^2}{\pi r_{\mathrm{b}}^2}, \tag{8}$$

The spectrum of radial velocity measured by a lidar beam is expressed as (Mann et al., 2009)

100   $$F_{v_{\mathrm{r}}}(k_1) = n_i n_j \iint |\hat{\varphi}(\boldsymbol{k} \cdot \boldsymbol{n})|^2 \, \Phi_{ij}(\boldsymbol{k}) \mathrm{d}k_2 \mathrm{d}k_3, \tag{9}$$

where $\hat{\varphi}$ is the Fourier transform of the lidar weighting function. For a CW lidar, the Fourier transform of Eq. (7) is approximated by

$$\hat{\varphi}(\boldsymbol{k} \cdot \boldsymbol{n}) = \exp\left(-|\boldsymbol{k} \cdot \boldsymbol{n}| z_{\mathrm{R}}\right). \tag{10}$$

From Eq. (9), the theoretical radial velocity variance of a CW lidar is calculated as

105   $$\sigma_{v_{\mathrm{r}}}^2 = \int\limits_{-\infty}^{\infty} F_{v_{\mathrm{r}}}(k_1) \mathrm{d}k_1. \tag{11}$$

If the lidar probe volume can be fully circumvented and the single-beam nacelle lidar is well aligned with the mean wind, the 'unfiltered' radial velocity variance is equal to the along-wind variance, i.e., $\sigma_{v_{\mathrm{r}},\mathrm{unf}}^2 = \sigma_u^2$. With the impact of the probe volume, the 'filtered' radial velocity variance is smaller than the along-wind variance, i.e., $\sigma_{v_{\mathrm{r}},\mathrm{f}}^2 < \sigma_u^2$. Based on the Mann turbulence model, Fig. 1 shows the along-wind spectrum, the radial velocity spectrum and the ratio $\sigma_{v_{\mathrm{r}},\mathrm{f}}^2/\sigma_u^2$ using different

110   model parameters. The frequency can be transferred from the wave number by $f = k_1 U/(2\pi)$. The turbulence attenuation in the lidar spectrum can be clearly seen in the high-frequency range. The amount of variance attenuation $(1 - \sigma_{v_{\mathrm{r}},\mathrm{f}}^2/\sigma_u^2)$ is inversely proportional to L and Γ. The dissipation rate acts like a scaling factor to both the lidar radial and the along-wind spectra, which does not influence the amount of attenuation. Therefore, if the value of Γ is known or assumed, the $\sigma_{v_{\mathrm{r}},\mathrm{f}}^2/\sigma_u^2$ is a function of L.
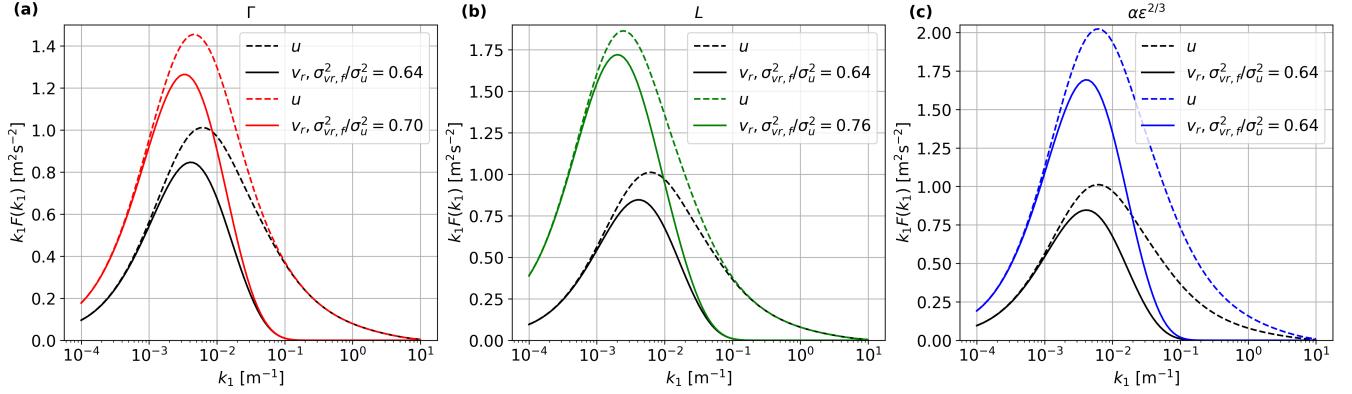
4

Figure 1. Influence of Mann parameters on the shape of the along-wind spectrum (dashed lines), the radial velocity spectrum (solid lines), and the ratio of lidar-measured to the true along-wind variance. (a) black: $\Gamma = 3$, red: $\Gamma = 4$. (b) black: $L = 40$ m, green: $L = 100$ m, (c) black: $\alpha\varepsilon^{2/3} = 0.5$ m$^{4/3}$s^{-2}, blue: $\alpha\varepsilon^{2/3} = 1$ m$^{4/3}$s^{-2}. Black curves in (a)-(c) are the same. The lidar probe volume size is fixed.

2.3 Estimation of the filtered and unfiltered radial velocity variance

As shown in Held and Mann (2018) and Fu et al. (2022a), the radial velocity variances computed from the time series of the median- or centroid-derived radial velocity are 'filtered' because none of these methods considers the whole Doppler spectrum. The centroid-derived variance is more affected by the probe volume than the median one.

The ensemble-averaged Doppler spectrum can be used to account for the spatial averaging effect and provides the 'unfiltered' radial velocity variance. Assuming that all velocity fluctuations detected in the lidar probe volume are contributed by turbulence, the mean of the Doppler spectra $p(v_{\rm r})$ accumulated in a period can be seen as a probability density function, where the 'unfiltered' radial velocity variance is estimated as the second-order central statistical moment

$$\sigma_{v_{\rm r},\mathrm{unf}}^2 = \int\limits_{-\infty}^{\infty} (v_{\rm r} - \mu_{v_{\rm r}})^2 p(v_{\rm r})\mathrm{d}v_{\rm r}, \tag{12}$$

in which $\mu_{v_{\rm r}}$ is the mean radial velocity

$$\mu_{v_{\rm r}} = \int\limits_{-\infty}^{\infty} v_{\rm r}p(v_{\rm r})\mathrm{d}v_{\rm r}. \tag{13}$$

In practice, the ensemble-averaged Doppler spectrum can be computed as the mean of the area-normalized Doppler spectra within a given time period (Fu et al., 2022a). The accurate estimation of the 'unfiltered' variance relies on 'clean' Doppler spectra, in which the noise and contamination due to reflections of hard targets, moving objectives, etc., are removed. The noise and contamination also affect the estimation of radial velocities. Therefore, the Doppler spectra are carefully filtered and processed to eliminate the noise and contamination as much as possible before being used to estimate the 'unfiltered' variance and the radial velocity spectrum, which is described in Section 5.

5

2.4 Estimation of turbulence length scale and dissipation rate

Two methods are used to estimate the turbulence length scale and the dissipation rate from the single-beam nacelle lidar measurements. Both methods assume that the turbulence anisotropy is constant, i.e., $\Gamma = 3.5$.

Assuming that the 'unfiltered' radial velocity variance of the single-beam nacelle lidar is the along-wind variance as it is measured by a sonic anemometer, the first method estimates the turbulence length scale L_{est} by interpolating the measured ratio $\sigma^2_{v_{\text{r}},\text{f}}/\sigma^2_{v_{\text{r}},\text{unf}}$ from the theoretical ones, which is pre-computed based on the Mann model using $\Gamma = 3.5$ and different values of L, as shown in Fig. 2. For computing the theoretical ratio, the integrals in Eq. (4) and Eq.(11) were discretized and truncated by $k_{1,\text{min}} = 10^{-3}$ m^{-1} and $k_{1,\text{max}} = 10$ m^{-1} in order to match the length of the analyzed lidar measurements (in periods of 30 min). Then, the theoretical radial velocity spectrum $F_{v_{\text{r}}}(k_1; \Gamma = 3.5, L = L_{\text{est}}, \alpha\epsilon^{2/3})$ is fitted to the measured radial velocity spectrum to obtain $\alpha\epsilon^{2/3}$. The second method estimates L and $\alpha\epsilon^{2/3}$ simultaneously by fitting the theoretical radial velocity spectrum $F_{v_{\text{r}}}(k_1; \Gamma = 3.5, L, \alpha\epsilon^{2/3})$ to the measured one without considering the ratio $\sigma^2_{v_{\text{r}},\text{f}}/\sigma^2_{v_{\text{r}},\text{unf}}$. Both fittings minimize the sum of the squared residuals between the estimated theoretical spectrum and the measured one in the wave number range of $k_{1,\text{min}} = 10^{-2}$ m^{-1} and $k_{1,\text{max}} = 1$ m^{-1}.
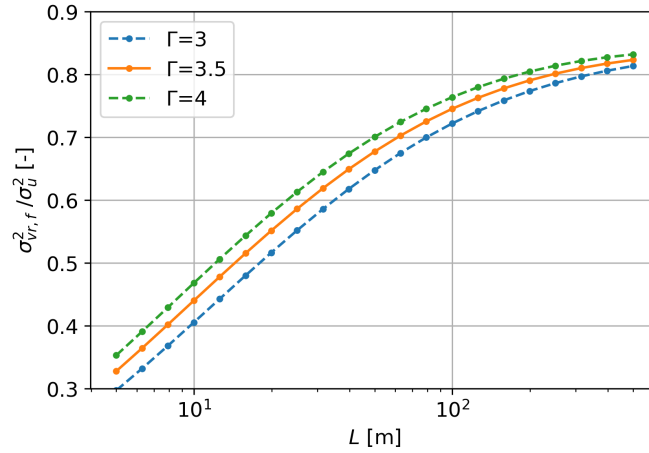

Figure 2. The theoretical ratio of 'filtered' radial velocity variance to the along-wind variance computed from the Mann model with different turbulence length scales and anisotropy. We assume $\Gamma = 3.5$ in the study.

3 Site and measurements

The measurements used in this work were collected in an anonymous inland wind farm from 30 September 2021 to 20 December 2022. There is no coast nearby the wind farm. The dominant wind direction is southwest. The wind turbines in the wind farm, marked in Figure 3, have a rotor diameter D of 62 m, a hub height of 49 m, and a rated power of 1.3 MW. This study focuses on the wake effect from T3 (upstream wind turbine, marked in green) on the power deficit of the T10 (downstream wind

150   turbine, marked in red). The 10-min mean active power outputs of the two wind turbines are recorded in the supervisory control
and data acquisition (SCADA). The SCADA data also contains 10-min averaged wind speeds measured by a cup anemometer
on the nacelle of T3, both wind turbines' yaw angle (relative to the north) and the yaw error, and the turbines' status indicating
if they are spinning and generating power. For measurements before 23 August 2022, we applied the yaw angle correction of
$-7.5°$ (northing offset) for T3.
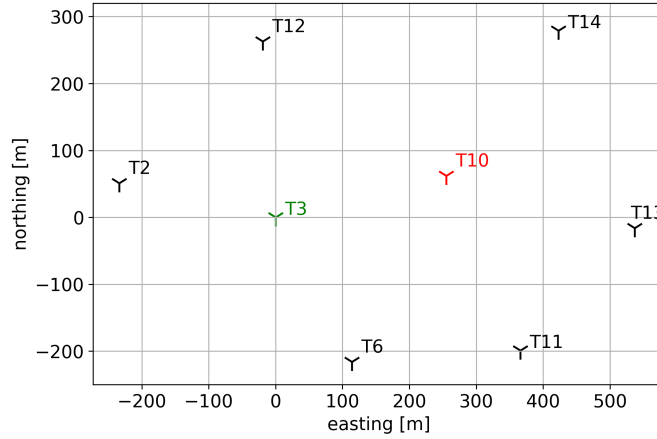
Figure 3. Layout of the wind farm, in which the coordinates of wind turbines are relative to the location of T3 wind turbine. The study
focuses on the T3 wake effect on the T10 turbine.

155   On the nacelle of T3, a single-beam CW lidar measures the flow horizontally in a staring mode. The measurement range is
80 m, at which the lidar Rayleigh length is 18.02 m. The lidar system streams out Doppler spectra at a rate of 48.8 Hz. Each
Doppler spectrum is represented in 256 frequency bins corresponding to a radial velocity resolution of 0.1528 m s^{-1}. The
system also reports high-frequency wind data at 10 Hz, which contains the radial velocities derived using the median method,
the turbulence intensity (TI), the spectra-averaged turbulence intensity (SATI, a sonic-equivalent measure of TI), the spectral
160 spreads (the width of the spectrum indicating the amount of turbulence or flow complexity within the probe volume), and the
backscatter (a measure of lidar signal-to-noise ratio).

4   Impact of the ambient turbulence intensity on the wake losses

We first study the relations between the lidar-estimated ambient TI and the wake shape, which is represented by the power
deficit in different wind directions. Figure 4 shows the ratio of the 10-min mean active power of T10 to T3 over the wind
165 direction, which is the sum of the 10-min averaged T3 yaw position and its yaw error. The following filtering criteria are
applied to select 10-min periods for the analysis

- T3 and T10 are both generating power. To study the wake effect, we select time periods when T3 active power is between
 0.2 - 1 MW (14514 10-min periods left).

- T3 yaw error is below $5°$ and the difference between T3- and T10-measured wind directions is below $10°$ (10644 10-min periods left).

- In addition, we dropped some consecutive days to remove the outliers of the T10/T3 power ratio (10458 10-min periods left).
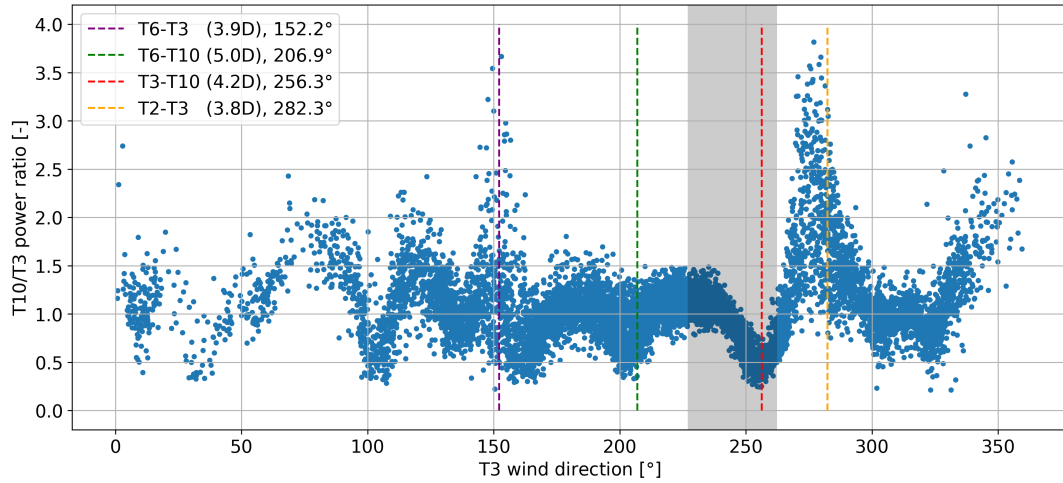

Figure 4. The ratio of the 10-min mean active power of T10 to T3 over wind directions, which is the sum of T3 yaw position and yaw error. The total number of points is 10458. Wind sectors used for analysis are shadowed in a grey square.

The dashed vertical lines in Fig. 4 mark four of the wind directions, in which T3 or T10 can be affected by the surrounding turbines. The legend of the figure gives the distance and directions between two turbines calculated from the turbine coordinates. When T3 is in free stream and T10 is only shadowed by the wake of T3, we see the power reduction of T10 in wind directions of $240° - 266°$ in Fig. 4, where the points form a U shape and its bottom is at the T3-T10 direction. When both T3 and T10 are in the free stream, their power ratio is close to but slightly above 1, as can be seen in wind directions of $210° - 240°$. When the wind direction is around $280°$, we see a peak in the figure because T3 is shadowed by the wake from T2. T3 can also be affected by the wake from T6 when the wind comes from $152°$. We can roughly see a U shape around $203°$ due to the impact of T6 on the T10 but blended with the points that have a power ratio around 1. This is probably because T6 was offline for quite some months in 2022. Our main interest is the wind sectors where T3 is in free stream and T10 is only affected by the wake of T3. We apply further filtering criteria to select 10-min periods:

- Assuming the wake expands horizontally within $20°$, we use the samples in wind directions of $226.9° - 262.3°$, as marked in a grey square in Fig. 4. The nacelle lidar should be concurrently operating. This leaves us 2042 10-min periods.

- To eliminate the impact of the wind turbine thrust coefficient on the wake shape, we use the time periods, when the wind speed measured by the cup anemometer on the T3 nacelle is between $7 - 10 \text{ ms}^{-1}$. We have 1170 periods of 10 min for the analysis.

We describe the wake shape with the so-called *wake depth*, which is the difference between the *wake-free level* and the *wake level* and reflects the amount of power deficit. The *wake-free level* is estimated using the T10/T3 power ratio when both turbines are in the free stream. We fit a parabolic curve ($f(x) = ax^2 + bx + c$) to the samples in the wake-free sector ($226.9° - 242°$, marked in orange) and take the peak of the fitted curve as the *wake-free level*, as shown in Fig. 5(a). The algorithm provides optimum $f(x)$ so that the sum of the squared residuals between $f(x)$ and the samples is minimized. Again, we fit the parabolic curve $f(x)$ to the samples in the wake sector ($242° - 262.3°$, marked in pink) and take the power ratio at the bottom of the curve as the *wake level*. To remove outliers, the points in the selected wind sectors are filtered by their mean ± 2 times their standard deviation (the unused points are marked in blue). Fig. 5(b) shows the distribution of the lidar-measured TI values of the samples in Fig. 5(a). The TI values are mostly below 0.12.
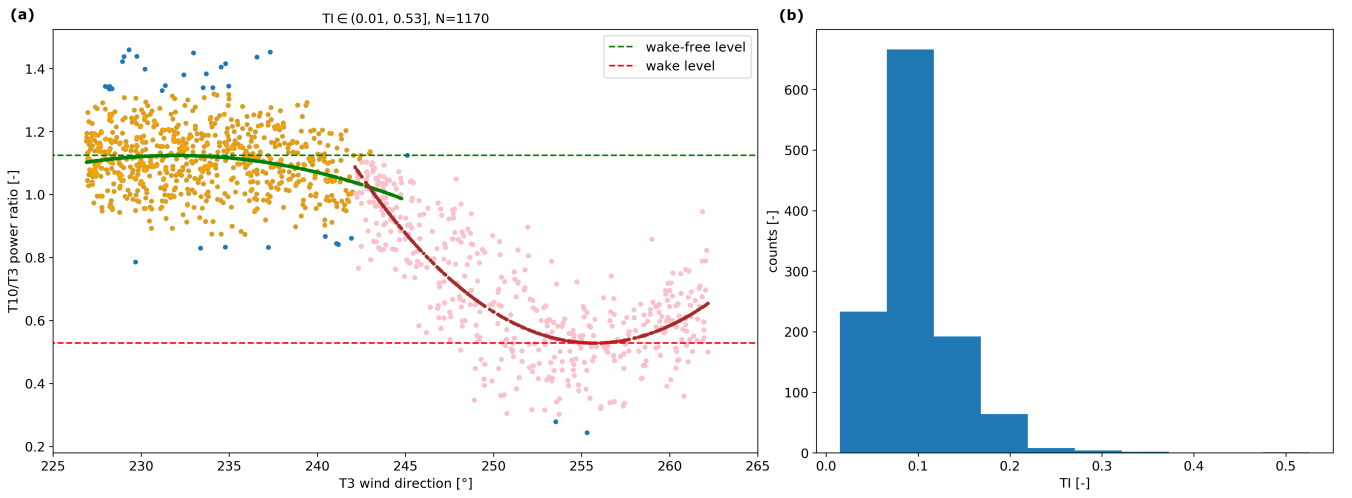
Figure 5. (a) Definition of the wake-free level and the wake level estimated by fitting parabolic curves to the samples. See the text for more details. (b) Distribution of TI values of the samples in (a).

We divide all samples in Fig. 5 into six groups according to the TI values measured by the nacelle lidar. The wake-free levels and wake levels are estimated for each group, as shown in Fig. 6(a). The selection of the TI ranges is arbitrary but we try to balance the number of samples in each group to reduce the fitting uncertainty. Figure 7 shows the trend of the wake-free levels, wake levels, and wake depths with the increasing TI levels. It can be seen that the wake-free level remains close to 1.15, which is slightly above 1 probably owing to the terrain effect; the height of ground for T3 is 268 m while for T10 is 275 m. The wake level increases from 0.42 to 0.62 with TI levels from $(0.01,0.06]$ to $(0.12,0.53]$. Consequently, the wake depth (power deficit) decreases from nearly 0.7 to 0.5.
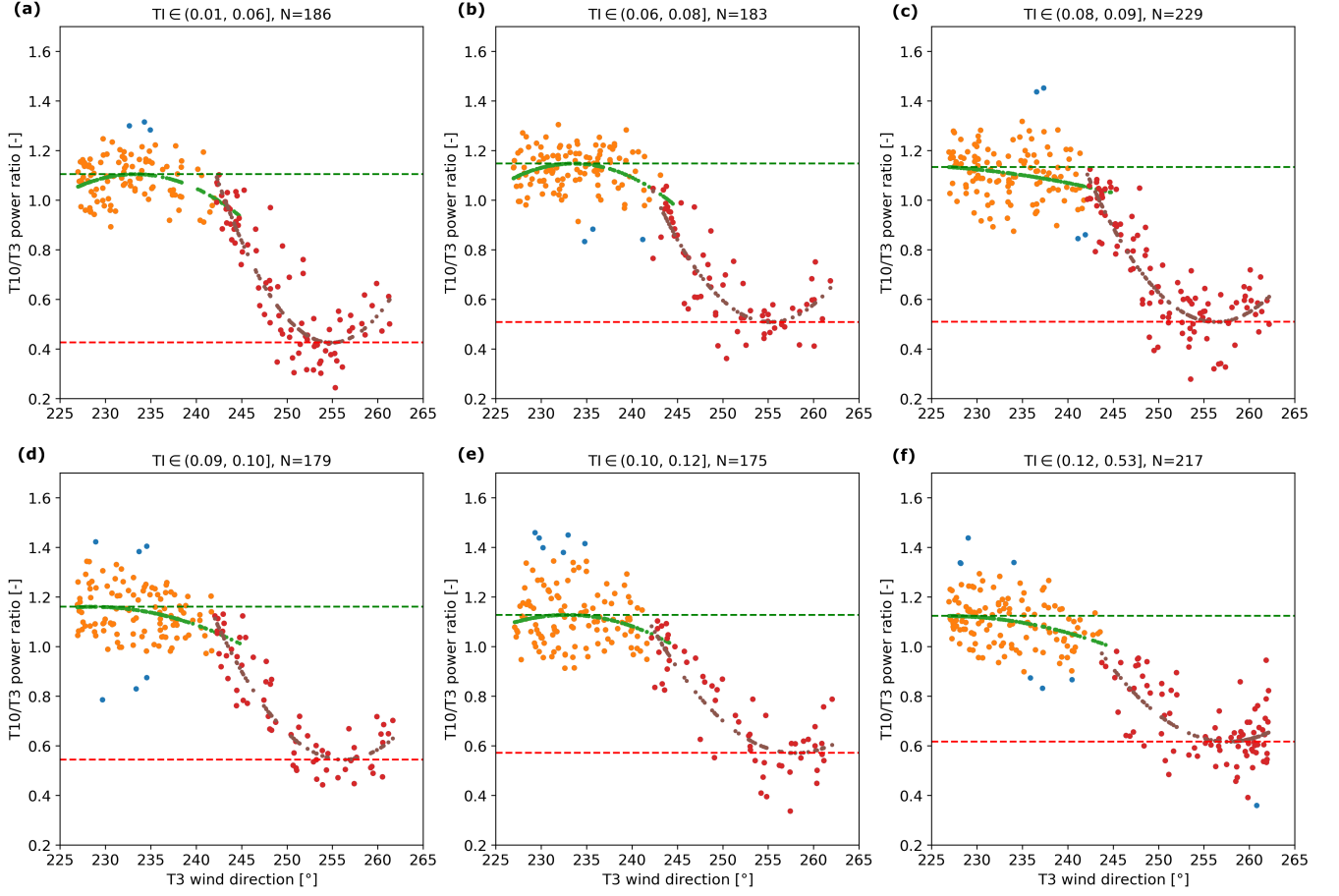
Figure 6. Estimation of the wake-free level and wake level in different TI groups. The TI is measured by the single-beam nacelle lidar. N is the number of samples in each group.

5 Estimation of length scale and dissipation rate from lidar measurements

205 In order to get the measured radial velocity spectra that can reach down to 10^{-3} Hz, we analyze the SCADA data and lidar measurements based on periods of 30 min. The same filtering criteria of the turbines' status and yaw error in Section 4 are applied, which leaves us 4042 periods of 30 min over full available wind directions and wind speeds. Again, we focus our analysis on the wind sectors between $226.9° - 262.3°$ so that the nacelle lidar on T3 is not affected by wakes, which leaves us 840 periods of 30 min.

210 The lidar Doppler spectra in 48.8 Hz are first integrated into 10 Hz spectra, which are then filtered based on the 10 Hz system-reported radial velocities, backscatters, and spectral spreads. The following filtering criteria are applied:

– Since the lidar beam is perpendicular to the rotor, the blades act just like a shutter. Thus, the blade-blocked signals are detected and removed when $v_\mathrm{r} = 0 \text{ ms}^{-1}$ or the spectra in all frequency bins are NaNs.
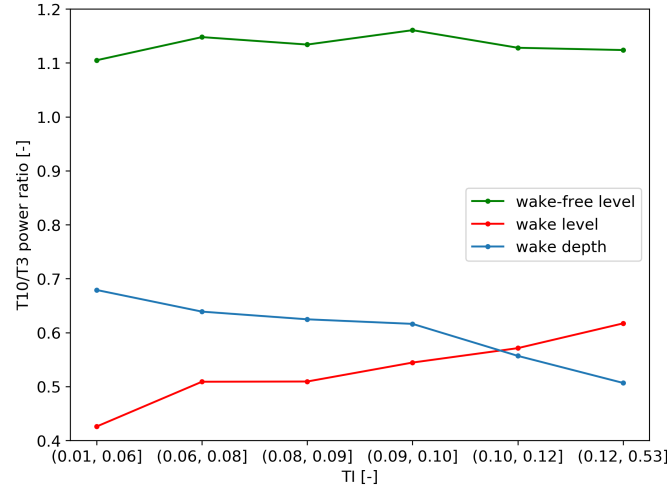
10

Figure 7. Estimated wake-free levels, wake levels, and wake depths in different TI groups.

- The anomalously high radial velocities are removed when $v_r \geq 30$ ms^{-1} .

- The backscatter is the sum of all spectral signals above the noise threshold, which is a measure of the lidar signal-to-noise ratio. Measurements are dropped if the backscatter is lower than 0.06.

- The contaminated Doppler spectra are identified and removed if the spectral spread is greater than $0.75v_r$ ms^{-1}.

- We remove the spectral values that belong to the radial velocity bins lower than 2.45 ms^{-1} in all Doppler spectra to eliminate strong low-frequency signals (contaminations), which might be caused by remaining blade signals or optical reflections.

After applying the filters, the number of 10 Hz Doppler spectra for a 30-min period is typically between 9800 to 14000 in a 30-min period. We estimate the centroid radial velocities from the Doppler spectra to calculate the 'filtered' radial velocity variance because the centroid method can best reveal the probe volume averaging effect. To remove the impact of the mean wind velocity on the variances, the centroid radial velocities and the Doppler spectra are detrended before being used to calculate the 'filtered' and 'unfiltered' radial velocity variance, respectively.

We compute the lidar radial velocity spectrum using the 10 Hz centroid radial velocities, which are linearly interpolated so that there are 18000 measurements in each 30-min period. The radial velocity spectrum is calculated using Welch's method, which divides the time series into overlapping segments, computes the modified periodogram for each segment, and takes the mean of all periodograms. As shown in Fig.8, increasing the length of the segment allows the spectrum to go down to lower wave numbers (or frequencies), but makes the spectrum noisier especially below the wave number of 10^{-2} m^{-1} due to less averaging. In our case, each segment has 6000 measurements that correspond to a 10-min time series and the

11

number of overlapping measurements is 5400 (90% of the segment length). Therefore, the spectrum is the mean of roughly 21 periodograms.
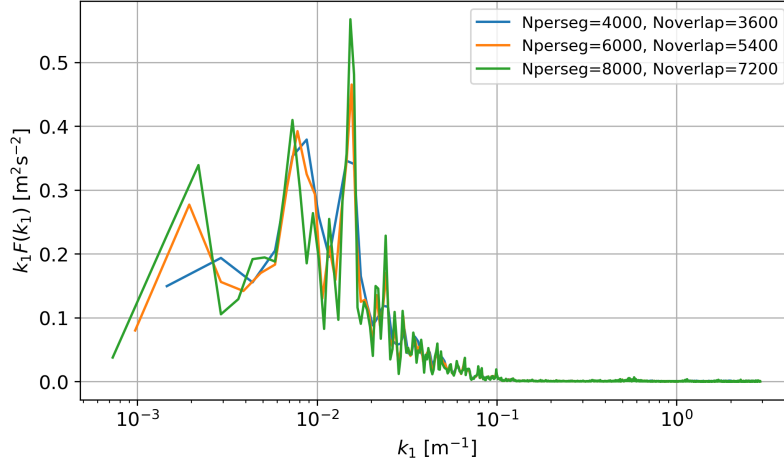

Figure 8. Impact of the number of measurements per segment for computing the radial velocity spectrum using Welch's method.

Figure 9 shows the distribution of the estimated ratio $\sigma^2_{v_{r,f}}/\sigma^2_{v_{r,unf}}$ from the Doppler spectra analysis of the 796 periods of 30 min. All values are below 1, which is expected. However, some very low and high values are outside the ratio predicted by the model, which has a range from 0.32 to 0.82, as shown in Fig. 2. The $\sigma^2_{v_{r,f}}/\sigma^2_{v_{r,unf}}$ of the high values indicate that there is less spatial filtering in the measurements than predicted in the model, or the probe volume size in the model is overestimated. Assuming a higher anisotropy will generally increase the modelled ratio, but the maximum ratio with $\Gamma = 4$ is 0.91, which cannot fully explain the highest ratio in the measurements. The measured ratio could also be influenced by the remaining outliers in the measurements. For time periods when the estimated $\sigma^2_{v_{r,f}}/\sigma^2_{v_{r,unf}}$ is out of the range of the pre-computed ratio, the first method does not work.

We found that the estimated length scales using the two methods described in Section 2.4 are different most of the time. There are some anomalously high and low estimations from both methods. The first method works well when the estimated raio $\sigma^2_{v_{r,f}}/\sigma^2_{v_{r,unf}}$ is $0.6 - 0.7$, as shown in Fig. 10(a) and (b). In these cases, the estimated length scales seem realistic, and the resulting lidar spectrum captures the main shape of the measured spectrum, especially in the range close to the inertial subrange. However, when the ratio $\sigma^2_{v_{r,f}}/\sigma^2_{v_{r,unf}}$ gets large, as shown in Fig. 10(c), the estimated length scale is too high and the dissipation rate might be also greatly overestimated in order to ensure the best fit of the two spectra below the wave number of 10^{-2} m^{-1}. Consequently, the estimated lidar radial velocity variance (proportional to the area below the spectrum) and the along-wind variance (proportional to the lidar variance) are overestimated. Method 2 can generally better capture the shape of the spectrum in Fig. 10(c) but is sensitive to noise, as shown in Fig. 10(b) and (d). We observe that after applying all the filters, there are still some outliers in some time periods that are causing noises in the high-frequency part of the measured spectrum. This leads to some unrealistic estimations of the length scale by method 2.
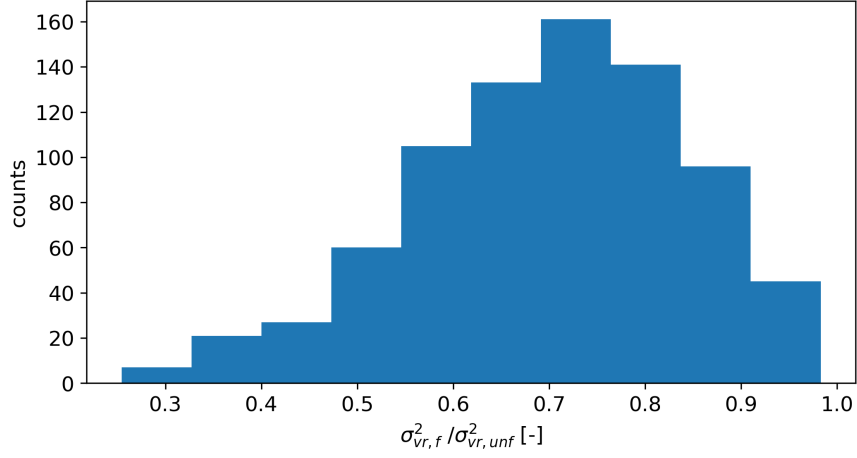
12

Figure 9. (a) Estimated $\sigma^2_{v_{r,f}}/\sigma^2_{v_{r,\text{unf}}}$ compared to the ratio of TI to SATI in the system. (b) Distribution of the estimated $\sigma^2_{v_{r,f}}/\sigma^2_{v_{r,\text{unf}}}$.
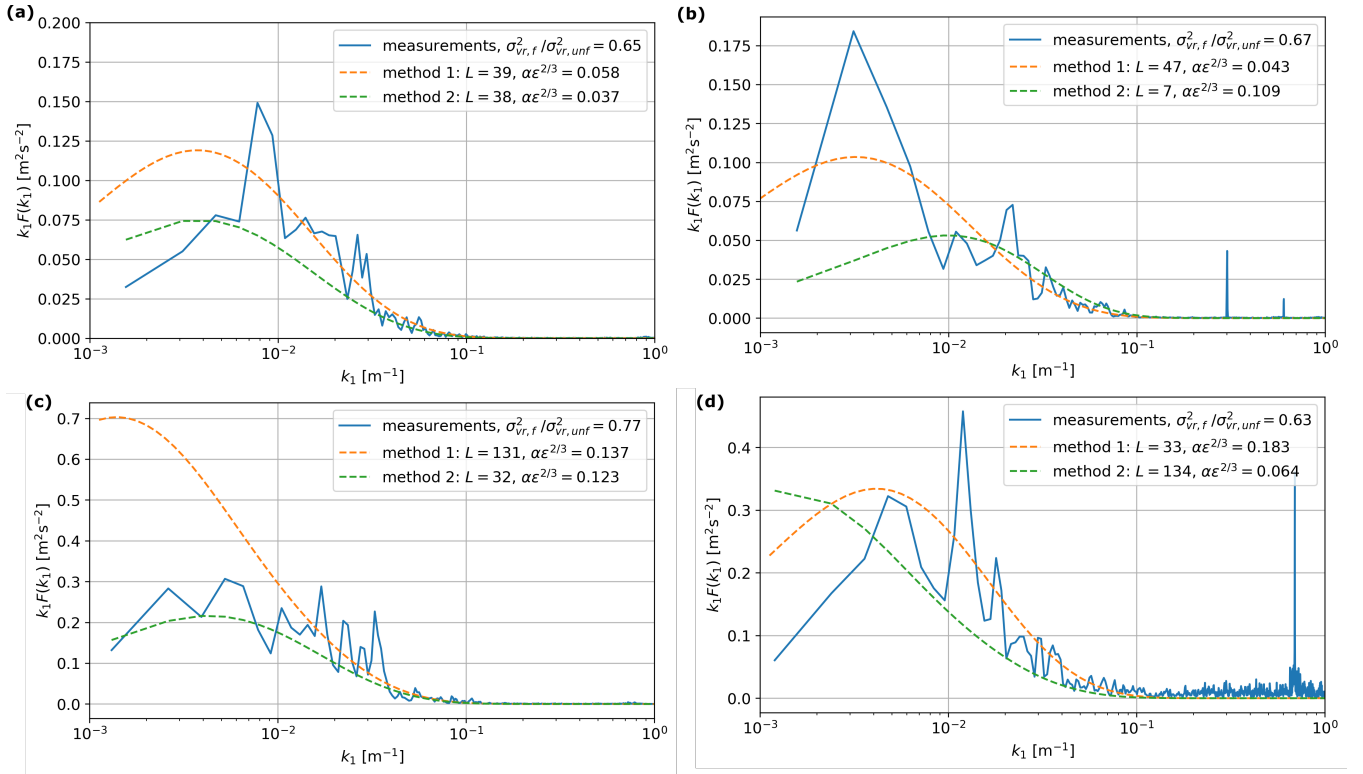

Figure 10. The estimated L, $\alpha\epsilon^{2/3}$ (in legends) and the modelled radial velocity spectra (dashed lines) from the measured radial velocity spectrum (solid line) in three periods of 30 min. The two methods are described in Section 2.4.

13

6 Discussion

This manuscript is under preparation, so there are still many things that could be improved. First, we study the relations of the wake shape, characterized by the power deficit of two wind turbines inside a wind farm, with the ambient atmospheric turbulence intensity measured by a single-beam nacelle lidar. The wake shape is fitted with a parabolic curve to the samples. The samples can be smoothed and averaged in moving wind direction bins. Due to the limited number and the dispersal of points, the fittings are involved with some uncertainties, which should be evaluated and plotted in Fig. 7. In addition, despite using the constraint on the wind speeds, we cannot totally exclude the influence of the thrust coefficient on the wake behavior due to the lack of the turbines' thrust curve. We plan to verify the findings with a narrower wind speed bin.

The turbulence length scale and dissipation rate of the ambient flow are estimated from the single-beam lidar measurements using two methods. Both methods fit the theoretical radial velocity spectrum from the model to the measured one assuming the anisotropy is 3.5. Additionally, The first method uses the amount of attenuation of the lidar-measured turbulence by the probe volume. Since there are no point-wise anemometers near the upstream wind turbine, such as the cup and sonic anemometers, it is hard to verify the estimated parameters. International Electrotechnical Commission suggests that the length scale parameter of the Mann model at the hub height of our reference wind turbine (47 m) should be approximately $0.8 \times 0.7 \times 49 = 27.44$ m. Comparing the two methods, method 1 is model-dependent, and it needs successful estimations of the 'unfiltered' radial velocity variance or the along-wind variance from a sonic anemometer. Method 2 can in principle better capture the whole shape of the measured radial velocity spectrum, but it is sensitive to noises. We are planning to improve the fitting algorithm of method 2 by log-smoothing the spectrum and dropping signals up from the wave number of 10^{-1} m^{-1}.

7 Conclusion

A single-beam lidar is flexible, robust and low in cost. This work shows the potential of using a single-beam CW nacelle lidar for estimating wake losses and studying the wake behavior. By analyzing the power output of two wind turbines inside a wind farm and measurements of a single-beam nacelle lidar on the upstream wind turbine, we found a clear trend that the wake-induced power deficit decreases with the increasing ambient turbulence intensity estimated by the lidar. This trend indicates that the wake recovers faster when the ambient flow is more turbulent. This shows that a single-beam nacelle lidar can potentially aid in wind turbine control and help to make decisions if the turbine needs downrating or more advanced turbine operation modes. The relations between the power deficit and ambient turbulence characteristics can eventually be useful for validating existing wake models (Peña et al., 2014).

Furthermore, we show that the amount of turbulence attenuation by the lidar probe volume varies with turbulence length scale and anisotropy. Based on this, we introduce two methods to estimate the turbulence length scale and dissipation rate from the measured radial velocity spectrum assuming a fixed anisotropy. Due to the lack of references from e.g. cup or sonic anemometers, the estimates cannot be verified. Further work is needed to optimize the fitting algorithms and test the methods. We aim to correlate the estimated length scale and dissipation rate to the wake deficits as we did with the turbulence intensity to study the wake behavior.

References

Aitken, M. L., Banta, R. M., Pichugina, Y. L., and Lundquist, J. K.: Quantifying Wind Turbine Wake Characteristics from Scanning Remote Sensor Data, Journal of Atmospheric and Oceanic Technology, 31, 765–787, https://doi.org/10.1175/JTECH-D-13-00104.1, 2014.

Banakh, V. A., Smalikho, I. N., Köpp, F., and Werner, C.: Measurements of Turbulent Energy Dissipation Rate with a CW Doppler Lidar in the Atmospheric Boundary Layer, Journal of Atmospheric and Oceanic Technology, 16, 1044–1061, https://doi.org/10.1364/AO.34.002055, 1999.

Branlard, E., Pedersen, A. T., Mann, J., Angelou, N., Fischer, A., Mikkelsen, T., Harris, M., Slinger, C., and Montes, B. F.: Retrieving wind statistics from average spectrum of continuous-wave lidar, Atmospheric Measurement Techniques, 6, 1673–1683, https://doi.org/10.5194/amt-6-1673-2013, 2013.

Breton, S. P., Nilsson, K., Olivares-Espinosa, H., Masson, C., Dufresne, L., and Ivanell, S.: Study of the influence of imposed turbulence on the asymptotic wake deficit in a very long line of wind turbines, Renewable Energy, 70, 153–163, https://doi.org/10.1016/j.renene.2014.05.009, 2014.

Fu, W., Peña, A., and Mann, J.: Turbulence statistics from three different nacelle lidars, Wind Energy Science, 7, 831–848, https://doi.org/10.5194/wes-7-831-2022, 2022a.

Fu, W., Sebastiani, A., Peña, A., and Mann, J.: Dependence of turbulence estimations on nacelle-lidar scanning strategies, Wind Energy Science Discussions, 2022, 1–21, https://doi.org/10.5194/wes-2022-85, 2022b.

Hansen, K. S., Barthelmie, R. J., Jensen, L. E., and Sommer, A.: The impact of turbulence intensity and atmospheric stability on power deficits due to wind turbine wakes at Horns Rev wind farm, Wind Energy, 15, 183–196, https://doi.org/10.1002/WE.512, 2012.

Harris, M., Hand, M., and Wright, A.: Lidar for turbine control, National Renewable Energy Laboratory, Golden, CO, Report No. NREL/TP-500-39154, https://www.nrel.gov/docs/fy06osti/39154.pdf, 2006.

Held, D. P. and Mann, J.: Comparison of methods to derive radial wind speed from a continuous-wave coherent lidar Doppler spectrum, Atmospheric Measurement Techniques, 11, 6339–6350, https://doi.org/10.5194/amt-11-6339-2018, 2018.

International Electrotechnical Commission: IEC 61400-1. Wind turbines – Part 1: design guidelines, Tech. rep.

Maeda, T., Kamada, Y., Murata, J., Yonekura, S., Ito, T., Okawa, A., and Kogaki, T.: Wind tunnel study on wind and turbulence intensity profiles in wind turbine wake, Journal of Thermal Science, 20, 127–132, https://doi.org/10.1007/s11630-011-0446-9, 2011.

Mann, J.: The spatial structure of neutral atmospheric surface-layer turbulence, Journal of Fluid Mechanics, 273, 141–168, https://doi.org/10.1017/S0022112094001886, 1994.

Mann, J., Cariou, J.-P., Courtney, M. S., Parmentier, R., Mikkelsen, T., Wagner, R., Lindelöw, P., Sjöholm, M., and Enevoldsen, K.: Comparison of 3D turbulence measurements using three staring wind lidars and a sonic anemometer, Meteorologische Zeitschrift, 18, 135–140, 2009.

Mann, J., Peña, A., Bingöl, F., Wagner, R., and Courtney, M. S.: Lidar scanning of momentum flux in and above the surface layer, Journal of Atmospheric and Oceanic Technology, 27, 959–976, https://doi.org/10.1175/2010JTECHA1389.1, 2010.

Peña, A., Réthoré, P. E., and Rathmann, O.: Modeling large offshore wind farms under different atmospheric stability regimes with the Park wake model, Renewable Energy, 70, 164–171, https://doi.org/10.1016/j.renene.2014.02.019, 2014.

Peña, A., Mann, J., and Dimitrov, N.: Turbulence characterization from a forward-looking nacelle lidar, Wind Energy Science, 2, 133–152, https://doi.org/10.5194/wes-2-133-2017, 2017.

330 Peña, A., Mann, J., and Thorsen, G.: SpinnerLidar measurements for the CCAV52, Tech. Rep. DTU Wind Energy E Vol. 0177, DTU Wind Energy, 2019.

Sjöholm, M., Mikkelsen, T., Mann, J., Enevoldsen, K., and Courtney, M.: Spatial averaging-effects on turbulence measured by a continuous-wave coherent lidar, Meteorologische Zeitschrift, 18, 281–287, https://doi.org/10.1127/0941-2948/2009/0379, 2009.

Sonnenschein, C. M. and Horrigan, F. A.: Signal-to-noise relationships for coaxial systems that heterodyne backscatter from the atmosphere,
335 Applied Optics, 10, 1600–1604, https://doi.org/10.1364/AO.10.001600, 1971.

Taylor, G. I.: The spectrum of turbulence, Proceedings of the Royal Society of London. Series A - Mathematical and Physical Sciences, 164, 476–490, https://doi.org/10.1098/rspa.1938.0032, 1938.

Troldborg, N., Larsen, G. C., Madsen, H. A., Hansen, K. S., Sørensen, J. N., Mikkelsen, and Robert: Numerical simulations of wake interaction between two wind turbines at various infl ow conditions, Wind Energy, https://doi.org/10.1002/we.433, 2011.

340 Wu, Y. T. and Porté-Agel, F.: Atmospheric Turbulence Effects on Wind-Turbine Wakes: An LES Study, Energies 2012, Vol. 5, Pages 5340-5362, 5, 5340–5362, https://doi.org/10.3390/EN5125340, 2012.

17

B | Conference and workshop contributions

B.1 Oral presentations

- Fu, W., Peña, A., Mann, J. and Urban, A.M.: Turbulence characterization using a multiple-, a four- and a two-beam nacelle lidar system (Wind Energy Science Conference, Hannover, Germany, 25-28 May 2021)

- Fu, W. and Peña, A.: Atmospheric turbulence characterization using nacelle-lidar measurements (EAWE's PhD Seminar, Porto, Portugal, 3-5 November 2021)

- Fu, W.: Turbulence estimation from forward-looking nacelle lidars (Lidar Knowledge Europe Joint Industry Workshop, Bilbao, Spain, 4 April 2022)

- Fu, W.: Turbulence estimations from nacelle-lidar measurements (IEA Task 32 TI Round Robin final meeting, online, 5 December 2022)

- Fu, W., Guo, F., Schlipf, D., and Peña, A.: Feedforward control for a 15-MW wind turbine using a spinner-mounted single-beam lidar (Abstract accepted for Wind Energy Science Conference, Glasgow, UK, 23-26 May 2023)

B.2 Poster presentations

- Fu, W., Sebastiani, A., Peña, A., and Mann, J.: Influence of nacelle-lidar scanning patterns on inflow turbulence characterization (EAWE's The Science of Making Torque from Wind (TORQUE) conference, Delft, Netherlands, 1-3 June 2022)

- Fu, W., Peña, A., Mann, J. and Schlipf, D.: Inflow characterization using nacelle lidars with different scanning strategies (EERA DeepWind, Lidar Knowledge Europe: Innovative Training Network side-event, 19 January 2023)